UNIVERSITY OF BIRMINGHAM

Surface Labelling of Gold Nanoparticles with Inorganic Lumophores and Targeting Vectors for Cell Imaging Applications

CHRIS J. STEPANEK

A thesis submitted to the

University of Birmingham

for the degree of

DOCTOR OF PHILOSOPHY

School of Chemistry

PSIBS Doctoral Training Centre

College of Engineering and Physical Sciences

University of Birmingham

September 2017

Contents

0.1 Foreward . . . 1
0.2 Abstract . . . 1
0.3 Acknowledgements . . . 1

1 Introduction **3**
1.1 A Brief History of Gold Nanoparticles . . . 3
1.2 Luminescence Imaging . . . 4
1.2.1 Principles of Luminescence . . . 4
1.2.2 Classes of Luminescent Microscopy Agents . . . 5
1.3 Gold nanoparticles in Biomedicine . . . 11
1.4 Optical Properties of Gold Nanoparticles . . . 11
1.5 Assembly of metal complexes onto gold ganoparticle scaffolds . . . 13
1.6 Cellular Interactions of Gold Nanoparticles . . . 13
1.7 Promoting Cellular internalization of Gold Nanoparticles using Cell Penetrating Peptides . . . 14
1.7.1 The Trans-activating Transcriptional Activator (TAT) Peptide . . . 14
1.7.2 The pH-Low Insertion (pHLIP) Peptide . . . 15
1.8 Detection of Luminescent Gold Nanoparticles within biological Samples . . . 16
1.8.1 Light Microscopy . . . 16
1.8.2 Imaging Mediated by the Enhancing Properties of Gold Nanoparticle Plasmon Resonance 19
1.8.3 Transmission Electron Microscopy . . . 20
1.8.4 Flow Cytometry/ Fluorescence-Activated Cell Sorting . . . 21
1.8.5 Inductively Coupled Plasma Mass Spectrometry . . . 23
1.9 Project Aims & Thesis Outline . . . 24

2 Synthesis and Characterisation of Peptide-labelled, Luminescent Gold Nanoparticles **26**
2.1 Introduction . . . 26
2.1.1 Designing Multimodal Imaging Probes based on Gold Nanoparticles . . . 27
2.1.2 Design of multilabelled AuNPs to target Cancer cells . . . 28

2.2 Results and Discussion . . . 31
2.2.1 Preparation of [Ru(bpy)$_2$(4,4-di-(5-lipoamido-1-pentoxy)-2,2-bipyridine)]$^{2+}$, RubpySS 32
2.2.2 Preparation of Citrate-coated AuNPs . . . 33
2.2.3 Monitoring Nanoparticle Coating via UV/Vis Absorption Spectroscopy . . . 34
2.2.4 Synthesis of pHLIP-stabilised, ruthenium-luminescent Au^{13}NPs . . . 35
2.2.5 Structural & Morphological Characterisation of Peptide-labelled, Luminescent AuNPs 43
2.2.6 Luminescent Characterisation of pHLIP-labelled, luminescent AuNPs . . . 55
2.2.7 Structural & Luminescent Properties of labelled-AuNPs within Buffered Environments 65
2.3 Conclusions . . . 71
2.4 Future Work . . . 73
2.5 Experimental . . . 73
2.5.1 Synthesis of luminescent ruthenium complex, RubpySS . . . 73
2.5.2 Ion Exchange of RubpySS.$(PF_6)_2$ for RubpySS.(Cl_2) . . . 74
2.5.3 Synthesis of colloidal gold . . . 74
2.6 Data Analysis Methods . . . 76

3 pHLIP-mediated uptake of AuNPs into Cancer Cells 78
3.1 Introduction . . . 78
3.1.1 Acidosis: A property of Tumour Cell Microenvironments . . . 79
3.1.2 The pH Low Insertion Peptide (pHLIP) . . . 79
3.1.3 pH Low Insertion Peptides as Cargo Delivery Agents . . . 85
3.1.4 pH Low Insertion Peptides as Delivery Agents for Therapeutics . . . 86
3.1.5 Introduction Summary . . . 88
3.2 Results and Discussion . . . 89
3.2.1 Preliminary Cellular Uptake Experiments . . . 89
3.2.2 pH-Resolved Uptake of Peptide-labelled, Luminescent Gold Nanoparticles . . . 93
3.2.3 Assessing the Effect of labelled-AuNP Treatments on Cell Viability using the 3-(4,5-Dimethyl-2-thiazolyl)-2,5-diphenyl-2H-tetrazolium bromide (MTT) Reduction Assay . 127
3.3 Conclusions . . . 130
3.4 Future Work . . . 132
3.5 Experimental . . . 133
3.5.1 Chemicals and Reagents . . . 133
3.5.2 Preparation of cells for Flow Cytometry/Fluorescence-Activated Cell Sorting (FACS) 133
3.5.3 Preparation of cells for Confocal Microscopy . . . 133
3.5.4 Preparation of cells for Inductively Coupled Plasma - Mass Spectrometry . . . 134
3.5.5 Preparation of cells for Transmission Electron Microscopy . . . 134
3.5.6 Analysing Cell Viability of Nanoparticle-treated HeLa cells . . . 134

4 The effect of Cellular Glutathione on the uptake of Labelled-Gold Nanoparticles into HeLa Cervical Cancer Cells 135

4.1 Introduction . . . 135

4.1.1 Glutathione . . . 136

4.1.2 Glutathione Production . . . 137

4.1.3 Cellular Compartmentalisation of Glutathione . . . 137

4.1.4 Measuring Glutathione Concentration . . . 140

4.1.5 Glutathione and AuNPs . . . 140

4.2 Results and Discussion . . . 141

4.2.1 Quantfication of GSH concentration in HeLa cells treated with Buthionine Sulfoximine and N-Acetyl Cysteine by fluorimetric Assay . . . 141

4.2.2 Measuring Cell viability of [GSH]-modified HeLa Cells by MTT Assay . . . 143

4.2.3 Measuring the uptake of functionalised AuNPs into [GSH]-modified HeLa Cells by Flow Cytometry . . . 145

4.3 Conclusions . . . 153

4.4 Future Work . . . 154

4.5 Experimental . . . 154

4.5.1 Modifying [GSH] of cultured HeLa cells . . . 154

4.5.2 Measuring [GSH] of cultured HeLa cells by fluorimetric assay . . . 154

4.5.3 Analysing Cell Viability of [GSH]-modified HeLa cells . . . 155

4.5.4 Preparation of cells for Flow Cytometry . . . 155

4.5.5 Preparation of cells for Confocal Microscopy . . . 156

4.5.6 Preparation of cells for Inductively Coupled Plasma - Mass Spectrometry . . . 156

5 Lipid-coated AuNPs, co-labelled with a Luminescent Europium Complex 157

5.1 Introduction . . . 157

5.1.1 Lumophores based on Lanthanide Complexes . . . 157

5.1.2 Lanthanide Complexes as Biological Lumophores . . . 158

5.1.3 Gold nanoparticles labelled with Lanthanide Lumophores as Cell Imaging Probes . . . 159

5.1.4 Lipid-coated gold nanoparticles for cell delivery applications . . . 160

5.1.5 Myristic Acid . . . 162

5.2 Results and Discussion . . . 163

5.2.1 Preparation of EuL . . . 163

5.2.2 Preparation of Luminescent, Lipid-coated Gold Nanoparticles . . . 164

5.2.3 Photophysical Characterisation of Luminescent, Lipid-coated Gold Nanoparticles . . . 167

5.2.4 Structural Characterisation of Luminescent, Lipid-coated Gold Nanoparticles . . . 169

5.2.5 internalization of Luminescent, Lipid-coated Gold Nanoparticles by HeLa Cervical Adenocarcinoma Cells . . . 170
5.2.6 Viability of HeLa Cells treated with Luminescent, Lipid-coated Gold Nanoparticles by the 3-(4,5-dimethyl-2-thiazolyl)-2,5-diphenyl-2H-tetrazolium bromide (MTT) reduction assay . . . 173
5.3 Conclusions . . . 175
5.4 Future Work . . . 175
5.5 Experimental . . . 175
5.5.1 Chemicals and Reagents . . . 175
5.5.2 Synthesis of luminescent Europium complex, EuL . . . 176
5.5.3 Synthesis of colloidal gold . . . 176
5.5.4 Preparation of cells for Fluorescence-Activated Cell Sorting (FACS) . . . 177
5.5.5 Preparation of cells for Confocal Microscopy . . . 178
5.5.6 Preparation of cells for Inductively Coupled Plasma - Mass Spectrometry . . . 178
5.5.7 Preparation of cells for Transmission Electron Microscopy . . . 178
5.5.8 Analysing Cell Viability of Nanoparticle-treated HeLa cells . . . 179

6 Project Evaluation & Future Study 180
6.1 Project Conclusions . . . 180
6.2 Future Work . . . 182

7 Materials & Methods 183
7.1 Materials . . . 183
7.2 Molecular Structure Analysis . . . 183
7.2.1 Nuclear Magnetic Resonance (NMR) Spectroscopy . . . 183
7.2.2 Electrospray Ionisation (ESI) Mass Spectrometry . . . 183
7.3 Nanoparticle Structure Analysis . . . 184
7.3.1 UV/Vis Absorption Spectroscopy . . . 184
7.3.2 Laser Doppler Velocimetry/Dynamic Light Scattering . . . 184
7.3.3 Inductively Coupled Plasma Mass Spectrometry (ICP-MS) . . . 184
7.3.4 Laser Doppler Micro-Electrophoresis . . . 184
7.4 Luminescence Characterisation Techniques . . . 184
7.4.1 Luminescence Spectroscopy . . . 184
7.4.2 Time-resolved luminescence measurements . . . 185
7.5 Cell Culture . . . 185
7.6 Flow Techniques . . . 185
7.6.1 Fluorescence-Activated Cell Sorting (FACS) . . . 185

7.7 Nanosight . . . 185
7.8 Imaging Techniques . . . 186
7.8.1 Confocal Microscopy . . . 186
7.8.2 Epifluorescence Microscopy . . . 186
7.8.3 Transmission Electron Microscopy . . . 186
7.9 Colorimetric Assays . . . 186

Bibliography **187**

8 Appendices **213**

0.1 Foreward

"It is xenophobia and ignorance that threaten conflict, not alliances and friendships." – Unknown author, and unfortunately relevant in 2017.

0.2 Abstract

Transition metal complexes are attractive imaging probes as they offer distinctive photophysical, electrochemical and synthetic advantages over organic dyes, quantum dots and fluorescent proteins due to their high photo-stability, long luminescence lifetimes and large Stokes shifts. Gold nanoparticles have also revolutionised the design, delivery and functionality of imaging probes, being attractive scaffolds to bind luminescent complexes, targeting vectors and therapeutic substances. Previous work in the group has demonstrated that gold nanoparticles can be efficiently coated with transition metal complexes, with the resulting coated particles useful in cellular imaging. In this work, a water-soluble luminescent ruthenium complex and pH-low insertion peptides (pHLIPs) were coupled to gold nanoparticles, and these labelled-nanoparticles exhibited enhanced uptake into human cervical adenocarcinoma cells. The mechanism of pHLIP-mediated nanoparticle delivery was investigated, by conducting time and pH resolved experiments, with an interest in contrasting the benefits of two pHLIP variants as nanoparticle delivery vectors. Subsequent investigations revealed the concentration of intracellular glutathione imposed an effect on nanoparticle internalization efficiency and the colloidal stability of labelled gold nanoparticles, and that providing gold nanoparticles with a hydrophobic lipid coating also enhanced the efficiency of nanoparticle internalization into cells.

0.3 Acknowledgements

In all honesty I have a lot of people to thank for helping me get to where I am.

I would firstly like to thank my supervisors, Nikolas Hodges, Iain Styles, Steve Thomas and Zoe Pikramenou for helping me work towards my PhD. I'd also like to give thanks to the brilliant members of my research group, John, Shani, Siobhan, Sunil, Sam, Sully & Abiola who even on difficult days always provided support and an enjoyable, thriving work environment.

I would also like to thank Jackie Hamblin, who I am enormously indebted to and who sadly is no longer with us. Without a phone call from her back in 2007, inviting me to visit the University of Birmingham, I would have in all likelihood accepted my offer to the University of Cardiff, and forgotten about Birmingham completely. Thanks to her call, I've had the privilege of studying at a wonderfully exciting & inspiring university, I've met so many wonderful people, and have 9 years worth of memories and experiences that I will cherish for the rest of my life. Your call is probably the smallest single act that has had the largest effect on my life; it's really hard to articulate in just a few lines how grateful I am, and I wish I could thank you in person.

I'm also indebted to my parents and my sister Kathryn, three of the most wonderful people in the world, for the love, support and reassurance that they have always given me to ensure that I've always been OK. And I've also been very lucky to have such a wonderful support network of friends in Birmingham, at home in Chippenham, and now dispersed throughout the country and abroad. I must give a shout out to the UBMC, who provided me with an enormous wealth of friendships, memories and experiences, as well as what I know will be a life-long hobby. And I must mention the Chemical Brethren: my chemistry coursemates who were the first group of people that I properly integrated with in Birmingham, and were the ones who first made Birmingham feel like my home.

I could really spend my entire 50,000 word limit thanking everyone who in some way has provided help, guidance, love, or support to me during my years in Birmingham, and while I'm reluctant to mention names, there are a small group of people who know the spectrum of my being from best to worst, and know how difficult I've found the last four years. Without their love and support, I wouldn't have reached anywhere near a finished PhD. You all have my lifelong love and gratitude.

I hope this thesis makes for an interesting read to whomever may be picking it up from the chemistry library or stumbling across my own copy, and I wish you luck in all your academic efforts.

Chris Stepanek

Chapter 1

Introduction

This chapter reviews the reported uses of gold nanoparticles within biomedicine, providing an introduction into their first discovery, adaptation of synthetic methods, their use as delivery vectors and subsequent applications in imaging/diagnostics and therapeutics. The chapter also contrasts the archetypal metal lumophores available, their photophysical properties, and their development as biological imaging probes. The review then focuses on how surface-labelling gold nanoarticles with a lumophore permits detection within biological samples using a plethora of imaging, spectroscopic and spectrometric techniques.

1.1 A Brief History of Gold Nanoparticles

The noble element Gold, has long been a subject of scientific research, and currently resides in many diverse applications throughout a multitude of fields. While colloidal gold nanoparticles have been known to have been used for centuries in stained glass, they didn't receive scientific evaluation until Michael Faraday began in 1852 [1]. Nanoparticles are defined as ultrafine particles with lengths in two or three dimensions that fall within the boundaries of 1 and 100 nm, and a facile synthetic route for aqueous gold nanoparticles was first pioneered by Turkevich in 1951 [2], refined by Fren in 1972 [3], and since then has had a great number of adaptations. Gold colloids have notable interactions with light and electrons, enabling them to serve as useful contrast agents within light and electron microscopies. These techniques are two of our most valuable tools for investigating intracellular structure and function, thus prompting the increasing presence of gold nanoparticles in contemporary biomedical imaging research. Gold nanoparticles have also strongly influenced the field of theranostics, first appearing in the literature in 2002 [4, 5] where the potential for incorporating diagnostic and therapeutic tools into a single structure is becoming more promising. In contemporary research, gold nanoparticles have been applied to drug delivery [6], DNA delivery [7], plasmonic photothermal therapy [8], photodynamic therapy [9] , and tumour targetting [10, 11, 12], to name a few examples.

1.2 Luminescence Imaging

Light microscopy has revolutionised the way biologists are able to peer inside a cell and visualise intracellular structure and processes. Static environments can be imaged through fixed cell imaging, or functional processes through live-cell imaging[13] [14]. Three very attractive features of light microscopy include firstly the sensitivity, where it is possible for single molecules to be detected, depending on the intrinsic properties of the fluorophore, and within the context of imaging biosystems, also dependent on the amount of background autofluorescence [15]. Secondly, the timescale of fluorescence is rapid, typically ranging from nanoseconds to microseconds depending on the molecular emitter [16], permitting visualisation of rapidly occurring biomolecular processes in real-time, with new adaptations of the technique continuing to push the limits of available temporal resolution.[17] And finally, contemporary super-resolution techniques such as the sophisticated far field techniques of Stimulated Emission Depletion (STED)[16, 18, 19, 20] and Structured Illumination (SIM)[21] along with the pointillism techniques of Photo-activated Localization (PALM)[22, 23] and Stochastic Optical Reconstruction (STORM) [24], which are capable of pushing the spatial resolution to less than 20 nm are becoming more and more routine [25].

1.2.1 Principles of Luminescence

Luminescence is the release of electromagnetic radiation, in the form of light, from a substance that did not receive any heat input. Luminescence was first reported by Sir George G. Stokes in 1852 when he reported red light emission when the mineral fluorospar was illuminated with utraviolet light, and later when he reported a blue glow from a quinine solution under ultraviolet excitation [26]. Luminescence requires an energy input, and although some substances will luminesce after chemical reactions (chemiluminescence), physical agitation (mechanoluminescence), or application of an electical current (electroluminescence) by far the most common form of luminescence is photoluminescence where the absorption of light provides the energy required for emission. The specific energy levels that are involved in luminescence transitions are specific to the luminescent species, and will each have their own unique energy and symmetry. Generally speaking however, in photoluminescence a molecule absorbs incident light and transitions into an electronically excited state, upon which a fraction of moleules that reside in that excited state will relax back to their ground state by radiative decay mechanisms. The time a molecule spends in its excited state can range from femtoseconds to milliseconds depending on the molecular emitter, and the time taken for the number of emitting molecules to decay to $1/e$ (36.8%) is termed the luminescent lifetime. Additionally, another useful measure of a species luminescence is the luminescence quantum yield (Φ_F) which is a ratio of the number of photons absorbed and the number of photons emitted. Becquerel was the first to report that the wavelength of the emission light was longer than the incident wavelength [27], George Stokes also noticed this and this statement later became the Stokes law, with the wavelength difference between incident and emission light being termed the Stokes shift.

1.2.2 Classes of Luminescent Microscopy Agents

Luminescence imaging requires initial staining or transfection of biological specimens with fluorescent markers (fluorophores), often with the intention of marking a specific intracellular compartment or process. Amongst the literature lies a vast arsenal of fluorescent probes with which a microscopist can use. Such probes include organic fluorophores (e.g. fluorescein, BODIPY and anthracene families), inorganic fluorophores (e.g. metallocomplexes, quantum dots) and fluorescent proteins (GFP, RFP, YFP, etc). Unsurprisingly, each class of fluorophore offers advantages and drawbacks.

Organic Dyes as Biological Lumophores

Organic fluorophores may covalently bind to, or associate with their target biomolecule, forming their respective conjugates and there is a very substantial library of organic fluorophores with emission across the UV, visible and Near-IR regions of the electromagnetic spectrum. However, organic fluorophores often undergo radiative decay from their first excited singlet state (S1), leading to small Stokes shifts, and in cases to self-absorption (in the case of fluorescein) making the separation of emission and excitation channels more difficult. They typically have high quantum yields (typically ranging from 40 - 90%) but have similar fluorescent lifetimes to tissue autofluorescence from natural organic components (1 - 10 ns), making time resolved studies difficult. In many cases they are not very photostable, with complicated synthesis, with often poor aqueous solubility [28].

Fluorescent Proteins as Biological Lumophores

Fluorescent proteins have become a powerful tool for imaging living cells or organisms [29, 30]. Gene transfection techniques have provided a remarkable means of studying transgenic organisms, ranging from microorganisms and mammalian cell lines [31], to much larger organisms such as mice [29], zebrafish [32], and the frog Xenopus Laevis [33]. The proteins are naturally occurring, and therefore non-toxic, with similar quantum yields to that of organic dyes. However, some disadvantages include firstly their unfolding requirement in order to become fluorescently active, which can take hours, hence they are unsuitable for imaging rapidly occurring intracellular processes. Secondly, their larger size can affect the functionality, and kinetics of the species being tagged [34], and thirdly they typically exhibit short luminescence lifetimes.

Quantum Dots as as Biological Lumophores

Quantum dots are fluorescent semiconductor nanocrystals [35]. They have had wide use in optical imaging as they offer high fluorescence quantum yields, narrow band luminescence and resistance to photobleaching [36]. In addition, as QDs have heavy metal cores with sufficient electron density, they can be used as imaging agents in electron microscopy [37]. However, while the main photophysical attributes are ideal, QDs are susceptible to blinking behaviour, where periods of no emission between fluorescent periods are common

[38, 39] tailoring size and emission wavelength independently is difficult, their cellular toxicity is under high debate [40].

Inorganic Metal Complexes as as Biological Lumophores

Luminescent metal complexes have found increased widespread use, offering desirable chemical and photophysical attributes not available to their organic competitors. Such general attributes include larger Stokes shift (typically ≈100 nm, as opposed to ≈30 nm from organic fluorophores) owing to luminescence from higher multiplicity states, and significantly longer luminescence lifetimes than organic fluorophores (from hundreds of nanoseconds to microseconds) as luminescence often arises from Laporte forbidden transitions, which are much slower than organic transitions. The complexes are often water soluble, and their synthesis relatively simple often with simple stepwise addition of ligands to the metal centre.

Luminescent metal complexes can be subdivided further to those consisting of a central lanthanide ion, and those consisting of a central transition element ion. The use of lanthanides as luminescent probes is extensive [41, 42]. Some of the advantages lanthanides offer over transition elements are i) longer luminescence lifetimes, more suitable for time-resolved studies, and ii) sharp emission lines, thus permitting use of more fluorescent channels without unwanted luminescence bleedthrough. There are also disadvantages, firstly the lanthanides are poor absorbers as their electronic transitions are Laporte forbidden, and very weak vibronic coupling exists among lanthanides as orbitals are primarily non-bonding. Therefore in order to electronically excite Lanthanides, light absorbing ligands (sensitizers) must be used, which does to an extent limit the functionality of the complex. Additionally, the luminescence quantum yields of lanthanide complexes are typically lower than that of transition metals.

The transition metal series offers a wealth of luminescent species with a range of chemical characteristics and photophysics not accessible to organic molecules; furthermore the relative ease of tuning their spectral properties over organic fluorophores is also appealing. Contrasting with organic fluorophores; fluorescent proteins; luminescent lanthanide complexes and quantum dots; the transition metal series offer i) direct excitation within the visible region of the electromagnetic spectrum, ii) reasonable luminescence quantum yields iii) long luminescence lifetimes, iv) good photostability, v) large Stokes shift (≈ 100 nm), vi) relatively simple synthesis, vii) solubility in water, and viii) are reactively inert, imperative for use as biological imaging agents. The lifetime of transition metal complex emission is very sensitive to the environment of the complex, and as a result will be impacted upon by any change in pH, concentration, O_2 concentration, dielectric constant and potential [43]. This is advantageous as a wealth of luminescence lifetime experiments can be performed, and possession of a long luminescence lifetime increases the sensitivity within time resolved studies.

The archetypal luminescent transition metal complex is ruthenium(II) tris-bipyridine $[Ru(bpy)_3]^{2+}$ (Fig. 1.1). Although $[Ru(bpy)_3]^{2+}$, is not functionally very useful by itself, it is still a good molecular probe starting point as the metal ion in its +2 oxidation state (d^6) will oxidise relatively easily, and the presence of

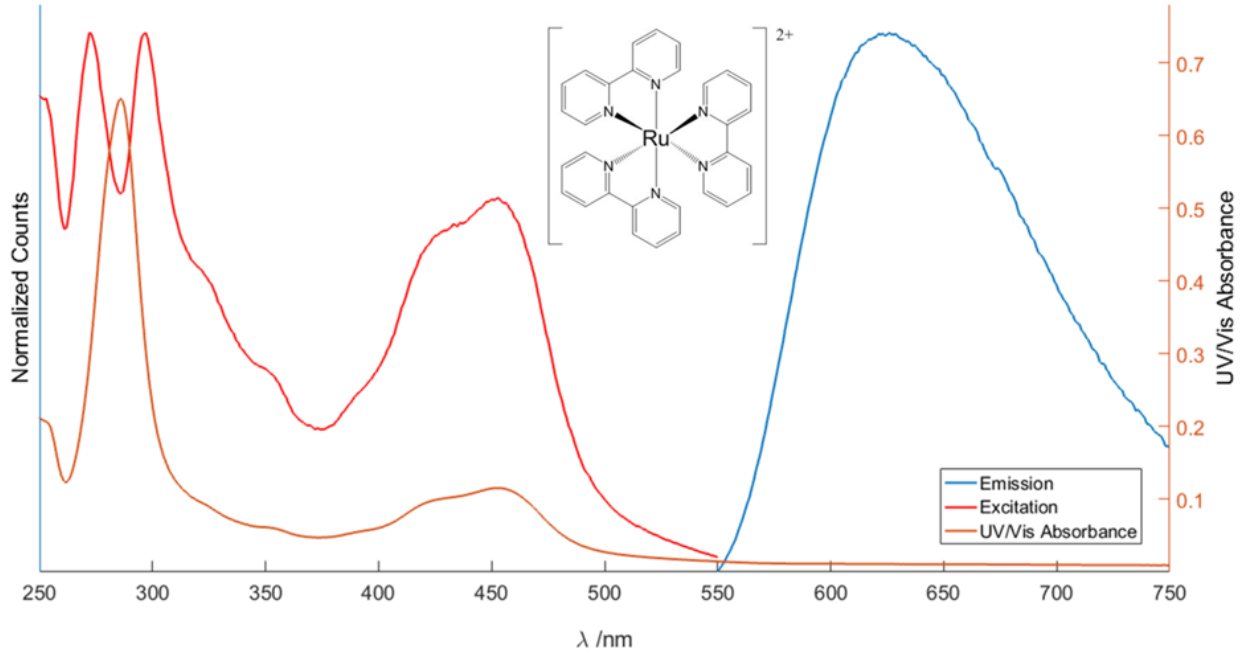

Figure 1.1: UV/Vis absorption, excitation and emission spectra of ruthenium(II) tris-bipyridine (13 μM) in water. Excitation scans were taken with the emission monochromator set to 650 nm, with a 590 nm long pass filter, and for emission measurements the excitation monochromator was set to 465 nm with a 500 nm long pass filter.

strongly $\pi-$accepting bipyridine ligands leads to metal-to-ligand charge transfer (MLCT) transitions to low energy excited states, where energy input required to induce an MLCT transition is in the visible region of the electromagnetic spectrum. This is ideal for compatibility with standard visible lasers which are not as damaging to biological specimens as ultraviolet lasers. Fig. 1.1 shows the excitation, emission, and UV/Vis absorption spectra of $[Ru(bpy)_3]^{2+}$, and Fig. 1.2 shows a Jablonski diagram illustrating the metal-to-ligand charge transfer transitions accessible to a ruthenium trisbypyridine complex. The absorption band at 290 nm is a $\pi^* \longleftarrow \pi$ transition localised on the bipyridine ligand orbitals. The absorption shoulder band at 350 nm is an electronic transition between two of ruthenium's d-orbitals. This transition is weak as the states have the same symmetrical parity which is forbidden by Laporte selection rules, however is allowed by vibronic coupling. The broad absorption band at 450 nm is a ^{1}MLCT transition where a ruthenium d electron is promoted to an excited singlet state on a bipyridine π^* orbital. As a second row transition element, ruthenium exhibits strong spin-orbit coupling, which is an interaction between an electrons spin magnetic moment, and its orbital angular momentum. Ruthenium's possession of a large nuclear magnetic moment, and therefore a large spin-orbit coupling increases the likelihood of the singlet and triplet states having similar vibrational energy, rendering the intersystem crossing transition from singlet to triplet states more favourable [44]. The ^{3}MLCT radiative decay transition under which the excited electron is demoted to the ground state valency orbital is spin forbidden, therefore proceeds slowly with an approximate radiative

lifetime of 500 ns [45] (far longer than typical organic lifetimes of 1 $\longrightarrow$ 10 ns [46]) and a luminescence quantum yield of 4.2% in water [47]. As ruthenium exhibits strong vibronic coupling, the electron also relaxes through a cascade of vibrational levels, this leads to a broad emission band at 650 nm, as seen in the emission spectrum in Fig. 1.1.

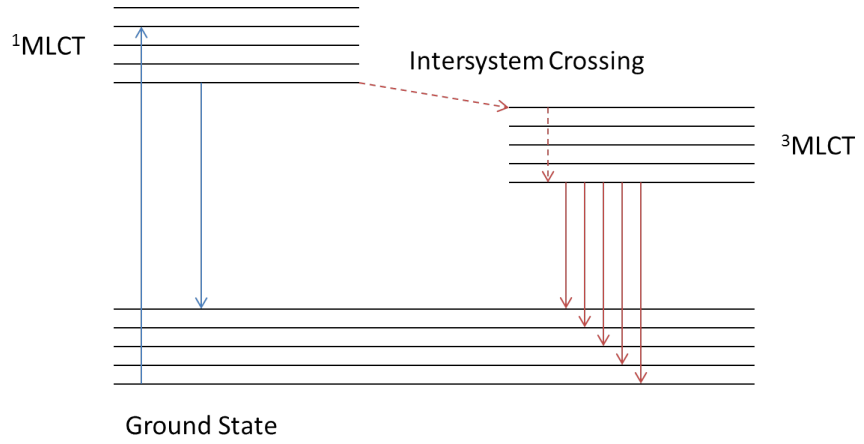

Figure 1.2: Standard Jablonski diagram for a ruthenium polypyridyl complex. Solid lines and dashed lines are radiative and non-radiative decay processes, respectively.

The use of ruthenium as a luminescent probe in light microscopy is well documented. Unfortunately, $[Ru(bpy)_3]^{2+}$ is very poorly uptaken into cells and while cellular uptake is visible after using techniques such as electroporation, transfection and through use of detergents [43], these are not suitable for live cell imaging or in vivo studies. However, it is relatively easy to functionalize this complex for use as a biological luminescent probe by functionalizing the complex ligands. For example it was shown by Puckett and Barton [48] that increasing the lipophilicity of [Ru(bpy)3]2+ bipyridine ligands permits plasma membrane transduction. They also found that incorporation of phenyl rings onto bipyridine ligands results in dramatically increased luminescence of the complex [Ru(bpy)2(dppz)]2+ (dppz = dipyrido[3,2-a:2,3-c]phenazine, a known DNA intercalator) demonstrating the tunability of these complexes. Furthermore, a similar dppz derivative of [Ru(bpy)3]2+ was demonstrated as a proficient cell viability marker within rat hepatocytes whereby the Ruthenium luminescence intensity increases upon DNA binding of the intercalating moiety [49]. Ruthenium also has potential as an oxygen sensor due to the quenching effect of triplet state O_2 on rutheniums triplet excited state [50] where fluorescent lifetime imaging microscopy (FLIM) was used to map O_2 concentrations in macrophages [51, 52]. Further attempts to promote uptake by functionalising [Ru(bpy)3]2+ derivatives have included tethering it to Cell Penetrating Peptides (CPPs) such as the further work by Puckett and Barton [53] where the uptake and localization of a Ru-octaarginine conjugate was studied, and the endocytic path was believed to have changed from passive diffusion of the unconjugated complex to endocytosis for the conjugate.

Recently, ruthenium-based probes have been adapted for in vivo imaging such as the work by Komatsu et

al. [54]. In this work, a ruthenium tris-bypyridine complex was used to image ischemia-based hypoxia within mice, where the quenching effect of molecular oxygen facilitated a boost in signal within hypoxic regions. Gill et al. [55] also reported the synthesis of a dinuclear ruthenium(II) complex where the metal centres were conjugated by a phenazine derivative. This complex was then shown to bind to specific membrane structures such as the lipid-dense endoplasmic reticulum within human breast adenocarcinoma (MCF7) cells, resulting in a comparable cytotoxic effect with anticancer agent, cis-platin. Ruthenium based probes have also found applications within multiphoton excitation, such as the work by Baggaley and coworkers [56]. Here they reported the synthesis of a dinuclear, ruthenium (II) tpphz complex, and demonstrated luminescence lifetime imaging of human breast adenocarcinoma (MCF7) cells, where the ruthenium probe produced a lifetime of 200 ns within the nuclei, and a shorter lifetime of 124 ns within cytosolic regions. Additionally, the complexes bound to DNA through a non-intercalative mechanism, switching on their luminescence.

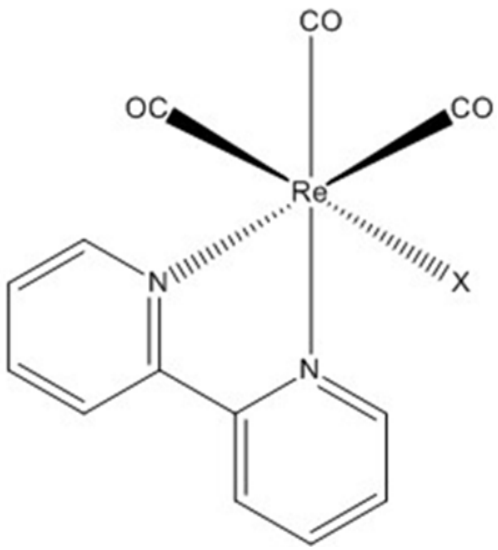

Figure 1.3: Structural formula of the archetypal luminescent rhenium complex, $Re(bpy)(CO)_3X$

Another transition metal complex with very similar properties to ruthenium(II) tris-biypridine is the carbonylrhenium(I) complex $Re(bpy)(CO)_3X$, where X is a monodentate ligand such as a halide or pyridine [57]. These complexes also rely on ^{3}MLCT emission as the main luminescent pathway. Rheniums potential as an imaging agent was explored by Amoroso et al. [58] who synthesized a series of who synthesized a series of rhenium complexes, with varied lipophilicity and polarity, where it was deemed that the $[Re(bisim)L(CO)_3]+$ series offered good cellular accumulation (apparently through phagocytosis), and retainment of their useful fluorescent properties in biological systems without compromising cell viability. Recently, Lo [59] reported the synthesis of a biotinylated thiorea complex that internalized into the golgi apparatus of HeLa cervical adenocarcinoma cells, however it was also reported that biotinylation rendered the complexes less lipophillic, and therefore were less efficiently uptaken into cells.

Among other commonly used archetypal luminescent transition metal complexes include those based on

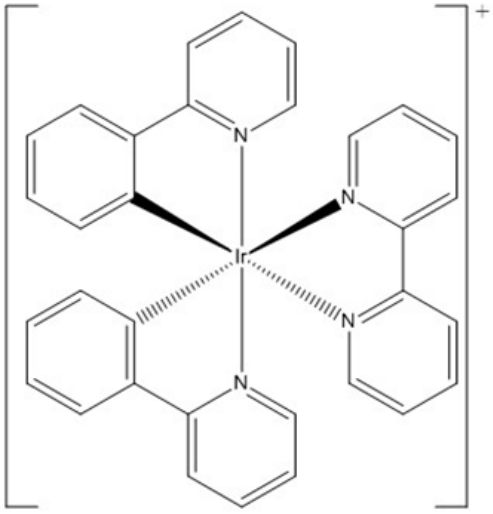

Figure 1.4: Structural formula of the archetypal luminescent iridium complex, $[Ir(NC\text{-}ppy)_2(NN\text{-}bpy)]^+$

iridium $[Ir(NC\text{-}ppy)_2(NN\text{-}bpy)]^+$ [60] and platinum Pt(dpyb)Cl, where their photophysical properties as well as applications in sensing and imaging have been reviewed [61, 62]. Time resolved emission and two photon imaging using an inert platinum complex Pt(dpyb)Cl derivative has been demonstrated by Botchway et al.[63] who reported exceptionally high luminescence quantum yields of upto 70%, and luminescence lifetimes into the microseconds, as well as demonstrating the ability of this complex to function as an emission label within a small variety of eukaryotic cell types. Whilst it is often reported that iridium complexes generally show non-specific localization throughout the cytoplasm, it has been demonstrated that conjugation to DNA intercalators leads to nucleolar localization as reported by Zhang et al. via co-localization with a nuclear stain [64]. The efficient cellular and nuclear transduction is attributed to the high lipophilicity and low net charge of the iridium complex [58]. Additionally, Lo [59] reported the synthesis of a dual-emissive cyclometalated iridium (III) polypyridine complex that when conjugated to a biotin subunit, produced a ^{3}MLCT emission band at 602 nm when mixed with calf-thymus DNA, whereas when the complex was conjugated to a n-butyl group, it produced a vibrationally structured emission spectrum at 490 nm in the presence of avidin. More recently, a series of luminescent Pt complexes was developed by Mauro and coworkers [62] that offered and quantum yields as high as 60% in some cases. Chung et al. [65] developed pH-switchable near infrared emissive platinum complexes that showed efficient uptake into MadinDarby canine kidney (MDCK) cells. De Cola and coworkers [66] developed a series of Pt complexes that were internalized into HeLa cervical adenocarcinoma cells within a few minutes, and demonstrated how intracellular complex aggregation lead to an enhancement of luminescent properties

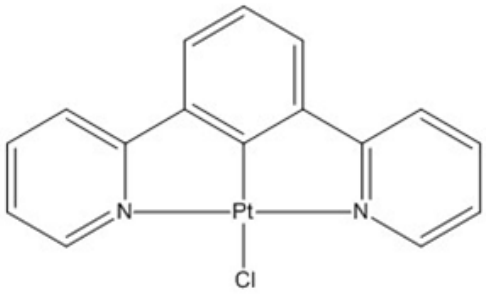

Figure 1.5: Structural formula of the archetypal luminescent platinum complex, Pt(dpyb)Cl

1.3 Gold nanoparticles in Biomedicine

The use of gold nanoparticles within biomedicine has greatly expanded over the last 20 years [67, 68]. They can be synthesised by a variety of facile synthetic methods which offer size and shape tunability throughout the nanoscale [69, 70], producing stable colloids which can be easily functionalised with substances such as thiol-containing substrates and other soft metal binders [71]. Applications of gold nanoparticles within biomedicine include plasmonic photothermal therapy due to their ability to convert light into heat [8, 72]; drug or gene delivery through serving as an inert scaffold which is readily uptaken into mammalian cells [73]; luminescence imaging applications through coating with chromophores [74, 75]; or using electron or dark field microscopies where contrast against cell features is provided by high electron density or coherent scattering through interaction with surface plasmon resonance, respectively [76, 77, 78]. Their resistance to chemical oxidation or degradation, along with low cellular toxicity has also been reported [79], and no apparent plasma membrane disruption [80].

1.4 Optical Properties of Gold Nanoparticles

Gold and indeed other noble metal nanoparticles exhibit useful optical properties from their surface plasmon resonance, an inherent property of some nanoscale materials, where the gold surface electrons coherently oscillate against the restoring force of gold nuclei upon stimulation using electromagnetic radiation at their natural frequency [81]. This manifests itself as a broad absorption band in the visible absorption spectrum (Fig. 1.6), where the band has a Gaussian profile and is modulated by morphology [82], core charge [83], solvent refractive index [84], inter-particle distance [85] and surface functionalization [86]. The SPR band is also dependent on particle structure and shape, and manipulation of these factors has shown to permit the tuning of the SPR band from the visible into the near infrared [87].

Fig. 1.6 shows the size dependency of the SPR band shape, where increasing size of the gold nanoparticle results in a bathochromic shift and broadening of the SPR. It is partly because of this surface plasmon resonance that gold nanoparticles exhibit a colour not accessible to individual atoms or bulk solid. Colloidal

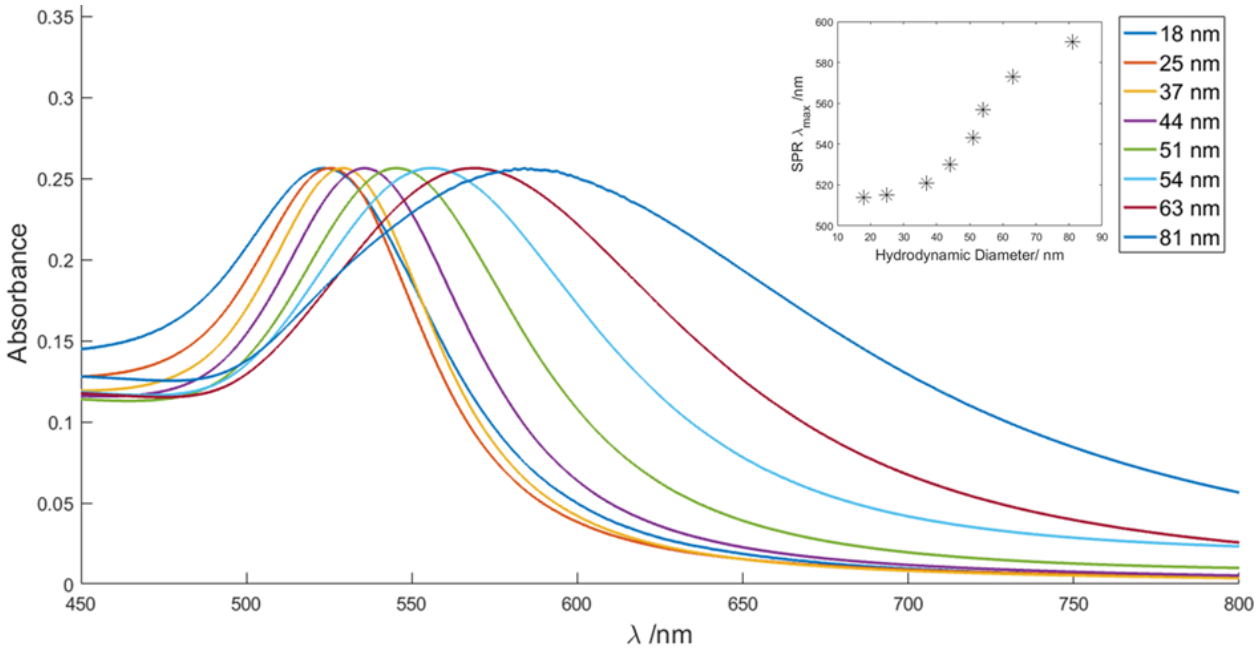

Figure 1.6: UV/Vis absorption spectra showing the nanoparticle size dependency of the surface plasmon resonance band of citrate stabilised gold nanoparticles. Inset, nanoparticle diameter plotted against SPR λ_{max}. Experiment repeated from [88].

gold (particle diameter $<$ 100 nm) absorbs strongly in the blue and green regions of the visible spectrum, but significantly less so in the red region, often giving the particles a deep red colour. As gold nanoparticle size increases, the SPR band shifts further into the red region of the spectrum, leading to a diminishing of the particles red colour.

The introduction of polycrystalline gold nanoparticles has prompted the curiosity of many research groups, due to their unique optical properties and reports of luminescent polycrystalline gold nanoparticles, without the need for a luminescent surfactant began to emerge in the literature [89, 90]. This class of luminescent gold nanoparticles is divided into molecular luminescent nanoparticles and plasmonic luminescent nanoparticles, and their emission bands can be tuned by controlling grain size, particle size, surface ligands and valence state [91]. The class of molecular luminescent nanoparticles are devoid of any surface plasmon resonance due to a low number of free electrons, but nevertheless offer emission within the visible and near infrared regions. As the size of the gold nanoparticles approaches the electron Fermi wavelength of gold metal (0.5 nm), the continuous band structure breaks down into discrete energy states, therefore no longer supporting plasmon resonance but will more closely resemble molecular transitions [92]. Plasmonic gold nanoparticles, and can be synthesised by tuning grain size of a polycrystalline AuNP, and retain their plasmonic properties due to the their continuous band structure. This coexistence of continuous band structure and discrete energy states within the same particle gives rise to strong singe particle emission [93].

1.5 Assembly of metal complexes onto gold ganoparticle scaffolds

The first report of labelling gold nanoparticles with surface bound fluorophores was published in 2000 by Thomas & Kamat [75]. A few years later the first reports of surface labelling of gold nanoparticles with luminescent metal complexes entered publication [94, 95]. Lewis et al. published the first synthesis of water soluble luminescent nanobeads consisting of 13 nm diameter AuNPs coated with a luminescent europium complex [94]. In this approach a neutral europium complex was equipped with terminal thiol groups bound to the complexes organic antenna which covalently bind to citrate stabilized AuNPs after displacing the citrate. This facile synthesis of monodisperse luminescent nanoparticles showed promise for application in cellular imaging. Europium is however, not an ideal cellular imaging lumophore as excitation within the ultraviolet region of the electromagnetic spectrum is required, and radiation within the ultraviolet range is particularly damaging to cellular samples. Transition metals offer direct excitation within the visible region of the electromagnetic spectrum which is far less destructive, and are therefore more suitable for this application. Transition metal complexes are however often charged, depending on the metal and the conjugated ligands, and therefore the nanoparticle coating protocol needs to be adapted in order to coat negatively charged citrate-stabilized nanoparticles with positively charged complexes where nanoparticle flocculation (aggregation) is avoided. There are a few literature examples where ruthenium complexes have been tethered to gold nanoparticles (AuNPs) [96, 97] demonstrating their potential use as imaging probes, furthermore the work of Zedler et al. [98] indicated that the photophysical properties of Ruthenium complexes fully conjugated to the AuNPs are preserved, or only slightly altered by the nanoparticle-complex conjugation.

Recently, Rogers and Claire et al [96] developed an approach for the coating of negatively-charged, citrate-stabilised AuNPs with a positively-charged ruthenium complex. In this work, prior to labelling nanoparticles with ruthenium, the nanoparticles were labelled with the fluorinated surfactant polymer Zonyl 7950 to provide the nanoparticles with a polar coating before the thiol-equipped ruthenium complex was titrated into the solution. This approach permitted the stabilization of larger AuNPs (13 & 100 nm diameter) along with efficient coating of the ruthenium complex.

1.6 Cellular Interactions of Gold Nanoparticles

Recent work in our research group demonstrated that gold nanoparticles labelled with a fluorosurfactant and a ruthenium complex were still readily uptaken (despite their new coating), and localized in perinuclear regions of A549 human alveolar adenocarcinoma cells [96]. One complication in the use of AuNPs as cellular delivery vectors comes when the nanoparticles are exposed to serum proteins within cell media. Exposure to these proteins leads to the formation of a protein corona [99, 100] that coats the NP and represents what the cell sees upon plasma membrane transduction, and ultimately determines the initial interaction of the AuNPs with, or within living cells. This protein corona can have effects on NP charge, size, crystallinity, surface

instability, electronic states and hydrophobicity [101]. Furthermore, it is known that citrate stabilised AuNPs can aggregate within the presence of serum proteins, which can influence cellular uptake of the nanoparticles by three orders of magnitude [102]. Lynch et al. [103] reported a method for quantification of nanoparticle corona proteins as well as rates of association and dissociation. A further drawback with AuNPs is that although they are readily taken up by cells, they are often confined to vesicular regions [77]. An ongoing challenge within the therapeutic industry is to functionalise the AuNPs with substances that mediate their escape from vesicular compartments, and into the cytosol, where a drug might exhibit its therapeutic action.

1.7 Promoting Cellular internalization of Gold Nanoparticles using Cell Penetrating Peptides

The use of cell penetrating peptides as delivery vectors to promote cellular delivery of gold nanoparticles has also been gaining momentum in recent years, particularly for delivery into cancerous cells or tissue. Until recently, many literature examples of gold nanoparticle uptake into tumours are based on manipulation of the enhanced permeability and retention (EPR) effect exhibited by tumour tissue [104, 105], or by targeting specific cancer cell biomarkers [106]. However it has been shown that the EPR effect is small or even non-existent for certain tumour types [107, 108, 109], and targeting specific tumour biomarkers is complicated by tumour cell heterogeneity [110, 111]. There are many examples of using peptides to facilitate nanoparticle delivery into cells [112, 41, 113] and even nuclear targeting [114, 115].

1.7.1 The Trans-activating Transcriptional Activator (TAT) Peptide

The most commonly used CPP is the Trans-activating Transcriptional Activator, a regulatory protein found within HIV-1 and is involved in viral transcription and replication [116]. Interestingly, the protein has an unusual ability to leave infected cells, translocate the membrane of a nearby healthy cell and navigate to the cell's nucleus [117, 116]. The TAT protein sequence has a selection of important domains vital to its function. Firstly, there is the domain essential for transactivation (amino acids 21-40) which is rich in cysteine residues. The next important domain (amino acids 49–72), includes the basic Arg-Lys-Lys-Arg-Arg-Gln-Arg-Arg-Arg motif which facilitates nuclear localisation and RNA binding and finally, (amino acids 73-101) the C-terminal domain contributes to cytotoxic activity in cells [118, 119]. While the full TAT peptide is comprised of 101 amino acid residues, the frequently used truncated version is comprised of 86 amino acids and contains a cysteine-rich region associated with metal dimerization *in vitro* [120], and a highly basic region involved in nuclear and nucleolar localization [121, 122] and causes little disruption to the plasma membrane integrity [123].

The cytotoxicity of TAT has been shown to be strongly dependent on the length of the peptide used, as well as the cargo the peptide is tethered to [60]. HeLa cells have been reported to undergo significant

necrosis when treated with TAT (residues 32 - 60) while this was considerably reduced when treated with TAT (residues 43 - 60) [124].

Richard et al. [125] reported that the rate of uptake of fluorochrome-tagged TAT derivatives into HeLa cells was not affected by a low temperature or depletion of the ATP pool, implying a non-dependence on endocytotic pathways. Different studies have proposed different cell surface proteins as TAT binding sites, including integrins [126, 127] and a 90kDA surface protein[128].

De la Fuente and Berry [129] demonstrated TAT-mediated delivery of gold nanoparticles into the nuclei of telomerase-immortalized primary human fibroblasts (hTERT-BJ1). To prepare the particles, the reduction of chlorauric acid ($HAuCl_4$) with tiopronin (N-(2-mercaptopropionyl)glycine) to form 3 nm diameter tiopronin-capped AuNPs, and the TAT peptide was subsequently conjugated to the carboxylate group of the tiopronin. Further work by Berry [119] demonstrated nuclear localisation of TAT-labelled gold nanoparticles with results very much depending on cell type and size of gold nanoparticles. The uptake and localization of gold nanoparticles within fibroblasts was studied using Transmission Electron Microscopy (TEM), and it was found that 30nm gold nanoparticles were present within the nucleus in significant quantities, and only small amounts remained in vacuoles and mitochondria, thus indicating that the TAT peptide was able to transport the nanoparticles away from endosomal/lysosomal pathways. Additionally, Torchillin et al. [130] demonstrated tat-mediated translocation of plain and poly ethylene glycol coated liposomes (up to 200 nm diameter) into mouse lewis lung carcinoma cells, human breast tumor BT20 cells, and rat cardiac myocyte H9C2 cells. In this instance, internalization was dependent on both the size of the liposomes and the cell type. While TAT is an efficient translocator and delivery agent, it offers little specificity between healthy and cancerous cells. Additionally, the conclusions of almost all reports of TAT-mediated translocation of gold nanoparticles rely on transmission electron microscopy studies only, leaving conjecture over how representative TEM-prepared cells are of their original viable state [125]. In fact a recent report by Wei et al. [131] demonstrated the uptake of TAT-labelled gold nanoparticles into HeLa cervical adenocarcinoma cells where the TAT peptide mediated little to no nuclear delivery of the gold nanoparticles.

1.7.2 The pH-Low Insertion (pHLIP) Peptide

A promising candidate for the targeting of nanoparticles to cancer cells is the pH-low insertion peptide (pHLIP). pHLIP is a short peptide derived from bacterial rhodopsin and was first reported in 1997 by Hunt et al. [132] who reported the spontaneous translocation of a transmembrane helix. pHLIP has received much attention since the its first publication, with numerous derivatives synthesised and its pH-dependent translocation has been demonstrated in a variety of cell types and mouse models [133, 134, 135, 136, 137, 138]. This is a particularly interesting feature of a CPP as cancerous cells have been shown to produce more acidic extracellular regions than healthy cells, owing to higher rates of intracellular glycolysis. This prompted our choice to use pHLIP variants within our functional imaging probe design, and a more comprehensive review of the pHLIP literature is in Chapter 3.

1.8 Detection of Luminescent Gold Nanoparticles within biological Samples

The binding of a luminescent substrate onto an electron-rich core of a gold nanoparticle enables detection of the imaging probe through a variety of light and electron based imaging and cytometric techniques, as well as certain spectrometric techniques.

1.8.1 Light Microscopy

Biologists have access to a plethora of imaging fluorophores and light microscopy techniques that can be significantly tailored to suit the sample type and experiment. Light microscopy encompasses a multitude of microscopy modes in which an image of a sample is constructed by spatially studying its interaction with light. This interaction can be based on transmission, scatter, reflection or luminescence. While chemical fixation is commonly used to prepare samples for imaging resulting in images with less blur, live-cell imaging is also commonly used to image functional processes in real time.

Epifluorescence Microscopy

Fluoresence microscopy is a widely used tool for studying intracellular components and processes. Samples are pretreated with exogenous fluorescent substrates which are termed fluorophores, and are designed to target a specific organelle or intracellular component, while being excitable at a specific wavelength such that they emit light at a useful intensity. The cell biologist currently has access to a wide contemporary library of fluorophores which enables high specificity for sub micron intracellular components and high contrast amid weakly fluorescent background depending on the autofluorescent properties of the sample. The fundamental function of a fluorescence microscope is to irradiate a sample with a specific band and wavelength of light, collect longer-wavelength light emitted from the sample, filter out unwanted excitation light and subsequently direct the emitted light to a detector, where ultimately an image of the sample can be built up. For an epimicroscope, a wide field illumination source such as an arc lamp is used, and the detection method is commonly a CCD camera. Acquisition is typically rapid, as the imaging system will concurrently read and process data from the entire field of view, producing a luminescent map of the sample. Luminescence imaging has high sensitivity, far higher than reflection imaging, and permits the visualisation of gold nanoparticles too small to be imaged by the reflection modality [139, 140].

Epifluorescence imaging permits rapid collection of light from all depths of the illuminated sample, however with no intrinsic filters for light arriving from depths outside the imaging focal plane. Therefore the images often contain significant amounts of image blur, and with limited depth perception it is difficult to perform co-localisation experiments. The technique has been adapted and derivatised into a multitude of more specialised techniques since its conception.

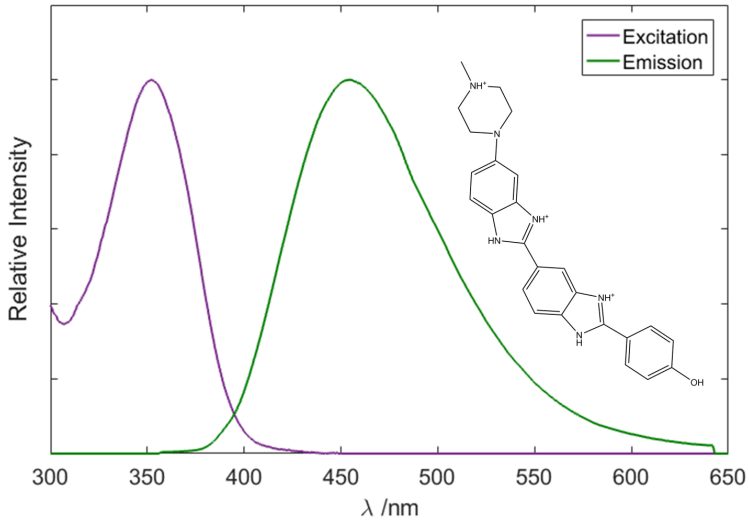

Figure 1.7: Steady state absorption and emission spectra of Hoechst 33258 nucleic acid stain with inset structural formula.

Confocal Microscopy

Confocal microscopy is a more specialised form of light microscopy where the imaging system features optical sectioning hardware, a non-invasive technique for building up 2D images of a small depth of field comparable to 200 nm z-slices of a specimen independently. Confocal Laser Scanning Microscopes (CLSM) are the most widely used, and a basic representation of the fundamental components of a laser scanning confocal microscope is shown in Fig. 1.8.

Briefly, one or more focused beams raster across the specimen, and emission light is collected from each raster point. The emission light is refocused by the objective through the dichroic mirror and into a second pinhole aperture. This pinhole allows light that has been refocused to its small aperture through, and blocks out light originating from depths outside the focal plane. The position of this second pinhole aperture is tunable across the z-dimension, allowing modulation of the chosen image focal plane. Light passing through the second pinhole is then refocused using a second lens and subsequently channelled to a photomultiplier tube detector, and processed into an image.

The principle limitations of this technique revolve around the physical properties of light, where there is a physical limitation on accessible spatial resolution due to the diffraction limit of light. As light propagates away from a point source (i.e a molecular fluorophore), it aberrates and diffracts around objects on its path to collection by the microscope objective. As light aberrates and diffracts, it interferes with itself in either constructive or destructive manners, resulting in the detected signal appearing as a central bright cone, surrounded by a series of diffraction rings, known as a 2-dimensional airy function. The central cone is known as the zeroth-order diffraction spot, and its diameter is dependent on the wavelength of the light and the numerical aperture of the microscope. The size of the zeroth order diffraction spot, as a consequence

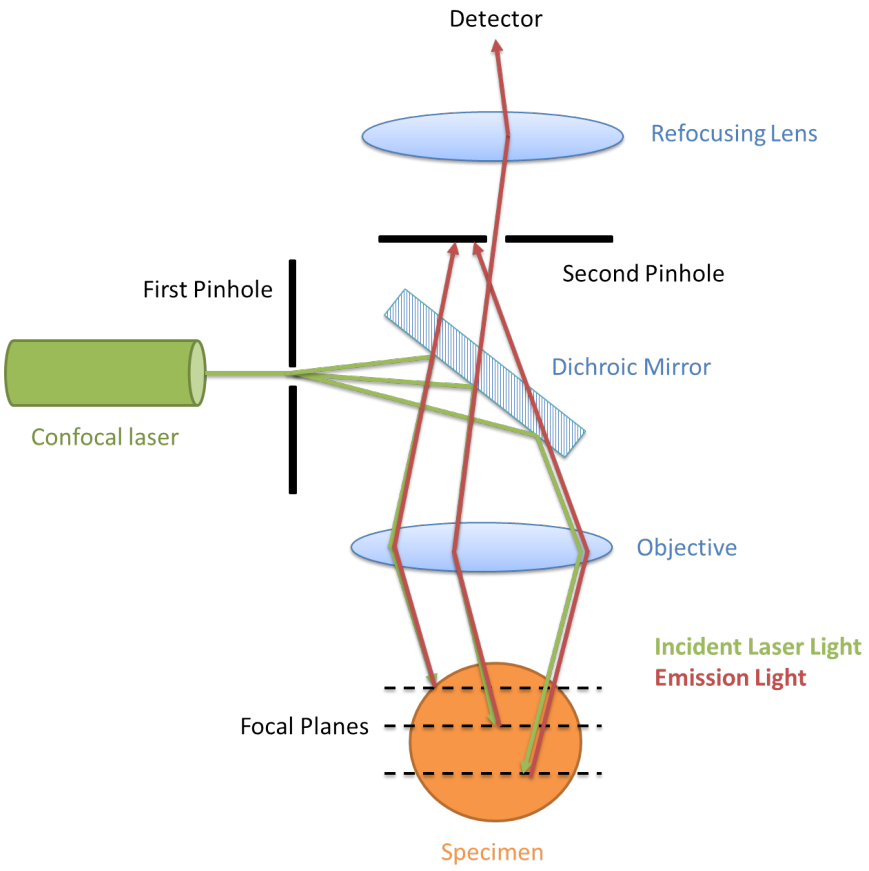

Figure 1.8: Fundamental components of a laser scanning confocal microscope.

of the imaging system, is governed by the diffraction limit which defines the minimum distance between two resolvable point sources. For two or more point sources that are nearer in space than the diffraction limit, their airy functions will overlap too considerably for them to be discernible, and instead of appearing as individual point sources, appear as a single point source. The mathematical definition of the diffraction limit is defined as (Abbe Resolution$_{x,y}$) $= \lambda/2NA$ where λ is the wavelength of light, and NA is numerical aperture, which itself is defined as $NA = n * sin(\theta)$, where n is the refractive index of the imaging medium (e.g, air, water or oil) and θ is the aperture angle. Additionally, there is also a limit on achievable temporal resolution which is primarily due to the time required to raster across the field of view, however that is being countered with more contemporary spinning disk methods [141].

Most contemporary confocal microscopes can also be operated in reflectance mode, and individual and clusters of gold nanoparticles that are of a diameter close to the diffraction limit can be easily visualised by surface plasmon resonance scattering [142, 143]. The technique of confocal microscopy has facilitated in somewhat routine imaging of luminescent gold nanoparticles within cells [144, 145, 146, 139, 96].

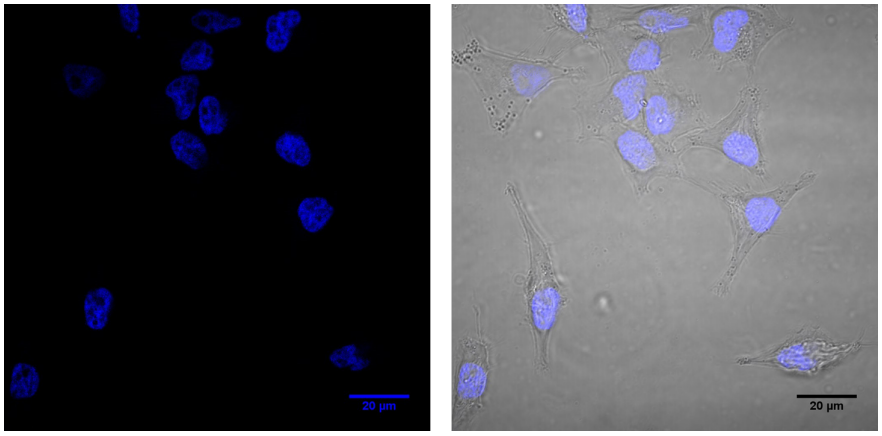

Figure 1.9: Confocal microscopy image of cells treated with Hoechst 33258 nucleic acid stain. Hoechst luminescence from excitation at 405 nm (left) and an overlay of hoechst emission and transmitted light image at 488 nm (right).

1.8.2 Imaging Mediated by the Enhancing Properties of Gold Nanoparticle Plasmon Resonance

Recent advances have been made within the application of gold nanoparticles within raman and dark field microscopies due to the enhancing nature of gold nanoparticle plasmonic interactions with incident light.

Aioub et al [147] recently developed a technique that revolutionised dark field imaging by utilising the plasmonic properties of gold nanoparticles. It was found that the irradiation of cells treated with spherical gold nanoparticles with light at their surface plasmon resonance frequency, the cells rayleigh scattering underwent a significant enhancement [148, 142]. The intensity of this resonantly scattered light is sensitive to nanoparticle size and aggregation state [149]. This technique, referred to as Plasmon Enhanced Rayleigh Scatter Imaging Spectroscopy (PERSIS) offers real time imaging without photobleaching, or the imaging complications of using multiple fluorescent channels. Aioub et al. applied this technique to the study of anticancer drug efficacy. In short, human oral squamous carcinoma were sequentially treated with gold nanoparticles and an anticancer drug, and the time resolved effect of the drug was monitored by measuring changes in scattered light from cells. Initially the cell's rayleigh scattering remained normal, but increased as cell death progressed [150].

Since the introduction of raman confocal microscopy, where spatially-resolved vibrational raman spectra are taken of the sample in a label free acquisition, spatial resolution improvements have been sought due to the intrinsically weak raman signal arising from intracellular constituents [151, 152]. Gold nanoparticles have been demonstrated to enhance the raman signal of neighbouring biological molecules during the formation of nanoaggregates [153]. Kang et al used targeted plasmonically enhanced single-cell imaging spectroscopy (T-PESCIS), a technique that combines raman imaging with AuNP plasmon enhanced dark field imaging to study cell apoptosis. Briefly, apoptosis was induced in human oral squamous cell carcinoma cells that

had been treated with nuclear targeted-AuNPs, and time resolved monitoring of scattered light intensity provided an assessment of apoptic progression, whereas raman imaging permitted the identification and real time monitoring of cellular events such as protein denaturation, proteolysis, and DNA fragmentation [154].

1.8.3 Transmission Electron Microscopy

Transmission Electron Microscopy (TEM) is a technique that studies the interaction of matter with a plane of projected electrons. A transmission electron microscope consists of three sections: *i)* the electron source *ii)* the image producing system & *iii)* the image recording system. The electron source consists of an electron gun (most commonly a tungsten filament), and a condenser lens that focuses the beam of electrons onto the specimen. Upon transmission through the specimen, some electrons are scattered by regions of high electron density within the specimen, while electrons passing through regions of low electron density are only weakly scattered. Once the beam of electrons has passed through the specimen, a series of sequential lenses magnify the transmitted electron beam for detection by a fluorescent screen. Gold nanoparticles offer good contrast within electron microscopy, as their dense electron clouds scatter incident electrons efficiently. For instance Mat et al. reported imaging of 10, 25 & 50 nm gold nanoparticles within autophagosomes. The technique offers far superior spatial resolution than light microscopy alternatives owing to the much smaller de broglie wavelength of electrons versus visible light. However, biological samples require extensive sample preparation for the ultra high vacuum of an electron microscope, and resultantly are imaged in a state not always truly representative of the original viable sample. Due to the electron dense nature of gold nanoparticles, and the spatial resolution of TEM, there have been many reports of using TEM to visualise gold nanoparticles internalized by cells [119, 130, 139, 146, 96, 77, 155].

Most contemporary electron microscopes are equipped with Energy Dispersive Analysis of XRays (EDAX) detectors, because incident electrons have enough energy to eject electrons from core atomic orbitals. When a core electron is removed, a valence electron drops down to the core orbital from its valence orbital via a radiative process. The energy of the emitted radiation is within the X-ray region of the electron spectrum, and as elements have unique arrangements of electrons, EDAX provides a way of identifying elements within the sample. Fig. 1.10 shows the EDAX spectrum of untreated HeLa cells, overlaid with the EDAX spectrum of HeLa cells treated wth 13 nm diameter AuNPs, where the EDX emission bands at 2, 9 and 11 eV are consistent with reported gold EDX signal [156].

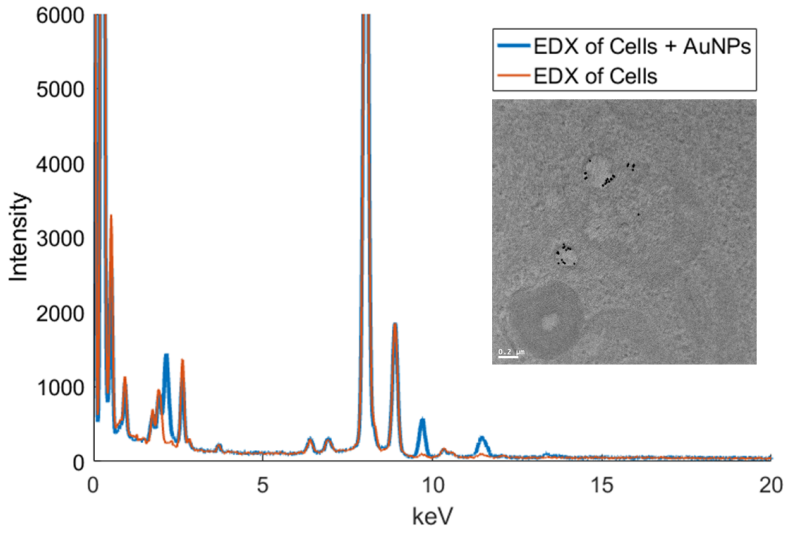

Figure 1.10: Energy Dispersive Analysis of XRays (EDAX) spectrum of HeLa cervical cancer cells treated with 13 nm diameter gold nanoparticles. Inset, TEM image of the region used for spectrum acquisition. Work repeated from [96].

1.8.4 Flow Cytometry/ Fluorescence-Activated Cell Sorting

Flow cytometry, also commonly referred to as Fluorescence-Activated Cell Sorting (FACS) is a technique that passes a fluid of single particles (usually cells) through a beam of light in order to simultaneously measure and record physical characteristics of the particles from their light interaction. These characteristics include size, density, granularity and relative fluorescence intensity.

A FACS cytometer has a flow system that runs the fluid containing the suspended cells through a laser intercept. The particles scatter light as they pass through the laser beam, and fluorescent species on or within the cell are excited, and emission light is separated from excitation light by a combination of filters and dichroic mirrors which also channel the light to the appropriate detectors. Light scattering can be compartmentalised into Forward Scattered light (FSC) and Side Scattered light (SSC). FSC light's main contribution is diffracted light, and detector is positioned at a small angle off the axis of the incident laser line. The principle cell characteristics that affect forward scatter are size and surface topology. Conversely, detected SSC light is constituted of reflected and refracted light, and is more dependent on granularity and internal complexity. If gold nanoparticles are uptaken by HeLa cervical cancer cells, the granularity of the cells increases, leading to more reflection of incident light resulting in greater side scatter signal as depicted by Fig.1.11. The relative increase in SSC signal resultant from AuNP uptake is strongly dependent on quantity of internalized particles, as well as the size of individual particles, both of which impose a strong influence over light reflectance. Experiment repeated from Rogers et al [96].

Fluorescence, as described above, is the photoinduced release of light from a substance. The higher-energy excitation and lower-energy emission light occupy an energy difference known as the Stokes shift and is, along

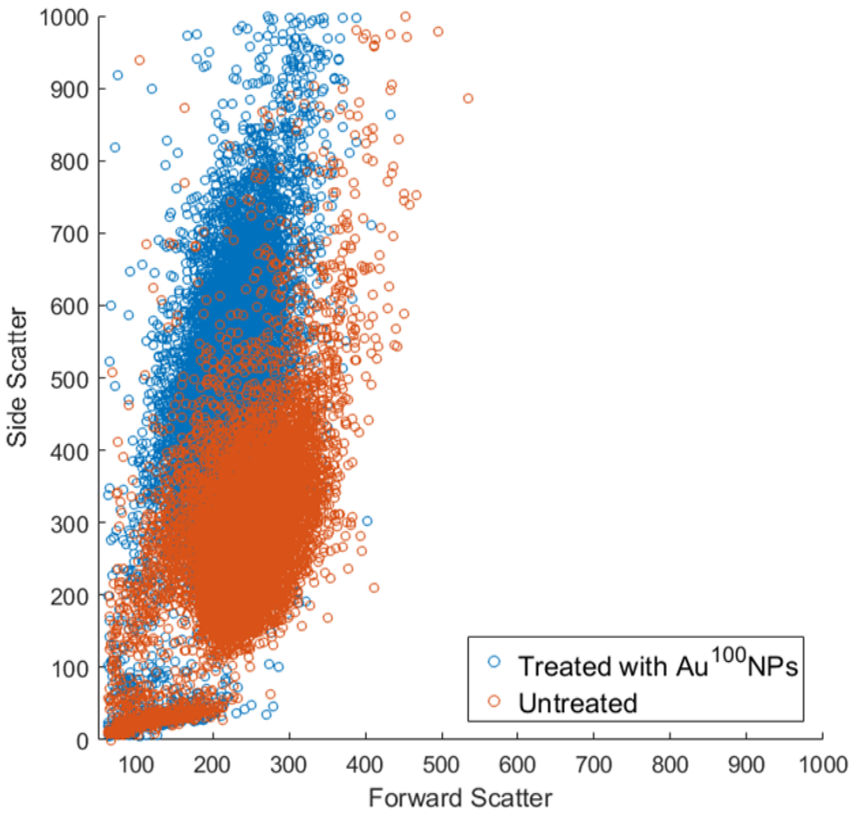

Figure 1.11: Flow Cytometry Forward and Side scatter measurements of HeLa adenocarcinoma cells treated with ruthenium-labelled Au^{100}NPs for two hours. Experiment repeated from [96].

with the quantum yield (the quantifiable measure of fluorescence efficiency), characteristic of the molecular emitter. Flow cytometers are commonly equipped with a variety of laser lines, enabling multiplexing of numerous fluorophores, using suitable filters and dichroic mirrors to separate emission channels prior to detection. However, multiplexing with too many fluophores within a single experiment can incur significant bleedthrough and crosstalk problems.

If fluorescent subtrates are uptaken by cells, while assuming the concentration of the subtrate and the fluorescence quantum yield of the subtrate are both large enough to release a useful quantity of emission light after photo-illumination. Often the quantity of autofluorescent emission light emanating from cells upon excitation is well within the sensitivity range of the instrument, therefore when measuring the luminescence of cells treated with a luminescent substrate it is important to analyse the luminescence of untreated cells in order to establish the magnitude of their contributions to overall signal, as shown in Fig. 1.12 where HeLa cervical adenocarcinoma cells were treated with ruthenium-labelled AuNPs according to the protocol reported by Rogers et al. [96].

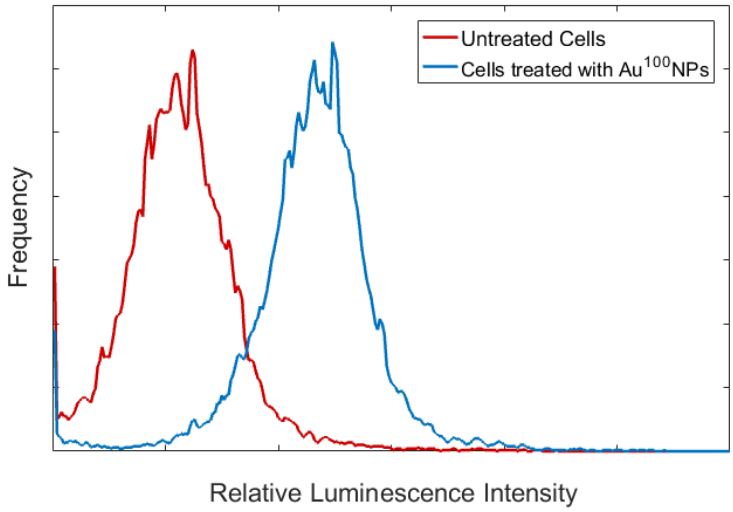

Figure 1.12: Flow cytometry luminescence histograms of HeLa adenocarcinoma cells treated with ruthenium-labelled Au^{100}NPs for two hours. Experiment repeated from [96].

1.8.5 Inductively Coupled Plasma Mass Spectrometry

Inductively Coupled Plasma Mass Spectrometry (ICP-MS) is an technique for determining & quantifying elemental composition of a sample. The technique can be applied to solid, liquid or gaseous samples, although prior to atomisation, solid samples require vaporisation, and liquid samples require nebulisation. Detection limits for ICP-MS are as low as parts per trillion (ppt) and can discriminate between isotopes of the same element.

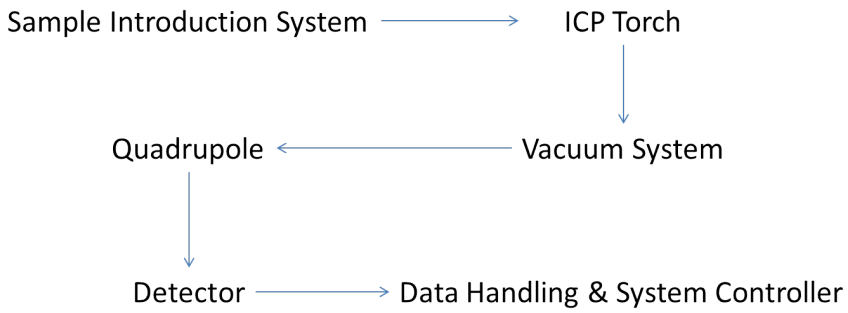

Figure 1.13: Constituents of an inductively-coupled plasma mass spectrometer and the process of data acquisition.

An example of an ICP-MS system is outlined in Fig. 1.13. The sample introduction system consists of a peristaltic pup, a nebulizer and a spray chamber. The ICP torch generates the plasma, and serves as the ion source of the instrument. In the interface, cooled conical aperture plates are used to extract sample ions from the central plasma channel. The vacuum system provides a high vacuum for the ion optics, quadrupole

mass analyser, and detector. The quadrupole mass analyser scans the elemental mass range (3 - 250 amu) while using oscillating currents to channel selected mass:charge ratios (m/z) to detection while deflecting undesired m/z. The detection system commonly involves either direct current measurements via an ion collector or consists a secondary ion generation system that feeds into a multiplier before channelling into an ion collector. Quadrupole mass analysers are more sensitive for higher amu elements than lower ones due to effects such as the zero blast effect, where analysis of small elements is complicated by larger amu ions reach detection despite mathematically unstable paths. Moreover, The use of ICP techniques to quantify AuNP uptake into cells is used relatively routinely [155], and the technique can also be applied to assess the number of heavy metals occupying surface space of gold nanoparticles as studied by Lewis et al [94]. Data included in this thesis all had R^2 values of greater than or equal to < 0.99.

1.9 Project Aims & Thesis Outline

The goal of this work was to develop cancer cell-targeting imaging probes by surface labelling gold nanoparticle scaffolds, whereby sequential labelling processes would provide the nanoparticle with a functional surfactant intended to promote cellular delivery, and a luminescent label to permit visualization. The functional surfactants investigated include cell penetrating peptides, an anionic fluorosurfactant and a lipid carboxylate, and these were each chosen because of their desired interactions with eukaryotic cells. We were also interested in developing the use of inorganic metal complexes as biological lumophores, and to demonstrate the advantages they provide within luminescence imaging of biological samples. The structural, physicochemical and luminescence properties of all labelled nanoparticles were comprehensively characterized, and protocols were refined until labelled-nanoparticles offered good labelling homogeneity and monodispersity, as well as being suitably luminescent for application within fluorescence microscopies and flow cytometry. Additionally, labelled-nanoparticle interactions, internalization and stability within human cervical adenocarcinoma cells was investigated, and the impact of nanoparticle internalisation on cell viability was also assessed. This project represents the opening steps towards the synthesis of nanosized, cancer cell-targeting photothermal therapy agents.

Chapter 1 contains a broad literature review and is a useful prelude to all chapters, however each chapter contains its own introductive literature as a preface to the results. Chapter 2 focuses on the synthetic elements of the project, documenting the synthesis of the luminescent complex RubpySS and gold nanoparticles, and subsequently the labelling of the gold nanoparticles with a pH low insertion peptide and a ruthenium lumophore. The labelled-AuNPs are characterized with a plethora of structural, physicochemical and luminescent characterisation techniques while addressing the benefits and difficulties of synthesising imaging agents using gold nanoparticles and transition metal complexes. The chapter then focuses on how colloidal dispersion and stability of the labelled-AuNPs is affected by adjusting the pH of the colloidal solution to either side of the peptide's pH insertion window (pH 6.5 & 7.4), characteristic of cancerous and healthy cell

peripheral microenvironments. Chapter 3 reports pH-dependent, peptide-mediated delivery of luminescent gold nanoparticles into cancer cells, using a multitude of techniques to study relative and quantified uptake of internalized gold nanoparticles. Cell viability assessments were then performed to study any cytotoxic effects of nanoparticle internalisation. Chapter 4 reports how the concentration of intracellular glutathione, the mammalian cells most prevalent reducing agent, exerts an effect on labelled-AuNP stability and internalization into human cervical adenocarcinoma cells. Chapter 5 reports the synthesis of hydrophobic luminescent gold nanoparticles and demonstrates the effect of the hydrophobic coating on the efficiency of nanoparticle internalization into cancer cells. Chapter 6 provides an overall evaluation of project results and describes what the next direction of the project should be. Chapter 7 reports all materials and methods, including the technical specifications of all instruments used. This is then followed by the thesis bibliography and appendices.

Chapter 2

Synthesis and Characterisation of Peptide-labelled, Luminescent Gold Nanoparticles

2.1 Introduction

Luminescence imaging is a powerful tool that allows the microscopist to image at high sensitivity, low background intensity, and with routine spatial resolutions of approximately 200 nm. These boundaries are continually being pushed, for example the introduction of the Confocal imaging system permitted 'optical sectioning' of specimens, thereby significantly reducing the detection of unwanted unfocused light. Additionally, novel super resolution microscopy techniques such as Stochastic Optical Reconstruction Microscopy (STORM) have pushed spatial resolution limits to around 10 nm [24], and Spinning Disk Confocal Microscopy has reduced the time taken for confocal image acquisition from seconds down to milliseconds [141].

Transmission electron Microscopy (TEM) is an imaging technique that offers nanometer resolution, far superior to that of conventional fluorescence microscopies, and can be applied to biological or materials sciences. The technique involves the measurement of how a plane of electrons projected at a sample are scattered through interactions with the electrons of sample atoms. Regions of high electron-density scatter electrons more so than regions of low electron-density, and image contrast is drawn in a 'bright field' format with white-to-dark scale, where highly scattering elements or structures result in darker regions appearing in the TEM image, and poorly scattering regions appear as brighter regions. When TEM is applied to biological cells, exposure of cell monolayers to an ultra-high vacuum is disastrous for cell integrity, so samples are embedded into a resin for protection from the destructive vacuum. Additionally, most available TEM instruments run at a voltage where electrons projected at a sample are fully attritioned after a path of 200

nm into the specimen, therefore cells are sectioned into slices of 100 nm prior to analysis. For these reasons, there is debate over how representative samples prepared for TEM are of the original, unmodified viable cell sample [157].

2.1.1 Designing Multimodal Imaging Probes based on Gold Nanoparticles

Synthesis of Stable and Monodisperse Colloidal Gold Nanoparticles

The synthesis of colloidal gold was first pioneered by Turkevich in 1951 [2], and later built on by Frens in 1972 who brought attention to the effect that tuning citrate concentration had on particle size [3]. Later Grabar et al. improved the Turkevich method by provided a protocol for more uniformly spherical particles [158], and a number of further adaptations to the Turkevich method have been published [159] including nucleation methods for yielding larger particles while maintaining spherical shape often lost during the synthesis of large gold nanoparticles by direct citrate reduction [69]. There has also been a large focus on biosynthesis of colloidal gold, in order to establish more renewable synthetic protocols. Ahmad et al. [160] developed a protocol for AuNP synthesis using the alkalothermophilic actinomycete, Thermomonospora sp. The enzyme-mediated synthesis yielded 8-9 nm monodisperse particles, without the need for toxic reagents. Singaravelu et al. [161] continued the trend of development of eco-friendly, semi-spherical, gold nanoparticles using an extract of the marine alga Sargassum wightii.

Labelling Gold Nanoparticles with Luminescent Substrates

The labelling of gold nanoparticles with luminescent substrates presents the opportunity to develop a multimodal, nanosized imaging probes where the rich electron density provides useful contrast for electron and light reflectance microscopes, and the luminescent substrate provides the option of luminescence detection by fluorescence microscopies and flow imaging techniques.

Thomas & Kamant [74] developed gold nanoparticles labelled with an organic fluorophore in order to study the fundamental interactions between a metal core and a surface-bound molecular emitter. Wilton later applied this approach to metal complexes, where he studied the binding of transition metal complexes to gold nanoparticles via thiol linkers for catalytic applications and sensing [95], which was later expanded on by Knight et al. [162].

Lewis at el [94] was first to demonstrate the labelling of 13 nm-diameter gold nanoparticles with a luminescent europium complex. The complex was equipped with thiol moieties bound to the complexes phenylamide sensitiser groups that rapidly bind to gold via dative covalent bonds. The labelling process modulated a change in the nanoparticle's surface electric field, resulting in an adjustment of the natural frequency of gold electrons oscillating about the surface of the gold nanoparticles, and this was easily monitored by UV/Vis absorption spectroscopy. After labelling, the particles were purified using a size exclusion resin to remove any unbound complex, upon which steady state and time resolved luminescence experiments confirmed the

unquenched luminescent signal of europium emission. Furthermore, laser doppler velocimetry confirmed an increase in particle hydrodynamic diameter upon europium labelling.

Rogers & Claire et al. [96] developed an approach for the coating of negatively-charged, citrate-stabilised AuNPs with a positively-charged ruthenium complex. Citrate ions initially provide the gold colloid with its stability, and displacement of citrate anions for cationic species can cause nanoparticle flocculation, however, the polar fluorinated surfactant polymer Zonyl 7950 was used to coat the nanoparticles in aqueous solution before the ruthenium complex RuSH was titrated into the solution. This approach permitted the synthesis of monodisperse, stable colloids that bear the luminescent signature of ruthenium. Unlike lanthanide-based chromophores which require ultraviolet excitation, ruthenium is excited by visible light (450 - 490 nm) making it a more desired chromophore.

This zonyl fluorosurfactant approach was then applied by Lewis et al. [163] to 500 nm silica nanoparticles. In this instance, a luminescent iridium (I) complex had been incorporated into the silica particles, before treating the prticles with the zonyl 7950 fluorosurfactant which firstly improved colloidal stability, and offered greater luminescence intensity than the unsurfacted analogue by protecting the environment of the iridium from quenching.

Enhancing the luminescent properties of AuNP-bound chromophores

There has been a long running debate over the luminescence quenching effects that nanogold imposes over surface-bound substrates. It has been reported a number of times that a "near field" effect involving energy or electron transfer between the molecular emitter and the delocalised gold surface electrons [164, 165]. Osborne et al. [166] investigated firstly the effect the distance between the ruthenium centre and the gold nanoparticle surface imposed on ruthenium luminescence, and secondly the effect of gold nanoparticle size on ruthenium's luminescent properties. It has also long been known that molecular oxygen imposes a quenching effect on ruthenium luminescence [50], while this has enabled application of ruthenium-based probes as oxygen sensors [167, 168], for the use of ruthenium as a cellular imaging probe, this is clearly not advantageous. However, this quenching effect experienced by ruthenium complexes in the presence of molecular oxygen has been shown to reduce upon addition of hydrophobic surfactants and when the complex is assembled onto a gold nanoparticle, both for assisting to shield the complex from oxygen diffusion [166, 96]. It has also been reported that local concentrations of $Ru(bpy)_3$ assembled onto AuNP surfaces can exert luminescence quenching effects. For instance, sufficiently high local concentrations result in photo-mediated charge transfers such as the transfer of an electron from an excited molecule of $Ru(bpy)_3^{2+}$ to another nearby $Ru(bpy)_3^{2+}$ molecule producing +1 and +3 oxidation state daughter molecules as shown in Fig. 2.1.

2.1.2 Design of multilabelled AuNPs to target Cancer cells

An enormous benefit of using gold nanoparticles as scaffolds for functional imaging agents lies in the opportunity to multi-label the surface, which is made facile by using thiol moieties to covalently bind subtrates to

$$2Ru(bpy)_3{}^{2+} + h\upsilon \longrightarrow [Ru(bpy)_3{}^{2+}]^* + Ru(bpy)_3{}^{2+} \longrightarrow Ru(bpy)_3{}^{3+} + Ru(bpy)_3{}^{+}$$

Figure 2.1: Photo-induced charge transfers in $Ru(bpy)_3$-labelled gold nanoarticles. Mechanism adapted from work by Pramod et al. [169]

the gold surface. This permits the synthesis of gold nanoparticles co-labelled with a targeting vector and a metal lumophore. In this chapter, pH-low Insertion Peptides were used as targeting vectors for cancer cells, while a luminescent ruthenium complex was used as the lumophore. Highlighted here is an introduction to the pHLIP series.

pH-Low Insertion Peptides

pH Low Insertion peptides (pHLIPs) are a class short peptides (often around 40 residues) which have an increased affinity for plasma membrane transduction under acidic conditions and does not require binding to a specific membrane receptor [170]. From the first publication where Hunt et al reported of 'Spontaneous, pH-dependent membrane insertion of a transbilayer α-helix' [132] in 1997, to date the pHLIP family has evolved and expanded to between $20 - 30$ published variants. While each variant has a unique primary structure mainly consisting of neutral hydrophobic amino acids such as Alanine (Ala, A) and Leucine (Leu, L), the sequence will also contain a number of hydrophillic residues crucial to the peptides pH-switching insertion. These residues give the peptide an overall negative charge, unlike most other cell penetrating peptides which tend to have positive charges, to offer electrostatic attraction to membrane phosphate head groups. The important residues that play an active role in a pHLIP insertion are the Glutamic Acid (Glu, E) and Aspartic Acid (Asp, D), which have been shown to have effective pKas of ≈ 6.5 in close proximity of a plasma membrane. An example of a pHLIP variant is illustrated in Fig. 2.2 where the transduction and flanking domains, as well as positive, neutral and negatively charged residues are highlighted.

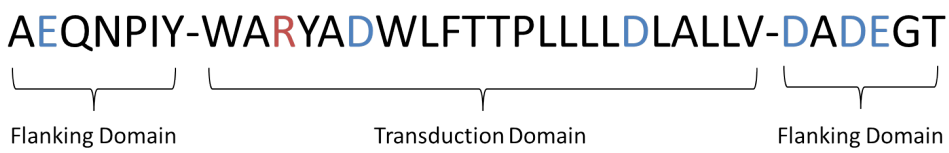

Figure 2.2: pHLIP peptide sequence from the 2010 review by Andreev et al. [133] with the transduction and flanking domains labelled. Positively-charged residues labelled in red; negatively-charged residues in blue, and neutral residues in black.

At pH 7.4 or greater, pHLIP will exist as soluble unstructured monomer units. In the presence of phospholipid bilayers at neutral pH, the peptide will adopt an equilibrium, existing as soluble and membrane-bound unstructured forms, the unprotonated hydrophillic residues anchoring pHLIP at the surface of the plasma membrane [134]. A fall in pH to 6.5, past the pKa values of Glu and Asp will result in their

protonation, rendering the peptide overall more hydrophobic, and increasing its plasma membrane affinity. With its newfound hydrophobicity, the peptide folds reversibly into an alpha helix to arrange its hydrophobic functional groups on the outside of the helix, whist keeping its hydrophilic amide groups away from the hydrophobic environment of the transmembrane space, and inserts itself C-terminus first into the plasma membrane [134]. Andreev et al. reported some of the kinetics of pHLIPs insertion [133]. pHLIP undergoes a rapid (0.1s) interfacial conformation change to a helical structure upon plasma membrane binding at pH 6.5. Insertion of the peptide into the bilayer to form a transmembrane helix is much slower, typically taking $\approx$ 100s. Exit from the bilayer, initiated by a rapid increase in pH leads has a rate 400 times faster than insertion, with the peptide already beginning to unfold whilst still immersed in the bilayer. This pH window of $6.5 - 7.4$ is an important window, as cancer cell microenvironments often have a pH ≈ 6.5, and healthy mammalian cells have a pH ≈ 7.4, thus leading to the use of pH as a general cancer biomarker [171, 172]

Current knowledge of members of the pHLIP family, as well as application pHLIPs as imaging agents and delivery vectors is more extensively reviewed in Chapter 3. pHLIPs posession of an overall negative charge makes it a good candidate to *i)* stabilise the gold sol in the absence of citrate, and *ii)* function as a cell penetrating peptide with a general preference for uptake into cancer cells.

Zonyl FSA Polymeric Fluorosurfactant

In order to assess the efficiency and pH dependency of pHLIP mediated uptake of AuNPs, suitable non-pH switchable control particles are required for comparisons. Zonyl FSA fluorosurfactant has been used by the group as a surfactant for gold nanoparticle coating prior to the labelling of a ruthenium complex. The surfactant consists of a fluorinated alkyl chain with a polar hydrophilic head group, and its binding to gold nanoparticle surfaces through its hydrophillic head group has been reported [173, 174]. Recently, Rogers & Claire et al. reported coating of gold nanoparticles with Zonyl variant permitted subsequent efficient coating with a ruthenium complex, and demonstrated their application as fluorescence imaging agents [96]. Later, Osborne et al. synthesised gold nanoparticles colabelled with Zonyl FSA and a ruthenium complex, and reported an increase in ruthenium luminescence lifetime and quantum yield when Zonyl was added to the solution [166]. Zonyl & RubpySS labelled AuNPs will also have similar size and zeta potential to peptide & RubpySS labelled AuNPs, making the class of Zonyl-Au-RubpySS particles suitable control samples.

2.2 Results and Discussion

In this chapter, the luminescent complex, RubpySS, was prepared by the protocol according to Adams et al. [175]. RubpySS was chosen due its high photostability, excitation by blue light, emission within the red region (reducing likelihood of re-absorption by biological media), large Stokes shift and long luminescence lifetime. Gold nanoparticles of diameters 13 and 100 nm were prepared, and were co-labelled with a pHLIP variant and the RubpySS lumophore via a sequential labelling procedure as shown in Fig. 2.3.

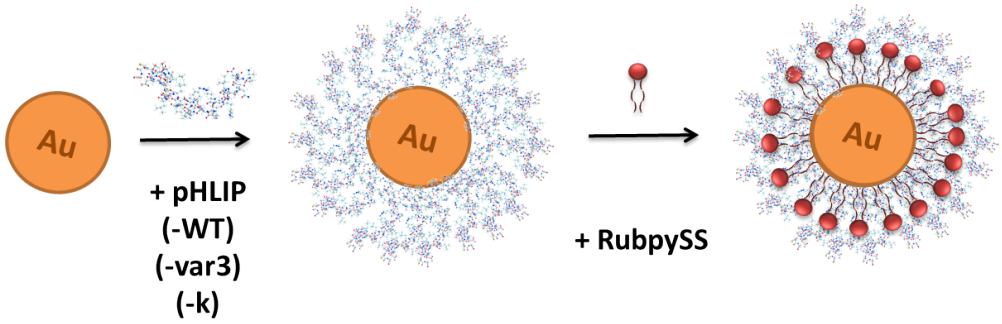

Figure 2.3: Schematic for sequential co-labelling of aqueous AuNPs with a pHLIP variant and ruthenium complex, RubpySS.

The labelled gold nanopparticles were subjected to numerous structural, morphological, physicochemical and luminescence characterisation techniques. The three pHLIP variants, along with their primary structures and charges are shown in Table 2.1. pHLIP is the peptide most widely studied and reported within our group, having a very similar sequence to the original pHLIP sequence reported by Hunt et al. in 1997 [132]. The sequence consists of a central transduction domain with terminal flanking domains on either side, with a mixture of aspartic acid (D) and glutamic acid residues (E) throughout its sequence that control the peptide's pH-switching nature. The peptide is 38 amino acids long with a charge of -5. kpHLIP is an analogue of pHLIP which has undergone lysine substitution for two aspartic acid residues within the transduction domain, reducing its pH switchable nature, thus serving as a suitable control for cell treatments. The peptide is 38 amino acids long with a charge of -3. pHLIPvar3 is a recently created variant published by Weerakkody et al. [176]. This variant had been truncated from the original pHLIP sequence, removing much of the flanking domains on either side of the transduction domain, and the amino acid residues responsible for pH-switching are exclusively aspartic acid residues. The pHLIPvar3 peptide is also shorter with only 28 residues, and has a charge of -4, equating to a higher charge density.

Peptide	Sequence	Charge
pHLIP	AAEQNPIYWARYADWLFTTPLLLLDLALLVDADEGTC(thiopyridyl)G	-5
kpHLIP	AAEQNPIYWARYAKWLFTTPLLLLKLALLVDADEGTC(thiopyridyl)G	-3
pHLIPvar3	ACDDQNPWRAYLDLLFPTDTLLLDLLWC	-4

Table 2.1: Primary structures of pHLIP (38 residues), kpHLIP (38 residues), and pHLIPvar3 (28 residues) peptides used in this work.

2.2.1 Preparation of $[Ru(bpy)_2(4,4\text{-di-}(5\text{-lipoamido-1-pentoxy})\text{-}2,2\text{-bipyridine})]^{2+}$, RubpySS

Ruthenium trisbypyridine ($Ru(bpy)_3$) is the archetypal luminescent transition metal complex, and has been very well studied [177, 178, 179]. RubpySS Fig. 2.4 is an analogue of $Ru(bpy)_3$ designed to bind to gold surfaces whilst maintaining the luminescent signature of $Ru(bpy)_3$. The complex has a ruthenium centre, with two unmodified bipyridine chelates and a third bipyridine chelate equipped with long legs to distance the ruthenium centre from quenching effects on the gold surface [166], and terminal thiol moieties for gold nanoparticle binding. RubpySS was prepared using the protocol developed by Adams et al. [175].

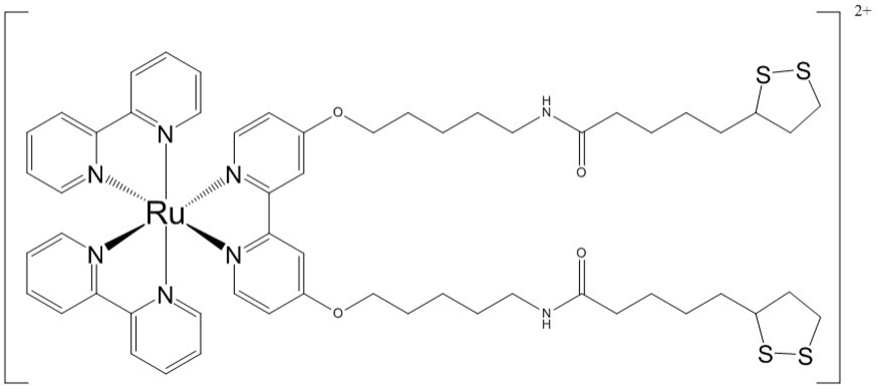

Figure 2.4: Structural formula of $[Ru(bpy)_2(4,4\text{-di-}(5\text{-lipoamido-1-pentoxy})\text{-}2,2\text{-bipyridine})]^{2+}$, RubpySS

The yielded complex was synthesised with PF_6 counterions, and was subjected to ion exchange in Dowex 8x1, 200 MESH ion exchange resin in an acidic environment, to substitute the PF_6 counterions for chloride counterions in order to permit solubility in methanol. The resultant complex exists as a dichloride in aqueous solution (RubpySS.Cl_2) but is herein abbreviated to RubpySS.

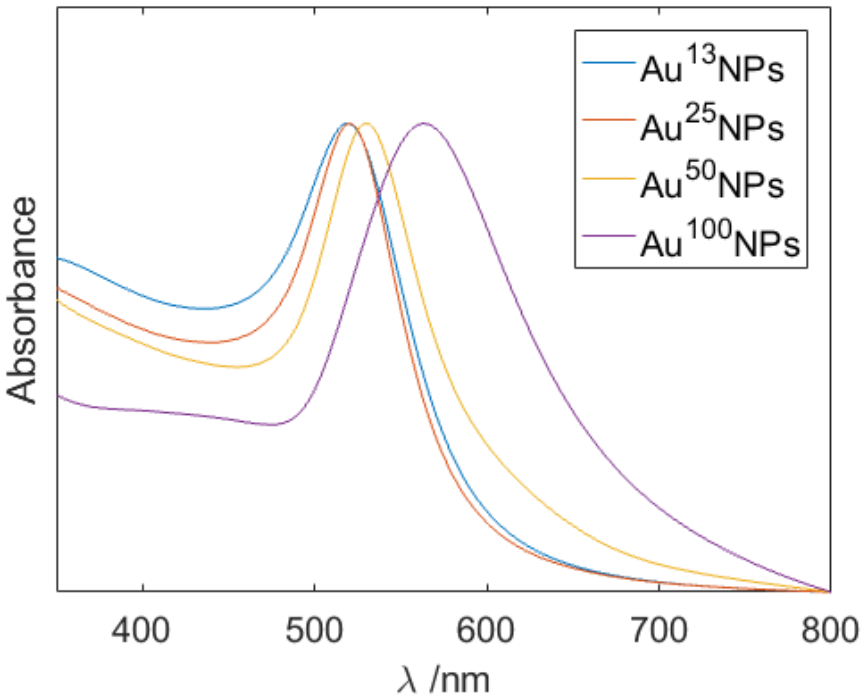

Figure 2.5: UV/Vis absorption spectra of citrate stabilised gold nanoparticles of 13 nm (1.6 nM), 25 nm (0.7 nM), 50 nm (80 pM) and 100 nm (20 pM) diameters in H_2O.

2.2.2 Preparation of Citrate-coated AuNPs

13 nm diameter spherical gold nanoparticles were prepared by previously published methods [158, 159]. Au^{13}NP seeds were then grown up to approximately 100 nm diameter particles using the seeded growth protocol of Ziegler & Eychmuller [69]. This procedure involved growing 13 nm diameter gold nanoparticle seeds (Au^{13}NPs) into 25 nm AuNPs (Au^{25}NPs), followed by another growth step into 50 nm gold nanoparticles (Au^{50}NPs) and a final growth step into 100 nm gold nanoparticles (Au^{100}NPs). These citrate stabilized AuNPs were characterized by dynamic light scattering (DLS) intensity distribution and number distribution along with zeta potential (ζ) measurements and a size dependent characteristic gold surface plasmon resonance (SPR) band in the UV/Vis absorption spectrum. In this work, only Au^{13}NPs and Au^{100}NPs were subjected to surface labelling and cellular uptake experiments.

The UV/Vis absorption spectra of all citrate coated gold nanoparticles are shown in Fig. 2.5, illustrating the size dependency of the surface plasmon resonance band shape and position. The concentration was calculated for each particle size and the pH of the AuNPs was adjusted to 6.5-7.4 before coating.

Coating of AuNPs displaces negatively citrate ions that provide stabilization to the colloidal suspension, in which it was found that direct addition of RubpySS or ruthenium trisbipyridine ($Ru(bpy)_3$) to citrate stabilised gold nanoparticles resulted in nanoparticle flocculation as shown in Fig. 2.6. A solution of

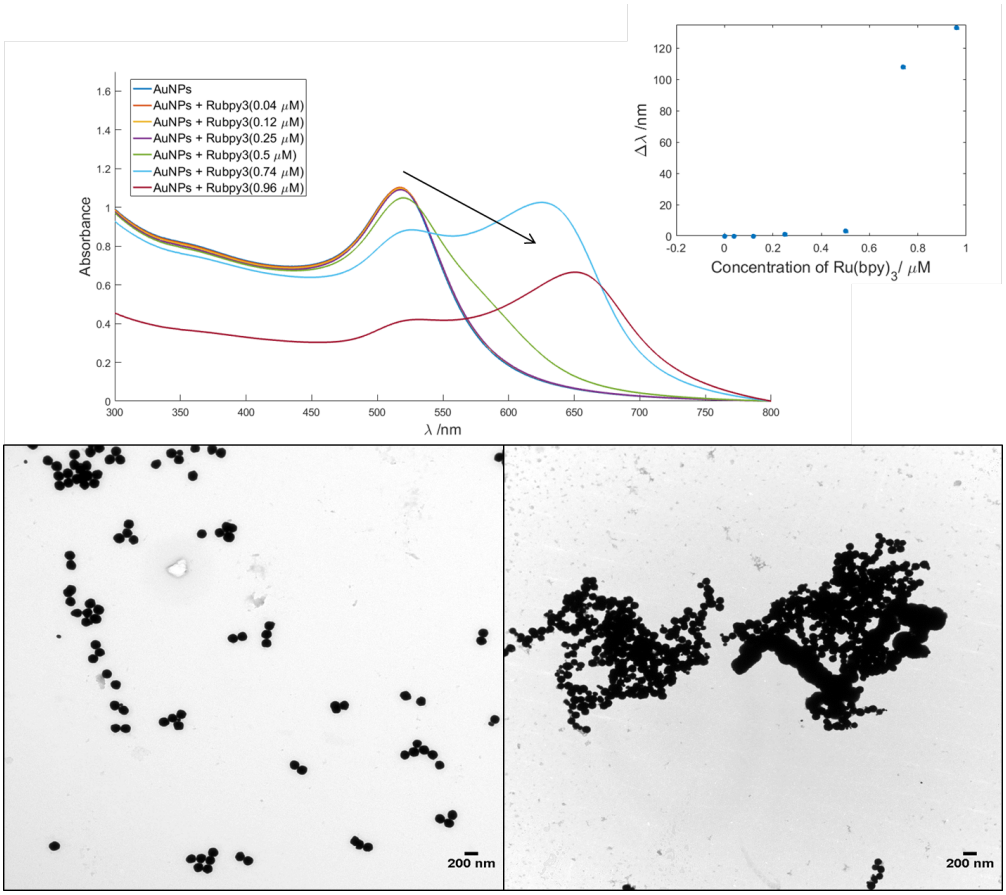

Figure 2.6: UV/Vis absorption spectra (top) monitoring of Au^{100}NPs (4.8 nM, 1.5 ml) during the addition of $Ru(bpy)_3$ (13 μM in H_2O), where inserted arrows indicate the trend of SPR band profile change, and inset SPR λ_{max} shifts as a function of $Ru(bpy)_3$ concentration. And TEM micrographs (bottom) of nanoparticles prior to addition (left) and post-addition (right) of $Ru(bpy)_3$ (13 μM in H_2O).

$Ru(bpy)_3$ (13 μM) was titrated into a rapidly stirred solution of Au^{13}NPs (4.8 nM, 1.5 ml) and before 1 μM of complex had been added, the solution turned a deep purple and the SPR band within the solution's UV/Vis absorption spectrum had bathochromically shifted more than 100 nm as shown in Fig. 2.6. Aggregation was then confirmed by transmission electron microscopy of the particles. Direct addition of RubpySS was also performed, and also resulted in flocculated AuNPs (data not shown).

For co-labelling gold nanoparticles with a pHLIP variant, and the RubpySS complex, coating with the pHLIP variant was performed before labelling with RubpySS, in order to coat the particles with a negatively charged substrate, suitable to stabilize the gold nanoparticles in the absence of citrate.

2.2.3 Monitoring Nanoparticle Coating via UV/Vis Absorption Spectroscopy

Three measurements provide us with an indication of surface changes within the nanoparticle colloid, *i)* bathochromic or hypsochromic shifts of the SPR band, *ii)* Absorbance and *iii)* SPR band full-width-at-half-

maximum (FWHM) broadening/narrowing. In order to extract more sensitive information from UV/Vis data, for each sample a Gaussian model was fitted to the SPR band of the sample's absorption spectrum (Fig. 2.40). The model was fitted to the data using a Levenberg-Marquandt non-linear fitting algorithm, which iterated until acceptable solutions to the SPR λ_{max}, the band intensity and sigma values were found. The LM algorithm incorporates Gradient Descent and Gauss-Newton algorithms, and will switch between the two depending on how close to convergence the algorithm is. With each iteration the parameters of the gaussian model were initially adjusted using the a Gradient Descent approach, and as the algorithm neared convergence, the Gauss-Newton method was predominantly used.

2.2.4 Synthesis of pHLIP-stabilised, ruthenium-luminescent Au^{13}NPs

Binding of pHLIP and RubpySS to Au^{13}NPs

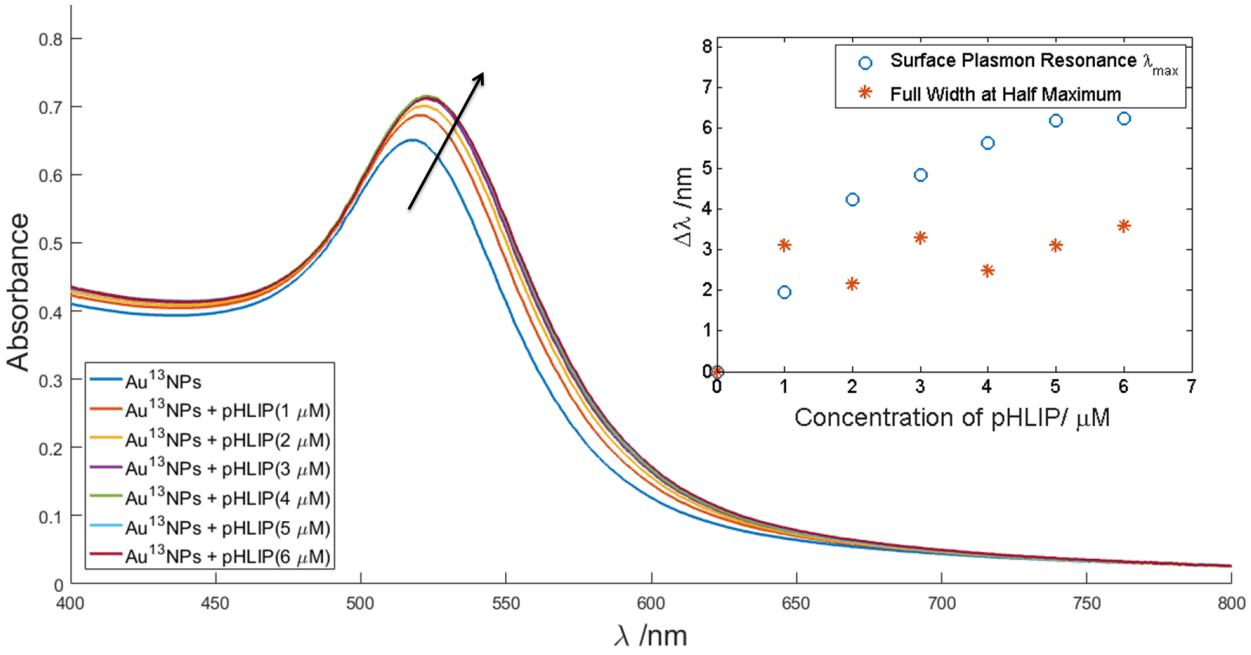

Figure 2.7: UV/Vis absorption spectra monitoring of pHLIP-Au13 preparation. Au^{13}NPs (4.8 nM) were stirred rapidly while 3 μl aliquots of pHLIP (0.5 mM in 5% DMF in PBS) were added upto a final pHLIP concentration of 6 μM.

Au^{13}NPs (4.8 nM, 1.5 mL) were stirred rapidly using a magnetic stirrer such that a stir vortex appeared within the colloid. pHLIP (0.5 mM) was titrated into the stirred AuNP solution in 3 μl aliquots, acquiring a UV/Vis absorption spectrum inbetween each addition. As shown in Fig. 2.7, the SPRλ_{max} bathochromically shifted with each addition of pHLIP. This bathochromic shift of the gold SPR band λ_{max} (Fig. 2.7, inset) upon pHLIP titration was characteristic of a saturation binding curve, consistent with that reported by Davies et al [139], and ceased to redshift after 6 μM of pHLIP had been added to the AuNPs indicating no further changes were occurring on the surface of the nanoparticles. The FWHM of the SPR band did not

show any significant change up to 6 μM addition suggesting no significant aggregation was occurring within the colloid. For the repeat of the procedure, a single aliquot of pHLIP (0.5 mM, 20 μL) was added and colloid was left to stir for 5 minutes. After pHLIP addition, it was noteable that gold SPR had undergone a bathochromic shift (λ_{max} increased to 522 nm), the hydrodynamic diameter of the colloid increased to 15 $\pm$ 4 nm, and Zeta potential decreased to -23 $\pm$ 7 mV.

After the labelling of Au^{13}NPs with pHLIP, a titration of RubpySS into pHLIP-Au^{13} was performed immediately afterwards, and was also monitored using UV/Vis Absorption Spectroscopy, acquiring a spectrum inbetween each 10 μl titre as shown in Fig. 2.8. With each addition of RubpySS, the SPRλ_{max} shifted to a longer wavelength, where the shift eventually plateaued after 7 μM of RubpySS had been added, where the ΔSPRλ_{max} as a function of RubpySS concentration again resembles a saturation binding curve (fig. 2.8, inset).

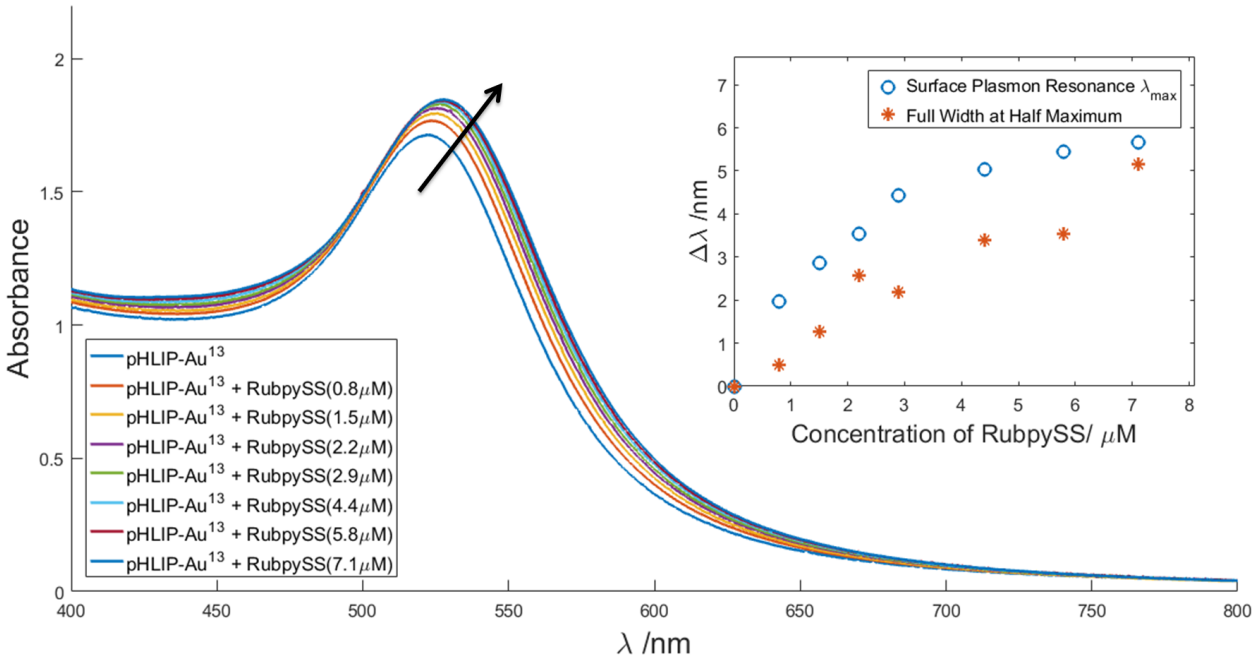

Figure 2.8: UV/Vis absorption spectra monitoring of pHLIP-Au^{13}-RubpySS preparation. pHLIP-Au^{13} nanoparticles were stirred rapidly while 10 μl aliquots of RubpySS were added upto a final concentration of (7 μM) which induced an 5 nm SPR bathochromic shift. The arrow indicates the trend.

A repeat of the procedure whereby a single aliquot of RubpySS (7 μM) was added to pHLIP-Au^{13} resulted in another SPR bathochromic shift (λ_{max} increased to 527 nm), the hydrodynamic diameter of the colloid increased to 19 $\pm$ 5 nm, and Zeta potential decreased to -36 $\pm$ 8 mV. This SPR bathochromic shift of 5 nm is consistent with other reports on the effect of thiol binding on the dielectric constant at a gold nanoparticle surface [86, 180]. It is noteworthy that Lewis et al. [94] reported the labelled 13 nm AuNPs with a methanol-solubilised europium complex where there was no solvatochromic contribution to the SPR of citrate stabilized AuNPs from methanol, so it can be assumed that all contributions to SPR shift are from changes to the

gold surface dielectric constant, resultant from thiol binding. Again the change in SPR λ_{max} as a function of RubpySS concentration resembled a saturation binding curve, with a final RubpySS concentration of 7 μM. The prepared pHLIP-Au^{13}-RubpySS nanoparticles were purified by size exclusion chromatography using fine Sephadex G-25 size exclusion resin with H_2O as the eluent. The functionalised AuNPs eluted rapidly off the column, while uncoated AuNPs and unbound subtrates were retarded by the gel. Fig. 2.9 shows the final UV/Vis absorption spectra from monitoring the preparation of pHLIP-Au^{13}-RubpySS after each stage of preparation. It is noteworthy that the molecular weights of pHLIP and RubpySS both lie within the fractionation region of sephadex-G25, and that uncoated citrate particles aggregated within the column. After purification, particles were subjected to size, charge, dispersity, morphological, elemental and luminescence characterisation, which is presented in future sections.

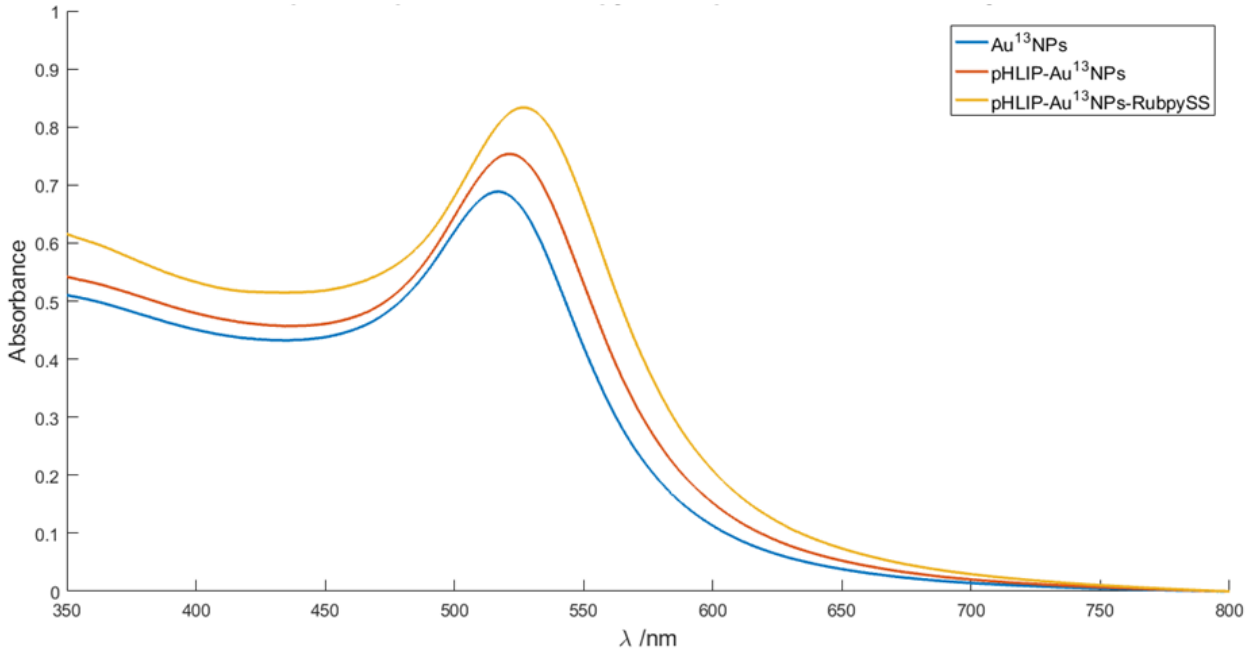

Figure 2.9: UV Vis absorption spectra monitoring of pHLIP-Au^{13}-RubpySS (4.8 nM) preparation. Au^{13}NPs.

Given the nature of dithiol groups to spontaneously form, the possibility of pHLIP and RubpySS binding directly was studied by UV/Vis absorption. Lewis et al. [94] reported the assembly of a heterometallic Lanthanide macrocycle bound via a disulfide bond. The binding event between the macrocycles was monitored using UV/Vis absorption where formation of the disulfide bind resulted in displacement of pyridyl-2-thione from the Terbium macrocycle, which induced the creation of a pyridyl-2-thione absorbance band over time. pHLIP possesses the same pyridyl-2-thione group conjugated to its cysteine residue, so release of the pyridyl-2-thione would indicate the presence of a binding event. The same protocol used by Lewis was applied to pHLIP and RubpySS. RubpySS (25 μM in H_2O, 1 mL) was stirred rapidly before pHLIP (25 μM) was added in a single aliquot to the vortex of the solution. The Absorption spectrum of the solution was taken at regular intervals for an hour and the final solution was analysed using electrospray mass spectrometry.

However no band appeared within the 300 - 400 nm range of the visible absorption spectrum indicating no binding event, and no conjugate was detected using electrospray mass spectrometry, concluding no conjugate between pHLIP & RubpySS spontaneously forms in aqueous solution.

Binding of pHLIPvar3 and RubpySS to Au^{13}NPs

Au^{13}NPs (4.8 nM, 1.5 mL) were stirred rapidly using a magnetic stirrer such that a stir vortex appeared within the colloid. pHLIPvar3 (0.65 mM) was titrated into the rapidly stirred Au nanoparticles in 3 μl aliquots, and a UV/Vis absorption spectrum was acquired inbetween each addition. Fig. 2.10 shows the change in the absorption of Au^{13}NPs as a function of pHLIPvar3 concentration, revealing an SPR(λ_{max} bathochromic shift upon each pHLIPvar3 addition which plateaued after 7.7 μM of pHLIPvar3 had been added.

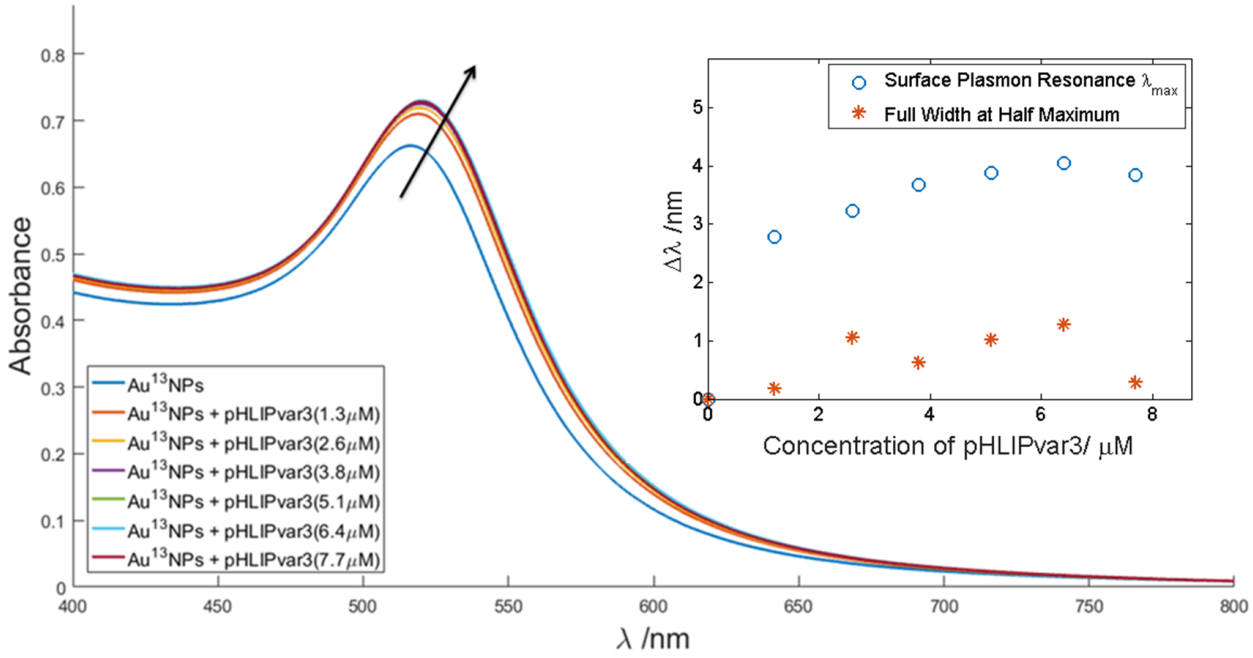

Figure 2.10: UV/Vis Absorption spectrum monitoring the titration of pHLIPvar3 (0.65 mM in 5% DMF in PBS) into Au^{13}NPs (4.7 nM, 1.5 mL).

For the repeat of this procedure, a single aliquot of pHLIPvar3 (0.65 mM, 20 μL) was added and colloid was left to stir for 5 minutes. After pHLIPvar3 addition, it was noteable that gold SPR had undergone a bathochromic shift (λ_{max} increased to 522 nm), the hydrodynamic diameter of the colloid increased to 15 $\pm$ 4 nm, and Zeta potential decreased to -54 $\pm$ 14 mV.

The bathochromic shift of the gold SPR band λ_{max} (Fig. 2.10, inset) upon pHLIP titration was characteristic of a saturation binding curve, which is again consistent with the SPR bathochromic shift reported by Davies et al [139] and ceased to redshift after 7.7 μM of pHLIPvar3 had been added to the AuNPs indicating no further changes were occurring on the surface of the nanoparticles. The FWHM of the SPR band did

not show any significant change up to 7.7 μM addition suggesting no significant aggregation was occurring within the colloid.

After the labelling with pHLIPvar3, the titration of RubpySS into pHLIPvar3-Au^{13} nanoparticles was performed immediately afterwards, and was also monitored using UV/Vis Absorption Spectroscopy.

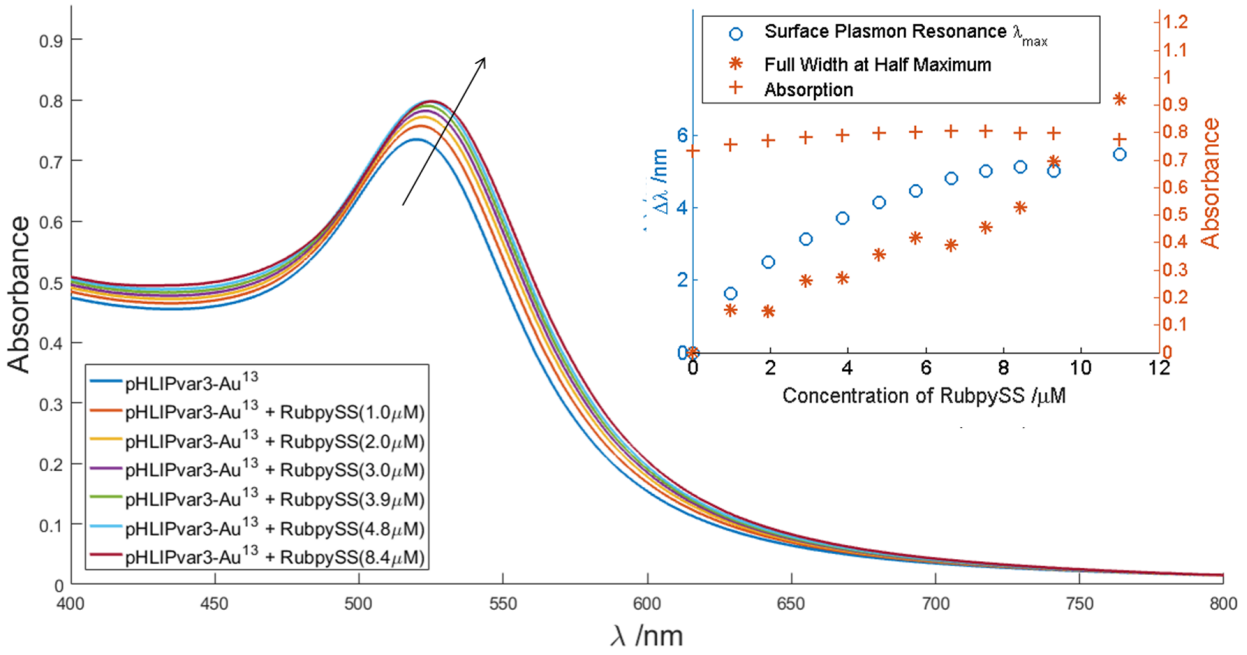

Figure 2.11: UV/Vis Absorption spectrum monitoring the titration of RubpySS (0.15 mM in 10% MeOH in H_2O) into pHLIP-Au^{13}NPs (4.7 nM, 1.5 mL).

Aliquoted addition of RubpySS into pHLIPvar3-Au^{13} nanoarticles (Fig. 2.11) resulted in another bathochromic SPR response which plateaued after 8.4 μM of RubpySS had been added.

Repetition of this coating procedure, where a single aliquot of RubpySS was added to the pHLIPvar3-Au^{13} nanoarticles resulted in another SPR bathochromic shift (λ_{max} increased to 527 nm), the hydrodynamic diameter of the colloid increased to 16 $\pm$ 5 nm, and Zeta potential increased to -30 $\pm$ 8 mV. The bathochromic shift of the gold SPR upon RubpySS addition is again consistent with other reports of gold SPR bathochromic shifts induced by thiol binding [86, 180]. Again the change in SPR λ_{max} as a function of RubpySS concentration resembled a saturation binding curve, with a final RubpySS concentration of 7 μM. Labelled nanoparticles were purified by size exclusion chromatography using fine Sephadex G-25 size exclusion resin with H_2O as the eluent. The functionalised AuNPs eluted rapidly off the column, while uncoated AuNPs and unbound subtrates were retarded by the gel. Fig. 2.12 shows the final UV/Vis absorption spectra from monitoring the preparation of pHLIPvar3-Au^{13}-RubpySS after each stage of preparation.

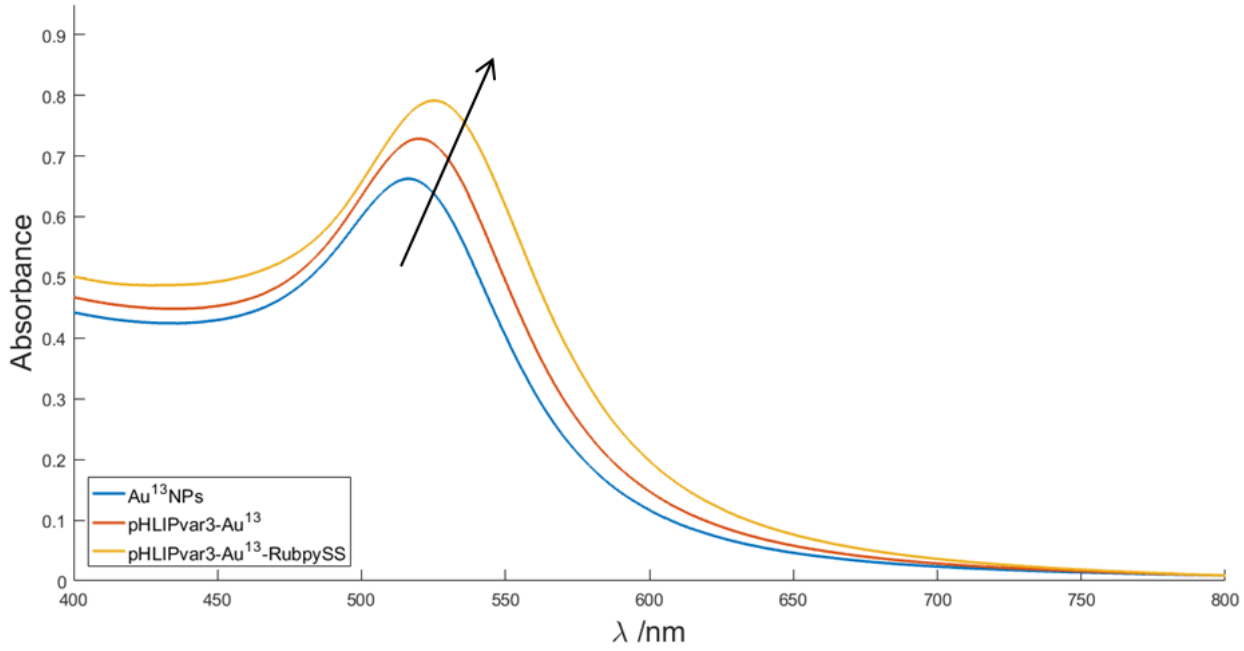

Figure 2.12: UV/Vis Absorption spectrum of Au^{13}NPs (4.7 nM, 1.5 mL) before and after the sequential additions of pHLIPvar3 (7.7 μM) and RubpySS (8.4 μM).

Binding of kpHLIP and RubpySS to Au^{13}NPs

13 nm AuNPs (4.8 nM, 1.5 mL) were stirred rapidly using a magnetic stirrer such that a stir vortex appeared within the colloid. kpHLIP was dissoluted in the same solvent mixture as pHLIP for continuity, however dissolution yielded a cloudy solution, indicative of peptide aggregation as reported for more hydrophobic variants of pHLIP [181, 182]. The gold SPR band was monitored while 5 μl aliquots of kpHLIP (0.5 mM in 5%DMF in PBS) was titrated into the rapidly stirred colloid. The UV/Vis absorption spectra of 13 nm AuNPs during the titration of the kpHLIP peptide is shown in Fig. 2.13. The change in SPR λ_{max} as a function of kpHLIP concentration (Fig. 2.13, inset) this time did not resemble a saturation binding curve, no plateau had been reached even after three times the concentration of pHLIP (which only required 6 μM before saturation), had been added. Subsequent addition of 1 μM of RubpySS into the kpHLIP-Au^{13} solution yielded a purple solution where the gold SPR had strongly redshifted (data not shown). Dynamic light scattering analysis of this solution confirmed the formation of large aggregates znd high polydispersity amidst the inefficient loading with RubpySS (reported in the next section). As the homogeneity of the labelling process along with colloidal stability of kpHLIP-labelled gold nanoparticles could not be sufficiently controlled, kpHLIP-Au^{13}-RubpySS and kpHLIP-Au^{100}-RubpySS were not subjected to *in vitro* cell experiments.

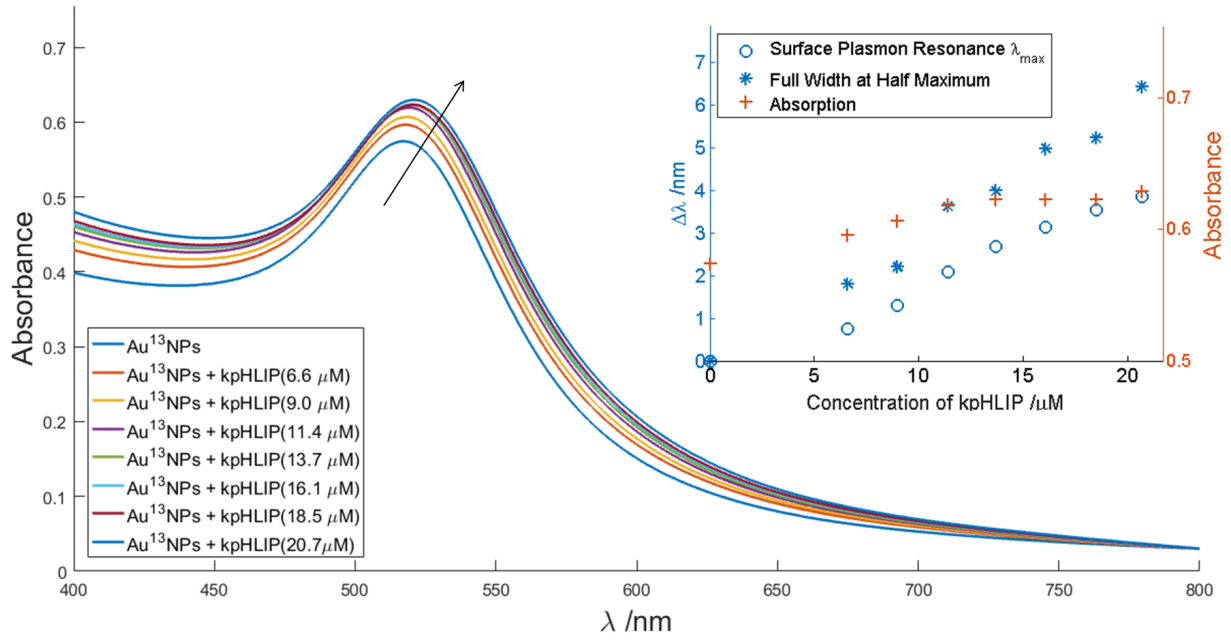

Figure 2.13: UV/Vis Absorption spectrum monitoring the titration of kpHLIP (0.5 mM in 5% DMF in PBS) into Au^{13}NPs (4.8 nM, 1.5 ml). Inset, analysis of SPR absorbance, λ_{max} & FWHM as a function of kpHLIP concentration.

Binding of pHLIP and RubpySS to Au^{100}NPs

100 nm AuNPs (Batch 1, 40 pM, 1.5 mL) were stirred rapidly using a magnetic stirrer such that a stir vortex appeared within the colloid. Prior to addition of surfactants, gold SPR = 597 nm, hydrodynamic diameter = 108 ± 27 nm, and Zeta potential = -45 ± 27 mV. pHLIP (0.5 mM, 10 μL) was added and colloid was left to stir for 5 minutes. After pHLIP addition, it was noteable that gold SPR increased to 600 nm and hydrodynamic diameter increased to 115 ± 28 nm.

Subsequently, RubpySS (0.15 mM, 50 μL) was added to the rapidly stirred colloid in 5 x 10 μL aliquots, and left for 5 minutes. The gold SPR λ_{max} increased to 602 nm (UV/Vis absorption spectra of unlabelled & labelled particles are shown in Fig. 8.7), the hydrodynamic diameter of the particles remained at 115 ± 27 while the zeta potential slightly increased to -42 ± 12 mV. Labelled particles were then purified using size exclusion chromatography using H_2O as the eluent, where particles rapidly eluted off the column leaving a brown colloidal solution.

Binding of pHLIPvar3 and RubpySS to Au^{100}NPs

100 nm AuNPs (Batch 2, 40 pM, 1.5 mL) were stirred rapidly using a magnetic stirrer such that a stir vortex appeared within the colloid. Prior to addition of surfactants, gold SPR = 571 nm, hydrodynamic diameter = 108 ± 27 nm, and Zeta potential = -45 ± 13 mV. pHLIPvar3 (0.65 mM, 10 μL) was added and colloid was left to stir for 5 minutes. After pHLIPvar3 addition, it was noteable that gold SPR underwet a small

increase to 572 nm, hydrodynamic diameter increased to 87 ± 25 nm, and Zeta potential = -42 ± 12 mV.

Subsequently, RubpySS (0.15 mM, 50 μL) was added to the rapidly stirred colloid in 5 x 10 μL aliquots, and left for 5 minutes inducing a larger SPR λ_{max} shift to 578 nm (Fig. 8.8). The hydrodynamic diameter increased to 99 ± 29 and the zeta potential decreased to -47 ± 9 mV. Labelled particles were then purified using size exclusion chromatography using H_2O as the eluent, where particles rapidly eluted off the column leaving a brown colloidal solution.

Synthesis of Zonyl–Au^{13}-RubpySS and Zonyl–Au^{100}-RubpySS nanoparticles

Zonyl FSA fluorosurfactant labelled, RubpySS-luminescent gold nanoparticles were synthesised according to the procedure of Osborne et al. [166], and are herein used as control samples for pH-dependent cell uptake experiments as outlined in Chapter 3, section: pH-Resolved Uptake of Peptide-labelled, Luminescent Gold Nanoparticles.

2.2.5 Structural & Morphological Characterisation of Peptide-labelled, Luminescent AuNPs

Hydrodynamic Diameters of Labelled Gold Nanoparticles

Hydrodynamic diameter is the diameter of a colloidal particle plus the extra distance between the particles hard surface, and the limit of its solvent coordination sphere. It is an important piece of particle characterisation as it is a good estimate of particle size, and can be measured through completely non-invasive techniques such as dynamic light scattering.

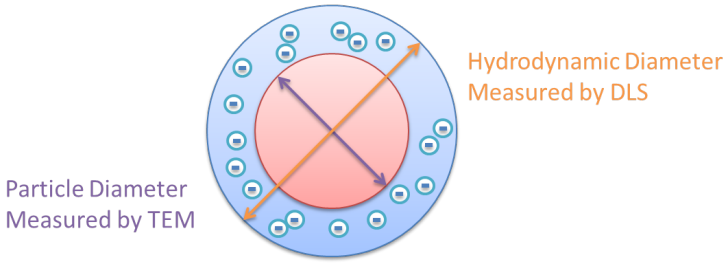

Figure 2.14: Diagram showing distinction between particle diameter, and hydrodynamic diameter of a spherical particle coordinated to solvent molecules in solution.

The hydrodynamic diameters of citrate-coated and labelled AuNPs were measured using Dynamic Light Scattering (DLS), a non-invasive technique that utilizes a particle's Brownian motion, the random thermal motion of the particle through its solvent, to calculate the particles size. Smaller particles rebound less with solvent molecules and therefore move through solution relatively quickly, and conversely larger particles that undergo more colliding events tumble more slowly. DLS measures hydrodynamic diameter, and not particle diameter because the particles coordination sphere influences the particles Brownian motion, see Fig. 2.14 for the distinction between particle diameter and hydrodynamic diameter.

$$D_h = \frac{3k_B T}{3\pi\eta D_t}$$

Figure 2.15: The Einstein-Stokes equation, a model function for a particles Brownian motion, where D_h = hydrodynamic diameter; D_t = translational diffusion coefficient; k_B = Boltzmann constant; T = temperature and η = solvent dynamic viscosity.

Briefly, the sample is illuminated using a 633 nm laser, and scattered light is either collected at a 90° or 173° from the illumination path. Collection of this optical signal as a function of time produces 'noise like' data that is processed in real time by a time correlator, which studies how the intensity of scattered light changes over time, and plots an autocorrelation function as a function of delay time. Analysis of

the autocorrelation function provides the translational diffusion coefficient (D_h), which if inserted into the Einstein-Stokes equation (Fig. 2.15), provides calculation of particle hydrodynamic diameter.

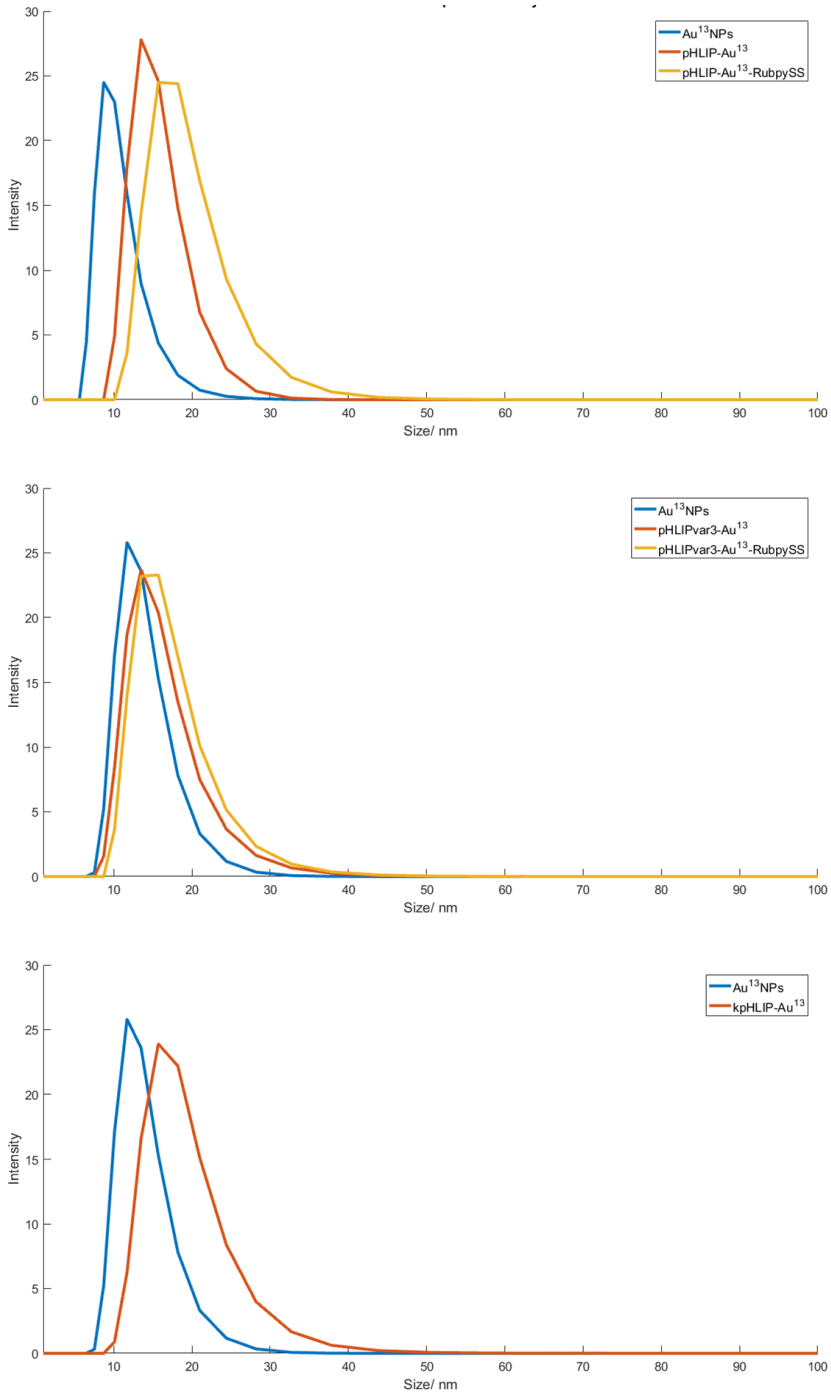

Figure 2.16: Number-weighted hydrodynamic diameter distributions of Au^{13}NPs (0.5 nM in H_2O) before and after labelling with pHLIP & RubpySS (top), pHLIPvar3 & RubpySS (middle) and kpHLIP (bottom), as measured by dynamic light scattering.

Sample	Hydrodynamic Diameter / nm	PdI
Au^{13}NPs	11 ± 3	0.13
pHLIP-Au^{13}	15 ± 4	0.14
pHLIP-Au^{13}-RubpySS	19 ± 5	0.19
pHLIPvar3-Au^{13}	15 ± 4	0.26
pHLIPvar3-Au^{13}-RubpySS	16 ± 5	0.19
kpHLIP-Au^{13}	18 ± 5	0.29

Table 2.2: DLS number distribution data of Au^{13}NPs, before and after particles were coated with pHLIP, pHLIPvar3, kpHLIP and subsequently with RubpySS, in H_2O.

Fig. 2.16 shows number distributions of hydrodynamic diameter monitoring the labelling of Au^{13}NPs with pHLIPs and RubpySS. The addition of pHLIP and pHLIPvar3 to Au^{13}NPs increased the number distribution average of 11 ± 3 nm to 15 ± 4 nm, whereas the addition of kpHLIP to Au^{13}NPs increased the value to 18 ± 5 nm, a greater increase in hydrodynamic diameter or solvation coordination. Subsequent additions of RubpySS to pHLIP & pHLIPvar3-Au^{13}NPs induced further increases in hydrodynamic diameter to 19 ± 5 & 16 ± 5 nm for pHLIP-Au^{13}-RubpySSS and pHLIPvar3-Au^{13}-RubpySS, respectively.

DLS was also used to monitor the hydrodynamic diameter of Au^{100}NPs during the labelling with pHLIPs and RubpySS, as shown in Fig. 2.17. Although labelling Au^{100}NPs with pHLIP & pHLIPvar3 induced a modest increase in hydrodynamic diameter, the diameter increased markedly when kpHLIP was added, from 79 ± 23 nm to 129 ± 30 nm. This continues to suggest that kpHLIP does not provide much stabilisation to the gold colloid, and that particles are significantly more polydisperse. However, pHLIP and pHLIPvar3 peptides suitably stabilised the colloidal nanoparticles during the RubpySS-labelling, providing small polydispersity indexes (PdI), which is a measurement equivalent to the full width at half maximum of the intensity weighted distribution of nanoparticle hydrodynamic diameters. This measurement effectively provides an indication of the range of hydrodynamic diameters, and is often used as a measurement of polydispersity, where the index value lies between 0 and 1. Smaller PdI values indicate more monodisperse nanoparticles, and it is often assumed within the literature that PdI values < 0.2 indicate a significantly monodisperse nanoparticle ensemble. This was important for us to achieve as it demonstrates an efficient labelling process, and provides homogenously labelled particles which should all interact with cells and biological media in a consistent fashion. Additional analysis of the particles with the Nanosight particle tracker show the dispersity of pHLIP-Au^{100}-RubpySS and pHLIPvar3-Au^{100}-RubpySS, luminescence images were also taken showing the particles are excitable using a 488 nm laser and a 520 nm dichroic mirror to remove scattered illumination. Scatter and luminescence images both show largely monodisperse particles that are luminescent under 488 nm excitation thus demonstrating that they're excitable using conventional lasers and also demonstrate potential for flow imaging.

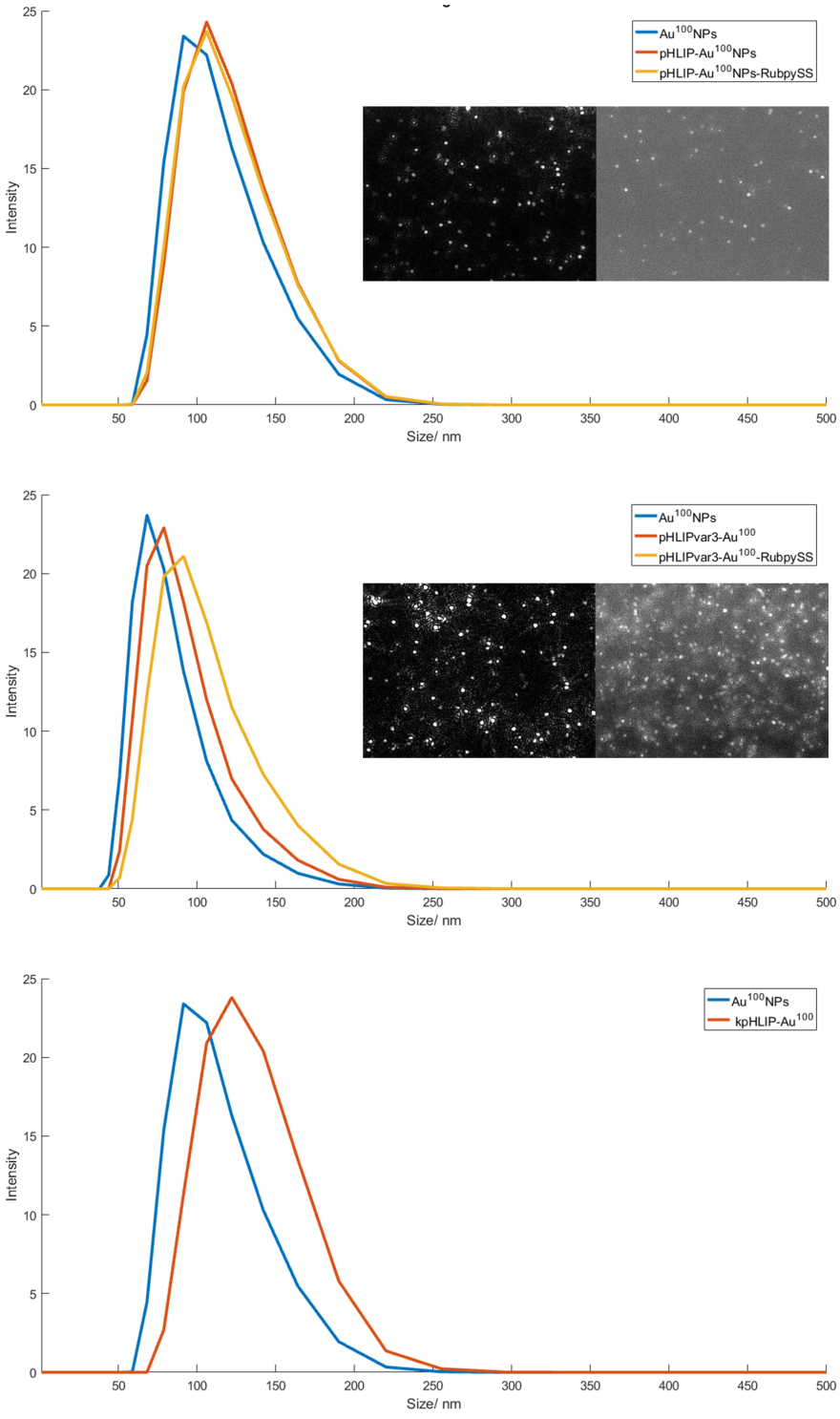

Figure 2.17: Number-weighted hydrodynamic diameter distributions of Au^{100}NPs (2 pM in H_2O) before and after labelling with pHLIP & RubpySS (top), pHLIPvar3 & RubpySS (middle) and kpHLIP (bottom), as measured by dynamic light scattering. Inset, for pHLIP-Au^{100}-RubpySS and pHLIPvar3-Au^{100}-RubpySS, in flow images of nanoparticle scatter (left) and luminescence (right) were acquired by nanosight.

Sample	Hydrodynamic Diameter / nm	PdI
Au^{100}NPs (Batch 1)	108 ± 27	0.03
pHLIP-Au^{100}	115 ± 28	0.03
pHLIP-Au^{100}-RubpySS	115 ± 28	0.03
Au^{100}NPs (Batch 2)	79 ± 23	0.06
pHLIPvar3-Au^{100}	87 ± 25	0.05
pHLIPvar3-Au^{100}-RubpySS	99 ± 29	0.06
kpHLIP-Au^{100}	129 ± 30	0.02

Table 2.3: Hydrodynamic Diameters, Polydispersity Indexes (PdI), Zeta Potentials (ζ) and Zeta Potential standard deviations of functionalised Au^{100}NPs in H_2O.

Zeta potential (ζ) of Labelled Gold Nanoparticles

Zeta potential is the potential difference between particle surface and particle's slipping plane, the edge of a colloidal particle's solvent coordination sphere (Fig. 2.18) and is useful for an understanding of how particles behave in solution, in particular providing an indication of colloidal stability.

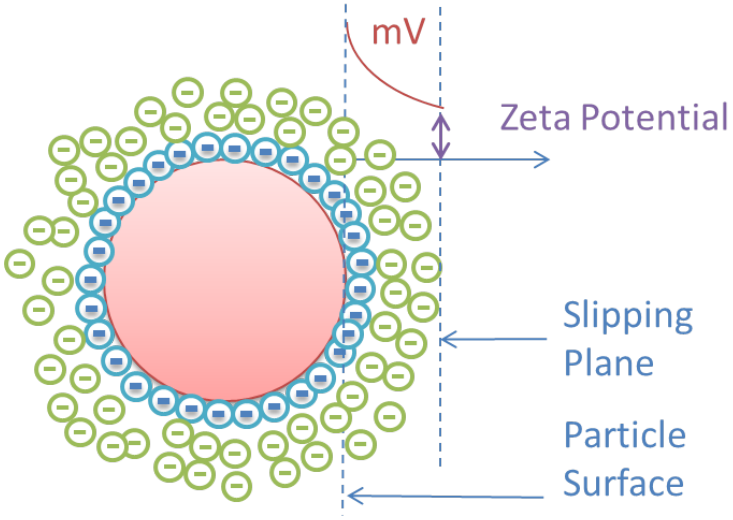

Figure 2.18: Graphic illustrating Zeta Potential, the potential difference between particle surface and particle's slipping plane.

Zeta potential is commonly measured by Laser Doppler Micro-electrophoresis electrophoresis or electrophoretic light scattering, and both study the mobility of particles while an electric field is applied to them. In a Laser Doppler Micro-electrophoresis acquisition, an electric field is applied to the colloidal solution, upon which the particles start moving at a speed related to their zeta potential. Particle electrophoretic mobility is then measured by Phase Analysis Light Scattering, a patented technique produced by Malvern Instruments.

Zeta potential measurements reveal that displacement of citrate ions on Au^{13}NPs ($\zeta = -37 \pm 7mV$, pH 5.0) for pHLIP resulted in an increase in zeta potential to -23 ± 7 mV, whereas displacement for pHLIPvar3

Sample	Zeta Potential/ mV	Standard Deviation/± mV
Au^{13}NPs	-37	7
pHLIP-Au^{13}	-23	7
pHLIP-Au^{13}-RubpySS	-36	8
pHLIPvar3-Au^{13}	-54	14
pHLIPvar3-Au^{13}-RubpySS	-30	8

Table 2.4: Zeta potentials of Au^{13}NPs, pHLIP-Au^{13} and pHLIP-Au^{13}-RubpySS in H_2O (pH 5.0), as measured using Laser Doppler Microelectrophoresis.

resulted in a large decrease in zeta potential to -54 ± 14 mV. Although pHLIP bears a change of -5 and pHLIPvar3 bears a charge of -4, pHLIP var3 is 74% the size of pHLIP, making it more densely charged, perhaps explaining the difference in zeta potential. Upon addition of RubpySS to both colloids the zeta potential of newly coated pHLIP-Au^{13}-RubpySS decreased to -36 ± 8 mV, and conversely the zeta potential of newly coated pHLIPvar3-Au^{13}-RubpySS increased to -30 ± 8 mV. These results generally indicate stable colloids, where zeta potentials $<$ -30 mV or $>$ 30 mV are generally considered stable for a colloid stabilised by electrostatic repulsion [183].

Zeta potential measurements of labelled and unlabelled Au^{100}NPs are shown in Table 2.5. For co-labelling Au^{100}NPs with pHLIPvar3 & RubpySS, after labelling particles with pHLIPvar3 the zeta potential remained close to -42 (± 7) mV, however after labelling the particles with RubpySS the zeta potential dropped to -47 (± 9) mV. Au^{100}NPs labelled with pHLIP & RubpySS exhibited a similar Zeta potential of -49 (± 9) mV, a strong indication of a stable colloid.

Sample	Zeta Potential/ mV	Standard Deviation/± mV
Au^{100}NPs	-41	6
pHLIP-Au^{100}	−−	−−
pHLIP-Au^{100}-RubpySS	-42	7
pHLIPvar3-Au^{100}	-42	12
pHLIPvar3-Au^{100}-RubpySS	-47	9

Table 2.5: Zeta potentials of labelled and unlabelled Au^{100}NPs in H_2O (pH 6.2), as measured using Laser Doppler Microelectrophoresis.

Elemental Ratios of Labelled Gold Nanoparticles by ICP-MS

ICP-MS analysis of the pHLIP-Au^{13}-RubpySS and pHLIPvar3-Au^{13}-RubpySS colloid indicated a RubpySS coverage of 13 nm gold nanoparticles of 141 and 230 complexes per nanoparticle, respectively. pHLIPvar3 is 10 residues shorter than pHLIP (74% of pHLIP size), and the higher loading efficiency of RubpySS onto pHLIPvar3-Au^{13}NPs, is perhaps explained by easier access of the RubpySS complex to a less crowded gold nanoparticle surface, but will require further investigation to confirm. The area coverage of a molecule of RubpySS on an Au^{13}NP was calculated to be 3.8 nm^2 and 2.3 nm^2 for pHLIP-Au^{13}-RubpySS and pHLIPvar3-Au^{13}-RubpySS, respectively. This calculation was based on particle diameters measured by dynamic light

scattering, and transmission electron microscopy leading to a calculated particle surface area of 530.93 nm^2. ICP-MS analysis of the pHLIP-Au^{100}-RubpySS and pHLIPvar3-Au^{100}-RubpySS colloids indicated a RubpySS coverage of 100 nm gold nanoparticles of 35,784 and 66,068 complexes per nanoparticle, respectively. It is interesting that coating gold nanoparticles with the pHLIPvar3 peptide permits more efficient subsequent coating with the RubpySS complex, correlating well with the 13 nm analogues of pHLIP & pHLIPvar3-Au^{100}-RubpySS. The area coverage of a molecule of RubpySS on an Au^{100}NP was calculated to be 3.5 nm^2 and 1.9 nm^2 for pHLIP-Au^{100}-RubpySS and pHLIPvar3-Au^{100}-RubpySS, respectively. This calculation was based on particle diameters measured by dynamic light scattering, and transmission electron microscopy leading to a calculated particle surface area of 126,000 nm^2.

Transmission Electron Microscopy Images of Labelled Gold Nanoparticles

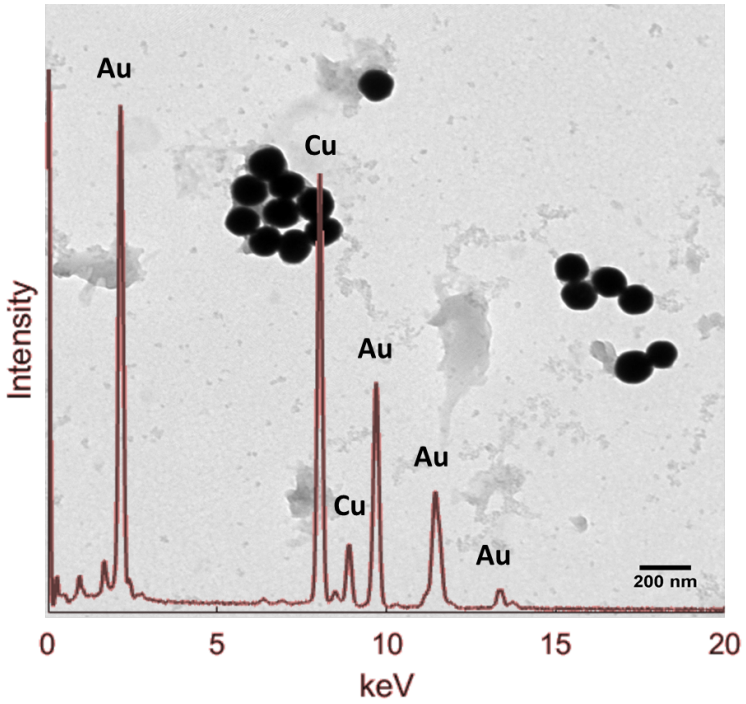

Figure 2.19: Transmission electron micrographs showing pHLIP-Au^{100}-RubpySS nanoparticles with overlaid Energy Dispersive Analysis of Xrays spectrum. Xray signals from gold and copper atoms labelled.

To study the size, mophology and dispersity of peptide labelled, luminescent AuNPs, the particles were dried onto a copper grid for visualisation using transmission electron microscopy. The Energy Dispersive Analysis of Xrays (EDAX) spectrum of the gold nanoparticles was also taken to confirm the presence of gold and ruthenium. Fig. 2.19 shows a TEM image of pHLIP-Au^{100}-RubpySS nanoparticles overlaid with the particles' EDAX spectrum. The characteristic bands for gold are clearly visible at 9, 12 & 14 keV, however the characteristic ruthenium band at 18 keV is not visible, most likely indicating that the concentration of ruthenium is too low for the sensitivity of the technique. Additionally, neither pHLIP-Au^{13}-RubpySS, pHLIPvar3-Au^{13}-RubpySS or pHLIPvar3-Au^{100}-RubpySS particles exhibited ruthenium EDAX bands (data not included), also indicating that Ru concentration is too low for detection. In order to visualise the expected corona around the labelled nanoparticles, peptide-labelled and citrated-coated AuNPs were treated with a 1% phosphotungstic acid aqueous solution prior to TEM sample preparation. With this treatment the gold particle core is visible due to its high electron scattering character, the periphery of the nanoparticle coating is outlined by the phosphotungstic positive contrast stain, leaving a white corona between the AuNP surface and the positive contrast halo.

Post preparation of pHLIP-Au^{13}-RubpySS and pHLIPvar3-Au^{13}-RubpySS, a drop of each colloid was spotted onto a 3 mm 200 MESH copper grid, and permitted to dry. A separate volume of each sample (200

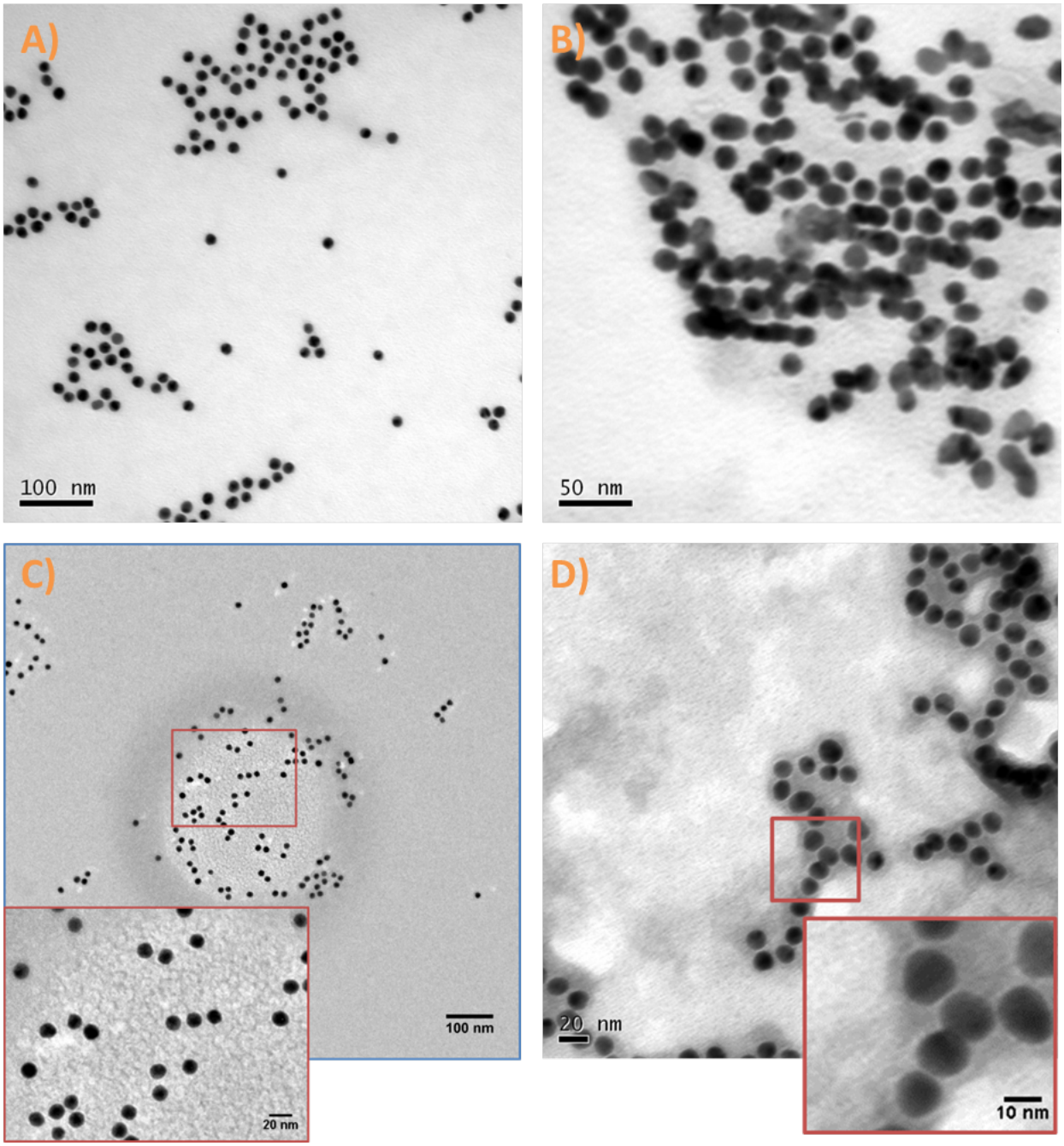

Figure 2.20: Transmission electron micrographs showing citrate-coated gold nanoparticles (A), citrate-coated gold nanoparticles with the positive contrast stain (B), pHLIP-Au^{13}-RubpySS (C) and pHLIP-Au^{13}-RubpySS with the positive contrast stain (D).

μL, 4.8 nM) was added to a 1% Phosphotungstic acid solution (200 μL) and left for 20 minutes. The stained colloid was then centrifuged (13,000 rpm, for 30 minutes), the supernatant was removed and the particles were redispersed in H_2O. A drop of each sample was spotted onto a 3 mm 200 MESH copper grid, and permitted to dry overnight before imaging.

Fig. 2.20 shows TEM micrographs of citrate-coated gold nanoparticles and pHLIP-Au^{13}-RubpySS, with and without treatment with 1% phosphotungstic acid. Untreated pHLIP-Au^{13}-RubpySS particles appear spherical, monodisperse and with an average diameter of 13 nm. Citrate-coated particles, imaged after treatment with 1% phosphotungstic acid showed little evidence of a peripheral corona around the gold core. pHLIP-Au^{13}-RubpySS particles imaged after treatment with 1% phosphotungstic acid showed distinct white coronas around particle peripheries with consistent homogeneity, indicating an increase in coating diameter between citrate-stabilised AuNPs and AuNPs coated with pHLIP and RubpySS.

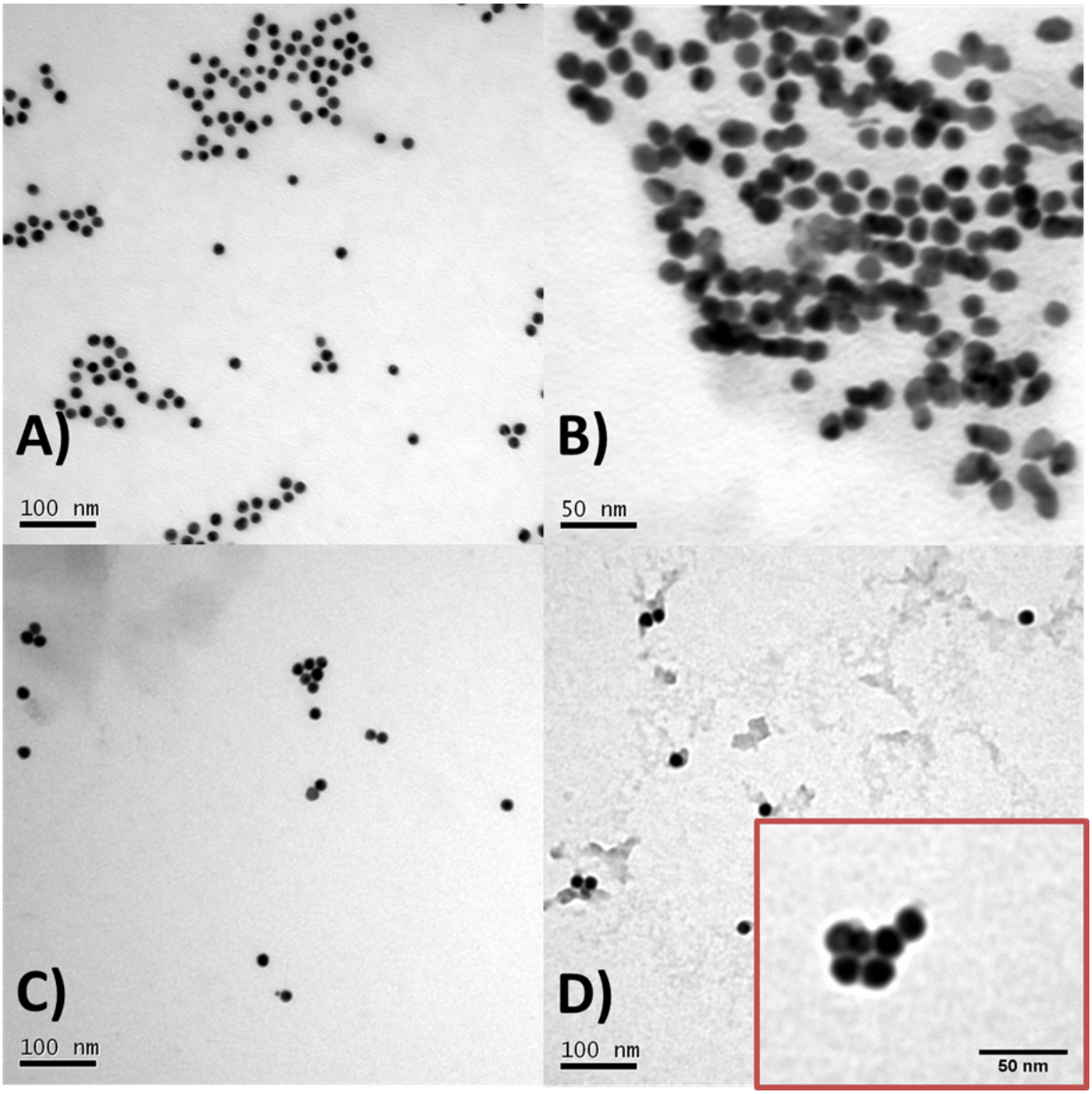

Figure 2.21: Transmission electron micrographs showing citrate-coated gold nanoparticles (A), citrate-coated gold nanoparticles with the positive contrast stain (B), pHLIPvar3-Au^{13}-RubpySS (C) and pHLIPvar3-Au^{13}-RubpySS with the positive contrast stain (D).

Fig. 2.21 shows TEM micrographs of citrate-coated AuNPs and pHLIPvar3-Au^{13}-RubpySS particles offering visualisation of their mophology, size, dispersity and coating radii. pHLIPvar3-Au^{13}-RubpySS particles appear spherical, with diameters comparable to the unlabelled citrate nanoparticles indicating that the labelling process has not induced particle aggregation. Additionally, as with pHLIP-labelled AuNPs, pHLIPvar3-labelled AuNPs treated with 1% PTA also show a peripheral halo, indicating an increase in nanoparticle coating radius upon labelling with pHLIPvar3 and RubpySS.

Visualisation of the coating corona on labelled Au^{100}NPs was also performed using TEM via positive contrast staining. Post preparation of pHLIP-Au^{100}-RubpySS and pHLIPvar3-Au^{100}-RubpySS, a drop of each colloid was spotted onto a 3 mm 200 MESH copper grid, and permitted to dry. A separate volume of each sample (200 μL, 40 pM) was added to a 1% Phosphotungstic acid solution (200 μL) and left for 20 minutes. The stained colloid was then centrifuged (13,000 rpm, for 2 minutes), the supernatant was removed and the particles were redispersed in H_2O. A drop of each sample was spotted onto a 3 mm 200 MESH copper grid, and permitted to dry before imaging.

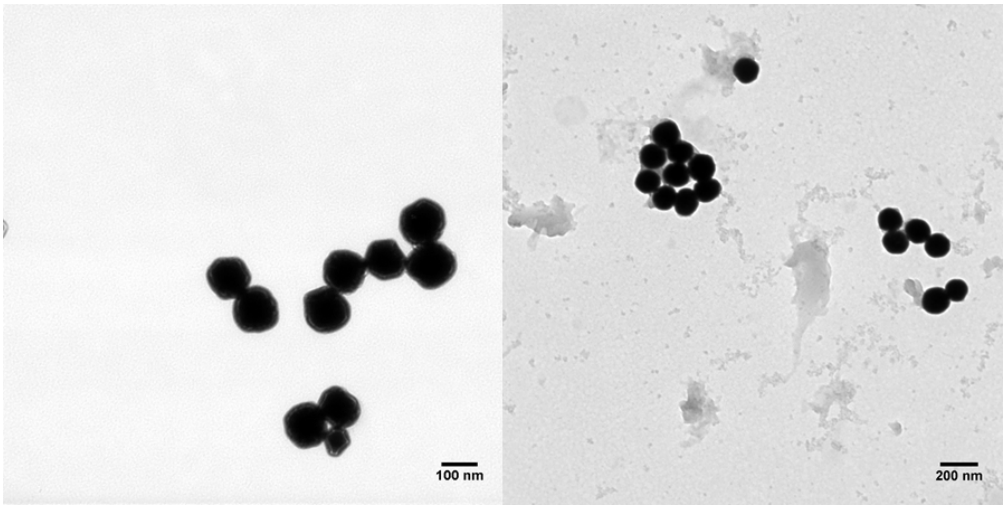

Figure 2.22: TEM micrographs showing pHLIPvar3-Au^{100}-RubpySS colloid dried onto copper grids. Untreated particles (left) and particles treated with positive contract phosphotungstic acid stain (right)

Fig. 2.22 shows TEM images of unstained pHLIP-Au^{100}-RubpySS and pHLIP-Au^{100}-RubpySS treated with a 1% solution of Phosphotungstic acid. The image of unstained pHLIP-Au^{100}-RubpySS shows independent, monodisperse particles that have grouped together on the copper grid possibly from the drying process, but without physical agglomeration into larger particles. As discussed earlier, DLS indicated (Fig. 2.17) that particles had not significantly changed hydrodynamic diameter during the labelling process, so it was expected that particle size had not significantly changed either. The image of stained particles shows a more dense positive contrast border around the particles, similar to that of the pHLIP-Au^{13}-RubpySS images (Fig. 2.20), with a white interface between the positive contrast and the gold core. The presence of the white corona is indicative of an increase in coating thickness, upon labelling with pHLIP & RubpySS.

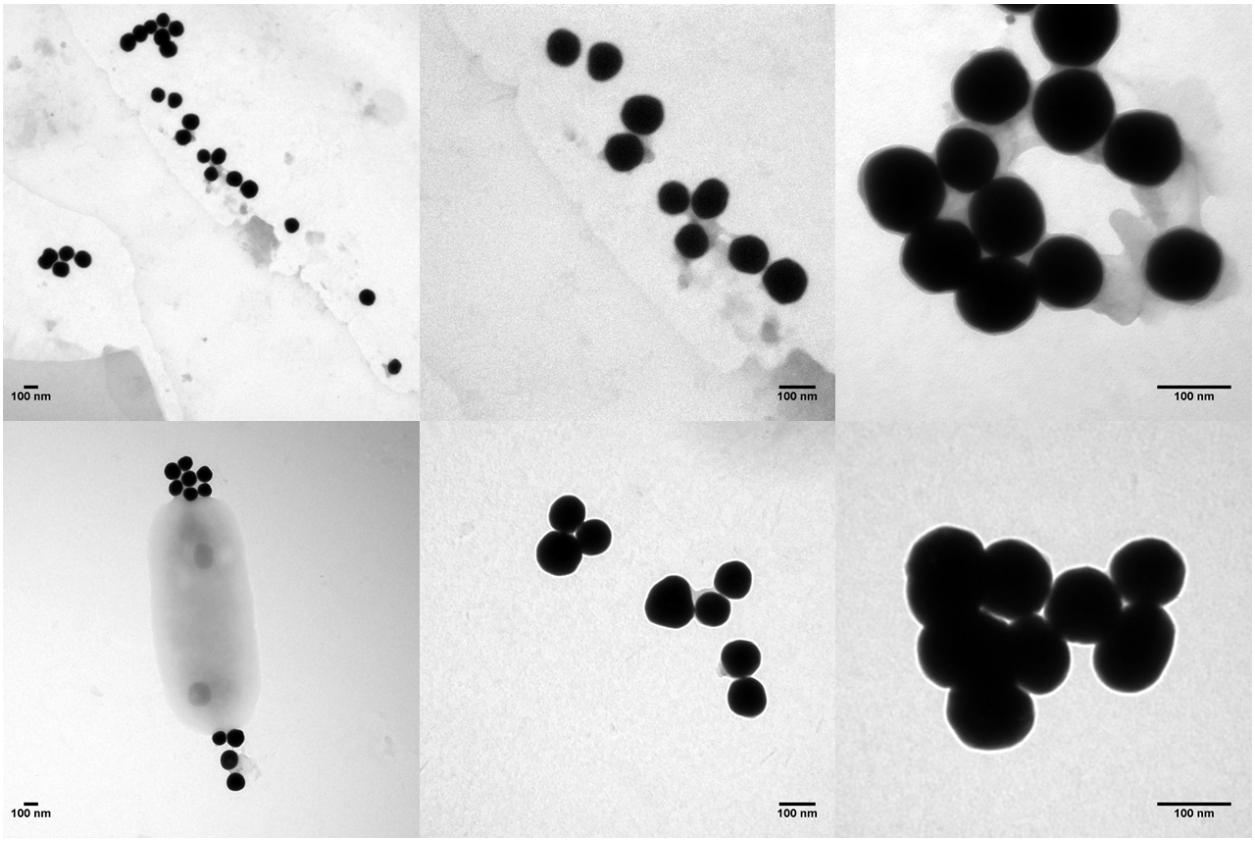

Figure 2.23: TEM micrographs showing pHLIPvar3-Au^{100}-RubpySS colloid dried onto copper grids. Rows show untreated particles (top) and particles treated with positive contract phosphotungstic acid stain (bottom), each frame showing magnifications of 50,000x, 120,000x and 250,000x, respectively.

Fig. 2.23 shows an image selection of unstained pHLIPvar3-Au^{100}-RubpySS (top row) and pHLIPvar3-Au^{100}-RubpySS with the positive contrast stain (bottom row) with different electronic magnifications. Images of unstained particles again show monodisperse particles, that in some cases have associated possibly during the drying process, but no indications of large particle agglomeration are present. Images of stained particles also remain monodisperse, with no large aggregates present, and with a significant white corona between the gold particles and the positive contrast stain, indicating an increase in coating thickness.

2.2.6 Luminescent Characterisation of pHLIP-labelled, luminescent AuNPs

Steady State Luminescence Characterisation of labelled-AuNPs

Being in a +2 oxidation state (d^6), RubpySS will oxidise relatively easily, and the presence of strongly π-accepting bipyridine ligands leads to Metal-to-Ligand Charge Transfer (MLCT) transitions to low energy excited states. This is manifested as a strong absorption at approximately 465 nm ($\epsilon = 14,600 M^{-1}$ for $Ru(bpy)_3$ [177]), corresponding to the ^{1}MLCT transition, ($\pi_L^* \longleftarrow \pi_M$). As a second row transition element, ruthenium exhibits strong spin-orbit coupling, which is an interaction between an electrons spin magnetic moment, and its orbital angular momentum.

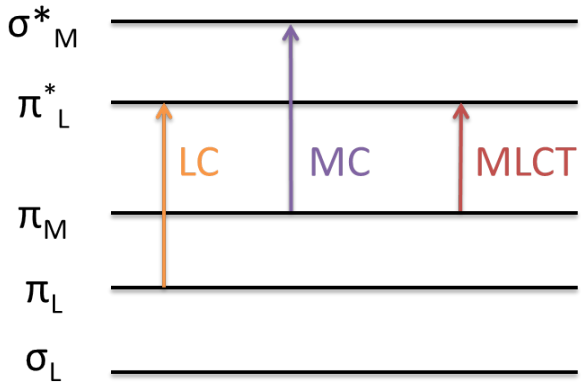

Figure 2.24: Electronic transitions of archetypal transition metal complex, ruthenium trisbypyridine.

Ruthenium's possession of a large nuclear magnetic moment, and therefore strong spin-orbit coupling increases the likelihood of the singlet and triplet states having similar vibrational energy, rendering the intersystem crossing (ISC) transition from singlet to triplet states more favourable. After ISC conversion of an electron from a singlet excited state into a triplet excited state, the electron relaxes back to the ground state via a ^{3}MLCT transition. This demotion of the electron from a triplet excited state back down to its singlet ground state orbital is spin forbidden, therefore proceeds slowly with an approximate radiative lifetime of 500 ns [45] (far longer than typical organic values of $1 \longrightarrow 20$ ns) and an overall photoluminescence quantum yield of 0.042 (in H_2O) [47]. As ruthenium exhibits strong vibronic coupling, the electron also relaxes through a cascade of vibrational levels, this leads to a broad emission band at 650 nm. In addition to MLCT transitions, Ligand $-$ Ligand charge transitions are inducable under UV excitation ($\pi_L^* \longleftarrow \pi_L$), and as ruthenium polypyridyl complexes are octahedral, promotion of a d-electron through the $e_g \longleftarrow t_{2g}$ transition ($\sigma_M^* \longleftarrow \sigma_M$) is also radiative (Fig. 2.24).

The steady state absorbance and luminescence spectra of pHLIP-Au^{13}-RubpySS and pHLIP-Au^{100}-RubpySS are shown in Fig. 2.25. For pHLIP-Au^{13}-RubpySS, the absorption profile shows the ruthenium $\pi^* \longleftarrow \pi$ absorption at 290 nm along with the gold surface plasmon resonance, the band with a gaussian

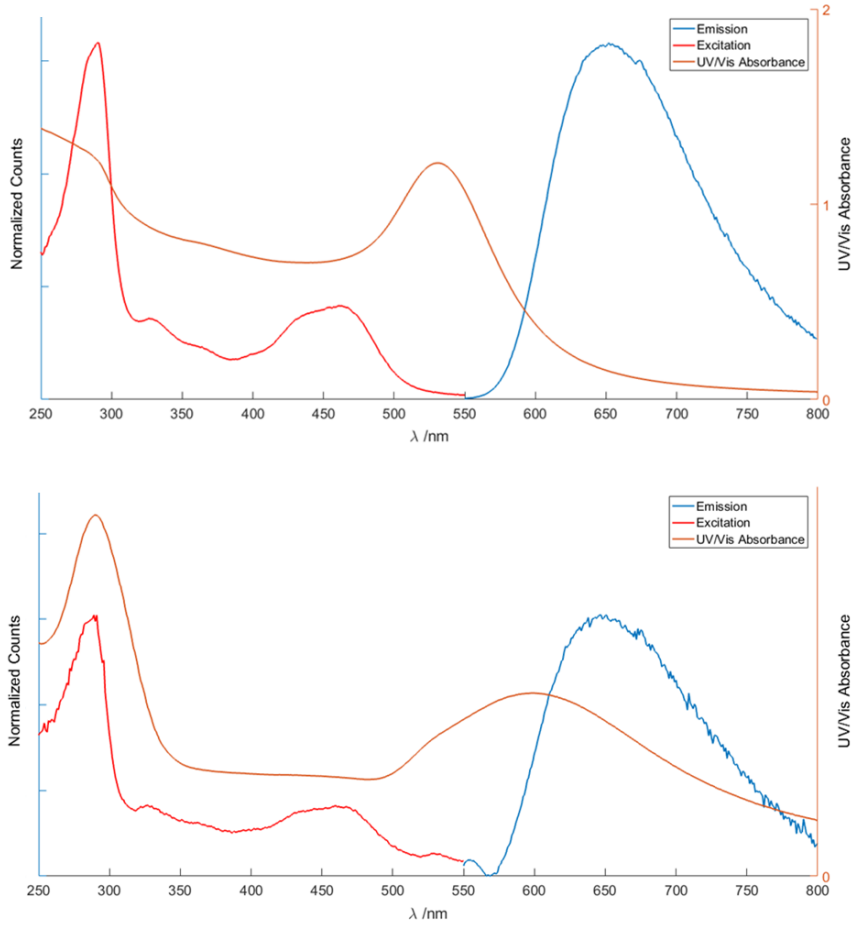

Figure 2.25: Top) Steady state absorption and luminescence spectra of pHLIP-Au^{13}-RubpySS (4.8 nM). For excitation scans, the instrument's emission monochromator was set to 650 nm, and for emission scans, the excitation monochromator was set to 465 nm (Abs = 0.72). Long pass filters were used to prevent detection of scattered light. Bottom) Steady state absorption and luminescence spectra of pHLIP-Au^{100}-RubpySS (40 pM). For excitation scans, the instrument's emission monochromator was set to 650 nm, and for emission scans, the excitation monochromator was set to 465 nm (Abs = 0.83). Long pass filters were used to prevent detection of scattered light.

profile, at 530 nm. For pHLIP-Au^{100}-RubpySS, the absorption profile shows the ruthenium $\pi^* \longleftarrow \pi$ absorption at 290 nm along with the gold surface plasmon resonance, the band with the broadened and skewed gaussian profile, at 575 nm. For both the 13 & 100 nm particles, the excitation spectra show the $\pi_L^* \longleftarrow \pi_L$ electronic transition at 290 nm, the $e_g \longleftarrow t_{2g}$ transition at 330 nm and the ^1MLCT ($\pi_L^* \longleftarrow \pi_M$) transition at 465 nm, confirming the luminescence from the labelled particles is originating from ruthenium photoluminescence. Both emission spectra show the broad emission band resultant from radiative decay of the ^3MLCT transition, however the λ_{max} for pHLIP-Au^{13}-RubpySS and pHLIP-Au^{100}-RubpySS are 627 nm and 641 nm, respectively. Hypsochromic shifts of the emission band of ruthenium complexes during interaction with biological structures has been previously reported [184], and is often associated with exposure of

the ruthenium complex to a less polar environment than water, where charge localisation on the bipyridyl groups during the MLCT state is less favourable.

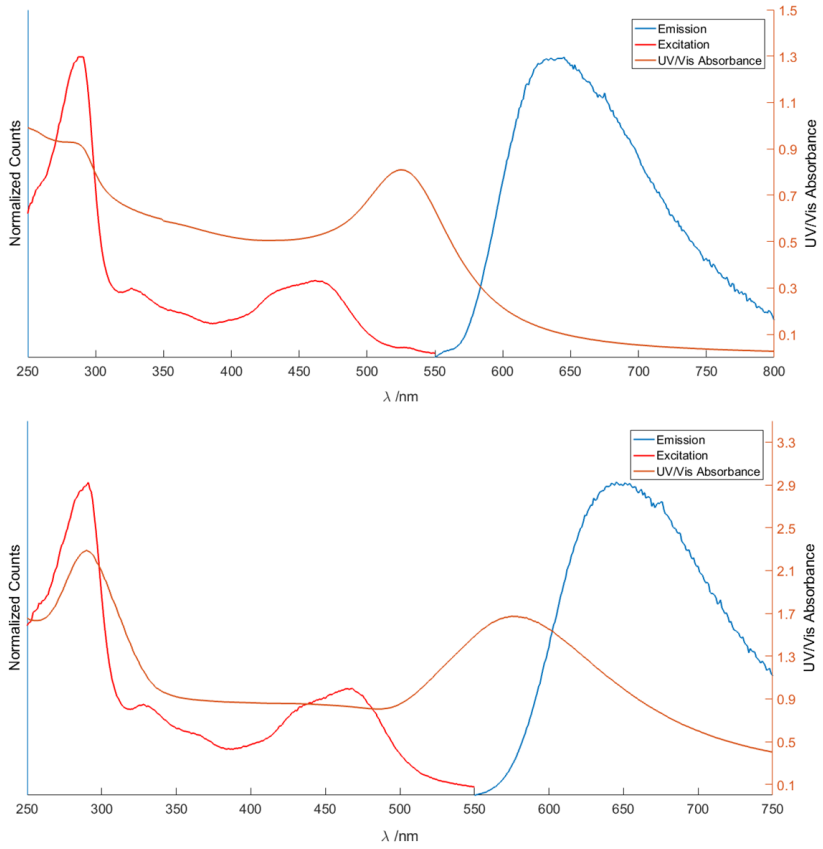

Figure 2.26: Top) Steady state absorption and luminescence spectra of pHLIPvar3-Au^{13}-RubpySS (4.8 nM). For excitation scans, the instrument's emission monochromator was set to 650 nm, and for emission scans, the excitation monochromator was set to 465 nm (Abs = 0.53). Long pass filters were used to prevent detection of scattered light. Bottom) Steady state absorption and luminescence spectra of pHLIPvar3-Au^{100}-RubpySS (40 pM). For excitation scans, the instrument's emission monochromator was set to 650 nm, and for emission scans, the excitation monochromator was set to 465 nm (Abs = 0.82). Long pass filters were used to prevent detection of scattered light.

The steady state absorption and luminescence spectra of pHLIPvar3-Au^{13}-RubpySS and pHLIPvar3-Au^{100}-RubpySS are shown in Fig. 2.26. For the 13 nm particles, the absorption profile shows the ruthenium $\pi^* \longleftarrow \pi$ absorption at 290 nm along with the gold surface plasmon resonance, the band with a gaussian profile, at 530 nm. For the 100 nm particles, the absorption profile shows the ruthenium $\pi_L^* \longleftarrow \pi_L$ absorption at 290 nm along with the gold surface plasmon resonance, the band with a gaussian profile, at 575 nm. For both the 13 & 100 nm particles, the excitation spectra show the $\pi^* \longleftarrow \pi$ electronic transition at 290 nm, the $e_g \longleftarrow t_{2g}$ transition at 330 nm and the ^1MLCT transition at 450 nm ($\pi_L^* \longleftarrow \pi_M$). Both emission spectra show the broad emission band resultant from radiative decay of the ^3MLCT transition, however the lambda$_{max}$ for pHLIPvar3-Au^{13}-RubpySS and pHLIPvar3-Au^{100}-RubpySS are 637 nm and 645 nm,

respectively. This hypsochromic shift of the emission bands is indicative of increased exposure of RubpySS to a less polar environment than water, which is most prominent for pHLIPvar3-Au^{13}-RubpySS. The zeta potentials of pHLIPvar3-Au^{13}-RubpySS and pHLIPvar3-Au^{100}-RubpySS (-30 ± 8 & -47 ± 9, respectively) indicate that pHLIPvar3-Au^{13}-RubpySS constitutes a less polar environment, and as a result, the MLCT state is not as stable.

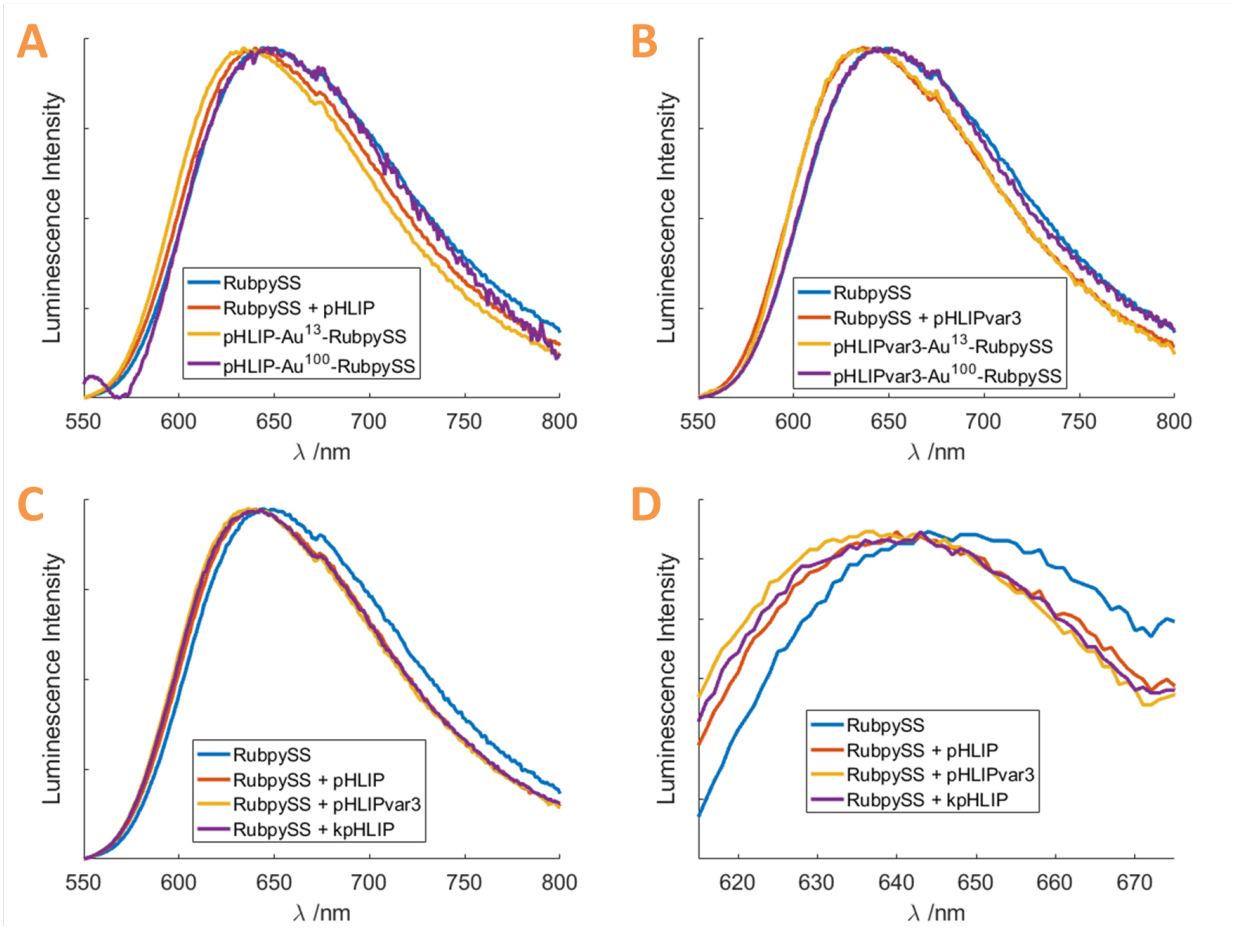

Figure 2.27: The effect of peptides and gold nanoparticles on the steady state emission of RubpySS. A) pHLIP (6 μM) & co-labelling of $Au^{13\&100}$NPs, B) pHLIPvar3 (7.7 μM) & co-labelling of $Au^{13\&100}$NPs, C) The effect of pHLIP (6 μM), pHLIPvar3 (7.7 μM) & kpHLIP (6 μM) variants on the emission of free RubpySS (7 μM) and D) Enlargement of lambda$_{max}$ region from (C). Spectra were corrected for instrument response.

To investigate how the steady state emission of RubpySS is affected by each peptide, as well as their co-labelling onto Au^{13} & Au^{100} nanoparticles, the emission of RubpySS within each of these samples was probed by luminescence spectroscopy. For pHLIP and pHLIPvar3 (Fig. 2.27, A & B, respectively), addition of the peptide to free RubpySS in H_2O induces a hypsochromic shift of the ^{3}MLCT transition. Additionally when pHLIP-Au^{13}-RubpySS and pHLIPvar3-Au^{13}-RubpySS are studied, the same effect is observed. However when pHLIP-Au^{100}-RubpySS and pHLIP-Au^{100}-RubpySS are studied this effect is not observed, and the

emission band of labelled Au^{100}NPs overlays well with the emission band of the free complex. Each pHLIP variant has a similar effect on the steady state emission of RubpySS, inducing a hypsochromic shift relative to free RubpySS in H_2O (Fig. 2.27, C & D). No significant difference was observed between the effect of each variant on RubpySS emission wavelength.

Interestingly, steady state emission from pHLIP-Au^{13}-RubpySS and pHLIPvar3-Au^{13}-RubpySS exhibited blueshifted emission λ_{max} whereas pHLIP-Au^{100}-RubpySS and pHLIPvar3-Au^{100}-RubpySS exhibited emission curves that almost perfectly overlaid with the emission spectrum of free RubpySS in water, Fig. 2.28. This suggests there is a plasmon effect on the emission of RubpySS, most markedly exhibited by the Au^{13}NPs and insignificantly by the Au^{100}NPs. Rogers & Claire et al. [96] and Osborne et al. [166] reported small surface plasmon resonance λ_{max} shifts when 13 nm AuNPs were labelled with a ruthenium complex. Prior to ruthenium complex labelling, these Au^{13}NPs were labelled with the Zonyl 7950 or FSA fluorosurfactant, in respective publications. Upon steady state luminescence measurements, both studies concluded there were no plasmon effects contributing to the luminescence properties of the ruthenium complex. In this work, the SPR λ_{max} shifts are far greater for Au^{13}NPs ($\approx$ 6 nm when labelling pHLIP-Au^{13} or pHLIPvar3-Au^{13} with RubpySS) suggesting that the pre label (peptides or fluorosurfactants in these cases) may impose desensitising effects on the gold's surface plasmon resonance. If true, this may explain why Au^{13} and Au^{100} nanoparticles labelled with pHLIP or pHLIPvar3, experienced different luminescent properties.

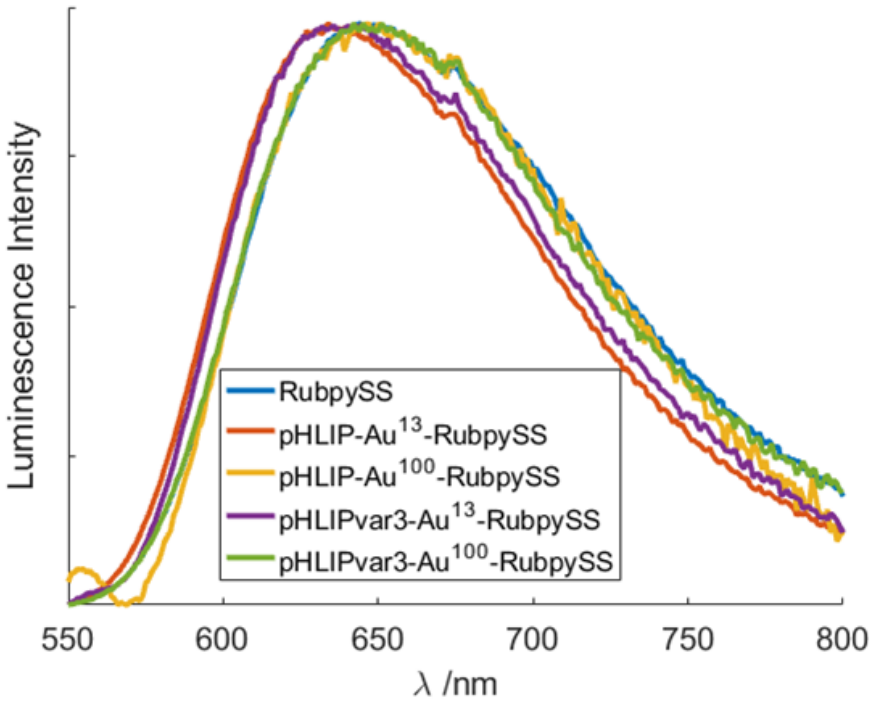

Figure 2.28: Steady state luminescence spectra of RubpySS, pHLIP-Au^{13}-RubpySS (4.8 nM), pHLIPvar3-Au^{13}-RubpySS (4.8 nM), pHLIP-Au^{100}-RubpySS (40 pM) & pHLIPvar3-Au^{100}-RubpySS (40 pM) resultant from excitation at 465 nm. Spectra were corrected for instrument response and 590 nm long pass filters were used to filter out Rayleigh scattering.

Time Resolved Luminescence Characterisation of Labelled-AuNPs

Luminescence lifetime is the time taken for the number of excited molecules to undergo radiative decay to $1/e$ or 36.8% of the original excited population, and is a more robust measurement than emission intensity because it is not dependent on intensity of excitation or fluorophore concentration. Acquisition of luminescence lifetime data was performed using the Time Correlated Single Photon Counting (TCSPC) module of an FLS920 fluorescence spectrometer and analysed using FAST lifetime fitting software. Upon acquisition of the lifetime data, the data was fitted by a Levernberg-Marquandt non-linear fitting algorithm using an arrhenius model function (Fig. 2.29, 2)

1) $$R(t) = \sum_{i=1}^{4} B_i \exp\left[-\frac{t}{\tau_i}\right]$$ 2) $$\frac{n^*(t)}{n^*(0)} = e^{-t/\tau}$$

Figure 2.29: Equations for luminescence lifetime fitting. Equation 1) the model function for exponential component fitting of lifetime data, and 2) governs the relationship between the number of excited and decayed molecules with luminescence lifetime.

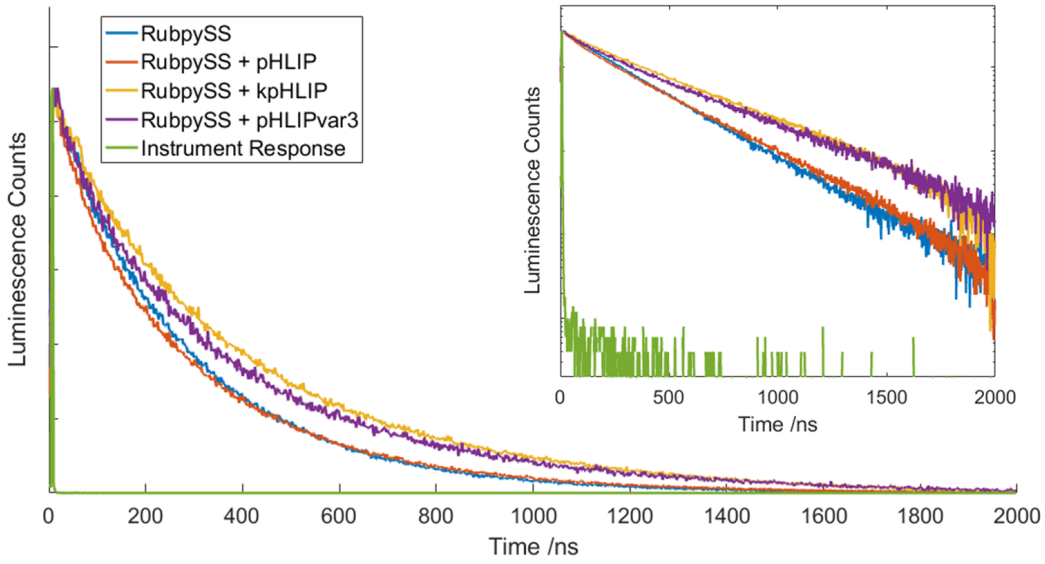

Figure 2.30: Time-resolved luminescent studies of the ^{3}MLCT radiative transition of RubpySS (7 μM), RubpySS + pHLIP (6 μM), RubpySS + kpHLIP (6 μM) and RubpySS + pHLIPvar3 (7.7 μM) resultant from 444 nm excitation and 650 nm detection. The normalised instrument response is also shown and was also recorded using excitation and detection at 444 nm.

All recorded lifetimes in this study are biexponential, with a small component occupying a small percentage of the overall signal, and a longer component occupying a majority of the overall signal. There is evidence to suggest that the small component is resultant from quenching of the RubpySS excited state either by energy or electron-transfer processes, however for ruthenium polypyridyl complexes assembled onto on gold nanoparticles, this quenching is more characteristic of electron-transfer processes [169]. It is also noteworthy that the RubpySS complex does not fall victim to previously reported AuNP-mediated luminescence quenching of ruthenium polypyridyl complexes [185] because for all lifetimes of labelled-AuNPs recorded in this study, all of them exhibit longer lifetimes than free complex.

As shown in Fig. 2.31 and tabulated in Table 2.6, Free RubpySS holds a luminescence lifetime of 97 (2%) and 287 (98%) ns and this lifetime increases when either peptide is added to the solution, or if the complex is used as a label for gold nanoparticles. Upon the addition of pHLIP to the solution, the RubpySS lifetime increased to 101 (9%) and 328 (91%) ns, which is believed to be a resultant from a favourable hydrophobic association between the peptide and the complex, helping to shield the complex from quenching by molecular oxygen [50]. The lifetime of the RubpySS triplet excited state subsequently increased to 114 (13%) and 438 (87%) ns when co-labelled with pHLIP onto Au^{13}NPs, significantly longer than the lifetime of free complex, and free complex mixed with pHLIP. When RubpySS is co-labelled with pHLIP onto Au^{100}NPs, the lifetime increased markedly to 103 (7%) and 417 (93%) ns, significantly longer than the lifetime of the free complex, somewhat shorter than the observed lifetime of pHLIP-Au^{13}-RubpySS however as the lifetimes are within 10% of each other, this difference is not deemed statistically significant. This increase in lifetime

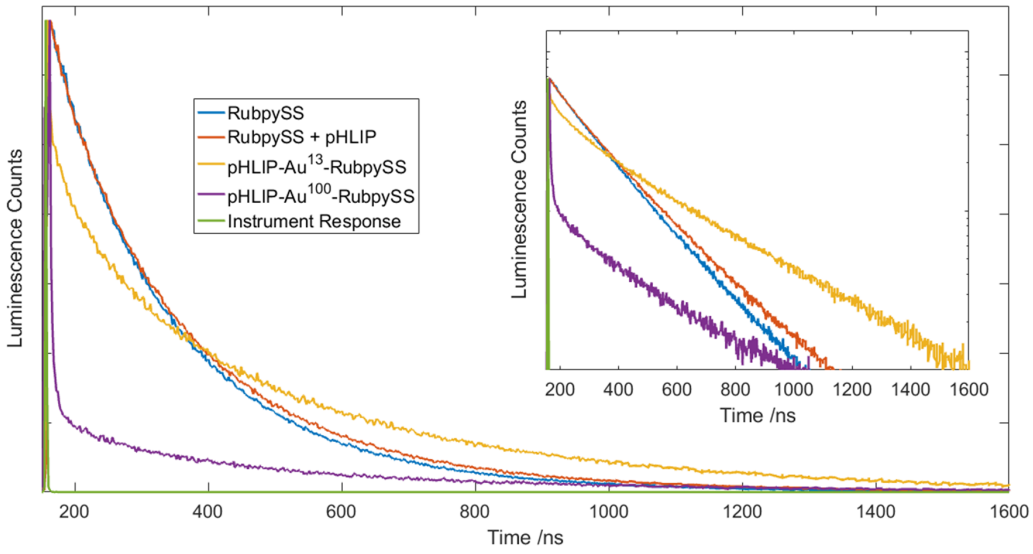

Figure 2.31: Time-resolved luminescent studies of the ^{3}MLCT radiative transition of RubpySS, RubpySS + pHLIP, pHLIP-Au^{13}-RubpySS and pHLIP-Au^{100}-RubpySS resultant from 444 nm excitation and 650 nm detection. The normalised instrument response is also shown and was also recorded using excitation and detection at 444 nm. Linear (main) and log (inset) plots both included.

for nanoparticle-bound complex is also believed to be indicative of a reduction in O_2 quenching.

As shown in Fig. 2.32 and tabulated in Table 2.6, upon the addition of pHLIPvar3 to a solution of RubpySS, the lifetime of the RubpySS excited state increased from 97 (2%) and 287 (98%) ns to 140 (11%) and 450 (89%), again believed to be resultant from a reduction in quenching by molecular oxygen. The luminescence lifetime of pHLIPvar3-Au^{13}-RubpySS was significantly greater than free complex, and slightly greater than free complex mixed with pHLIPvar3 at 51 (5%) and 499 (95%), and the lifetime of pHLIPvar3-Au^{100}-RubpySS was 137 (18%) and 434 (82%), similar to the lifetime of free complex mixed with pHLIPvar3 but again shorter than the pHLIPvar3-Au^{13}-RubpySS lifetime.

While each peptide offered an increased effect on RubpySS lifetime, this effect was most substantial for the kpHLIP peptide. Being the most hydrophobic peptide studied, it likely has an energetically more favourable interface with RubpySS, resulting in a more effective shielding from molecular oxygen. It is also interesting that the luminescence lifetimes of Au^{13}NPs co-labelled with RubpySS and a pHLIP variant are longer than the RubpySS lifetime of the Au^{100} analogues, (Fig. 2.33 and Table 2.6). This nanoparticle size dependency of the RubpySS excited state's lifetime indicates an interaction between the surface plasmons and the RubpySS excited state.

Attempts were made to measure the luminescence quantum yield (ϕ_F) of all functionalised gold nanoparticles. However, the accuracy of direct quantum yield measurement of is very dependent on how accurately scattered light is measured. For this procedure, in addition to synthesising the luminescent gold nanoparticles for measurement (luminescent sample), peptide coated gold nanoparticles which were devoid of ruthenium

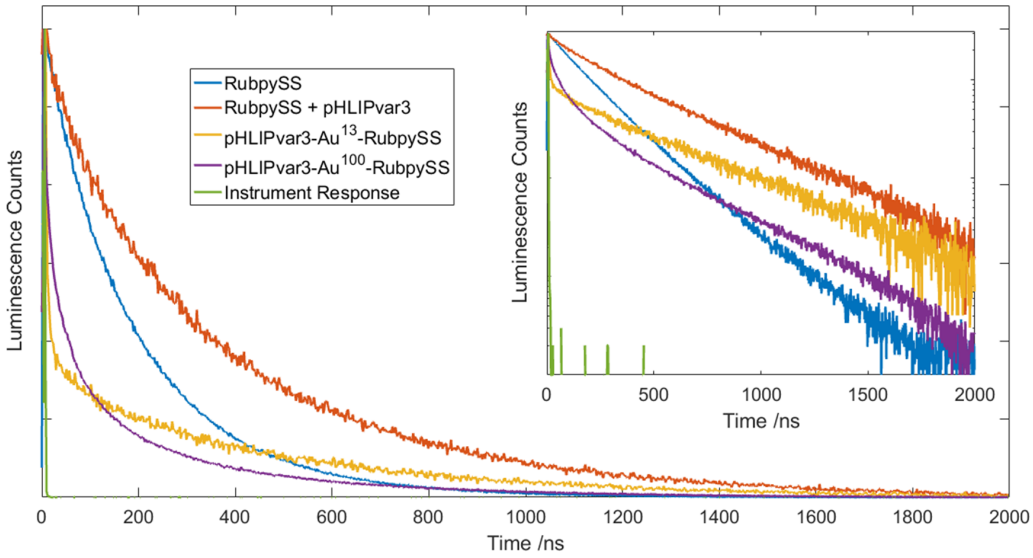

Figure 2.32: Time-resolved luminescent studies of the ^{3}MLCT radiative transition of RubpySS, RubpySS + pHLIPvar3, pHLIPvar3-Au^{13}-RubpySS and pHLIPvar3-Au^{100}-RubpySS resultant from 444 nm excitation and 650 nm detection. The normalised instrument response is also shown and was also recorded using excitation and detection at 444 nm. Linear (main) and log (inset) plots both included.

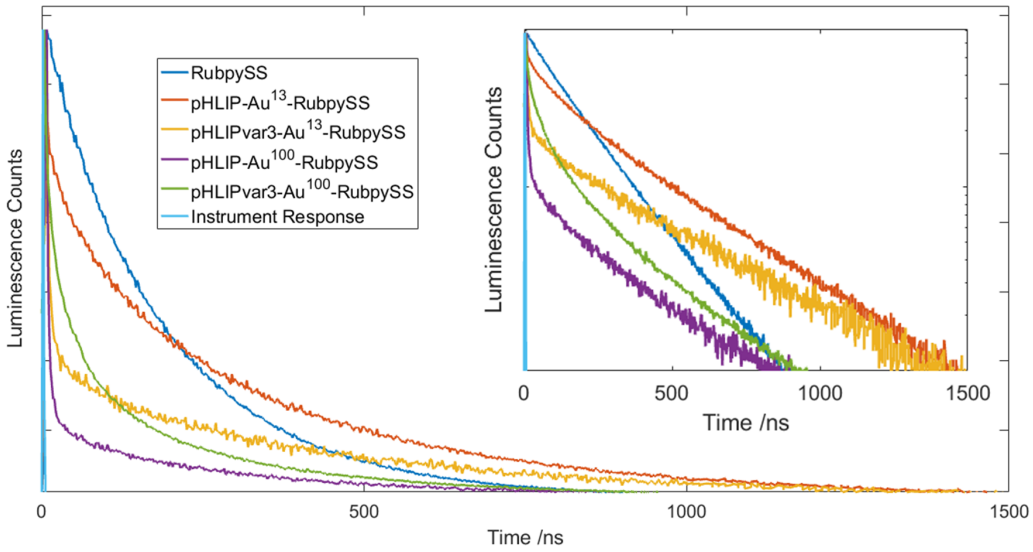

Figure 2.33: Time-resolved luminescent studies of the ^{3}MLCT radiative transition of RubpySS, pHLIP-Au^{13}-RubpySS, pHLIPvar3-Au^{13}-RubpySS, pHLIP-Au^{100}-RubpySS and pHLIPvar3-Au^{100}-RubpySS resultant from 444 nm excitation and 650 nm detection. The normalised instrument response is also shown and was also recorded using excitation and detection at 444 nm. Linear (main) and log (inset) plots both included.

Sample	**Emission Band λ_{max} / nm**	**Lifetime / ns**	χ^2
RubpySS	647	97 (2%), 287 (98%)	(1.071)
RubpySS + pHLIP	649	101 (9%), 328 (91%)	(1.016)
RubpySS + pHLIPvar3	636	140 (11%), 450 (89%)	(0.937)
RubpySS + kpHLIP	652	208 (18%), 524 (82%)	–
pHLIP-Au^{13}-RubpySS	627	114 (13%), 438 (87%)	(1.069)
pHLIPvar3-Au^{13}-RubpySS	637	51 (5%), 499 (95%)	(1.072)
pHLIP-Au^{100}-RubpySS	641	103 (7%), 417 (92%)	(1.011)
pHLIPvar3-Au^{100}-RubpySS	645	137 (18%), 434 (82%)	(1.023)

Table 2.6: Emission band λ_{max} (nm) and luminescence lifetimes (ns) of the emissive ^{3}MLCT transition of RubpySS before and after the addition of pHLIP peptide, and after complex has been assembled onto pHLIP-coated AuNPs. Steady state spectra were acquired using excitation at 465 nm, and a 444 nm picosecond-pulsed diode laser was used for time resolved studies. Luminescence lifetimes were fitted using an arrhenius model equation with a Levenberg-Marquandt non-linear fitting algorithm to iterate until suitable an acceptable convergence. χ^2 values are included as a measure of lifetime fitting accuracy.

complex was also prepared for control measurements (reference sample). The concentrations of each were adjusted until the absorbance of each sample's SPR band was equal, before transferring to the Integrated Sphere module of the FLS920 time correlated fluorescence spectrometer for quantum yield measurement. For luminescent and reference samples, scatter scans were performed where the excitation was set to 465 nm, and the emission monochromators were scanned from $455 - 475$ nm. In an accurate experiment, the scatter spectrum resultant from luminescent samples has lower intensity than the scatter of reference samples as the luminescent sample absorbs a portion of incident photons. When attempting this protocol however, the scatter of pHLIP-Au^{13} was of lower intensity than pHLIP-Au^{13}-RubpySS. Surface plasmon resonance ultimately contains absorption and scattering contributions, and as pHLIP-Au^{13} and pHLIP-Au^{13}-RubpySS have SPR λ_{max} 5 nm apart, it is the authors opinion that unlabelled AuNPs are not truly representative of gold scattering due to SPR-dependent spectroscopic interactions. Therefore no quantum yield measurements are included in this work.

2.2.7 Structural & Luminescent Properties of labelled-AuNPs within Buffered Environments

In the previous section, the pH-dependent cellular uptake of labelled-AuNPs was investigated using a cancer model of HeLa cells treated with Tyrode's buffer at physiological pH (pH 7.4, healthy cells) and low pH (pH 6.5, cancerous cells). The purpose of this section is to study the effect that experimental parameters had on recorded nanoparticle internalization data. Firstly, the pH dependency of RubpySS luminescence was investigated. AuNPs were co-labelled with a pHLIP peptide and the RubpySS complex, and photoluminescence from RubpySS was used as a measure of nanoparticle internalization in flow cytometry and light microscopy experiments. Secondly, a series of techniques were used to study pH-dependent colloidal stability.

The effect of pH on RubpySS luminescence

The steady state luminescence of RubpySS was studied as a function of pH using range that spanned the entire range of pH solutions used in previous cell treatments. Fig. 2.34 shows the steady state luminescence spectra of RubpySS (20μM) in a series of Tyrode's buffers (0.08 mM) ranging from pH 4.0 - 7.8. pH appears to have little effect on the luminescence intensity of RubpySS, with a small insignificant reduction in intensity at pH 5.2, but no net correlation with pH. Additionally, the λ_{max} of the ^{3}MLCT band is also unmodulated by pH of the solution.

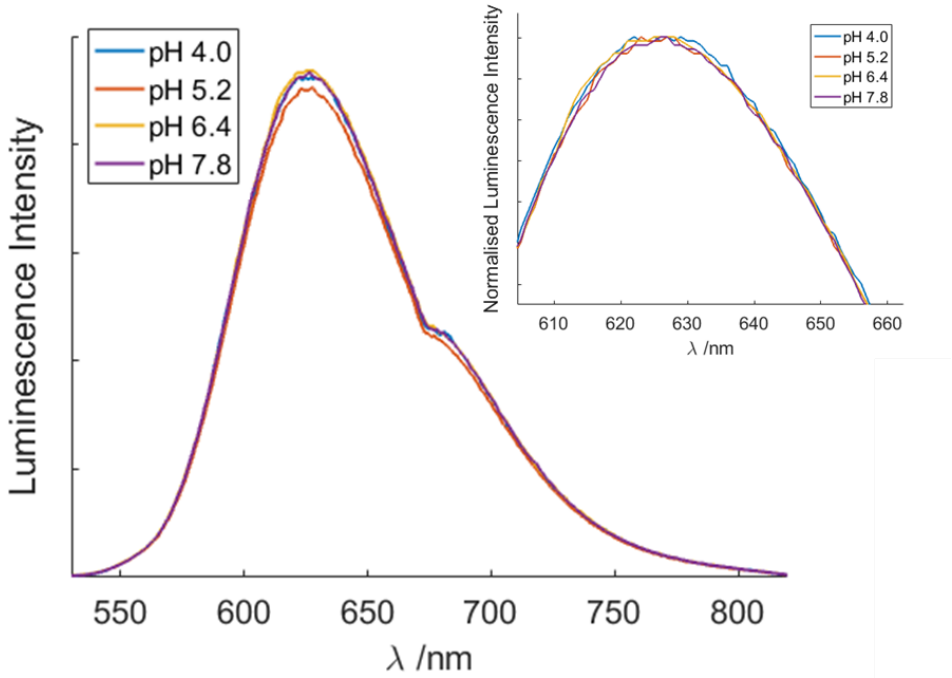

Figure 2.34: Steady state luminescence of RubpySS (20μM) dispersed in Tyrodes buffers (0.08 mM) in a pH range of 4.0 to 7.8. λ_{ex} = 465 nm, λ_{em} = 525 - 825 nm. Inset, data normalised to max intensity of pH 4.0 spectrum.

The effect of microenvironment pH on stability of labelled gold nanoparticles

In order to study the pH dependency of colloidal stability, solutions of pHLIP-Au$^{13\&100}$-RubpySS and pHLIPvar3-Au$^{13\&100}$-RubpySS were dispersed in Tyrode's solutions (pH 6.5 or pH 7.4) and subjected to ***i)*** dynamic light scattering analysis to study, hydrodynamic diameter of the colloid. ***ii)*** UV/Vis absorption spectroscopy to study the response of the gold surface electrons, and ***iii)*** TEM to study size and morphology of the colloid.

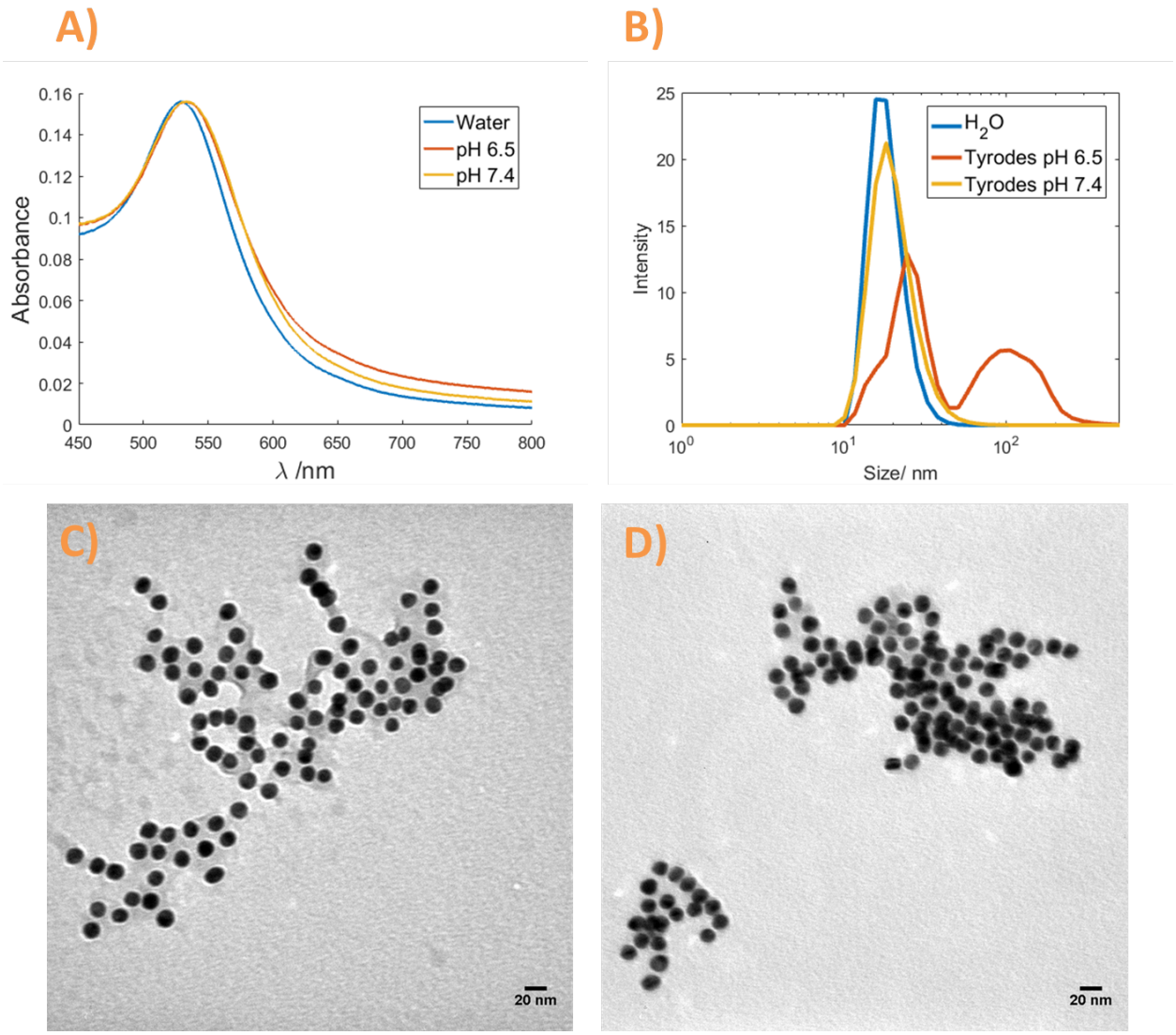

Figure 2.35: A) UV/Vis Absorption, B) Dynamic Light Scattering, C & D) Transmission Electron Micrographs of pHLIP-Au^{13}-RubpySS (1 nM) dispersed in Tyrodes Buffer (0.08 nM) pH 6.5 (TEM, Image C) and pH 7.4 (TEM, Image D).

For UV/Vis absorption analysis, the SPR λ_{max} was reported for samples of gold nanoparticles dispersed in water and Tyrodes solutions at pH 6.5 & 7.4. As previously discussed, the SPR band has a Gaussian

profile and is modulated by morphology [82], core charge [83], inter-particle distance [85] and surface functionalization [86]. The band also significantly broadens and loses intensity upon nanoparticle aggregation, and is a useful measure of colloidal stability. For DLS analysis, the colloid was dispersed into water or one of the tyrode's buffers, and the hydrodynamic diameter of the colloid was measured using dynamic light scattering. Often multiple peaks were present within the DLS histograms, which the program would express each peak as a percentage of total integration. For example, Fig. 8.36 shows the raw number distribution of hydrodynamic diameters of pHLIP-Au^{13}-RubpySS (1 nM) dispersed into Tyrode's buffer (pH 6.5, 0.08 mM). The two bands in the histogram are expressed as 689 nm (22.1%) and 161 (77.8%), where the weighted average of the two equates to 277 nm. For ease of comparing the DLS data in this section, the weighted averages of the number distribution are reported and contrasted.

pHLIP-Au^{13}-RubpySS (1 nM) was dispersed in Tyrode's solutions (0.08 mM, pH 6.5 or 7.4), and analysis by UV/Vis absorption (Fig. 2.35, A) showed the gold SPR λ_{max} was initially at 527 nm, and dispersion of the colloid in Tyrode's solutions resulted in an SPR shift of 5 nm for pH 6.5 (532 nm), and 5 nm for pH 7.4 (532 nm). This small 5 nm shift was identical for both samples, and no significant peak broadening or reduction in band intensity occurred post-dispersion, indicating no colloidal flocculation.

For DLS analysis of pH-dependent colloidal stability, upon dispersion into Tyrodes solutions the particle hydrodynamic diameter increased to 277 nm and 177 nm for pH 6.5 and 7.4, respectively, (Fig. 2.35, B). Particles dispersed in H_2O had a hydrodynamic diameter of 19 nm as previously in a previous chapter. This indicates that particles are associating in close proximity in both samples, but particles in the pH 6.5 solution are in motion as larger clusters. TEM imaging revealed that particles dispersed in either buffer had not flocculated into larger particles, but did appear to be associating together in larger clusters (Fig. 2.35, C - pH 6, D - pH7), supporting both the DLS and UV/Vis data. Additionally, the effect of serum proteins on colloidal stability was also investigated, as it is known that negatively charged colloidal nanoparticles can flocculate upon exposure to positively charged serum proteins[102]. For this experiment, pHLIP-Au^{13}-RubpySS particles were dispersed into water, serum-free media & serum-containing media and the colloids were studied by UV/Vis Absorption Spectroscopy Fig. 8.25 (Appendices). Dispersion of pHLIP-Au^{13}-RubpySS particles within water or serum-free media had negligible effects on the SPR band shape or λ_{max}, however dispersion of the nanoparticles into serum-containing media induced a 5 nm bathochromic shift of the SPR λ_{max}. However, a 5 nm SPR λ_{max} bathochromic shift is small relative to shifts characteristic of flocculating particles. Additionally, the band retained its gaussian shape and no additional bands appeared. This indicates no significant flocculation had occurred, suggesting that serum proteins are affecting the Au surface dielectric constant through proximal interactions, but are not destabilising the nanoparticles sufficiently to flocculate the colloid.

For pHLIP-Au^{100}-RubpySS, analysis by UV/Vis absorption (Fig. 2.36, A) indicated that the gold SPRλ_{max} moved from 614 nm to 624 nm for nanoparticles dispersed in Tyrode's pH 6.5, and did not move for particles dispersed at pH 7.4. This is indicative of pH-dependent changes on the gold surface leading to

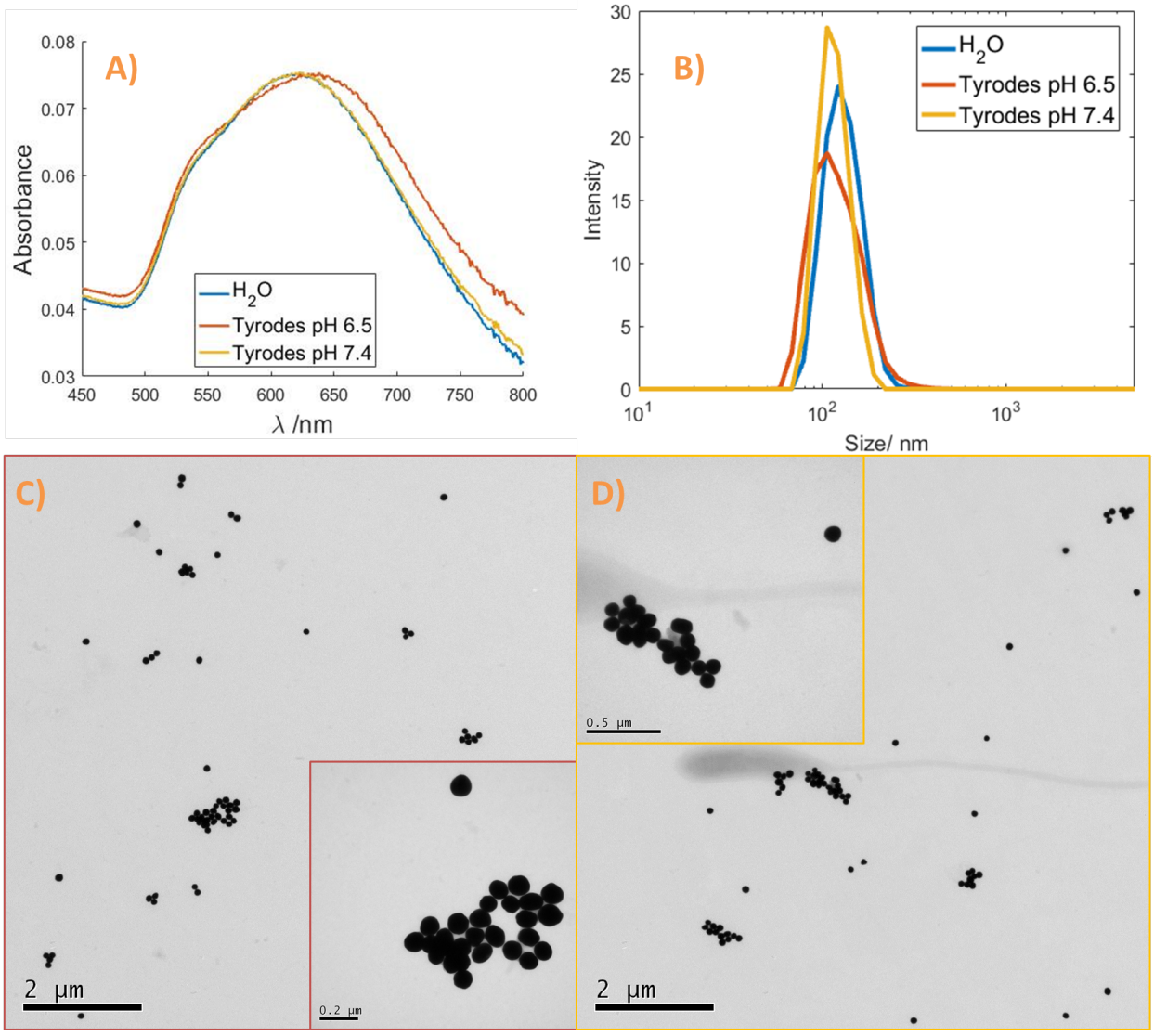

Figure 2.36: A) UV/Vis Absorption, B) Dynamic Light Scattering, C & D) Transmission Electron Micrographs of pHLIP-Au^{100}-RubpySS (8 pM) dispersed in Tyrodes Buffer (0.08 nM) pH 6.5 (TEM, Image C) and pH 7.4 (TEM, Image D).

electrons oscillating at a lower frequency at in the Tyrode's pH 6.5 solution. Number distributions of particle hydrodynamic diameter were also recorded (Fig. 2.36, B), indicating that particles in water had an average diameter of 92 ± 29 nm, and particles dispersed at pH 6.5 and 7.4 had hydrodynamic diameters of 123 ± 40 nm and 116 ± 22 nm, respectively. Transmission electron microscopy revealed clustered association of nanoparticles in both samples, however it was notable that particles were still spherical and no flocculation into large aggregates was visible, indicating that any surface changes at the gold surface were not resulting in sufficient degradation of the nanoparticle's surfactant layer.

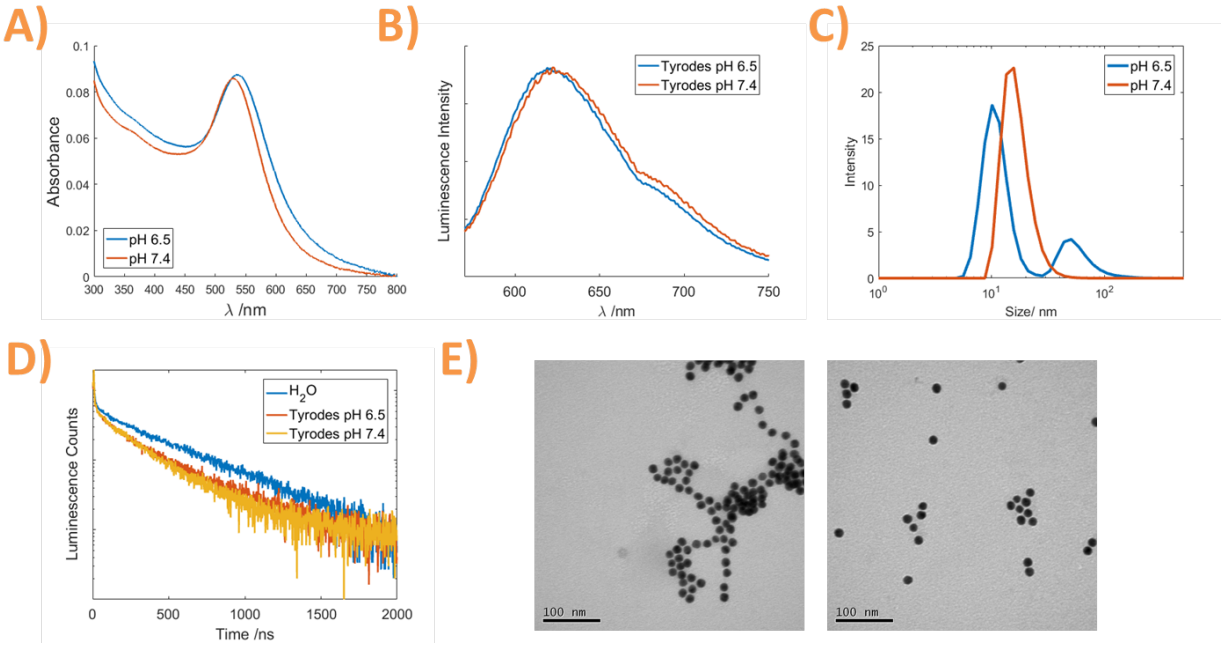

Figure 2.37: A) UV/Vis Absorption, B) Steady State Luminescence, C) Dynamic Light Scattering, D) Time-resolved Luminescence, and E) Transmission Electron Micrographs of pHLIPvar3-Au^{13}-RubpySS (1 nM) dispersed in Tyrodes Buffer (0.08 nM) pH 6.5 (TEM, Image C) and pH 7.4 (TEM, Image D).

For pHLIPvar3-Au^{13}-RubpySS, in addition to UV/Vis absorption, DLS, and TEM analysis, luminescence measurements were also taken to study whether they corroborated the former measurements. Particles (1 nM) were dispersed into a Tyrode's solution (0.08 mM, pH 6.5 & 7.4) and subjected to the following techniques.

Analysis of the UV/Vis absorption spectrum of dispersed particles indicated an SPRλ_{max} shift to 536 nm (+ 9 nm) and 529 (+ 2 nm) for pH 6.5 and 7.4, respectively. The full-width at half-maximum of the SPR band also changed markedly for each sample, increasing from 90 nm for citrate-labelled AuNPs to 146 nm and 130 nm for pH 6.5 and 7.4, respectively. The hydrodynamic diameters of pHLIPvar3-Au^{13}-RubpySS were also modulated in a pH dependent fashion upon dispersion into Tyrode's solutions. The hydrodynamic

Solvent	**Emission Band λ_{max} / nm**	**Lifetime / ns**	χ^2
Water	637	51 (5%), 499 (95%)	(1.072)
Tyrodes pH 6.5	636	3 (23%), 66 (9%), 363 (68%)	(1.080)
Tyrodes pH 7.4	649	3 (22%), 30 (4%), 273 (73%)	(1.096)

Table 2.7: Emission band λ_{max} (nm) and luminescence lifetimes (ns) of the emissive ^{3}MLCT transition of pHLIPvar3-Au^{13}-RubpySS (1 nM) before and after the dispersion of the particles into tyrode's solutions (0.08 mM, pH 6.5 or 7.4). Steady state spectra were acquired using excitation at 465 nm, and a 444 nm picosecond-pulsed diode laser was used for time resolved studies. Luminescence lifetimes were fitted using an arrhenius model equation with a Levenberg-Marquandt non-linear fitting algorithm to iterate until suitable an acceptable convergence. χ^2 values are included as a measure of lifetime fitting accuracy.

diameter of the colloid in water was 16 ± 3, and dispersion into the buffers increased the diameters to 21 ± 8 and 17 ± 5 for pH 6.5 and 7.4, respectively. Particle sizes according to TEM imaging remained at approximately 13 nm, with no evidence of large aggregates. However particles dispersed in Tyrodes pH 6.5 were associating in larger clusters significantly more so than particles dispersed in Tyrode's pH 7.4. Luminescence measurements were also quite revealing. Time-resolved luminescence measurements show a decrease in luminescence lifetime from 51 (5%), 499 (95%) in water, to 3 (23%), 66 (9%), 363 (68%) for pH 6.5, and 3 (22%), 30 (4%), 273 (73%) for pH 7.4. Expressed as weighted averages, the luminescent lifetime of pHLIPvar3-Au^{13}-RubpySS in water, Tyrode's pH 6.5 & Tyrode's pH 7.4 was 476 ns, 247 ns and 199 ns, respectively. The steady state measurements show a hypsochromic shift of the RubpySS ^{3}MLCT band from 637 nm in water to 636 nm at pH 6.5, and a bathochromic shift to 649 nm for pH 7.4. It is therefore the conclusion that lower buffer pH has caused the particles to associate in much closer proximity, either due to displacement mechanisms or charge imbalances. This is reflected by an increase in the SPRλ_{max}, the frequency of the oscillating gold surface electrons, which is sensitive to nearby particles [85]. This is supported by DLS measurements that show larger solvation structures tumbling through solution, and TEM which shows the colloid is still comprised of 13 nm spherical particles. Luminescence measurements show a pH dependent change in steady state and time resolved modes. Both modes indicate that emission flux from particles decreases upon dispersion into the buffers. It is not clear however whether this is a consequence of a pH-dependent cleaving effect of RubpySS from the gold surface, leading to shorter lifetimes or if it's resultant from a proximal effect between nearby particles (as indicated by DLS data) that perhaps contribute a quenching effect on RubpySS luminescence.

For pHLIPvar3-Au^{100}-RubpySS, hydrodynamic diameter measurements of the colloid upon dispersion into the buffers increased from 99 ± 29 nm to 150 ± 93 nm and 122 ± 45 nm, respectively. TEM imaging again did not indicate that nanoparticle flocculation had occurred, and instead indicated that the particles remained monodisperse. Again it appears that particles are associating in clusters, however it is not clear what effect that will exert on pHLIPvar3-mediated delivery of particles into eukaryotic cells.

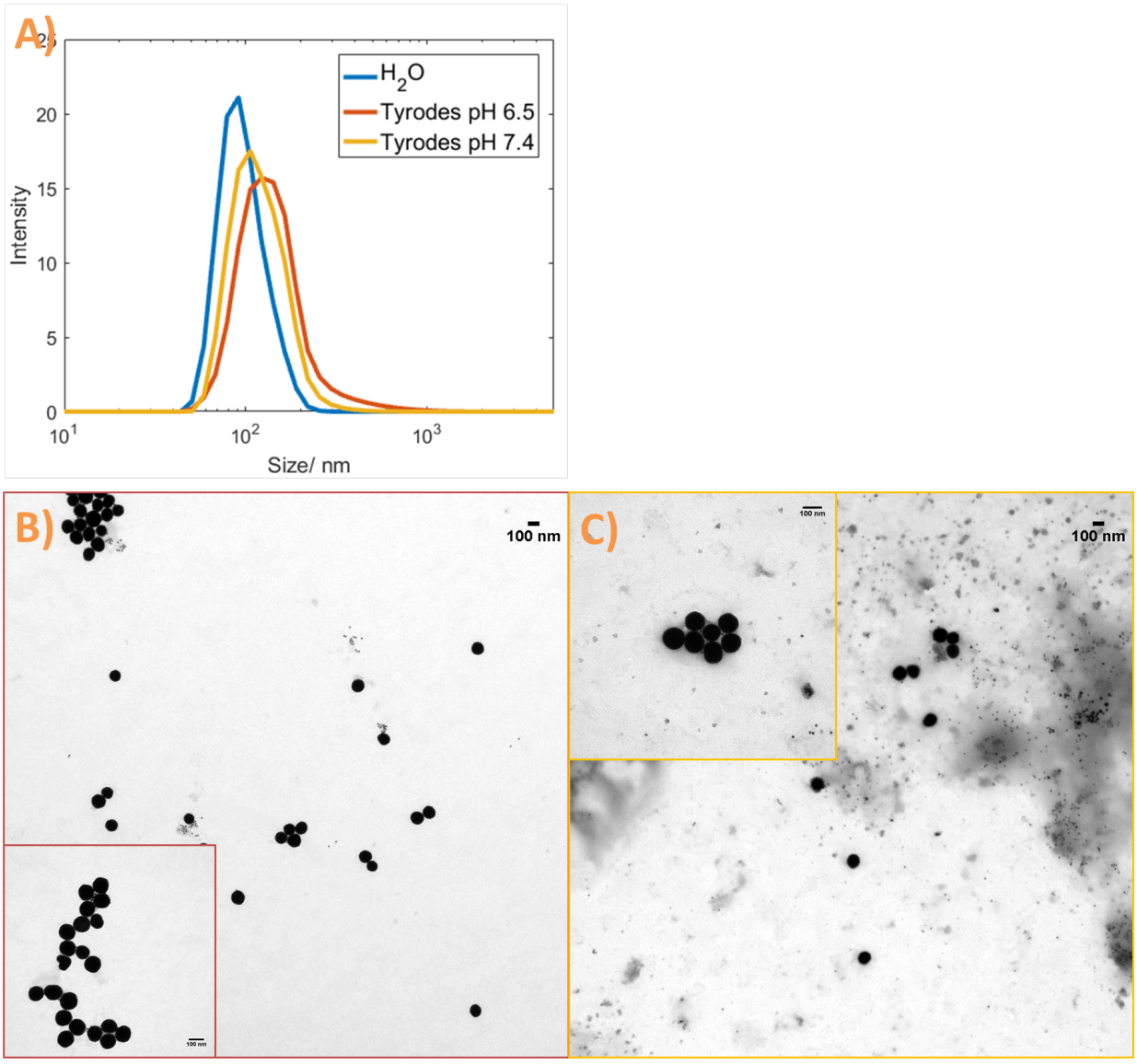

Figure 2.38: A) UV/Vis Absorption, B & C) Transmission Electron Micrographs of pHLIPvar3-Au^{100}-RubpySS (8 pM) dispersed in Tyrodes Buffer (0.08 nM) pH 6.5 (TEM, Image C) and pH 7.4 (TEM, Image D).

2.3 Conclusions

In summary, monodisperse Au^{13}NPs and Au^{100}NPs were synthesised and sequentially labelled with a pHLIP variant and the luminescent transition metal complex, RubpySS. Particles were then subjected to a plethora of structural and luminescent characterisations, in order to confirm the coating, and establish the effect of the coating on colloidal properties. The kpHLIP peptide, being the most hydrophobic variant studied, would not fully disperse in 5% DMF in phosphate buffered saline, and dynamic light scattering confirmed that when kpHLIP was used to label Au^{13}NPs, the particles were highly poly disperse and aggregated when small

amounts of RubpySS complex was added. As the labelling procedure, and ultimately particle monodispersity could not be controlled for kpHLIP-labelled AuNPs, these particles were neglected from further study in cellular uptake experiments. The nature of labelling gold nanoparticles that are initially stabilised by negative charge, with a positively charged substrate involved a significant trade off between efficiently coating the particles with the ruthenium complex, and maintaining good colloidal stability and monodispersity. Protocols were developed and tuned until strong luminescent signal was observed with narrow particle size distributions and low polydisersity indexes (PdI < 0.2) indicating excellent monodispersity, which was also confirmed by transmission electron microscopy of the labelled AuNPs. The coating of peptide labelled $Au^{13\&100}$NPs with RubpySS proved more efficient when labelling pHLIPvar3-coated AuNPs, possibly due to pHLIPvar3 being a smaller peptide, forming a thinner sheath around the gold, rendering the surface more accessible to incoming RubpySS. Steady state luminescence measurements indicated a destabilisation of the MLCT excited state of RubpySS when mixed with pHLIP variants, or when bound to Au^{13}NPs most likely due to charge destabilisation of the ^{3}MLCT state as a result of the complex being in a less polar environment [184]. However when bound to Au^{100}NPs the steady state luminescence very closely resembled that of free complex. It has been suggested in this work that the luminescence properties of the AuNP-bound ruthenium complex may be co-dependent on AuNP size-dependent plasmon effects and the co-label. Luminescence experiments in this work along with referral to previous work by the group [96, 166] indicated that the AuNP-bound co-label (peptides or fluorosurfactant) may impose a desensitising effect on gold surface plasmon resonance, which is reflected by the λ_{max} of RubpySS' steady state emission. However this will require further investigation. Across the board, mixing RubpySS with pHLIP peptides in solution resulted in an increased luminescent lifetime, which was increased further when the complex and peptides were assembled onto Au^{13}NPs. Lifetimes of pHLIP-Au^{100}-RubpySS and pHLIP-Au^{100}-RubpySS were shorter than their 13 nm analogues. pH dependent colloidal stability measurements indicated a pH-dependent response in the size of associated nanoparticles, particularly for pHLIPvar3 labelled-AuNPs. This does raise a question of pHLIP mediated uptake that to the knowledge of the author, has not been raised in a previous pHLIP publication. During it's pH mediated internalization into POPC liposomes pHLIPs have been shown to fold reversibly into an α-helix, permitting its transduction across the plasma membrane [132, 170, 181, 176], and indeed the same has been shown when pHLIP has been tethered to an AuNP [137]. How this translates into a more dynamic and complex cellular environment is not clear, particularly as aggregation of nanoparticles has been shown to strongly affect cellular uptake [102] and that many proteins have strong affinities for charged particle surfaces [103]. Although neither pHLIP-$Au^{13\&100}$-RubpySS or pHLIPvar3-$Au^{13\&100}$-RubpySS flocculated in the buffers that were used in these cell treatments, the effect that clustered association of nanoparticles has on nanoparticle internalization is unclear, and this should be a major component of future research.

2.4 Future Work

Additional work for this chapter would be to more fully characterise the bonding between the peptide's and the gold surfaces. pHLIPvar3's binding to gold surfaces would need to be investigated, particularly as pHLIPvar3 has two soft bonding donors from its two cysteine residues. X-ray photoelectron spectroscopy would be used to better understand the bonding configurations between pHLIPvar3 and gold surfaces. Additionally, analysing the effect of nanoparticle flocculation and the cleaving of RubpySS from Au surfaces on ruthenium luminescence would also be an interesting addition and useful when characterising the integrity of the surface labelling when nanoparticles are internalized into cells. Additional measurements of the effect that nanoparticle-bound surfactants impose on ruthenium luminescence will permit elucidation of why there is an apparent AuNP size-dependent emission λ_{max} for RubpySS in this work.

2.5 Experimental

pHLIP, kpHLIP and pHLIPvar3 peptides were purchased from Peptide Synthetics and used without any further purification. Peptides were dissolved in 5% DMF in PBS, and were used in stock solutions of 0.5 mM, 0.5 mM and 0.65 mM, respectively.

2.5.1 Synthesis of luminescent ruthenium complex, RubpySS

Synthesis of $[Ru(bpy)_2(4,4\text{-di-}(5\text{-lipoamido-1-pentoxy})\text{-}2,2\text{-bipyridine})]^{2+}$, RubpySS, was synthesised according to Adams et al. [175] and was characterised by ^{1}HNMR, ^{13}C ^{1}H PENDANT NMR, Electrospray Mass Spectrometry, UV/Vis Absorption Spectroscopy and Elemental Analysis. RubpySS was prepared via a modification to a method outlined by Sullivan et al. [186]. Briefly, a solution of bpySS (68.6 mg, 0.11 mmol) and $Ru(bpy)_2Cl_2$ (100.17 mg, 0.21 mmol) in ethanol (10 mL) was heated under reflux for 16 hours. The resultant red/orange solution was cooled to room temperature, whereby H_2O (35 ml) was added to the solution, forming a fine cream precipitate, which was filtered. A saturated methanolic solution of ammonium hexafluorophosphate (0.25 g, 1.5 mmol in 2 ml EtOH) was added to the solution, giving a red/orange precipitate. The precipitate was filtered and washed with ice-cold H_2O, followed by ice-cold Et_2O to give the crude product as an orange/red solid. The solid was dissolved in a minimal amount of acetonitrile and the solvent was removed in vacuo to give a red crystalline solid RubpySS (79.9 mg, 51%); Found: C, 45.9; H, 4.9; N, 7.4; Calc: C, 46.8; H, 4.9; N, 7.8; δH(300 MHz; $CDCl_3$), 1.67 1.73 (2H, m, H-53,72), 1.84 (4H, t, J = 7.2, H-47,64), 2.19 2.32 (4H, m, H-48,71), 2.85 3.10 (4H, m, H-44,61), 3.34 3.46 (2H, m, H-58,68), 4.04 (4H, t, J = 6.5, H-40,57), 6.24 (2H, s, NH), 6.75 (2H, dd, J = 6.5, 2.6, H-27,36), 7.20 (4H, dd, J = 6.6, 1.2, H-,25,26), 7.26 (4H, dd, J = 6.6, 1.2, H-2,8,17,22), 7.63 (4H, dd, J = 3.6, 0.77, H-3,7,16,23) 7.68 (4H, dd, J = 5.6, 0.8, H-3,7,16,23), 7.88 (6H, m, H-1,9,18,21,24,28), 8.24 (4H, dd, J = 8.0, 3.1, H-6,10,19,20); δC(100 MHz; $CDCl_3$), 23.6 (C-42,59) 25.2 (C-28,35), 28.8 (C-49,66), 29.4 (C-41,58), 35.3 (C-51,67), 36.3

(C-47,64), 39.2 (C-54,71), 39.3 (C-44,61), 41.0 (C-53,72), 57.4 (C-52,68), 70.6 (C-40,57), 111.3 (C-29,34), 115.1 (C-27,36), 125.0 (C-6,10,19,20), 128.4 (C-2,8,17,22), 138.3 (C-1,9,18,21), 153.7 (C-3,7,16,23), 158.2 (C-5,11,13,14), 167.6 (C-46,63); MS (ESI^+) m/z 1294 [(M PF_6)+].

2.5.2 Ion Exchange of RubpySS.$(PF_6)_2$ for RubpySS.(Cl_2)

Dowex® 1x8 200 MESH Ion Exchange Resin (10 g) was equilibrated in 30 mL deionised water, whereby the pH was lowered to pH 5 by dropwise addition of hydrochloric acid (1.2 M) followed by vigorous stirring for 1 hr. The Dowex® was collected by suction filtration and re-diluted in 30 mL methanol, to which RubpySS.$(PF_6)_2$ (100 mg) was added and the mixture was stirred vigorously for 2 hrs. The Dowex was then filtered off and washed through with methanol (3 x 10ml). The filtrate was collected and solvent removed in vacuo to give RubpySS.Cl_2 as a dark-red solid (86.0mg and 2.3mg respectively). RubpySS ES MS(+): m/z 1027.3 [M - Na+].

2.5.3 Synthesis of colloidal gold

13 nm citrate-stabilized AuNPs were synthesized by the method according to Schulz et al.[159] and subsequently a seeded growth protocol by Ziegler et al. [69] was used with 13 nm AuNP seeds to synthesise 100 nm diameter AuNPs. Particles were characterized by dynamic light scattering, capilliary electrophoresis, transmission electron microscopy and UV/Vis absorption spectroscopy. The approximate concentrations have also been estimated as 1.6 nM for Au^{13}NPs and 40 pM for Au^{100}NPs.

Synthesis of Au^{13}NPs

For Au^{13}NPs, the method of Schulz et al.[159] was followed with a few modifications. Briefly, a solution of trisodium citrate (60.6 mg), citric acid (13.3 mg) and ethylenediaminetetraacetic acid (1.0 mg) in H_2O (100 mL) was brought to reflux with rapid stirring. Rapid addition of $HAuCl_4$ (8.0 mg) in H_2O (25 mL) to the vortex of the solution resulted in a colour change from pale colourless to a deep wine red, approximately 30 seconds post-addition. Boiling was continued for an additional 10 minutes, the heating mantle was then removed and stirring was continued until particles had cooled to room temperature. The colloid was characterized by a UV/Vis absorption at 517 nm, a zeta potential (ζ) of -37 $\pm$ 7 mV (pH 6.2), and DLS number distribution indicated a particle size of 11 $\pm$ 3 nm. Transmission electron microscopy also confirmed the synthesis of approximately 13 nm seeds (Fig. 8.3).

Synthesis of Au^{25}NPs

Au^{13}NPs (34 mL) were diluted to 40 mL with H_2O, and stirred rapidly in a roundbottom flask equipped with a reflux condenser. Solutions of i) trisodium citrate and ascorbic acid in H_2O (20 mL) and ii) $HAuCl_4$ in H_2O were both simultaneously added to the colloidal solution in a dropwise fashion. After addition

was complete, the mixture was heated at 150°C for 30 minutes, and then allowed to cool slowly to room temperature.

Synthesis of Au^{50}NPs

Au^{25}NPs (9 mL) were diluted to 40 mL with H_2O, and stirred rapidly in a roundbottom flask equipped with a reflux condenser. Solutions of i) trisodium citrate and ascorbic acid in H_2O (20 mL) and ii) $HAuCl_4$ in H_2O were both simultaneously added to the colloidal solution in a dropwise fashion. After addition was complete, the mixture was heated at 150°C for 30 minutes, and then allowed to cool slowly to room temperature.

Synthesis of Au^{100}NPs

Au^{50}NPs (40 mL) were stirred rapidly in a roundbottom flask equipped with a reflux condenser. Solutions of i) trisodium citrate and ascorbic acid in H_2O (20 mL) and ii) $HAuCl_4$ in H_2O were both simultaneously added to the colloidal solution in a dropwise fashion. After addition was complete, the mixture was heated at 150°C for 30 minutes, and then allowed to cool slowly to room temperature. DLS, 108 ± 27 nm; SPR, 572 nm; Zeta potential (ζ) = -41 ± 6 mV (pH 2.95).

Calculation of AuNP Concentrations

For Au^{13}NPs: $HAuCl_4$ starting mass = 8 mg; Au% by mass = 3.94 mg; 3.94/196.67 (Au RAM) = $1.99x10^{-5}$ moles of Au; Moles (M) of Au = $1.99x10^{-5}/125x10^{-5}$ = 0.00159 M; volume of 13 nm AuNP = $2.74x10^{-25}$ m^3; volume of gold atom = $2.74x10^{-30}$ m^3; No. of atoms per AuNP = 100081.9; Conc Au (M) / No. atoms per AuNP = $1.59x10^{-9}$ M or 1.6 nM. For Au^{25}NPs, multiply by Au13/Au25 dilution ratios: 1.6 x (34/80) = 0.68 nM. For Au^{50}NPs, multiply by Au25/Au50 dilution ratios: 0.68 x (9/80 x 1000) = 78 pM. For Au^{100}NPs, multiply by Au50/Au100 dilution ratios: 1.6 x (20/40) = 38 nM.

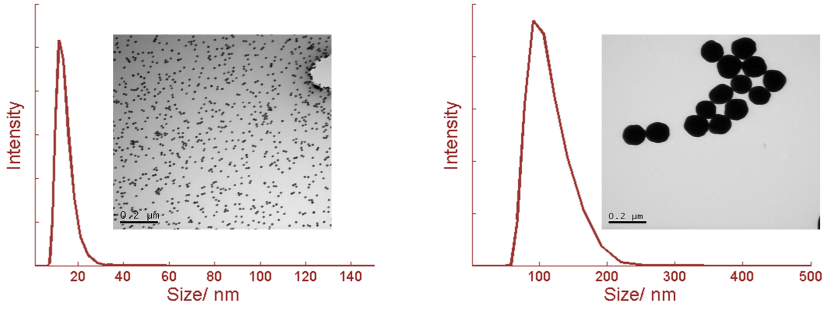

Figure 2.39: Hydrodynamic diameter of colloidal 13 nm (left) and 100 nm (right) gold nanoparticles. Distributions based on numerical analysis of dynamic light scattering intensity distributions. Inset both, transmission electron micrographs of particles studied.

2.6 Data Analysis Methods

UV/Vis of colloidal gold nanoparticle samples was analysed by fitting the SPR band with a gaussian model. A gaussian curve is a good model for doppler, natural and collision broadening experienced by molecules interact with light, and was fitted to the SPR band using a Levenberg-Marquandt Non-linear fitting algorithm that iterated until it had successfully converged upon parameters of λ_{max} and Absorbance. The Full Width at Half Maximum (FWHM) of the gaussian profile fitted to the SPR band was then subsequently fitted using a FWHM algorithm written by Patrick Egan and obtained through MathsWorks.

An example of an analysed dataset is shown in Fig. 2.40. The original data is shown followed by the fitting of each individual UV/Vis absorption spectrum of the dataset. The results are then compiled into a graph where the change in SPR λ_{max} and FWHM are displayed as functions of ligand concentration.

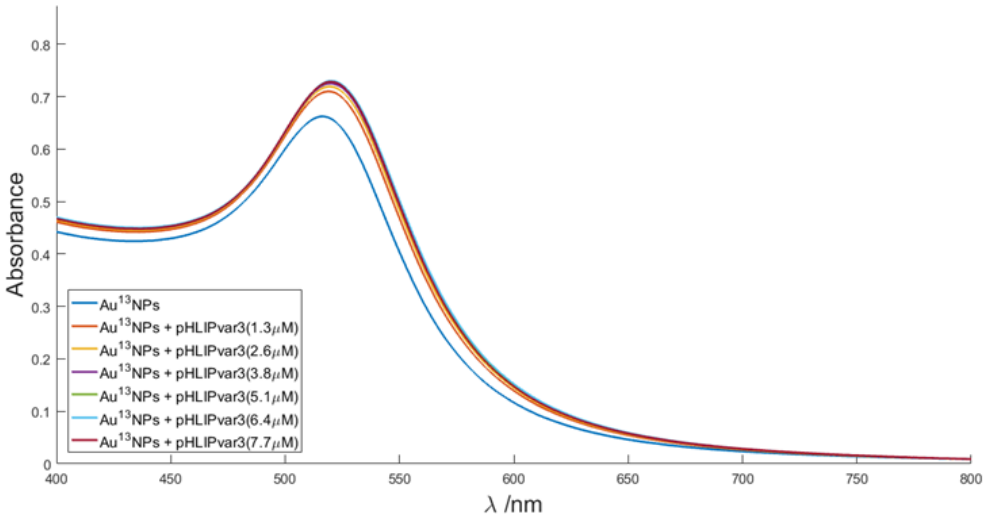

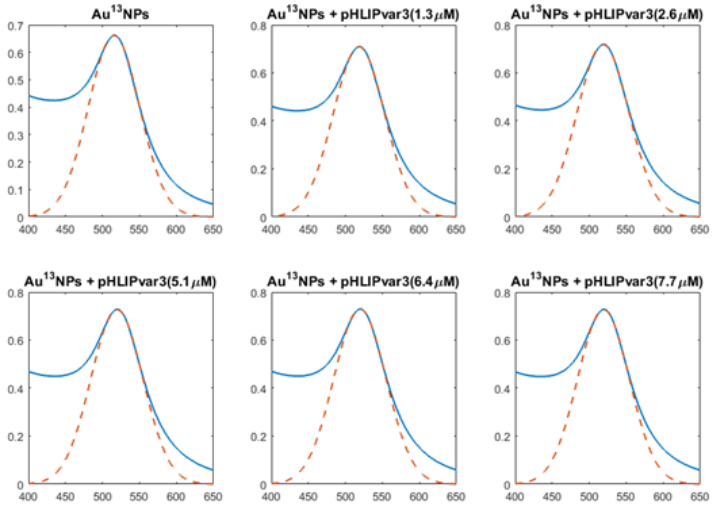

SPR	FWHM	lmerr
521.3812	83.8713	0.0019
523.0927	84.7086	0.0014
524.1575	85.2058	0.0012
524.8476	86.3984	0.0013
525.4407	86.7256	0.0011
526.1962	87.4855	0.0012
526.5487	87.9821	7.7446e-04
527.0683	88.7754	8.9805e-04

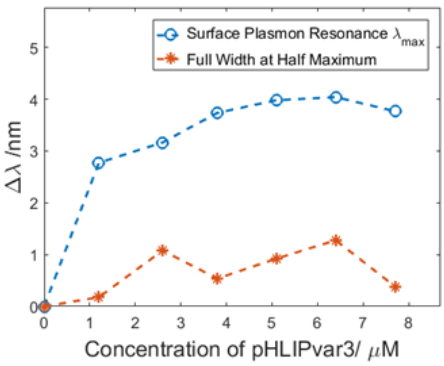

Figure 2.40: Sample UV data with a Gaussian function fitted to each SPR band, followed by the sequentially calculated lambda max, Full Width at Half Maximum (FWHM) and Last Squares Error.

Chapter 3

pHLIP-mediated uptake of AuNPs into Cancer Cells

3.1 Introduction

Tumour targeting delivery of anticancer drugs has attracted much attention over the past few decades because of the potential to deliver a drug to cancerous tissue whilst leaving healthy tissue unaffected, reducing the overall side effects of the drug. The major categories of tumour targeting drug delivery are i) the Enhanced Permeability and Retention (EPR) effect, where it has been shown that tumour cell angiogenesis results in irregular, dilated, and sometimes defective blood vessels with large fenestrations amongst endothelial cells permitting the leaking of macromolecules such as nanoparticles from the blood plasma into the tumour tissue [104, 105]; and ii) the targeting of specific cancer biomarker proteins [106]. It has however been shown that the EPR effect is small/non-existent for some tumour types [187, 109, 108] and the targeting of biomarkers is often complicated by tumour cell heterogeneity [110, 111]. Furthermore, many biologically active compounds, including large biomolecules need to be delivered to intracellular destinations to exert their therapeutic action, and often the lipophilic nature of the plasma membrane restricts which species of biomolecules are capable of internalization. A novel approach to deliver such molecules involves tethering them to peptides that translocate through the cellular membranes, thereby enhancing their delivery into the cell. These Cell Penetrating Peptides (CPPs), sometimes referred to as Protein Transduction Domains (PTDs), have several advantages over conventional techniques as they are often efficient over a range of cell types, can be applied to cells en masse, and have potential therapeutic applications [188]. CPPs often possess a net positive charge often from high abundance of arginine residues, and initial attraction of the CPP to the plasma membrane is resultant from the electrostatic attraction between the positively charged PTD and negatively charged surface proteoglycans. It was first demonstrated in 1999 that nanoparticles could be ferried across the plasma membrane by CPPs [189] where super-paramagnetic iron oxide nanoparticles were

derivatized with the PTD from the transactivating transcriptional activator (TAT) protein of HIV-1. Since then, CPP-mediated transport of cargo across the plasma membrane has been reviewed for nanoparticles [190], liposomes[190, 112] and double stranded DNA [188], peptides [188, 191] and proteins [192, 193].

3.1.1 Acidosis: A property of Tumour Cell Microenvironments

It was long believed that intracellular pH of tumour cells held acidic values, from Warburgs first observations of the "remarkable extent to which living tumour cells are able to convert carbohydrate into lactic acid" [194], until Griffiths and coworkers employed the non-invasive ^{31}P NMR and indicated that tumour cell pH was around neutral, and sometimes slightly alkaline [195]. It is now known that acidic tumour pH is characteristic of extracellular tumour fluid, and not from within tumour cells themselves [196]. Tumours have high rates of glycolysis, and although the reason for this has not been proven, it has been suggested that tumour cells resort to high rates of glycolysis to fill the ATP deficit resultant from the poorer abundance of mitochondria in cancer cells [197]. Protons generated through glycolysis are combined with the lactate counter ion and are removed from the cell by the monocarboxylate/H1 co-transporter in order to maintain the cells normal operational pH. The effect of acidosis provides a universal pH biomarker of cancer cells and continuing attempts to exploit this phenotype are being pursued [171, 172, 198].

3.1.2 The pH Low Insertion Peptide (pHLIP)

The spontaneous membrane-insertion of small peptides ($<$ 60 residues) was first reported ca. 1994, and these were followed with reports of suggested methods design and development [199, 200, 201]. The pH-low insertion peptide (pHLIP) was first reported by Hunt et al. in 1997 [132, 202] where they reported the spontaneous, rapid and reversible, pH-dependent insertion of a bacterially derived transmembrane α-helix. The peptide has been shown to undergo membrane insertion by a three step process, centred around an insertion trigger at approximately pH 6.0. It was found that this pH insertion threshold coincided with the pH of tumour cell micoenvironments, this prompted use as imaging and diagnostic tools for cancer [203, 204, 170, 205], inflammation [206] and ischemic myocardium[136]. Over the last twenty years there has been a strong expansion of the range of applications the peptide has been applied to, as well as an expansion of the pHLIP library, with new bespoke derivatives of pHLIP synthesised to suit applications.

Structure and physical properties

The pHLIP peptide was based on the Helix-C of the primary structure of bacteriorodopsin, and its original sequence consisted of 36 amino acids. The peptide is one of few anionic cell penetrating peptides, of which glutamic acid (Glu) & aspartic acid (Asp) residues lie responsible for the peptides net charge of -5, and contribute to a net hydrophilic property. The peptide was shown to weakly associate with phospholipid bilayers at neutral pH, and as a result was easily recoverable using sedimentation methods. The primary structure

of this peptide was theoretically shown to satisfy the hydrogen bonding requirements of the polypeptide backbone while burying its hydrophobic chains into the hydrophobic core of the plasma membrane. Circular dichroism experiments of pHLIP-membrane interaction revealed the appearance of α-helix bands during its insertion process, and revealed a pH threshold of membrane insertion of approximately pH 6.0. Table 3.1 shows the original Wt-pHLIP sequence reported by Hunt et al in 1997 [132]. Since then, over 20 variants of the peptide have been studied.

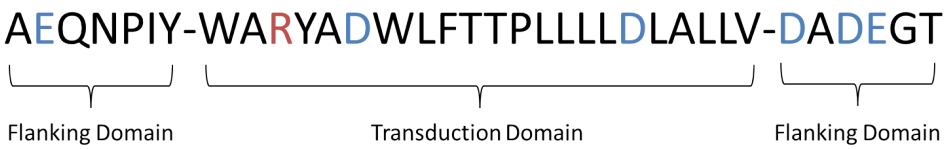

Figure 3.1: Wt-pHLIP peptide sequence from the 2010 review by Andreev et al. [133] with the transduction and flanking domains labelled. Positively-charged residues labelled in red; negatively-charged residues in blue, and neutral residues in black.

Stability & Solubility

The original pHLIP peptide (Wt-pHLIP), is water soluble and has been shown not to aggregate in aqueous solution, mediate pore formation, or form its α-helical structure while on the surface of the plasma membrane [170, 207]. However, it was shown that substitution of the aspartic acid residues within the transduction domain for alanine residues induced peptide aggregation in aqueous solution, and substitution of glutamic acid for asparagine rendered the peptide ineffective for tumour cell targeting [181, 182].

Process of pHLIP's Binding to Phospholipid Bilayers

In aqueous solution, the pHLIP monomer exists in a conformational equilibrium of three states and a solubility equilibrium also exists between monomeric pHLIP and oligomeric and aggregated analogues. The position of the conformational equilibrium is dependent on pH of the peptide's microenvironment and plasma membrane accessibility. Fig. 3.2 illustrates each component of the equilibrium, illustrating the conformation of the peptide at each stage. In state 1, when the pH of the solution > 6.5 and where plasma membranes are absent, the peptide adopts a free, unstructured and monomeric form. In state 2, In the presence of plasma membranes, and at $>$ pH 6.5, the peptide will loosely bind to the membrane periphery in an unstructured monomeric state. In state 3, when in the presence of plasma membranes and with pH < 6.5, the peptide's aspartic/glutamic acid residues become protonated, and the peptide folds into an α-helical structure inserting itself C-terminus first into the plasma membrane [204, 205]. At face value, pHLIP's insertion pH is unusual as the pKas of glutamic acid & aspartic acid are 4.1 and 3.9, respectively. Despite these low pKas, pHLIP's tranducting domain appears to undergo its pH switch at $\approx$ pH 6.0. This increased pKa is associated with a reduction of the dielectric constant of the peptide's environment when the peptide is proximal to a plasma

membrane. On this subject, there is a large amount of experimental data along with theoretical calculations that indicate the pKa of an amino acid could be significantly modified while on the border of, or within a plasma membrane [208, 209, 210, 211].

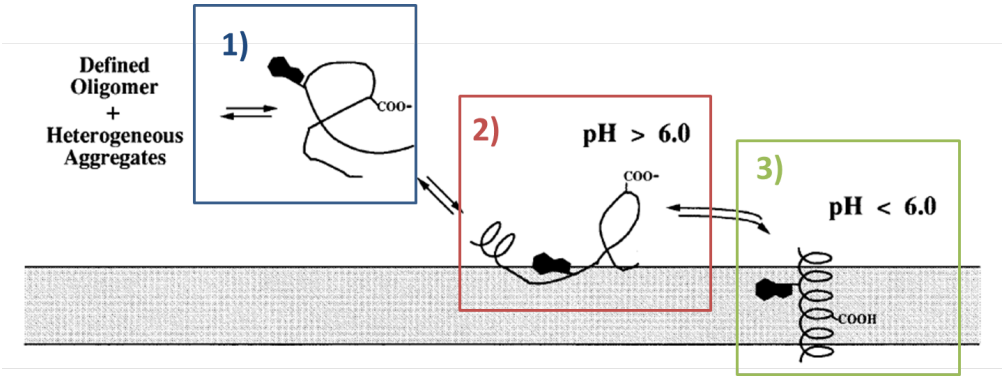

Figure 3.2: Schematic of conformation changes of the Wt-pHLIP peptide during it's pH-dependent membrane insertion, taken from [132].

At high and neutral pH, the peptide adopts an equilibrium between stage 1 and stage 2, with a dissociation constant largely influenced by electrostatic effects between the anionic peptide (-5 at pH 7.4) and anionic phosphate head groups. Favourable hydrophobic interactions drives the initial association of the peptide with plasma membranes, and thereafter membrane binding is dominated by N-terminal segments of the pHLIP peptide [212]. At neutral pH, the peptide is anchored at the surface of the membrane by pHLIP's hydrophilic residues, Glu & Asp.

Process of pHLIP's Insertion into Phospholipid Bilayers

Membrane insertion operates in a series of discrete stages. If the pH of a system of plasma membranes in aqueous solution is lowered to the insertion pH, the protonation of the Aspartic acid residues D14 and D25 side chains becomes the first instigator of insertion. This leads to the formation of two membrane-embedded pHLIP structure populations; one population (approximately 70% of total population) exists as a non-structured peptide which has been drawn deeper into the membrane than in Stage II (Stage II), with the second population (approximately 30% of total population) adopting an inserted motif with an α-helical structure between residues A10 - A27 (Stage III) as shown in Fig. 3.3. If system pH was further lowered to pH 5.3, an increased majority of pHLIP peptide will exist as a transmembrane helix [212].

The kinetic properties of pHLIP's pH-triggered insertion, stage II) to stage III), complied with first-order kinetics, as determined by tracking fluorescence changes and performing circular dichroism measurements upon insertion of pHLIP into POPC vesicles. pHLIP's insertion begins with rapid helix formation, and while it is not experimentally clear exactly how many helixes are formed, two folding intermediates were identified, occurring at 8 and 12 ms. The process of transbilayer insertion happens much slower, and there is a distinctly different, significantly more rapid process of peptide withdrawal which occurs within 100 ms of pH triggering

[133]. The change in Gibbs Free Energy (ΔG) of pHLIPs binding to a POPC surface (transition from State I to State II) at 37°C = -7 kcal mol^{-1} and the additional free energy of folding and insertion of pHLIP across a POPC bilayer = -2 kcal mol^{-1} (transition from State II to State III) [213]. It is theorized that this energy difference between States II & III, could be used to partition a cargo across the lipid bilayer. The overall insertion time has been reported as ≈ 40 seconds for Wt-pHLIP [176].

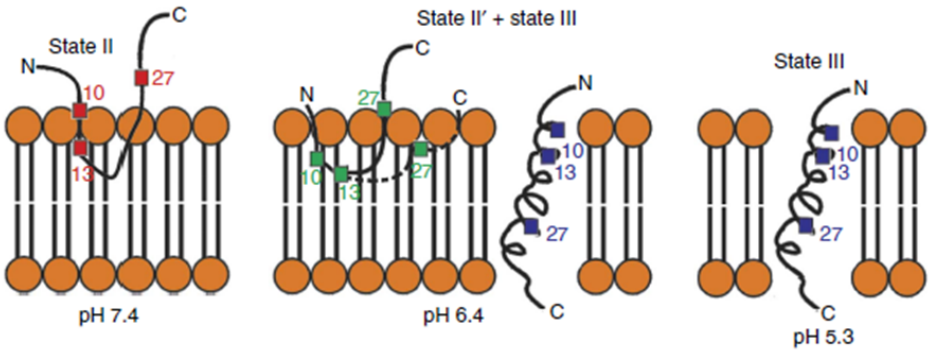

Figure 3.3: Schematic of pHLIP insertion process from Stage II to Stage III. In state II (pH 7.4), the N-terminal A10 (5.7 Å) and A13 (7.6 Å) residues are in close proximity to the head group phosphates. The C-terminal A27 (410 Å) is depicted as outside the membrane. In the adsorbed state II' at pH 6.4, pHLIP sinks deeper into the bilayer (with A10 at 7.6 Åand A13 at 410 Å), pulling A27 (6.4 Å) into close distance to head group phosphates. In state III (at both pH 6.4 and 5.3), A10 (5.7 Å) and A13 (7.8 Å) are located deeper in the membrane than in state II (pH 7.4) but maintain similarly close distances to phosphates, whereas A27 is still 410 Åaway from head group phosphates of the opposing monolayer lipids. Figure and caption taken from [212].

The effect of pHLIP's Primary Structure on Membrane Insertion

The pH threshold, window and insertion mechanism are bespoke according to the primary structure of the variant being studied. For example, the pH of insertion threshold of Wt-pHLIP moved from pH 6.0 to pH 6.5 after two key aspartic acid residues were substituted for glutamic acid, another hydrophilic amino acid, within the peptide sequence [181, 182]. Fendos et al. reported the how the location of these aspartic acid residues within the pHLIP sequence affected the penetration depth of pHLIP's insertion, and thereby affect pHLIP's insertion pKa and exhibited an effect on insertion reversibility and peptide aggregation. In the case of particular variants, this study revealed that pHLIP peptides with a lower threshold of pH-insertion and increased resistance to aggregation could be engineered by tuning the location of particular Asp residues [214]. Substitutions of specific aspartic acid residues Asp14 and Asp25 within the Wt-pHLIP sequence yielded adjustments to the pH insertion window. Substitution of Asp25 for α-aminoadipic acid, increased the threshold of pHLIP insertion to pH 6.74, and substitution of Asp14 for γ-carboxyglutamic acid narrowed the insertion window to 0.5 pH units. These effects were also additive when both substitutions were performed to the same sequence [215].

Peptide hydrophobicity has shown to have an effect on the number of transition states involved in pHLIP's

insertion [216]. Typically, if the peptide possesses a charge or a polar cargo attached at the C-terminal end, a helical interfacial intermediate will form prior to peptide insertion. The authors also note that the driving force for transmembrane insertion might be from lipid distortion by partial peptide insertion. This is supported by an earlier report from Bohinc et al. [217] of how membrane tension and stability are disrupted by the insertion of a helical polypeptide.

Process of pHLIP's Exit from Phospholipid Bilayers

pHLIP's exit from a phospholipid bilayer occurs orders of magnitude faster than insertion, completing approximately 100 ms after a sudden pH increase. This implies that the path of membrane exit differs from the bath of membrane insertion, and likely involves partial unfolding within the plasma membrane, before the peptide's exit from the bilayer [133].

Non-Specific Uptake of pHLIPs

Andreev et al. and Musial et al. reported on nonspecific uptake of the pHLIP peptide [181, 182]. An analogue of pHLIP (kpHLIP) was prepared, where the two aspartic acid residues within the peptide's transduction domain were substituted for lysine residues, and was shown not to exhibit tumour cell targeting. It was also reported in this study that substitution of pH-switchable aspartic acid residues for lysine rendered the peptide too polar to insert into the membrane at neutral or acidic pH.

Derivatives of Wt-pHLIP

Weerakkody et al. considerably expanded the reservoir of pHLIP variants in 2013 [176]. They modified the original Wt-pHLIP sequence using various reforms, including residue addition, substitution, and truncation. 16 new variants were synthesised based on a multitude of modifications, and each was subjected to routine circular dichroism and luminescence experiments to assess the new variants ability to interact with a phospholipid bilayer in a pH dependent manner. All variants exhibited a pH-dependent affinity for the plasma membrane, where the insertion threshold (peptide pK_as) ranged from pH 4.5 - pH 6.5 for entry into POPC vesicles, and insertion time ranged from tens of milliseconds to minutes. The variants also exhibited a range of Gibbs Free Energy differences ($\Delta\Delta G = \Delta G_{pH4.0} - \Delta G_{pH8.0}$) between insertion at pH 8.0 and pH 4.0, indicating that the insertion of some variants was energetically more favourable, or more switchable than others. For example, some variants exhibited very favourable energetics of membrane insertion at low pH, but also exhibited similar affinities for insertion at high pH resulting in poor insertion switching.

Having previously known that the hydrophilic constituents of pHLIP (Asp or Glu) were responsible for pH-switching, the effect of choosing one over the other was investigated. Variants equipped with Glu residues, rather than Asp, exhibited higher affinities for the plasma membranes at due to the presence of an extra methylene group in Glu that renders the peptide more hydrophobic.

For the most part, the series of truncated variants offered lower insertion affinities at low pH due to the reduction or absence of protonatable residues within the transduction domain. It was also apparent that truncated variants, which had hydrophobic sections removed from the sequence, offered lower plasma membrane affinities at neutral pH than non-truncated variants. However, truncated variants that still possessed three hydrophilic residues within the transduction domain exhibited very favourable $\Delta\Delta G$ values.

Previous work by Karabadzhak et al. [216] demonstrated that the number of protonatable residues on the C-terminal end of the peptide, along with the presence of polar cargo, offer an effect on the timescale of peptide insertion. Indeed it was seen that variants with this truncation of the insertion end of the peptide, such that fewer protonatable residues remained, resulted in faster membrane insertion. Interestingly, the reverse sequence of Wt-pHLIP offered faster insertion kinetics than Wt-pHLIP itself.

Variant 3 – ACDDQNPWRAYLDLLFPTDTLLLDLLW
Variant 4 – ACEEQNPWRAYLELLFPTETLLLELLW
Variant 5 – ACDDQNPWARYLDWLFPTDTLLLDL
Variant 7 – ACEEQNPWARYLEWLFPTETLLLEL

Figure 3.4: pHLIP variants 3, 4, 5 & 7 sequences from the 2013 article by Weerakkody et al. [176]. Positively-charged residues labelled in red; negatively-charged residues in blue, and neutral residues in black.

Of the 16 variants, several performed notably well in the study, and the following discussion focuses on 4 such variants, 3, 4, 5 & 7 (Fig. 3.4). Variant 3 was designed for a faster insertion rate than Wt-pHLIP, by removing a number of protonatable residues from the peptide's C-terminus, while keeping Asp residues within the transduction domain in position to handle the pH triggering. Variant 4 was identical to variant 3, except the peptide employed Glu residues for pH triggering. Variant 5 was a truncated version of Wt-pHLIP containing pH-triggered Asp residues, with variant 7 as it's Glu-populated equivalent.

Variants 3, 5 & 7 exhibited favourable energetics of pH-triggered insertion. Variant 3 (Asp-populated) exhibited a $\Delta\Delta G$ value of 2.23 kcal mol^{-1} whereas variant 4 (Glu-populated), resulted in a $\Delta\Delta G$ value of 1.79 kcal mol^{-1}, reflecting a less efficient pH-switching mechanism for pHLIP variant 4. Variants 5 & 7 showed similar energetic favourability of pH-triggered insertion into plasma membranes with $\Delta\Delta G$ values for pHLIPvar5 (Asp-populated), and variant 7 (Glu-populated) of 2.31 kcal mol^{-1} and 2.39 kcal mol^{-1}, respectively.

The pK_as of each of these four variants: 3; 4; 5 & 7 were 5.06, 5.31, 4.88 and 5.50, respectively. In general, the Glu-populated variants offered higher pK_as than Asp-populated analogues. the pK_as of variants 4 and 7 fall most appropriately into the acidotic window, with variant 3 only just scraping pH 5.0. In particular, the pKa of variant 5 was undesirably low, and while pHLIP's insertion is an equilibrium process, more extreme proton concentrations will be required to drive the equilibrium towards peptide insertion, conditions that are less likely to overlap with the proton concentrations of tumour cell microenvironments.

pHLIP Variant	$\Delta\Delta G$/ kcal mol^{-1}	pK$_a$	Insertion time/ ms
3	2.23	5.03	30 - 50
4	1.72	5.31	30 - 50
5	2.31	4.88	30 - 50
7	2.39	5.50	30 - 50

Table 3.1: pH resolved change in Gibbs Free Energy ($\Delta\Delta G$), Acid dissociation constants (pK$_a$) and insertion rates of the pH-dependent insertion process of pHLIP variants into POPC vesicles. Taken from Weerakkody et al. [176]

.

Each of the four variants displayed similar kinetics of membrane insertion with insertion times of approximately 30 - 50 milliseconds, significantly faster than the Wt-pHLIP which has an insertion time of approximately 40 seconds.

This paper illustrates well how the change in Gibbs free energy of insertion $\Delta\Delta G$, insertion time and peptide pKa all influence peptide insertion, and therefore the desirability of each variant. Variants 3 & 7 were put forward for further study due to highest tumour/kidney accumulation ratios, with significantly less accumulation in the liver in the case of variant 3, and high tumour targeting efficiency along with fastest measured blood clearance for variant 7. Additionally, pH-insensitive analogues of both peptides were synthesised with key hydrophilic residues replaced with Lysine residues (pHLIPs k-var3 & k-var7), and neither showed significant tumour targeting *in vitro*.

3.1.3 pH Low Insertion Peptides as Cargo Delivery Agents

pHLIP's ability to translocate cargo into cells was first demonstrated by Reshetnyak et al. [204] who conjugated pHLIP to a 20-base unit oligonucleotide with a FITC organic dye via a disulfide bridge to the peptides c-terminal cysteine residue. HeLa cells were then treated at pH 7.4, 7.0, 6.5 and 5.5, and mean % fluorescence was quantified at 18%, 48%, 78% and 100%, respectively. In the same publication, it was also shown that pHLIP could mediate the translocation of a cell-impermeable toxin, phalloidin. Phalloidin binds to filamentous actin, and was fluorescently labelled with a rhodamine dye enabling easy visualisation by fluorescence microscopy.

Wijesinghe et al [218] demonstrated how the hydrophobic nature of pHLIP's conjugated cargo affects overall peptide stability, and translocation efficiency. The cargo molecule in this instance was a phallicidin derivative, where the original phallidicin unit was conjugated to an alkyl chain via amide coupling to one of phallicidin's carboxylic acid terminals. The alkyl chains consisted of 4, 6 & 8 carbon atoms, and were called phall-C4, phall-C6 and phall-C10, respectively. Phallicidin binds to filamentous actin, preventing polymerisation/depolymerisation and thus preventing all future cell mobility, eventually leading to cell death [219]. It was found in this study that overall peptide solubility was critical, and the most hydrophobic variant pHLIP-phall-C10 aggregated when exposed to the low pH environment, which significantly hindered the peptide's translocation efficiency. For cell treatment with pHLIP-phall-C4 and pHLIP-phall-C6, an

antiproliferative effect was observed in both cases, with a concentration-dependent manner. The observed effect was strongest for pHLIP-phall-C6, being the most hydrophobic of the two variants, which emphasises the importance in the trade-off between hydrophobicity and solubility in cargo design.

Daumar et al. [220] demonstrated ^{18}F labelling of the Wt-pHLIP variant by conjugation to a 2- ethynyl-6-[18F]fluoro-pyridine unit, and used the radiolabelled variant to monitor in vivo stability, of which only mild defluorination was observed. Macholl et al. [135] later reported a robust and effective method of labelling pHLIP with the Single Positron Emission Computed Tomography (SPECT) agent ^{99m}Tc, and further optimised the agent to offer good clearance from the point of injection

Wijesinghe et al. [221] reported pHLIP-mediated delivery of conductive nano-pores, comprised of the linear hydrophobic peptide, gramicidin A into three carcinoma cell lines. pHLIP was demonstrated to promote the uptake of the liposomes into the cell's plasma membrane, resulting in liposomes-membrane fusion. The pores within the gramacidin A liposomes have an affinity for sodium ion channelling, and incorporation of these sodium ion channels into the membrane induced an increase in sodium ion internalization. This disruption of the cytoplasmic ion balance resulted in cytosolic acidification, subsequent mitochondrial polarisation, and ultimately cell death.

Davies et al. [139] were the first to report pHLIP-mediated transduction of AuNPs. In this work, human platelets were dosed with pHLIP-coated 13 nm AuNPs colabelled with a europium dye, and exclusive uptake was observed after a short incubation demonstrating a method of cellular delivery where transfection techniques are not possible. Yao et al [137] later took a very promising step in demonstrating pHLIPvar3-mediated, pH-dependent uptake of 1.4 nm gold nanoparticles into human cervix carcinoma cells.

A fluorescence reporter system was based on pHLIP-mediated delivery was demonstrated by Karabadzhak et al. [222] who conjugated the pHLIP peptide to a fluorophore reporter by a cleavable disulphide linker, where luminescence imaging experiments confirming significant dequenching of the fluorophore by the cells reducing environment when HeLa cells were treated at low pH.

pHLIP peptides have been shown to tether cargos to the plasma membrane, or transduct cargos into the cytoplasm and release them via cleaving of a di-sulphide bond. Successful cellular injection has to date been demonstrated for organic dyes, phalloidin-rhodamine, peptide nucleic acids,[204] gold nanoparticles [221, 139, 136, 137], liposomes [221] Positron Emission Tomography (PET) radionucleotides [223] and Single Photon Emission Computed Tomography (SPECT) contrast agents [135], both applied to in vivo tumour imaging.

3.1.4 pH Low Insertion Peptides as Delivery Agents for Therapeutics

The uptake of pHLIP into mouse breast adenocarcinoma models was reported by Andreev et al. [170] where the pHLIP peptide was conjugated to a near-infrared dye construct (pHLIP-NIR) and accumulation of the construct within tumours and organs was probed by intravital microscopy. The pHLIP-NIR constructs demonstrated high affinity for tumour accumulation within early and advanced stages of tumour development,

offering luminescence signal stable for days, and signal from within tumours was approximately 5 times more intense than signal from healthy tissue. Significant accumulation within mouse kidneys was also noted, resulting from reported acidic regions of kidney cells, being a site of catabolism of low-molecular-weight proteins. [224] Additionally, it was determined that kidney accumulation of the pHLIP-NIR was slower if the mice were pre-fed with bicarbonate-containing drinking water (pH 8.2) prior to the injection of pHLIP-NIR.

Moshnikova et al [225] developed a pHLIP-based drug delivery system by conjugation of the peptide to $\alpha-$amanitin, a toxin that induces cellular apoptosis within 48 hours. The toxin is too polar to traverse plasma membranes by itself, with the exception of the membranes of liver cells which have a specialised transport system [226]. The peptide was bound to the toxin by a $-S-S-$ cleavable linker in order to release the toxin into the cell. It was also interesting that amanitin bound to pHLIP via a non-cleavable linker was not able to induce cell death, and translocation efficiency could be tuned by incorporation of more or fewer hydrophobic moieties into the linker.

Zhao et al. [227] reported pHLIP-mediated transduction of large mesoporous silica nanoparticles (MSNs) across the plasma membrane. In this work, the 140 nm MSNs were initially loaded with Doxorubicin, an anti-cancer drug. The pHLIP peptide was then conjugated to MSNs via a disulfide bridge, in order to cap the pores after drug loading, yet cleave after membrane translocation, triggering the release of the loaded Doxorubicin into the cell.

pHLIP variant 7 was applied to detection of ischemic myocardium [136], where pHLIP-coated liposomes were shown to have high affinity for binding to ischemic regions of myocardium, and low affinity for binding to normal regions.

Antosh et al [228] recently demonstrated pHLIP's potential application in binary radiation therapy, the process of targeting cells at the biological level with a non-cytotoxic agent before activating the agent's cytotoxic action using low level radiation. In this work, pHLIP-conjugated gold nanoparticles offered an enhancement of the X-ray radiation effect felt by human lung carcinoma cells via stimulation of heat release from irradiated gold nanoparticles. pHLIP's pH trigger enabled higher affinity for cell uptake at low pH, and irradiation of treated cells resulted in a higher cell mortality over irradiation of untreated cells. This was recently adapted by Yu et al. [229] who constructed a photothermal/photodynamic theraputic constructed from hollow gold nanoparticles and the anticancer theraputic Chlorin e6 (Ce6) held in association by electrostatic interactions. The photothermal/photodynamic activity were both activated by ablation with a 670 nm laser that served to release (Ce6) and supply the energy input for the photothermal effect. Upon ablation, 70% of the loaded Ce6 was released along with a sharp increase in temperature of over 45°C reached within a minute of constant ablation.

3.1.5 Introduction Summary

Contemporary pHLIP research is currently expanding the library of cargos that pHLIP is able to deliver across plasma membranes, along with lengthening the list of diseases and conditions that pHLIPs are able to target. In addition, there has been a large swing towards theraputic delivery involving small molecule inhibitors, or large nano structures where therapy is administered by photothermal ablation.

Contrasting with the Trans-activating Transcriptional Activator peptide (TAT), pHLIP offers a preference for cancer cell uptake whereas the cell specific uptake of TAT is more difficult to manipulate. Novel variants of pHLIP are demonstrating rapid phospholipid bilayer entry times. pHLIP variants have had low reported toxicity, whereas certain TAT variants have been shown to have highly toxic effects on cells. Additionally, both demonstrate an independence from active-uptake mechanisms, TAT's entry is receptor mediated whereas pHLIP's transduction is reliant on hydrophobic interactions, however both have been demonstrated to deliver gold nanoparticles into cells.

In this work, (Wt-)pHLIP and pHLIPvar3 were selected for the application of pH-triggered transportation of luminescent gold nanoparticles into cancer cells. (Wt-)pHLIP was used as the group has previous experience with this variant, and has previously reported the pH dependent delivery of gold nanoparticles into human platelets [139], and pHLIPvar3 was chosen as another option as it possibly represented a faster more efficient alternative to pHLIP.

3.2 Results and Discussion

This section is divided into four subsections, ***i)*** Preliminary Treatments of HeLa cells with labelled-AuNPs, where samples of pHLIP-Au^{13}-RubpySS and Zonyl-Au^{13}-RubpySS were prepared and their internalization into HeLa cervical adenocarcinoma cells was studied using confocal microscopy to identify appropriate concentrations and treatment times to ensure significant nanoparticle uptake, as well as study internalization and localisation within the cells. ***ii)*** the pH-dependency of labelled nanoparticle internalization was then investigated. The cell culture model used for all pH-dependency experiments was HeLa cervical adenocarcinoma cells incubated in a solution of Tyrode's buffer at pH 6.5, and 7.4 representing cancerous and non-cancerous cells, respectively. Relative uptake of labelled gold nanoparticles was assessed and quantified using flow cytometry and luminescence & reflection microscopies, the latter also provided a spatial assessment of nanoparicle uptake. Additionally, live cell and fixed cell microscopies were both employed to demonstrate that particle uptake was not strongly influenced by formalin fixation. Absolute uptake was measured by quantifying the gold concentration of treated cells using Inductively Coupled Plasma Mass Spectrometry (ICP-MS), and Transmission Electron Microscopy (TEM) was used to study spatial distribution of internalized 13-nm labelled gold nanoparticles. ***iii)***, to assess the effect of any of the conditions used in these experiments on cell viability, the 3-(4,5-Dimethyl-2-thiazolyl)-2,5-diphenyl-2H-tetrazolium bromide (MTT) reduction assay was performed on treated HeLa cells, where all treatment parameters were individually assessed to identify any treatment-induced cell viability compromise. And ***iv)***, the effect of pH on the colloidal stability of the labelled gold nanoparticles used in this study was examined using a variety of spectroscopic and spectrometric techniques.

3.2.1 Preliminary Cellular Uptake Experiments

To investigate whether pHLIP & RubpySS co-coated AuNPs were readily uptaken by cancer cells, the widely studied HeLa cervical adenocarcinoma cell line were used as our cell model. Cells were grown in complete media, routinely passaged using a trypsin-EDTA protocol, and plated for experiments in cell culture well plates containing sterilised glass coverslips and grown to approximately 60% confluency before treatment with AuNPs. After treatment, cells were fixed using 4% paraformaldehyde, stained with the Hoechst 33258 nucleic acid stain before imaging.

For each sample, internalized particles were visualised by two confocal microscopy modes *i)* luminescence mode ($\lambda_{ex} = 488nm, \lambda_{em} = 561 - 750nm$), and *ii)* reflection mode ($\lambda_{ex/em} = 633nm$). The structure and morphologies of treated and non-treated cells were also visualised by two microscopy modes, *i)* transmission imaging ($\lambda_{ex/em} = 488nm$) and *ii)* reflection imaging ($\lambda_{ex/em} = 488nm$). Additionally, the DNA minor groove-binding Hoechst 33258 nucleic acid stain was used to mark the locations of cell nuclei in order to assess particle affinity for nuclear internalization ($\lambda_{ex} = 405nm$ and $\lambda_{em} = 400 - 500nm$).

Fig. 3.5 shows confocal images of HeLa cells treated with pHLIP-Au^{13}-RubpySS (1 nM) in complete

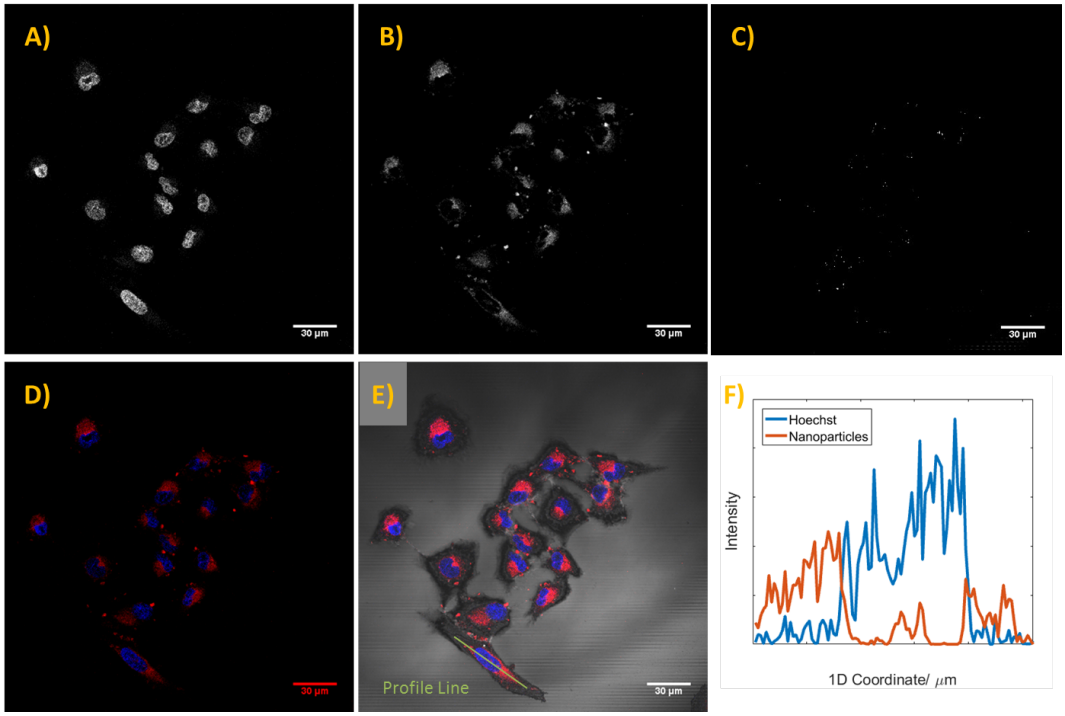

Figure 3.5: Confocal Microscopy images of Hela cells treated with pHLIP-Au^{13}-RubpySS in complete media for two hours at 37°C. A) Hoechst 33258 nucleic acid stain, B) Ruthenium luminescence, C) Reflection at 633 nm, D) Overlay of luminescence (red channel), and Hoechst (blue channel) images, E) Overlay of Reflection (gray channel), luminescence (red channel), and Hoechst (blue channel) images, and F) Profile plot of Reflection, Luminescence & Hoechst channels.

media for two hours at 37°C. Strong ruthenium luminescence signal is observed after a two hour treatment, indicating efficient uptake within the treatment time and suggesting minimal quenching of ruthenium emission from the gold nanoparticles, despite previous reports of surface-bound lumophore luminescence quenching mechanisms from gold surfaces [230, 74, 231]. Additionally, the internalized nanoparticle density appears to be evenly distributed throughout the cells cytoplasmic regions. The nucleic acid stain Hoechst 33258, was used to mark cell nuclei in order to establish the affinity of pHLIP-labelled AuNPs to internalise into cell nuclei. While there are examples of strong signal from perinuclear regions of some cells, the luminescence signal does not appear to colocalise significantly with signal from the Hoechst 33258 nucleic acid stain, indicating little internalization into cell nuclei. This is reillustrated by analysis of the line profiles from ruthenium and hoechst luminescence images. A line was drawn across a multi channel image of Hoechst and ruthenium signals, in which the line intersected cell nuclei and areas of strong ruthenium luminescence, and the luminescence intensities of the two channels across the line were plotted against distance coordinate (Fig. 3.5, F). The centre of the profile is strongest in Hoechst luminescence signal, and this region is mostly devoid of any ruthenium luminescence. The image of reflected 633 nm light (Fig. 3.5, C) shows insignificant signal, suggesting that no large nanoparticle agglomerates are formed within cell interiors, and the 488 reflection image shows cell morphologies indicating cells were adopting a spread morphology on glass coverslips after

treatment and at the time of fixation, suggesting good viability. Non-viable cells were identified by their spherical shape and their thicker depth as a consequence of becoming partially detached from coverslips.

A time frame of 0 - 2 hours was chosen for future experiments as a significant concentration of pHLIP-Au^{13}-RubpySS appeared to have internalized after two hours, and HeLa cells are likely to lose viability upon long durations without media or bovine serum. As nanoparticle diameter falls significantly short of the diffraction limit in light microscopy, clarification that individual pHLIP-Au^{13}-RubpySS particles had internalized into HeLa cells was confirmed by transmission electron microscopy (see section: transmission microscopy evaluation of pH-dependent cellular uptake).

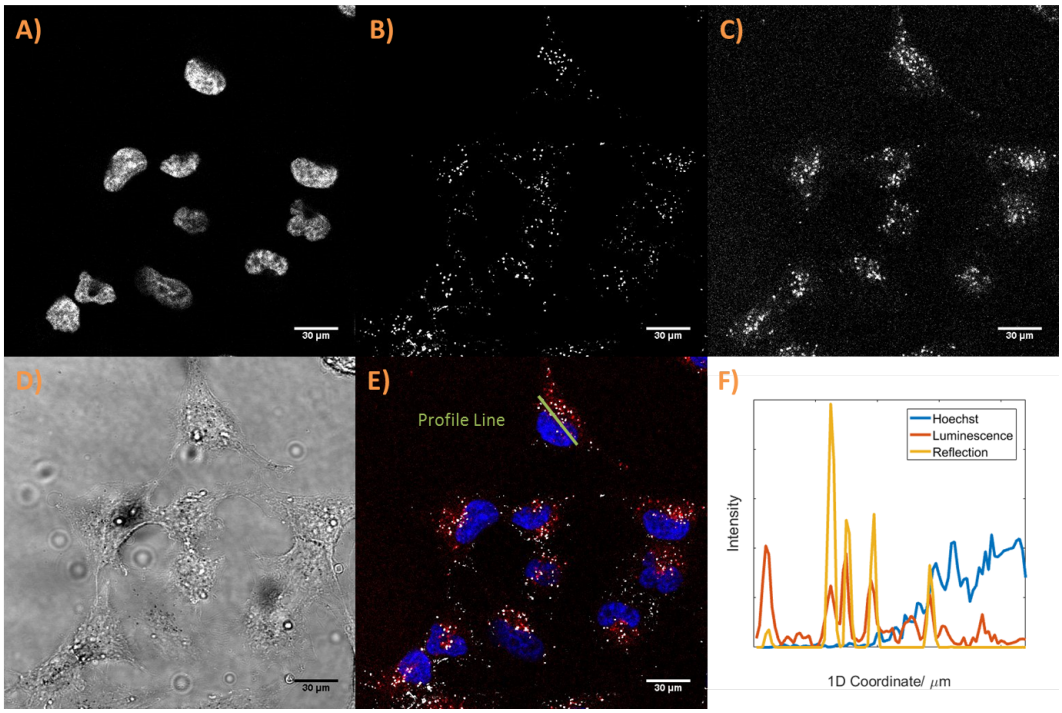

Figure 3.6: Confocal Microscopy images of Hela cells treated with Zonyl-Au^{13}-RubpySS (1 nM) in complete media for four hours at 37°C. A) Hoechst 33258 nucleic acid stain, B) Reflection at 633 nm, C) Luminescence from 488 nm excitation, D) Transmission image, E) Overlay of Reflection (gray channel), luminescence (red channel), and Hoechst (blue channel) images, and F) Profile plot of Reflection, Luminescence & Hoechst channels.

The uptake of Zonyl-Au^{13}-RubpySS into HeLa cells was also evaluated by confocal microscopy where HeLa cells were treated with Zonyl-Au^{13}-RubpySS (1 nM) in complete media for four hours at 37°C, and were subsequently prepared for fixed-cell confocal microscopy. Fig. 3.6 shows confocal microscopy images of HeLa cells treated with Zonyl-Au^{13}-RubpySS, and particles were again visualised by i) luminescence mode ($\lambda_{ex} = 488nm, \lambda_{em} = 561 - 750nm$), ii) reflection mode ($\lambda_{ex/em} = 633nm$).

The 633 nm reflection image (Fig. 3.6, B) shows intense signal that appears to colocalise with ruthenium luminescence. This signal is believed to be resultant from gold nanoparticles that have flocculated into larger particles which are now larger than the confocal system's diffraction limit, and as a result the particles scatter

incident light with sufficient efficiency for detection. A line was drawn on the image showing nanoparticle luminescence & reflection overlaid with Hoechst luminescence (Fig. 3.6, F) intersecting regions of strong nanoparticle signal and Hoechst signal, and the profile was plotted to analyse the colocalisation. Again, the regions of strong Hoechst signal are devoid of any nanoparticle reflection or luminescence, and the ruthenium luminescence profile overlays well with the nanoparticle reflection profile, indicating minimal quenching or disintegration.

Additionally, cells were treated with unlabelled (citrate-stabilised) Au^{13}NPs to determine whether unlabelled AuNPs were uptaken. Citrate-Au^{13}NPs aggregated upon addition to cell media, turning the solution dark grey, with dark precipitates of aggregated gold. Subsequent confocal images of these treated cells did not show significant signal within the nanoparticle emission channel (Fig. 8.26) indicating that unlabelled (citrate-stabilised) AuNPs do not make suitably stable or sufficiently emissive imaging agents.

3.2.2 pH-Resolved Uptake of Peptide-labelled, Luminescent Gold Nanoparticles

In order to study the pH-dependency of labelled gold nanoparticle uptake into cancer cells, a model for cancerous and non cancerous environments was constructed. This cell culture model consisted of HeLa cervical adenocarcinoma cells incubated in a solution of Tyrode's buffer. The buffer was adjusted to pH 6.5 or 7.4 using either HCl or NaOH, where HeLa cells incubated at pH 6.5 provided a model of cells with an acidotic microenvironment and HeLa cells incubated at pH 7.4 was used as a model for non-cancerous cells. The pH of Tyrode's buffer is easily adjustable within the 6.5 - 7.4 window of interest, and the buffer has similar isotonic properties to interstitial fluid, therefore has routine use within tissue culture. Cells were seeded into a culture well plate, and left to adhere and proliferate for 24 hours before treatment. After treatment, cells were washed to remove any non-internalized AuNPs before being processed for the appropriate technique used to measure pH dependency of gold nanoparticle internalization. One of the big advantages of utilising luminescently labelled gold nanoparticles as cellullar imaging probes is that their internalization into cells can be measured by a plethora of techniques. In this section, flow cytometry and luminescence microscopies were used to quantify ruthenium luminescence from treated cells and Transmission Electron Microscopy (TEM) & Inductively Coupled Plasma Mass Spectrometry (ICP-MS) were used to directly measure the presence of gold within treated cells.

Flow cytometry evaluation of pH-Dependent Cellular Uptake

Flow cytometry is a sensitive and high throughput technique often used for biomarker detection, or cell counting and sorting. The technique is discussed more deeply in Chapter 1, and is herein applied to the study the pH dependence of pHLIP, pHLIPvar3 and Zonyl-mediated uptake of luminescent gold nanoparticles.

Prior to treatment, cells were plated into a 12-well culture plate and allowed to grow to approximately 60% confluency. Cells were then washed with buffers before being treated with particles in a Tyrodes buffer (0.08 mM, pH 6.5 or 7.4), for a series of incubation times upto three hours. After treatment, cells were washed with phosphate buffered saline before being trypsinised to detach the cells from the bottom of the well. Cells were isolated by centrifugation, the supernatant removed and cells were redispersed in PBS. Cells were then transferred to a FACS tube for acquisition.

Flow Cytometry Analysis Procedure

For each sample, the flow cytometer was set up to record forward and side scatter, and to plot them against each other as a scatter plot (Fig. 3.7). Mean values for side scatter were used as a measure of gold nanoparticle internalization because of the ability of the electron-dense gold particles to scatter incident light. Mean values calculated from scatter plots were normalised to mean values of untreated control cells, which were set to 100%, and are herein presented as charts. The cytometer was also set to record in photoluminescence mode via excitation and detection of light emitted by the nanoparticle-bound ruthenium

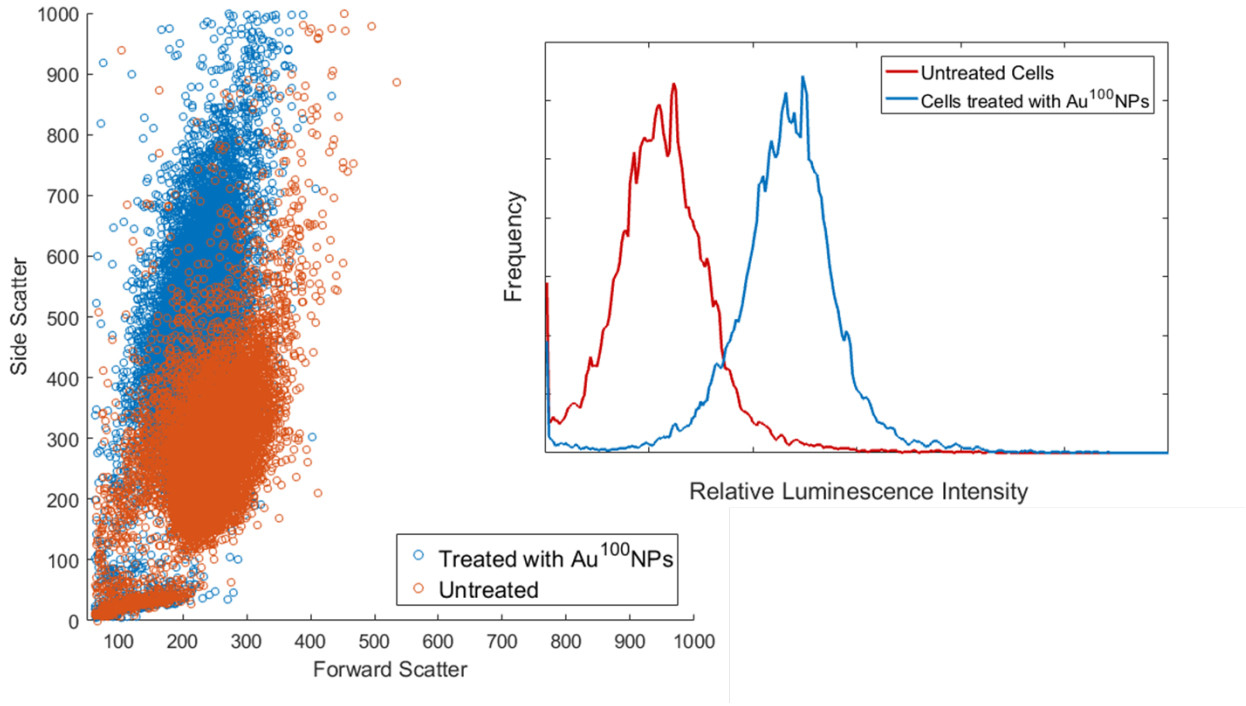

Figure 3.7: Example of the analysis procedure of flow cytometry data. Scatter plot (left) and luminescence histogram (right) of HeLa cells treated with pHLIPvar3-Au^{100}-RubpySS (8 pM) for two hours at 37°C.

complex, RubpySS. The 488 nm laser was selected and a dichroic mirror at 620 nm was used to block scattered light from detection. Again, mean values from the recorded luminescence histograms were normalised to the mean luminescence of untreated cells, which were set to 100%.

pH-resolved Treatment of HeLa Cells with pHLIP-Au^{13}-RubpySS

Fig. 3.8 shows flow cytometry of HeLa cells treated with pHLIP-Au^{13}-RubpySS (1 nM) in Tyrode's buffer (0.08 mM, pH 6.5 or 7.4) for up to two hours at 37°C, where luminescence at $>$ 620 nm was recorded and expressed as a percentage of untreated cells. Time resolved uptake shows an increase in luminescence signal over time, where % luminescence reaches between 150 - 200% of the untreated controls within 30 minutes and between approximately 300 - 400% after a two hour treatment. This increase in % luminescence is attributed to ruthenium emission as delivered into the cells on a AuNP scaffold. It is not clear yet whether the complex remains anchored to the particle after cell entry or possibly cleaved once inside the cell. The latter is however unlikely, as luminescence-in-flow measurements of free complexes have previously shown that ruthenium luminescence is severely prone to collisional quenching from $^3O_2$ [50]. pH resolved uptake indicates a general higher affinity for uptake at pH 7.4 than 6.5, which is represented across all treatment times. After a 30 minute treatment, cells treated at pH 6.5 exhibited a luminescence intensity of $\approx$ 150%, whereas cells treated at pH 7.4 exhibited a luminescence of 220%. This trend continued up to the final time point of two hours, where the final luminescence from cells at pH 6.5 and pH 7.4 were 290% and 390%, respectively. Side scatter measurements did not indicate a change in cell granularity as a function of

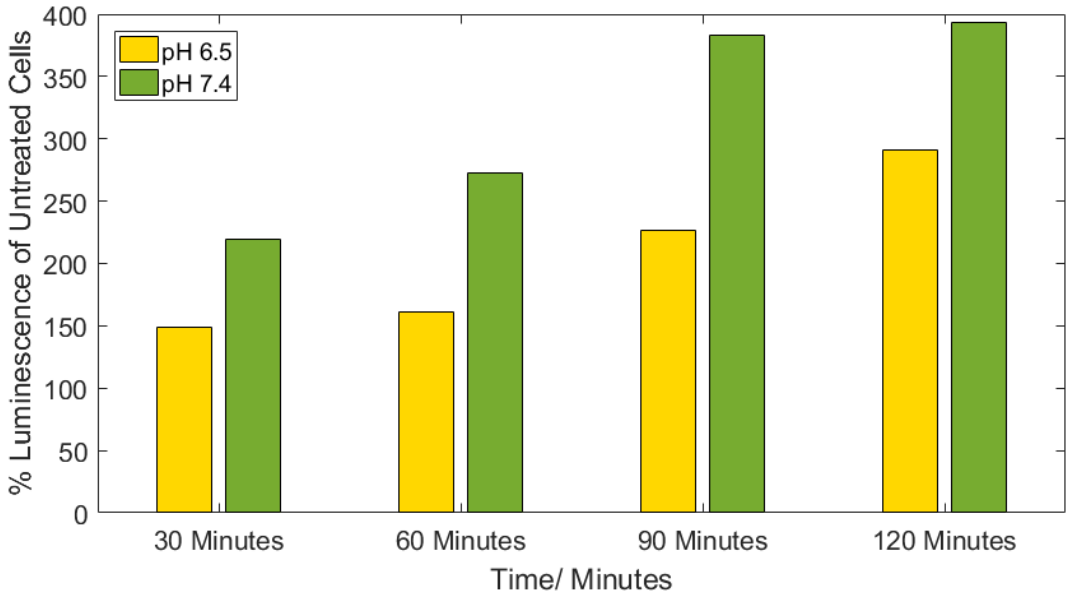

Figure 3.8: Mean Luminescence from HeLa cells treated with pHLIP-Au^{13}-RubpySS (1 nM) in Tyrodes buffers (0.08 mM, pH 6.5 or 7.4) at 37°C measured by flow cytometry. Single data set shown, however three replicates were performed.

treatment time, and based on previous microscopy experiments where pHLIP-Au^{13}-RubpySS was uptaken very readily by HeLa cells, this suggests that scattered signal from 13 nm particles is not intense enough for detection. Additionally, it is noteworthy that this experiment was performed multiple times, and the results of one representative dataset are shown.

Yao et al. [137] previously reported pHLIP-mediated delivery of 1.4 nm AuNPs using the variant 3 modified version of pHLIP. The volume of 1.4 nm AuNPs = 11.5 nm^2 and the volume of 13 nm AuNPs = 9202 nm^2, an 800-fold increase in volume. Based on this size increase, we theorised that pHLIP-mediated translocation of 13 nm gold nanoparticles could proceed at a much slower rate, and endocytotic processes could be competing far more strongly for overall AuNP uptake. It is also noteworthy, that as pHLIP is quite a hydrophobic peptide, it has a high affinity for binding to the surface of a phospholipid bilayer even at neutral pH, and this proximal contribution to endocytosis could result in faster endocytotic uptake. Temperature has shown to be a strong factor on the rate of endocytosis in a variety of cell lines, and culturing cells at 4°C is a widely employed method of shutting down endocytotic processes [232, 233, 234].

In order to assess pHLIP's ability to mediate gold nanoparticle uptake in the absence of endocytotic processes, the uptake experiment was performed at 4°C in order to inhibit endocytotic processes such that pHLIP-mediated translocation affords a larger contribution to net AuNP uptake.

Fig. 3.9 shows mean luminescence from cells treated with pHLIP-Au^{13}-RubpySS at 4°C for treatment times up to three hours measured by flow cytometry. Again, mean luminescence were normalised to that of untreated control cells, where mean side scatter & mean luminescence of control cells equated to 100%

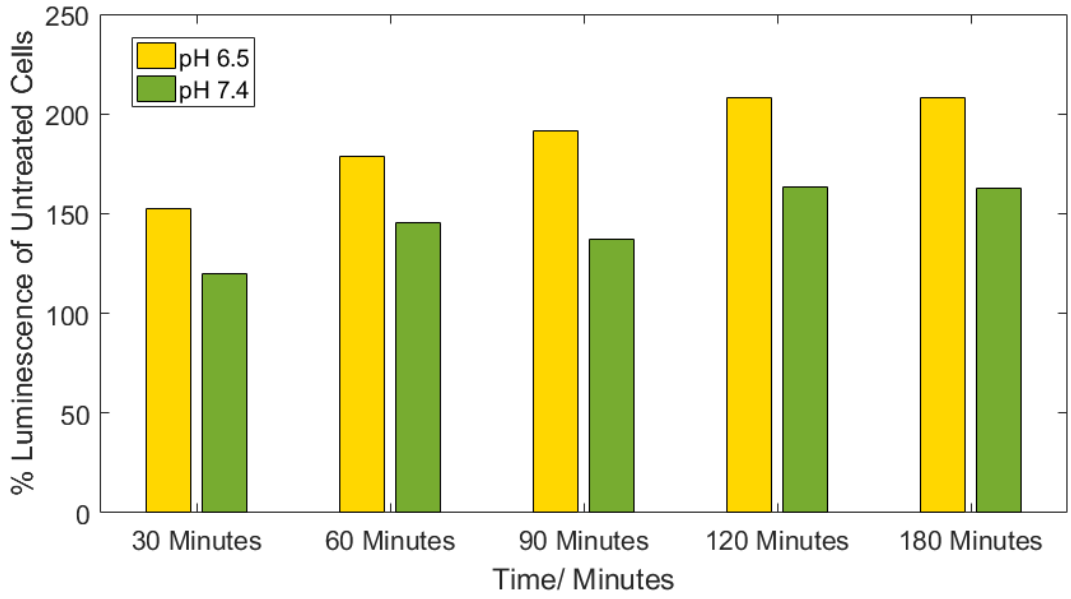

Figure 3.9: Mean Luminescence & Scatter from HeLa cells treated with pHLIP-Au^{13}-RubpySS (1 nM) in Tyrodes buffers (0.08 mM, pH 6.5 & 7.4) at 4°C measured by flow cytometry.

signal. Treatment at 4°C with pHLIP-Au^{13}-RubpySS at pH 6.5 and 7.4 revealed a minimal increase in cell side scatter of 106 ± 1%, and 102 ± 3%, respectively. However luminescence measurements of the same experiment revealed a significantly greater sensitivity with pH 6.5 and 7.4 samples displaying mean luminescence intensities of 210% and 165%, respectively.

Treatment at 4°C provides evidence that endocytotic uptake of labelled-AuNPs is occurring on a similar timescale to pHLIP-mediated transduction, and selective shutdown of endocytotic processes reveal a more efficient uptake of pHLIP-Au^{13}-RubpySS at pH 6.5. This is further investigated by ICP-Mass Spectrometry and Luminescence Microscopy in future sections of this thesis (see sections: Inductively-Coupled Plasma Mass Spectrometry (ICP-MS) evaluation of pH-Dependent Cellular Uptake, and Confocal Microscopy evaluation of pH-Dependent Cellular Uptake).

pH-resolved Treatment of HeLa Cells with pHLIPvar3-Au^{13}-RubpySS

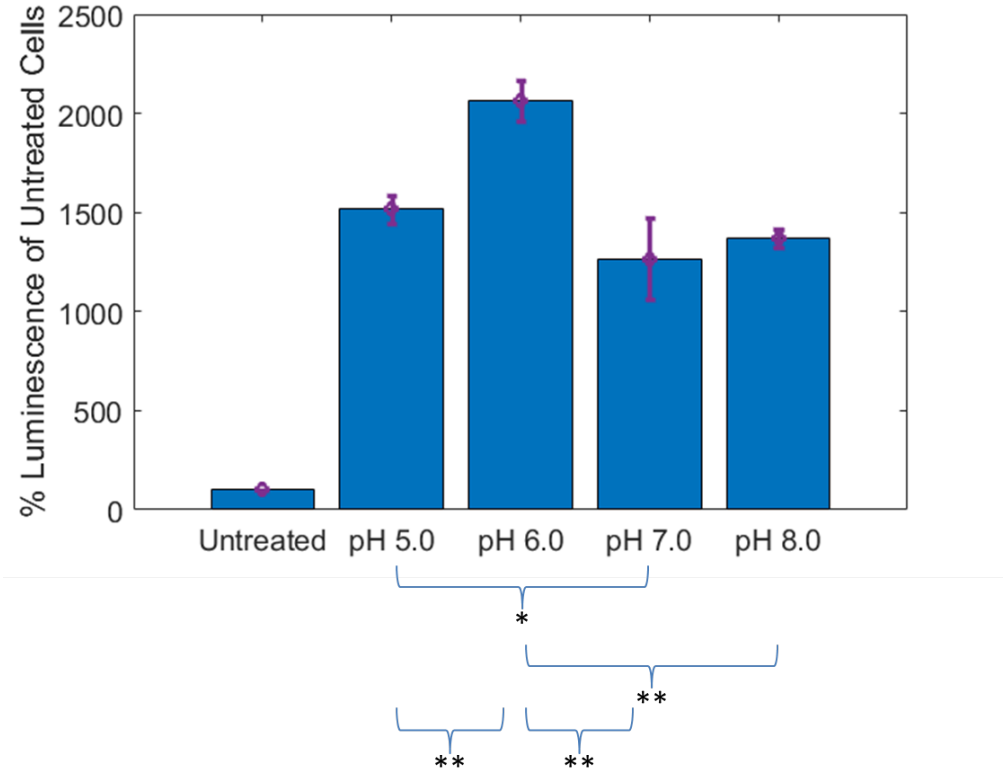

Figure 3.10: Mean Luminescence from HeLa cells treated with pHLIPvar3-Au^{13}-RubpySS (1 nM) in Tyrodes buffers (0.08 mM, pH 6.5 or 7.4) for 2 hours at 37°C measured by flow cytometry. Data composed of three biological repeats, presented with ± one standard deviation unit, and Tukey HSD test data was also included, where statistically significant p-values of <0.05, <0.01, <0.001 are indicated by *, **, and ***, respectively.

Fig. 3.10 shows the mean % luminescence from HeLa cells treated with pHLIPvar3-Au^{13}-RubpySS for two hours at 37°C as a function of buffer pH. Four Tyrode's buffers of ≈ pH 5.0 - 8.0 were prepared, and sterilised by filtering through 0.22 μm syringe filters. Three biological repeats were performed, and ANOVA and T-tests were performed on the raw data. Cells treated in the low pH buffers yielded the largest increase in % luminescence, with pH 5.0 and pH 6.0 at ≈ 1500% and ≈ 2000%, respectively. % luminescence of the cells treated in the high pH buffers of pH 7.0 and pH 8.0 were 1300% and 1400%, respectively. T-tests on the raw data revealed a strong statistically significant difference ($p < 0.01$ in all cases) between the % luminescence of cells treated at pH 6.0, and cells treated in all other buffers (pH 5.0, pH 7.0 & pH 8.0). Additionally, a one-way analysis of variance (ANOVA) of control and treated cells indicated that the treatments were significantly different ($p = 1.5x10^{-5}$).

Cells treated at pH 5.0 showed a lower % luminescence, believed to be resultant from cytotoxicity of HeLa cells exposed to the relatively acidic environment, which is corroborated by cell viability measurements later in this thesis (see section: Assessing the Effect of labelled-AuNP Treatments on Cell Viability using the

3-(4,5-Dimethyl-2-thiazolyl)-2,5-diphenyl-2H-tetrazolium bromide (MTT) Reduction Assay), along with a flow cytometry time course experiment of cells treated with at pH 5.0 and 7.4 (Fig. 8.27) that showed a initial increase in luminescence at pH 5.0 that was greater than analogous cells treated at pH 7.4, however this was followed by a luminescence depletion after 90 minutes whereas cells treated at pH 7.4 exhibited a consistent increase in luminescence across the time course. Cells treated at pH 7.0 & 8.0 show significantly less luminescence than cells treated at pH 6.0, characteristic of pHLIP's general pH-dependent cell uptake mechanism. It is interesting that in the case of pHLIPvar3, the treatment pH imposed such a marked difference in nanoparticle internalization at 37°C. pHLIPvar3 has been reported to internalise on the order of 30 - 50 ms, much faster than pHLIP which internalises in approximately 40 seconds [176]. However, as luminescence is an indirect measurement of nanoparticle internalization, future sections of this thesis focus on detecting the presence of gold nanoparticles directly was well as quantifying internalized gold concentration.

pH-resolved Treatment of HeLa Cells with Zonyl-Au^{13}-RubpySS

Zonyl-Au^{13}-RubpySS and Zonyl-Au^{100}-RubpySS particles were used as a non-pH-dependent uptake control in place of the kpHLIP peptide, which as shown in earlier sections, aggregated in aqueous solution. The internalization of these particles should provide an indication of whether the efficacy of gold nanoparticle internalization via non-specific/endocytotic processes possesses a pH dependency.

HeLa cells were treated with Zonyl-Au^{13}-RubpySS particles (1 nM) in Tyrode's buffer (0.08 mM, pH 6.5 or pH 7.4) for a series of incubation times up to 180 minutes at 37°C. Forward scatter, side scatter, and far red fluorescence intensities were then recorded by flow cytometry, with mean values expressed as percentages of untreated cells. The first apparent observation was that intensity of side scattered light from HeLa cells treated with Zonyl-Au^{13}-RubpySS did show a correlation with incubation time, an example is shown in Fig. 3.11. This differs from cells treated with pHLIP-Au^{13}-RubpySS or pHLIPvar3-Au^{13}-RubpySS where the intensity of side scatter as a function of treatment time offered negligible correlation. This strong increase in granularity from cells treated with Zonyl-Au^{13}-RubpySS is investigated in future sections using microscopy techniques (see section: Confocal Microscopy evaluation of pH-Dependent Cellular Uptake).

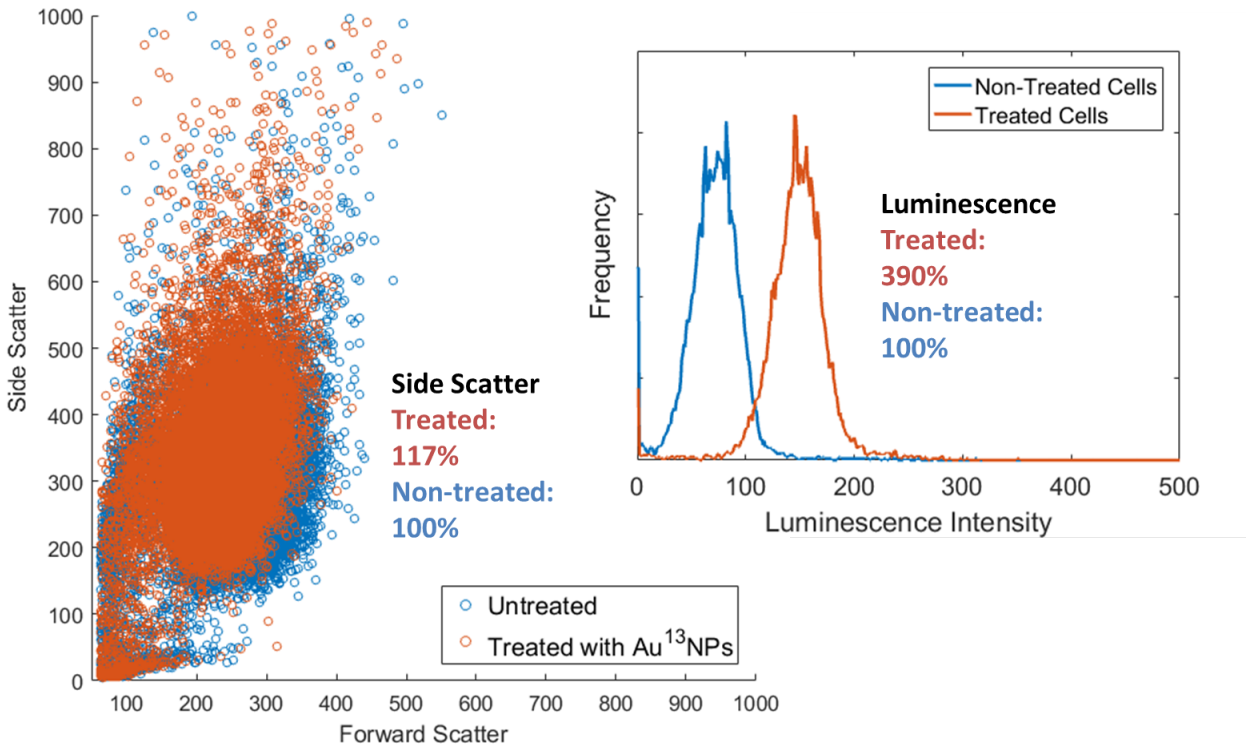

Figure 3.11: Scatter Plot and Luminescence Histograms (inset) of HeLa cells treated with Zonyl-Au^{13}-RubpySS (1 nM) for five hours in Tyrodes buffer (0.08 mM, pH 7.4) versus untreated cells at 37°C measured by flow cytometry.

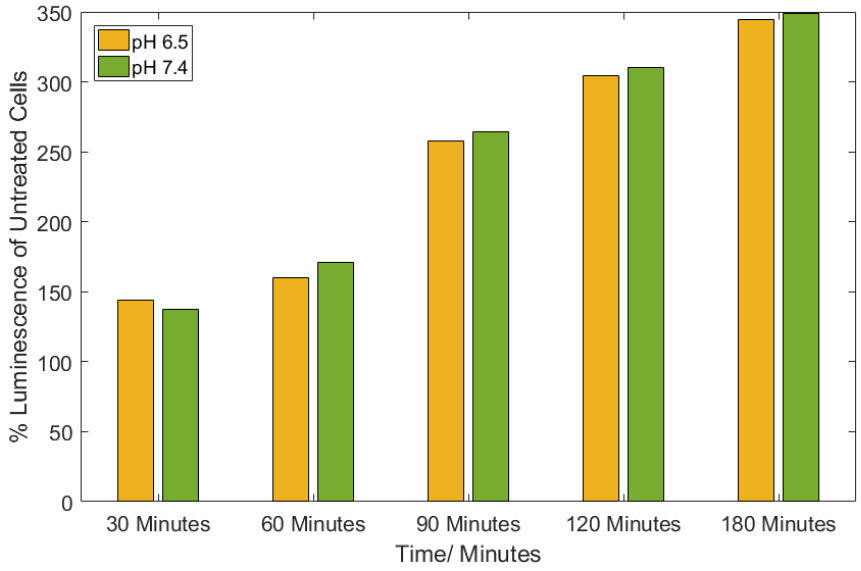

Figure 3.12: Mean Luminescence from HeLa cells treated with Zonyl-Au^{13}-RubpySS (1 nM) in Tyrodes buffers (0.08 mM, pH 6.5 or 7.4) at 37°C measured by flow cytometry.

Fig. 3.12 shows % mean luminescence from HeLa cells treated with Zonyl-Au^{13}-RubpySS by flow cytometry showed a near parallel increase in mean luminescence intensity with mean luminescence reaching almost 350% of untreated cells after 180 minutes (344% and 348% for samples treated at pH 6.5 and 7.4, respectively). Side scatter measurements indicate a significant increase in cell granularity upon treatment of cells with Zonyl-Au^{13}-RubpySS, suggesting that particles may be agglomerating after internalization, resulting in a significant increase in scattered light due to the $I \propto r^6$ relationship between intensity of scattered light and particle radii. pH appeared to have minimal effect on the luminescence intensity of cells treated with Zonyl-Au^{13}-RubpySS, where the luminescence intensity of cells treated at pH 6.5 & 7.4 were almost at equal magnitudes for each treatment time. This parallel trend indicates no pH-dependency in the uptake of Zonyl-Au^{13}-RubpySS, suggesting that non-specific internalization of gold nanoparticles through endocytotic mechanisms is proceeding at a rate independent of pH.

pH-resolved Treatment of HeLa Cells with pHLIP-Au^{100}-RubpySS

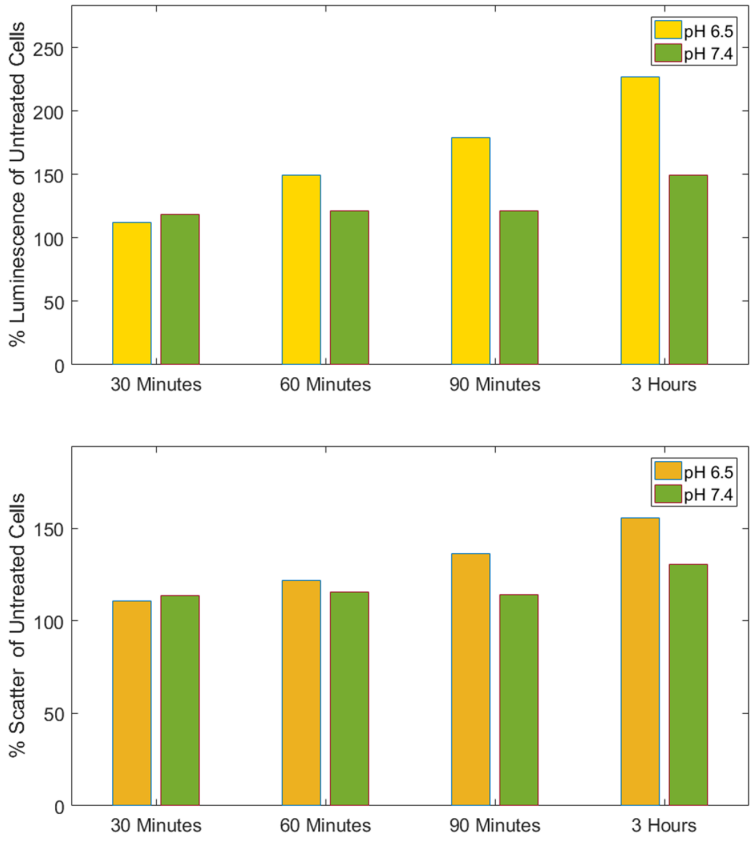

Figure 3.13: Time dependent Mean Luminescence & Scatter from HeLa cells treated with pHLIP-Au^{100}-RubpySS Tyrodes buffers (0.08 mM, pH 6.5 or 7.4) for up to three hours at 4°C measured by flow cytometry.

The uptake of pHLIP-Au^{100}-RubpySS was analysed by flow cytometry using luminescence and side scatter measurements, as one of the main benefits of 100 nm diameter particles is that they offer good light scattering within cytometry measurements, and previous work in the group has demonstrated imaging of individual 100 nm AuNPs using optical reflection microscopies [96]. A time resolved, pH treatment of HeLa cells with pHLIP-Au^{100}-RubpySS (8 pM) in Tyrodes buffer (0.08 mM, pH 6.5 or pH 7.4) at 4°C produced an increase in mean side scatter due to increased granularity of the cells, and mean luminescence due to higher concentration of internalized ruthenium lumophore, for all samples indicating that nanoparticles are internalized at pH 6.5 and at pH 7.4. This increase of mean scatter and luminescence increased with treatment length, and both indicated that particles internalized more quickly into cells treated in solution at pH 6.5 than at pH 7.4. After a three hour incubation the mean luminescence of cells treated at pH 6.5 and 7.4 was 230% and 150%, respectively. For the same experiment the mean side scatter of cells treated at pH 6.5 and 7.4 was 160% and 120%, respectively. Although only one biological repeat was performed of this experiment, this result is corroborated by luminescence microscopy and ICP-MS data (sections: confocal microscopy &

ICP-MS evaluation of pH-dependent cellular delivery, respectively). Analogous experiments performed at 37°C did not produce a statistically significant difference between cells treated at pH 6.5 and 7.4, indicating an inefficiency of pHLIP-mediated delivery of Au^{100}NPs under physiological conditions within a three hour treatment.

pH-resolved Treatment of HeLa Cells with pHLIPvar3-Au^{100}-RubpySS

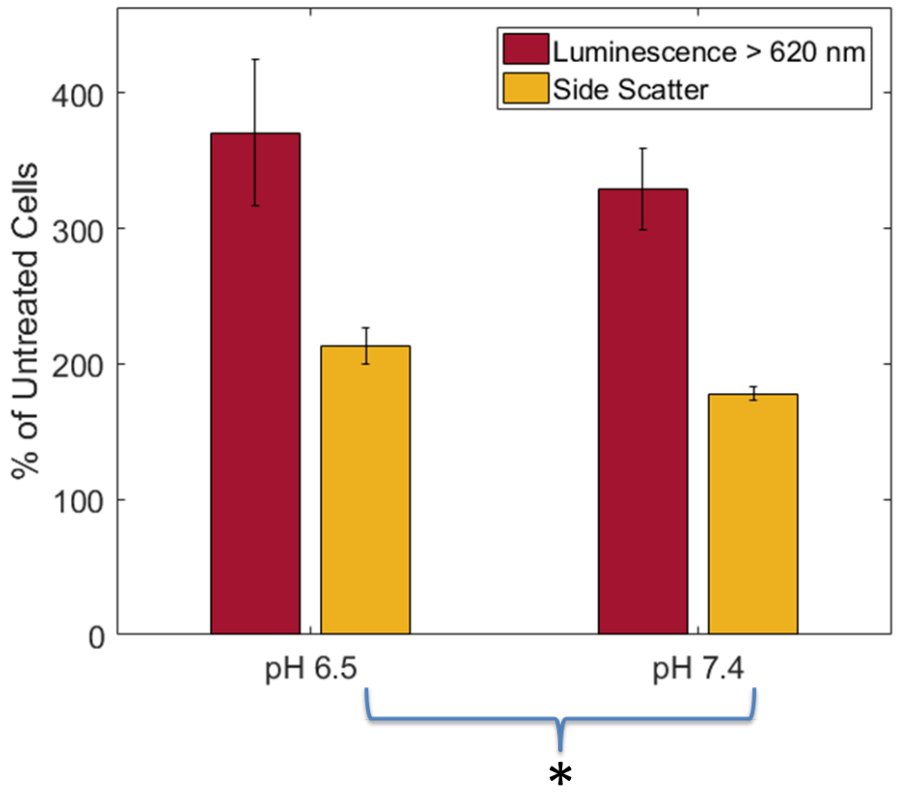

Figure 3.14: Mean Luminescence & Scatter from HeLa cells treated with pHLIPvar3-Au^{100}-RubpySS (8 pM) for 2 hours in Tyrodes buffers (0.08 mM, pH 6.5 or 7.4) at 37°C measured by flow cytometry. Data composed of three biological repeats, presented with ± one standard deviation unit, and Tukey HSD test data was also included, where statistically significant p-values of <0.05, <0.01, <0.001 are indicated by *, **, and ***, respectively.

The pH dependency of pHLIPvar3-Au^{100}-RubpySS internalization into HeLa cells was also studied by flow cytometry. Again, side scatter and luminescence of treated cells contrasted with analogous measurements of untreated cells were used as measures of nanoparticle internalization. Fig. 3.14 shows the mean luminescence and side scatter intensities of HeLa cells. The mean luminescence intensity of cells treated with pHLIPvar3-Au^{100}-RubpySS was 370 ± 54% and 328 ± 30% for cells treated at pH 6.5 & 7.4, respectively. While the

luminescence measured is greater for cells treated at pH 6.5 than at cells treated at pH 7.4, the difference is not statistically significant. However, side scatter measurements did reveal a statistically significant difference with percentage side scatter values of 213 ± 13% and 178 ± 5.5% ($p < 0.05$) for cells treated at pH 6.5 & 7.4, respectively. While luminescence measurements have been shown to be more sensitive than side scatter measurements for nanoparticles of all sizes studied in this work, side scatter measurements display smaller standard deviation values, likely due to side scatter being a more direct measurement of nanoparticle uptake.

pH-resolved Treatment of HeLa Cells with Zonyl-Au^{100}-RubpySS

Fig. 3.15 shows the mean luminescence and side scatter intensities of HeLa cells treated with Zonyl-Au^{100}-RubpySS (8 pM) for two hours at 37°C. The mean side scatter intensities for treated cells for pH 6.5 and pH 7.4 were 234 ± 5% and 234 ± 8%, respectively. Mean luminescence intensities for cells treated at pH 6.5 and 7.4 were 492 ± 33% and 565 ± 12%, respectively ($p < 0.05$, Tukey HSD). This statistically significantly less intense ruthenium luminescence at pH 6.5 is possibly indicative of significant cleavage of the ruthenium complex from the gold nanoparticle. As studied in Chapter 2, and published in [166] the luminescence lifetime of the ruthenium complex increases when mixed with the Zonyl surfactant, and when both substrates are bound to a gold nanoparticle. It is expected that cleaving the bonds holding together the nanostructure would result in a return to the shorter lifetime of the free complex but this has not been further investigated.

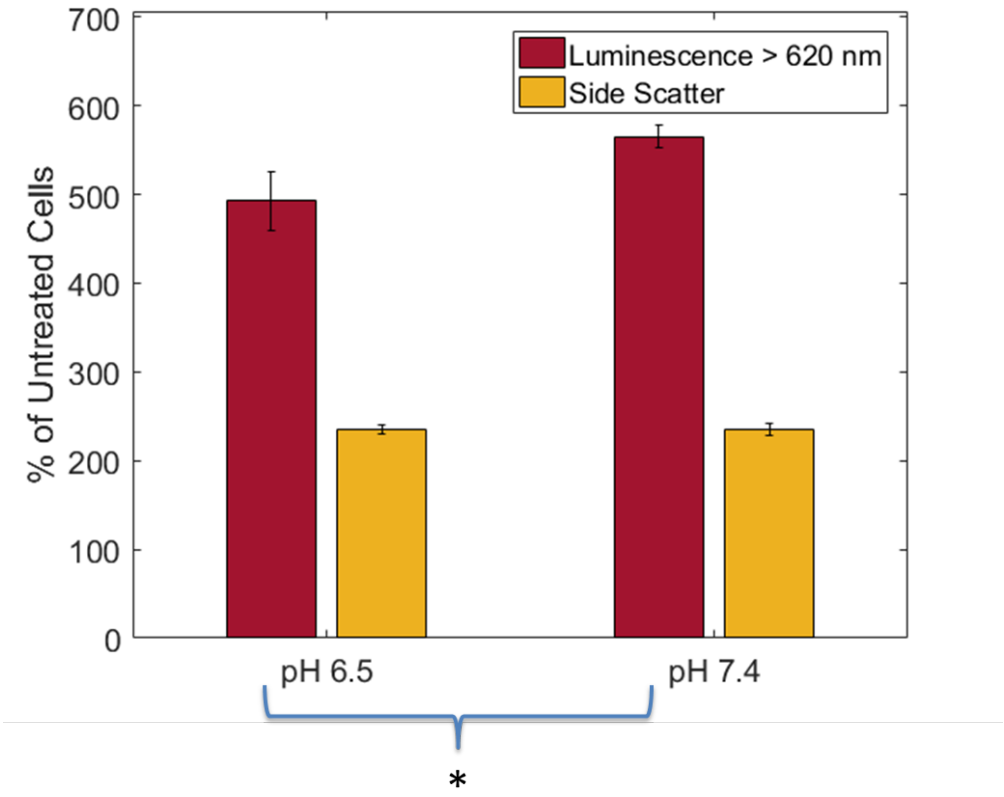

Figure 3.15: Mean Luminescence & Scatter from HeLa cells treated with Zonyl-Au^{100}-RubpySS in Tyrodes buffers for two hours at 37°C as measured by flow cytometry. Data presented with ± one standard deviation unit, and Tukey HSD test data was also included, where statistically significant p-values of <0.05, <0.01, <0.001 are indicated by *, **, and ***, respectively.

Confocal Microscopy evaluation of pH-Dependent Cellular Uptake

Relative uptake along with spatial analysis of the pH-dependent uptake of pHLIP, pHLIPvar3 and Zonyl-labelled luminescent gold nanoparticles into HeLa cells was studied using confocal microscopy. In addition to providing corroborative data to support the flow cytometry data, this technique was important for confirming the internalization of labelled-AuNPs because of the technique's ability to optically section biological samples, permitting the imaging of specific sample depths. The fundamental principles of the technique are outlined in Chapter 1, and outlined in this section, prior to the results, are the fundamentals of the acquisition procedure along with the processing methods used to calculate mean luminescence intensity values normalised to cell area.

For each sample, internalized particles were visualised by two confocal microscopy modes *i)* luminescence mode ($\lambda_{ex} = 488nm, \lambda_{em} = 561 - 750nm$), *ii)* reflection mode ($\lambda_{ex/em} = 637nm$). The structure and morphologies of treated and non-treated cells were visualised by two microscopy modes, *i)* transmission

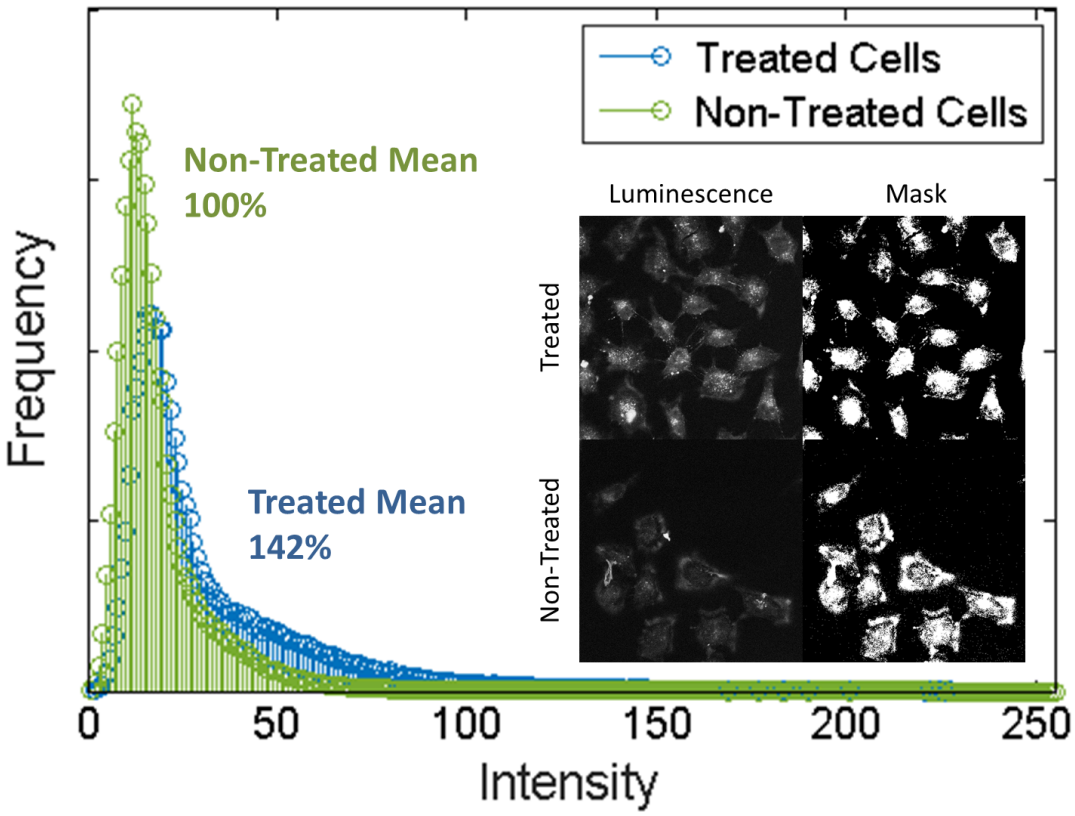

Figure 3.16: Analysis method applied to microscopy images of HeLa cells treated with labelled Au^{13}NPs. Foreground shows the image histograms of segmented confocal microscopy images, with inset raw images. Data consists of confocal image slices of Non-treated HeLa cells, and HeLa cells treated with pHLIP-Au^{13}-RubpySS (1 nM) for two hours in pH 7.4 Tyrodes buffer (0.08 mM) at 37°C. Binary masks are generated from luminescence images using the Otsu method [235]. Background is then excluded by segmenting cell regions. Mean intensity values were then calculated from cell regions and normalised to total cell area.

imaging ($\lambda_{ex/em} = 488nm$) and *ii)* reflection imaging ($\lambda_{ex/em}637nm$). Images of reflection at 637 nm provided cellular distribution of individual 100 nm nanoparticles, and 13 nm nanoparticles were also visible if particles agglomerated within cellular compartments. Luminescence imaging upon excitation at 488 nm provides a distribution of ruthenium signal within cells, permitting visualisation of the 13 nm AuNPs which are not visible in reflection imaging.

Herein is an example of the entire imaging & analysis procedure for cells treated with labelled-Au^{13}NPs. Fig. 3.16 shows an example of confocal image slices of *i)* untreated HeLa cells, and *ii)* HeLa cells treated with pHLIP-Au^{13}-RubpySS (1 nM) for two hours in pH 7.4 Tyrodes buffer (0.08 mM) at 37°C. Images were acquired using 488 nm laser excitation, with the emission collected from $561 - 741$ nm o n a spectral detector generating luminescence $\lambda-$stacks (18−image stack, 10 nm per image). Average intensities of each pixel were Z−projected into a 2-dimensional image, and average intensities of each slice were plotted as emission spectra to contrast against the steady−state emission of RubpySS.

Image processing was performed in MatLab, and consisted of an Otsu-based thresholding function permitting the segmentation of cell regions, followed by calculation of mean intensities of those cell regions. For each image, a binary image mask was generated by applying an intensity threshold to each image using the Otsu method [235] to remove as much of the image background as possible, and effectively discarding parts of the field of view that did not belong to cell regions. Mean values for each thresholded image were calculated, and then normalised to the area of the image mask (expressed as mean intensity pixel^{-1}), and expressed as a % of the control cells where the normalised mean value was set to 100%. The image histograms of the segmented images of treated and untreated cells are shown in the figure, showing the treated cells occupying a higher intensity range and a percentage mean of 142% of untreated cells.

pH-resolved Treatment of HeLa Cells with pHLIP-Au^{13}-RubpySS

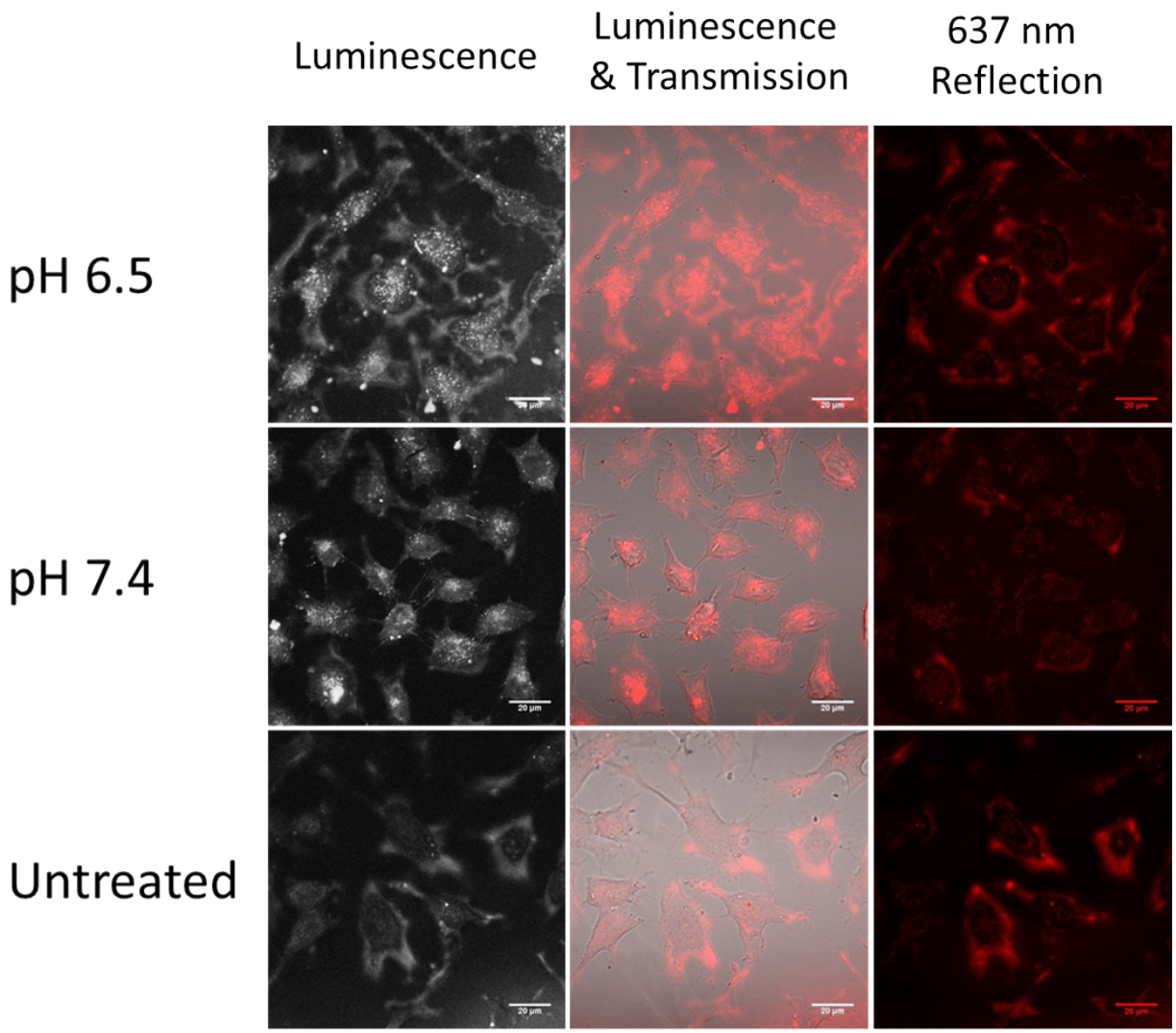

Figure 3.17: Confocal microscopy images of HeLa cells treated with pHLIP-Au^{13}-RubpySS (1 nM) in Tyrodes buffers (0.08 mM, pH 6.5 or 7.4) for two hours at 37°C. For each row, from left to right i) luminescence from 488 nm excitation, ii) luminescence from 488 nm excitation overlaid with transmission at 488 nm, and iii) reflection at 637 nm. Images are accompanied by luminescence spectra of treated and untreated cells, acquired on a multispectral detector. Scale bars set to 20 μm.

HeLa cells were treated with pHLIP-Au^{13}-RubpySS (1 nM) particles in sterilised Tyrode's buffers (0.08 mM, pH 6.5 or 7.4) and were stored in a cell culture incubator (37°C, 4% CO_2) for two hours, before being washed with PBS, and subsequently fixed and mounted for confocal imaging (imaged on a Nikon A1R confocal system). Fig. 3.17 shows *i)* luminescence, *ii)* luminescence & transmission and *iii)* reflection confocal images of HeLa cells treated at pH 6.5, HeLa cells treated at pH 7.4 and HeLa cells that were left untreated. The luminescence signal from cell interiors of treated samples is significantly greater than signal emanating from untreated samples, indicating an increase in luminescent substrate within treated

samples, where the luminescence signal increased as a function of treatment time (Fig. 8.28, appendix). The intracellular luminescent signal from treated samples indicates nanoparticles appear to be gathering into large clusters, possibly resultant from confinement of large groups of particles within endosomes. It has been known for some time that nanoparticles often become trapped in endosomal compartments after being uptaken by cells, and a significant amount of work has been applied into promoting their endosomal escape [236, 237]. There is significant autofluorescence within the luminescence images along with ruthenium signal resultant from the use of higher laser power in order to image significant signal from the low quantum yield RubpySS complex. The transmission images indicated the cells were still attached to glass coverslips at the time of fixation, and only few examples of non-viable cells visible, indicating that the cell population was overall viable. The transmission images did not show evidence of nanoparticle scattering, indicating minimal agglomeration of nanoparticles within cell compartments. This is corroborated by the 637 nm reflection image which also does not show scattered signal from nanoparticle agglomerates. This information indicates that internalized nanoparticles are internalized into cell compartments, but are remaining monodisperse and not flocculating into larger particles.

In order to confirm that treated-cell luminescence was resultant from ruthenium emission, the steady state emission of treated and non-treated cells were measured and contrasted. Fig. 3.18 shows an overlay of ***i)*** steady state emission spectra of HeLa cells treated with pHLIP-Au^{13}-RubpySS (1 nM) for two hours in Tyrodes buffer (pH 6.5, 0.08 mM), ***ii)*** the steady state emission spectra of untreated HeLa cells, ***iii)*** the emission spectrum of *ii)* subtracted from *i)*, and ***iv)*** the steady state emission of free pHLIP-Au^{13}-RubpySS. The strong overlay between the background-subtracted emission spectrum of cells treated with pHLIP-Au^{13}-RubpySS and the emission spectrum of free pHLIP-Au^{13}-RubpySS acts as strong supporting evidence that ruthenium emission is cause of greater luminescence intensity of treated cells.

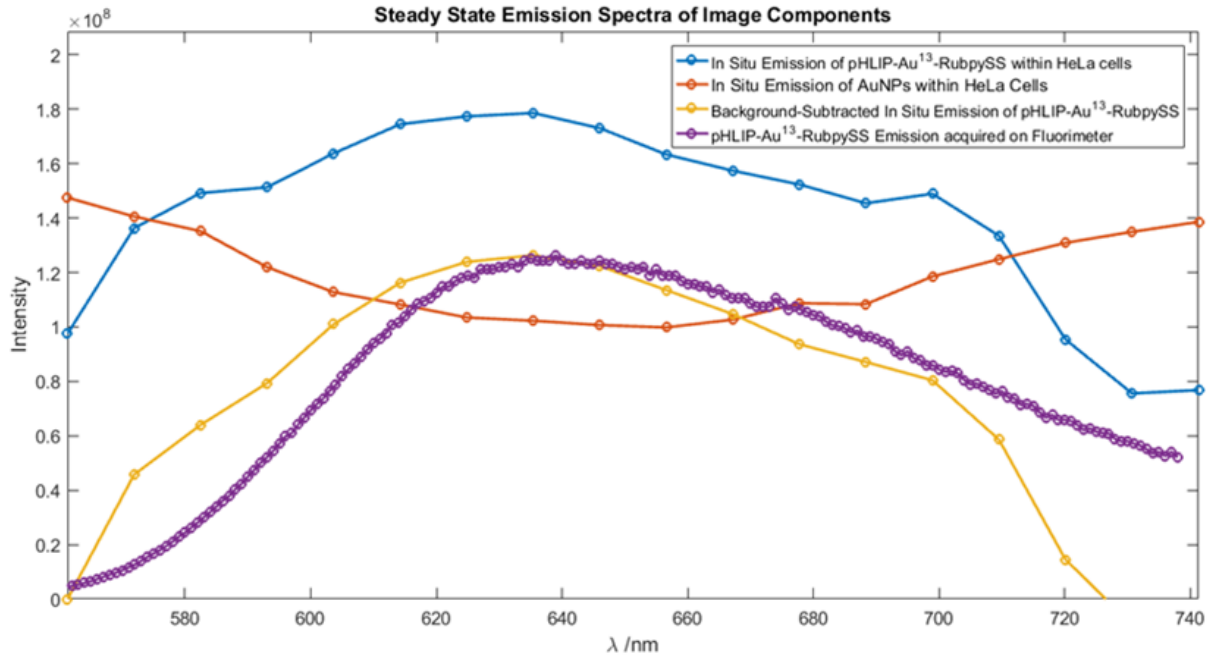

Figure 3.18: Steady state luminescence spectra from treated cells, non treated cells and particles prior to treatment. In situ spectra acquired on a Nikon A1R spectral detector, λ_{ex} = 488 nm, λ_{em} = 561 - 721 nm. perticle emission spectra acquired on an Edinburgh Instruments FLS920 time resolved luminescence spectrometer, λ_{ex} = 488 nm, λ_{em} = 561 - 721 nm.

Luminescence intensity analysis was performed for images of HeLa cells treated with pHLIP-Au^{13}-RubpySS. Fig. 3.19 shows a bar graph of the area weighted mean values across the treatment times. Analysis of the area-weighted mean values showed an increase up to 224% and 179% mean luminescence intensity for pH 6.5 and 7.4, respectively after a 90-minute treatment. This increasing trend of luminescence signal from treated HeLa cells as a function of treatment time corroborates with previously measured flow cytometry data, and the pH-independency of pHLIP-Au^{13}-RubpySS internalization into HeLa cells at 37°C is also consistent with flow cytometry data.

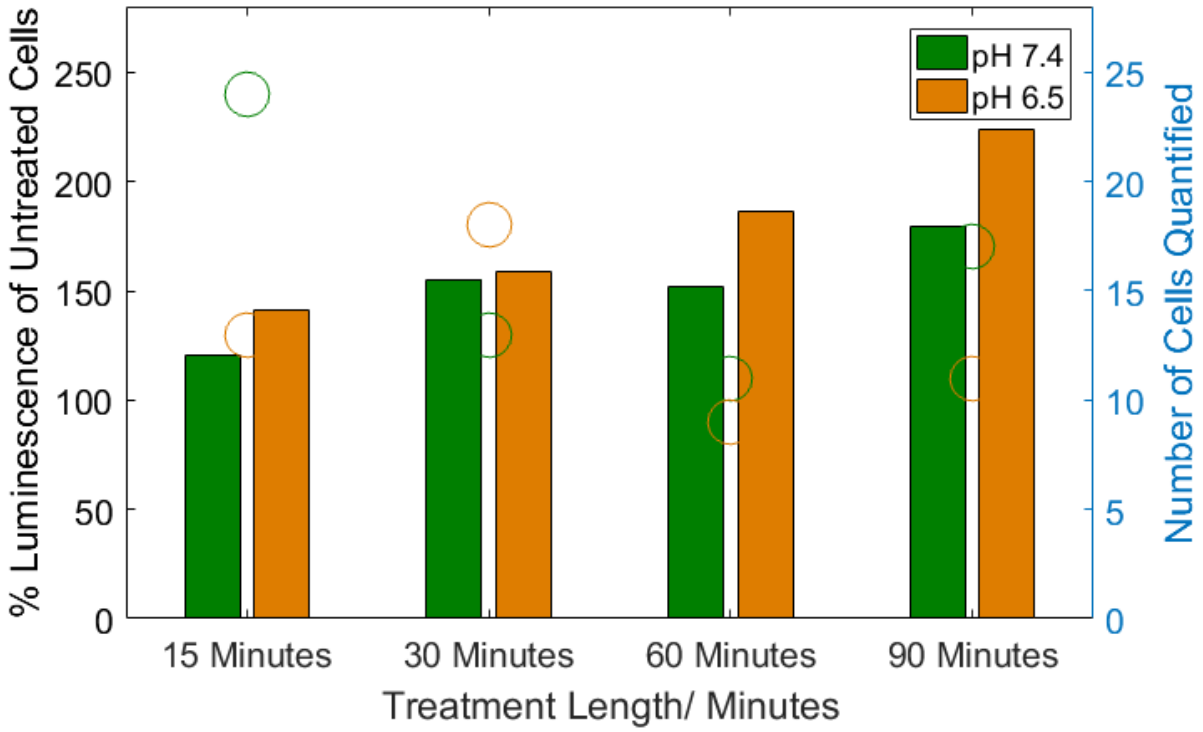

Figure 3.19: Area-weighted mean values calculated from confocal microscopy images of HeLa cells treated with pHLIP-Au^{13}-RubpySS (1 nM) in Tyrodes buffers (0.08 mM) pH 6.5 and pH 7.4 at 37°C. Included on right hand y-axis is the number of cells within the images used in the quantification for each sample at pH 6.5 (orange circles) and pH 7.4 (green circles.

As indicated in the flow cytometry section of this thesis, it is expected that in addition to pHLIP-mediated uptake, non-specific endocytotic uptake is also responsible for a significant amount of nanoparticle internalization and the measures of how strongly each contribute to overall uptake is unclear. To determine if low pH-triggered uptake process is present, a cold treatment at 4°C was performed in order to inhibit endocytotic processes and only observe pHLIP-Au^{13}-RubpySS signal from particles internalized by pHLIP and study their spatial distribution. Fig. 3.20 shows confocal microscopy images of HeLa cells treated with pHLIP-Au^{13}-RubpySS for two hours in Tyrodes buffer (0.08 mM, pH 6.5 or 7.4) at 4°C. For cells treated at each pH, images of the ruthenium luminescence channel, transmitted light, and reflection at 637 nm are presented. Red luminescence signal from each sample is markedly stronger from cells treated at pH 6.5, with apparent clusters of signal present from almost all cells within the field of view, contrasted with cells treated at pH 7.4 where there is little evidence of stronger luminescence. Transmission images of cells treated at pH 6.5 and 7.4 do not show unusual cell morphologies, indicative that cell viability is not compromised by particle treatment. Additionally, the reflection images of treated cells do not show evidence of agglomerates within the cells, indicating that although there are clusters of particles that appear to be spatially near to each other from the luminescence images, particles are not agglomerating due to the absence of cohesive reflection signal.

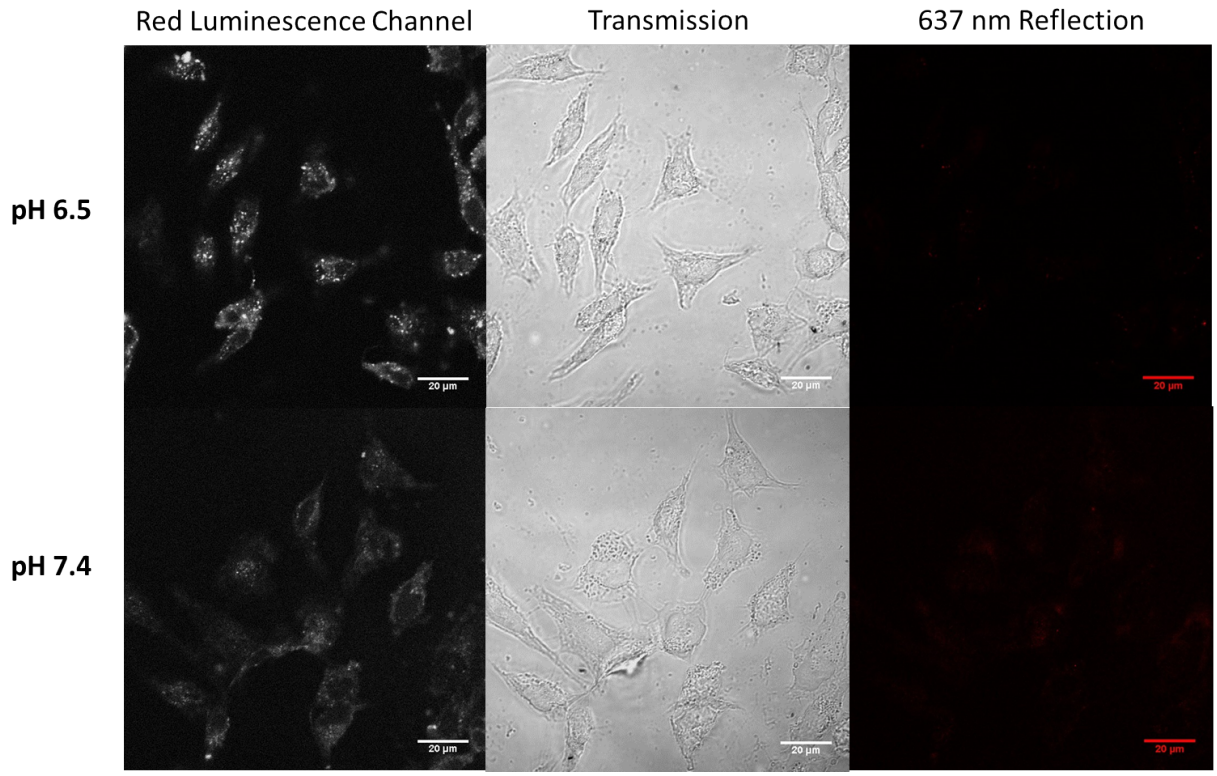

Figure 3.20: Confocal microscopy images of HeLa cells treated with pHLIP-Au13-RubpySS (1 nM) in Tyrodes buffers (0.08 mM, pH 6.5 or 7.4) at 4°C. For each row, from left to right i) luminescence from 488 nm excitation, and detection from $560 - 740$ nm ii) transmission at 488 nm, and iii) reflection at 637 nm

pH-resolved Treatment of HeLa Cells with pHLIPvar3-Au^{13}-RubpySS

HeLa cells were treated with pHLIPvar3-Au^{13}-RubpySS (1 nM) In Tyrode's buffer (0.08 mM, pH 6.5 & pH 7.4) for two hours at 37°C, (maintaining consistency with cytometry experiments) before being analysed by confocal microscopy. Images were acquired on a Zeiss LSM confocal microscope, and images of *i)* transmitted light, *ii)* 637 nm reflectance, *iii)* luminescence from 488 nm excitation and *iv)* lambda stacks from 488 nm excitation (stacks recorded from 490 − 730 nm, in 15 nm steps). Fig. 3.21 shows confocal microscopy images of *i)* luminescence from 488 nm excitation, *ii)* transmitted light, *iii)* 488 nm reflection and *iv)* overlay of 488 nm reflection & luminescence. Luminescence images of treated cells exhibit significantly greater intensity over images of untreated cells, and subtraction of the steady state emission of untreated cells from the spectrum of treated cells indicates the presence of a broad emission band with a λ_{max} of $\approx$ 620 nm, overlaying well with the steady state emission of pHLIP-Au^{13}-RubpySS. For the luminescence images, area-weighted mean values were calculated for three sets of images of cells treated at pH 6.5 and 7.4 and were expressed as a % of untreated cells. Mean luminescence intensity increased to 397 $\pm$ 75 % and 357 $\pm$ 59 % for pH 6.5 and 7.4, respectively. This represents a more marginal difference in uptake between treatments at pH 6.5 and 7.4 than indicated by flow cytometry, but it is important to highlight that cytometry offers significantly greater sensitivity than light microscopy.

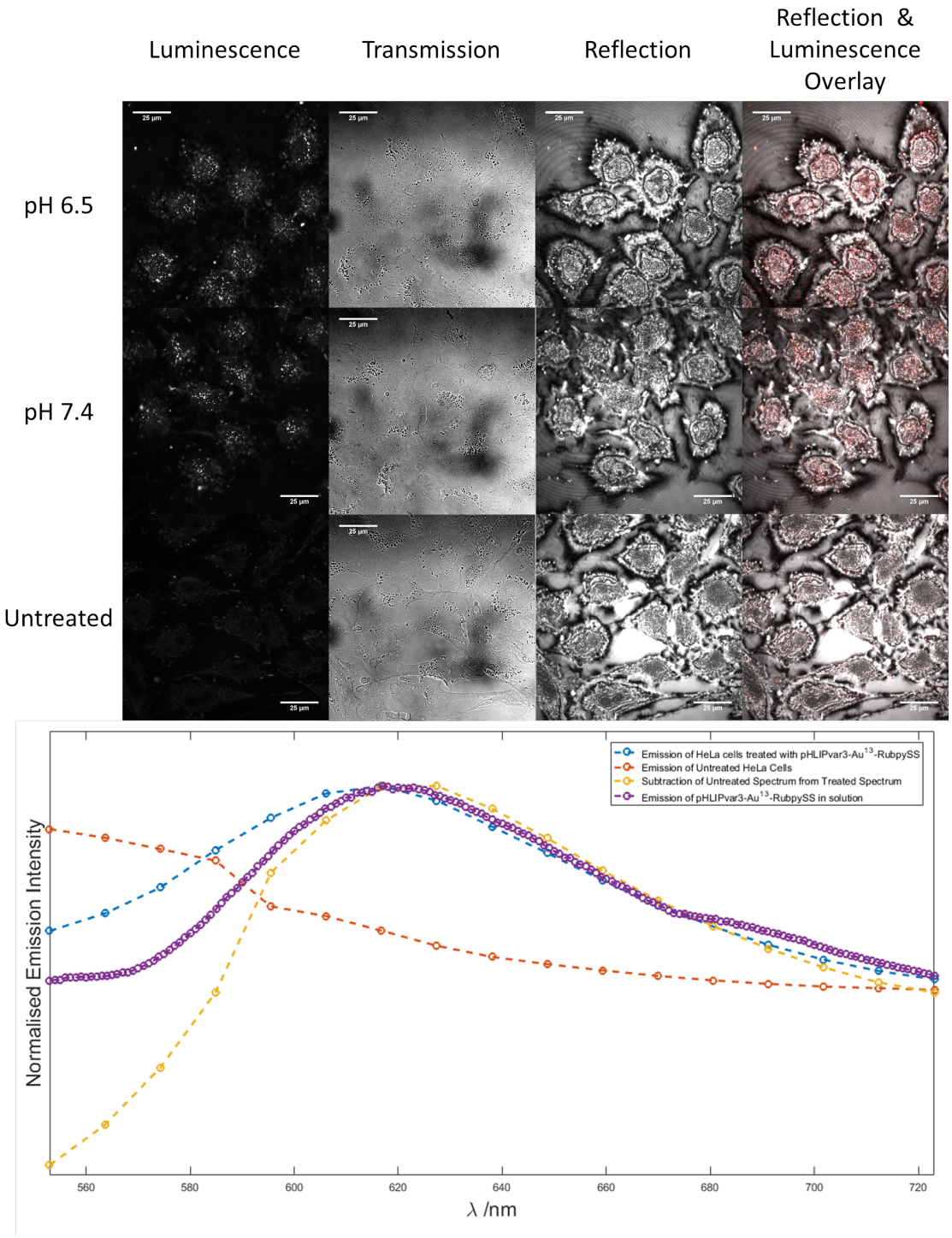

Figure 3.21: Confocal Microscopy images of HeLa cells treated with pHLIPvar3-Au^{13}-RubpySS (1 nM) in Tyrodes buffers (0.08 mM, pH 6.5 or 7.4) for two hours at 37°C, scale bars set to 25 μm. Images of untreated cells also shown, with accompanying luminescence spectra of treated and untreated cells, acquired by acquiring λ-stacks ($\lambda_{ex} = 488nm$, $\lambda_{em} = 550 - 725nm$).

Additionally the 488 nm reflectance and transmission images show a relatively homogenous monolayer of HeLa cells adhered to the glass coverslips with little evidence of non-viable (cells exhibiting spherical shape) amongst the population.

pH-resolved Treatment of HeLa Cells with Zonyl-Au^{13}-RubpySS

Confocal microscopy was also used to provide an indication of the extent of endocytotic gold nanoparticle uptake into HeLa cells. For this experiment, HeLa cells were treated with Zonyl-Au^{13}-RubpySS in Tyrode's buffer (0.08 mM, pH 6.5 or 7.4) for two hours at 37°C (imaged on a Nikon A1R confocal system). Fig. 3.22 shows confocal luminescence microscopy images resultant from the treatment, where there luminescence appears to originate from intense spots, likely indicating a large density of clustered nanoparticles within cells. Inset to each image is the steady-state emission spectra from each sample (Fig. 3.22, inset) which bears the characteristic broad emission band of RubpySS at ≈ 620 nm.

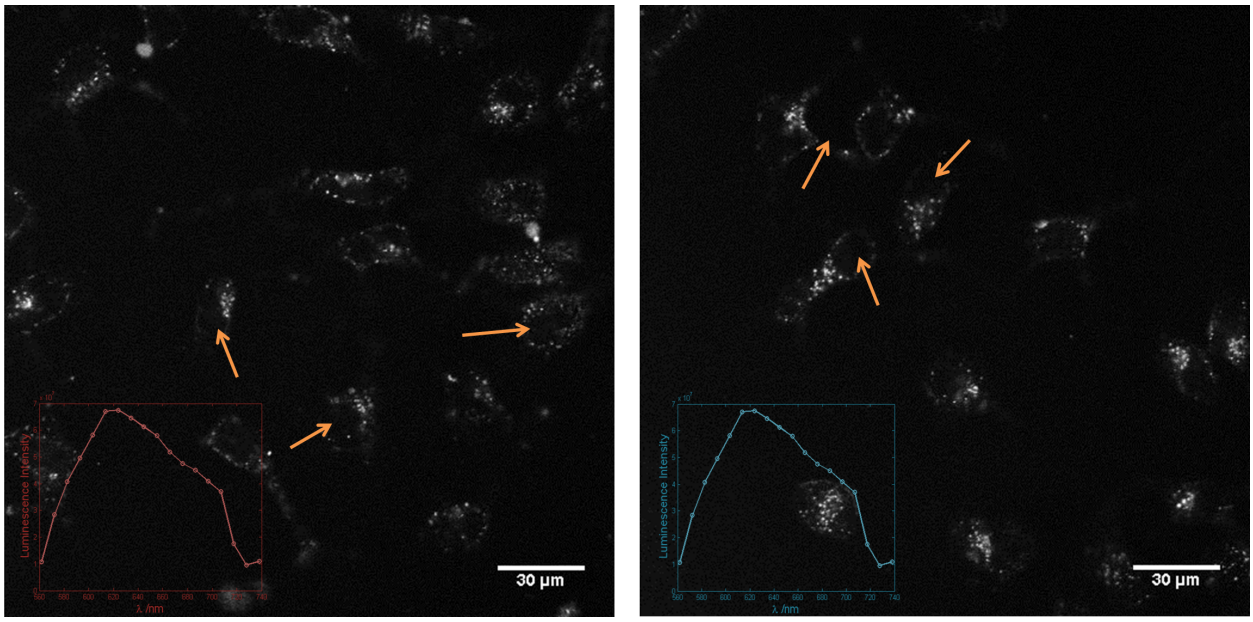

Figure 3.22: Confocal microscopy images of HeLa cells treated with Zonyl-Au^{13}-RubpySS (1 nM) in Tyrodes buffers (0.08 mM) pH 6.5 (left) and pH 7.4 (right) at 37°C. Inset, steady state emission scans taken of treated HeLa cells ($\lambda_{ex} = 488nm$) with arrows indicating positions of cell nuclei.

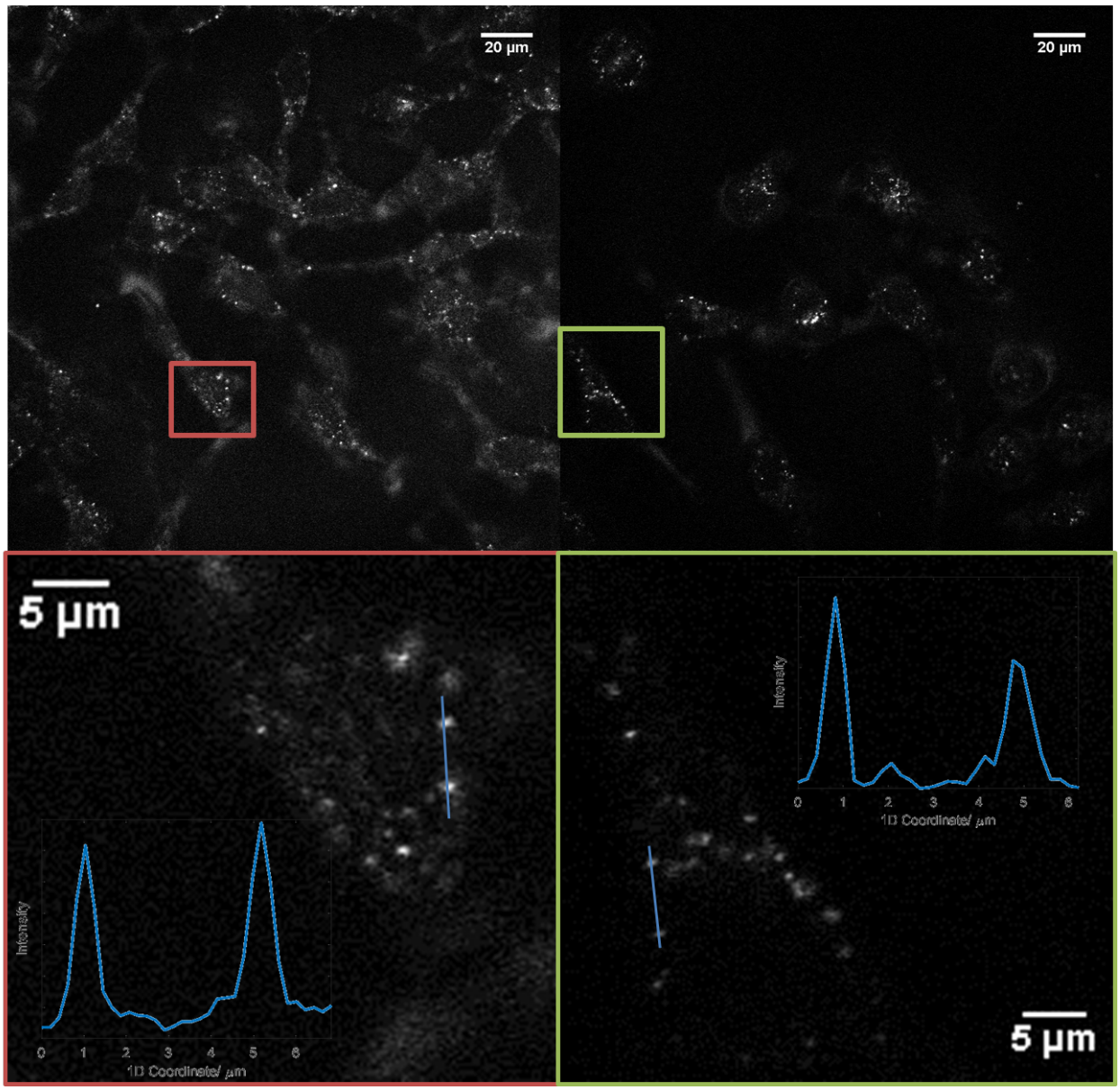

Figure 3.23: Confocal reflection microscopy images of HeLa cells treated with Zonyl-Au^{13}-RubpySS (1 nM) in Tyrodes buffers (0.08 mM pH 6.5 (left column) and pH 7.4 (right column)) at 37°C. Images acquired using illumination and detection at 637 nm. ROI indicated for each image, and 1D profiles drawn that intersect internalized gold clusters.

Fig. 3.23 shows reflection-mode confocal microscopy images of HeLa cells treated with Zonyl-Au^{13}-RubpySS (1 nM) in Tyrodes solutions (0.08 mM) buffered to pH 6.5 and 7.4. The strong signal from light-reflecting gold clusters is evident in both samples corroborating with the increase in side scatter as a function of treatment time previously measured by flow cytometry. The clusters have a FWHM of approximately 1 μm in diameter, indicating clusters are several orders of magnitude bigger than individual particles and likely representative of aggregating gold nanoparticles, which has been reported for some gold

nanoparticles internalized into endosomal or lysosomal compartments [238]. This presents a useful analysis of the stability of labelled-AuNPs post-internalization, as it appears that particles which maintain hold of their stabilising labels more efficiently do not appear to aggregate.

pH-resolved Treatment, and Confocal Image analysis of HeLa Cells with Labelled-Au^{100}NPs

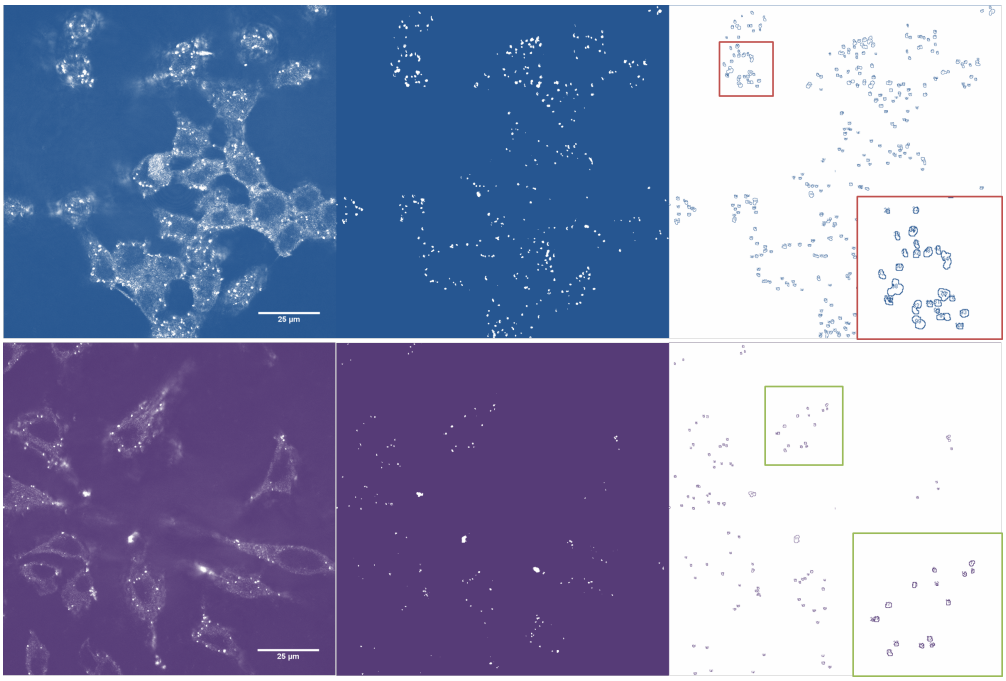

Figure 3.24: Stages of image analysis leading to nanoparticle quantification. From left to right, columnn 1 shows reflectance images obtained using 488 nm excitation; middle column shows thresholded image showing nanoparticle signal; and right column shows outlined particles with their assigned count number. Blue and purple-tinted images represent sample treatments at pH 6.5 and 7.4, respectively.

In addition to studying labelled 13 nm gold nanoparticles, the pH-dependent uptake of analogous 100 nm labelled-nanoparticles was also studied. A useful benefit of using 100 nm AuNPs is that the particles are more easily quantifiable because individual 100 nm gold nanoparticles can be identified [96], permitting more meaningful uptake quantification. Fig. 3.24 shows the stages of the quantification method. Reflection images were taken of treated cells using 488 nm excitation, containing elements of nanoparticles and cellular features. Images were thresholded into binary images to remove unwanted cell features, leaving behind nanoparticle reflection signal. The particles were then highlighted using the ImageJ outline tool, and subjected to the 'Analyse Particles' function which counts the number of outlined features. Corresponding transmission images of treated cells were then segmented for cell boundaries (Fig. 3.25) and cell area was calculated in square microns. In this segmentation, transmission images were thresholded using the Otsu method to produce a binary image, and the sobel edge operator was used to find edge features. The image was then dilated using linear structuring elements, and interior holes were filled. The image was then smoothened

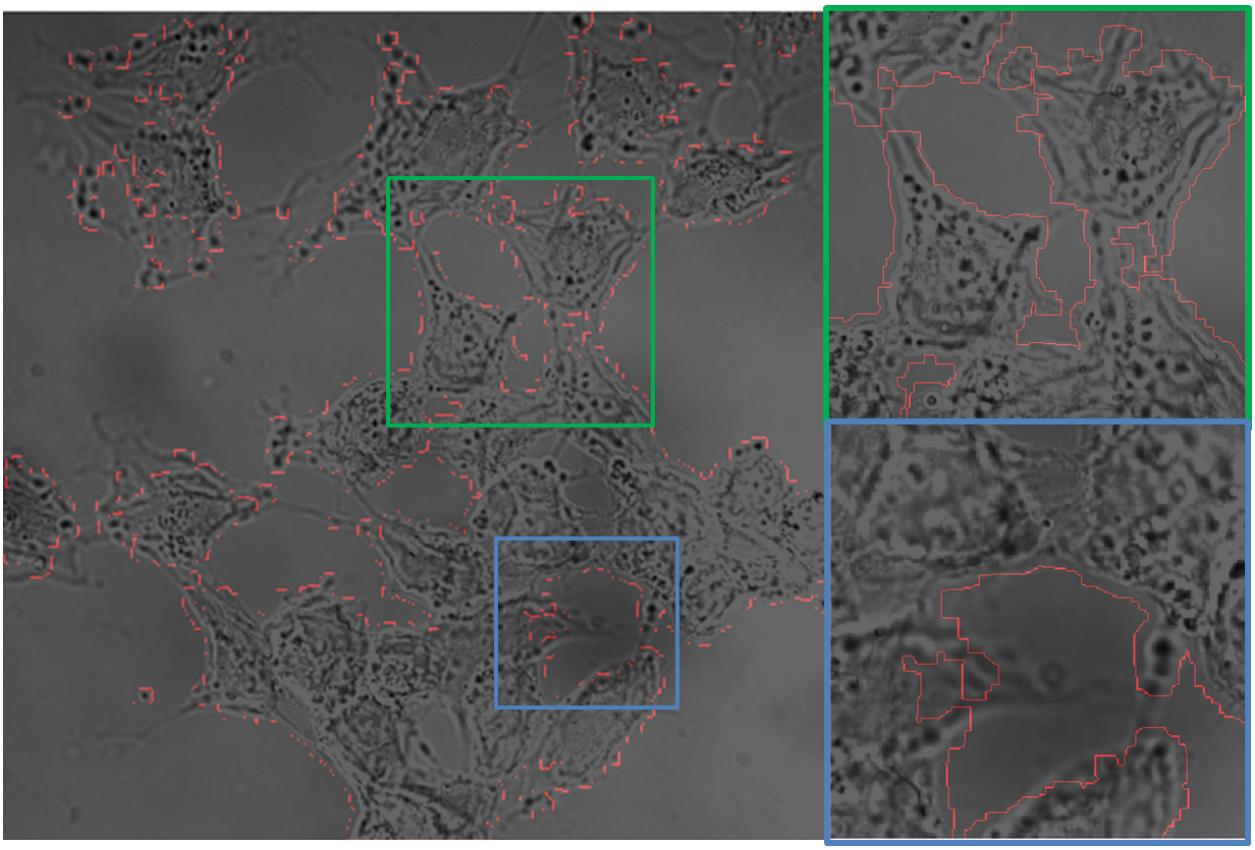

Figure 3.25: Segmented transmission images of HeLa cells treated with pHLIPvar3-Au^{100}-RubpySS (8 pM) in Tyrodes buffer (0.08 mM, pH 6.5) for two hours at 37°C. Segmented outline shown in red, and inset are two expanded regions (blue & green) showing segmented cell boundaries.

by eroding the image twice with a diamond structuring element, and the outline of this mask was used to segment cell regions. The full segmentation process is documented in Fig. 8.29 within the chapter's appendix. The resulting nanoparticle quantification was then expressed as the cell area a single nanoparticle occupies, e.g. 1 nanoparticle per x μm^2 of cell space.

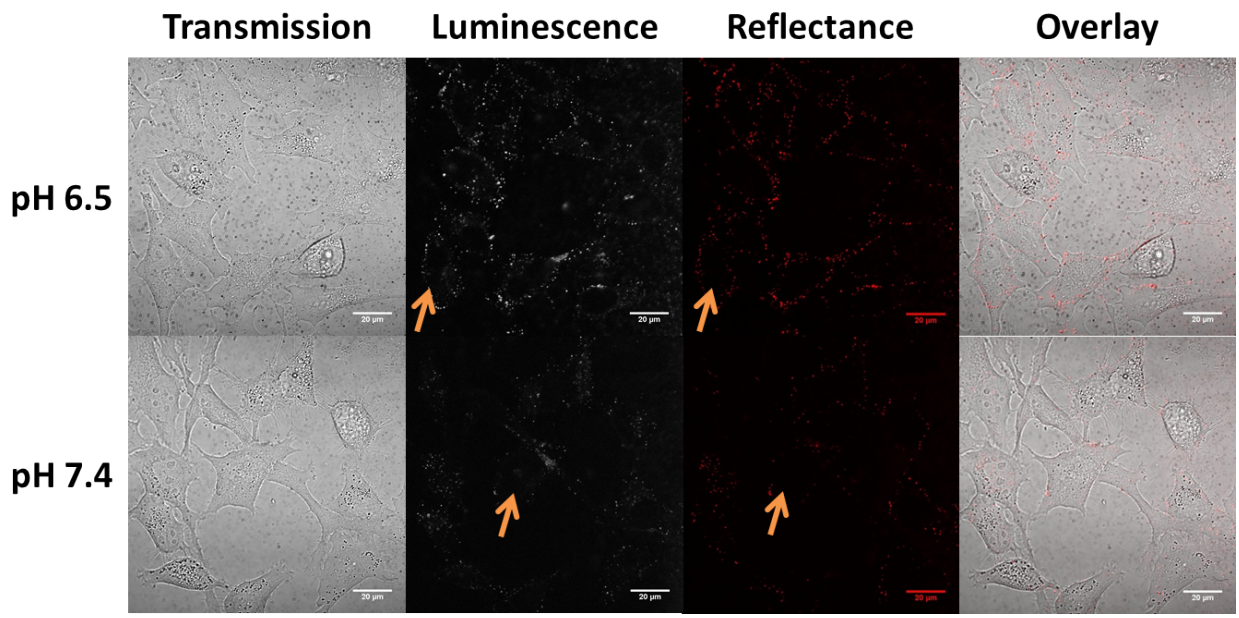

Figure 3.26: Live cell confocal microscopy images of HeLa cells treated with pHLIP-Au^{100}-RubpySS (8 pM) in Tyrodes buffers (0.08 mM, pH 6.5 & 7.4) for three hours at 4°C. Arrows indicate nuclear regions. Images show transmitted light at 488 nm, luminescence from 488 nm excitation (detection from 550–725 nm), reflectance at 633 nm, and an overlay of transmission and luminescence images. Scale bars set to 20 μm.

pH-resolved Treatment of HeLa Cells with pHLIP-Au^{100}-RubpySS

HeLa cells were grown to confluency in 35 mm MatTek glass bottom dishes before being treated with pHLIP-Au^{100}-RubpySS (8 pM) in Tyrodes buffers (0.08 mM, pH 6.5 & 7.4) for three hours at 4°C before being imaged live in phosphate buffered saline (Fig. 3.26). Transmission images indicate spread, viable morphologies, although cell viability is properly examined later in this thesis. Luminescence imaging shows that individual particles are luminescent when excited at 488 nm (detection from 561-720 nm), owing to the ruthenium dye, and the particles show strong reflectance when irradiated with 637 nm light. Particles appear to localise within cytosolic regions of the cells, and nuclear regions appear to be devoid of particles, as determined by identifying nuclei from 488 nm reflection images. It has been previously reported that the size boundary is 9 nm for nuclear diffusion, and 30 nm for internalization through nuclear pores [239, 240]. No significant evidence of nuclear internalization has been seen for the uptake of pHLIP-Au^{100}-RubpySS, demonstrating a potential drawback from the use of Au^{100}NPs as a scaffold for imaging probes. Quantitative analysis of nanoparticles internalized into HeLa cells revealed that HeLa cells treated at pH 6.5 had an average of 1 nanoparticle per 15 $\pm$ 2 μm^2 of cell space, whereas when cells were treated at pH 7.4 there was on average 1 particle per 21 $\pm$ 6 μm^2 of cell space, supportive of pH-dependent uptake and consistent with the uptake of pHLIP-Au^{13}-RubpySS. The author would like to note that the image data used in this calculation was acquired using three sets of technical repeats.

pH-resolved Treatment of HeLa Cells with pHLIPvar3-Au^{100}-RubpySS

Treatment of HeLa cells with pHLIPvar3-Au^{100}-RubpySS (8 pM) in Tyrodes buffer (0.08 mM, pH 6.5 & 7.4) was also performed under live cell conditions. Cells were treated for two hours at 37°C before being washed with PBS twice, and subsequently imaged in PBS.

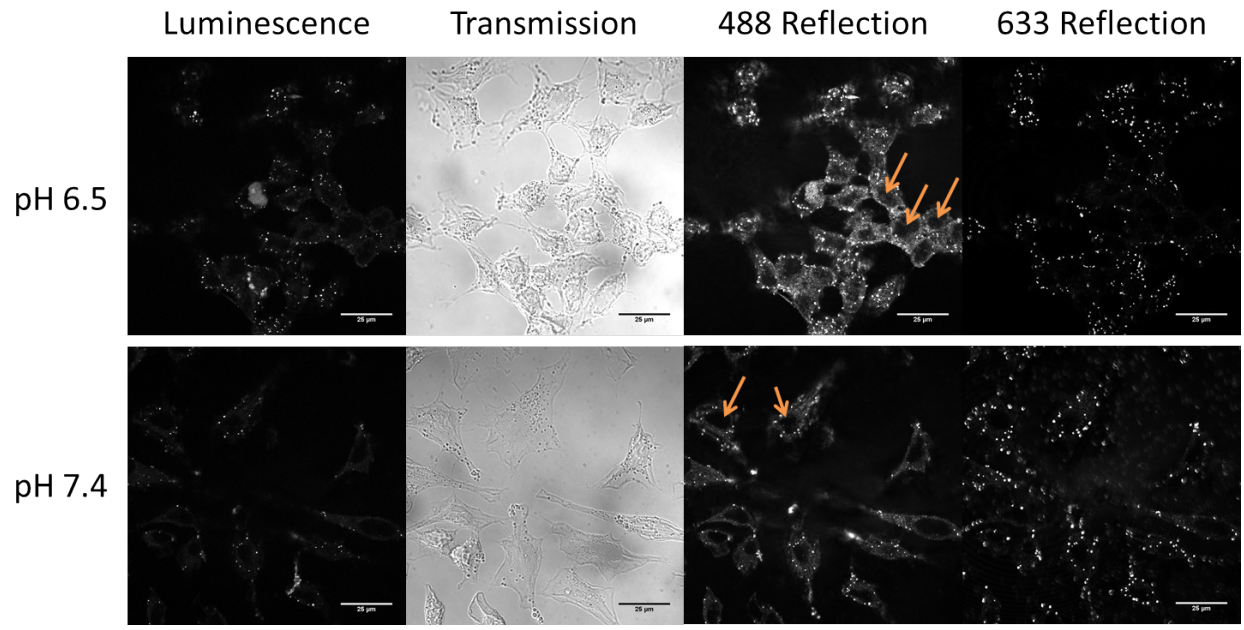

Figure 3.27: Confocal Microscopy images of HeLa cells treated with pHLIPvar3-Au^{100}-RubpySS (8 pM) in Tyrodes buffers (0.08 mM, pH 6.5 & 7.4) for two hours at 37°C. Scale bars set to 20 μm, and arrows indicate nuclear regions.

HeLa cells treated with pHLIPvar3-Au^{100}-RubpySS also exhibited a pH-dependent internalization of labelled-AuNPs at 37°C, consistent with the pH-dependent uptake of pHLIPvar3-Au^{13}-RubpySS. Cells treated at pH 6.5 appear to have greater nanoparticle density than cells treated at pH 7.4, and this was supported by quantitative analysis which showed that cells treated at pH 6.5 had an average of 1 particle per 26 $\pm$ 7 μm^2 of cell space, whereas when cells were treated at pH 7.4 there was on average 1 particle per 52 $\pm$ 8 μm^2 of cell space. The image data used in this calculation was acquired using two sets of technical repeats. It is also apparent from 488 nm reflection images that nanoparticles again appear to localise within cytosolic regions, and are devoid from nuclear regions, this is not surprising it is known that the maximum diameter of nuclear pores is $\approx$ 30 nm [239, 240].

pH-resolved Treatment of HeLa Cells with Zonyl-Au^{100}-RubpySS

Finally, to quantify the endocytotic uptake of gold nanoparticles as a function of microenvironmental pH, HeLa cells were treated with Zonyl-Au^{100}-RubpySS (8 pM) in Tyrodes buffers (0.08 mM, pH 6.5 & 7.4) for three hours at 37°C. Cells treated at pH 6.5 had an average internalized nanoparticle density of 1 particle per 9 ± 1 μm^2 of cell space, whereas when cells were treated at pH 7.4 there was on average 1 particle per 11 ± 6 μm^2 of cell space. This data indicates that internalized Zonyl-Au^{100}-RubpySS nanoparticle density is not responsive to extracellular pH differences within the window of pH 6.5 - 7.4. This corroborates well with the cytometry data, from which we also concluded a non-pH dependency of Zonyl-Au^{100}-RubpySS uptake into HeLa cells, and is also consistent with the uptake of Zonyl-Au^{13}-RubpySS. Data comprised of three technical repeats was used in this analysis.

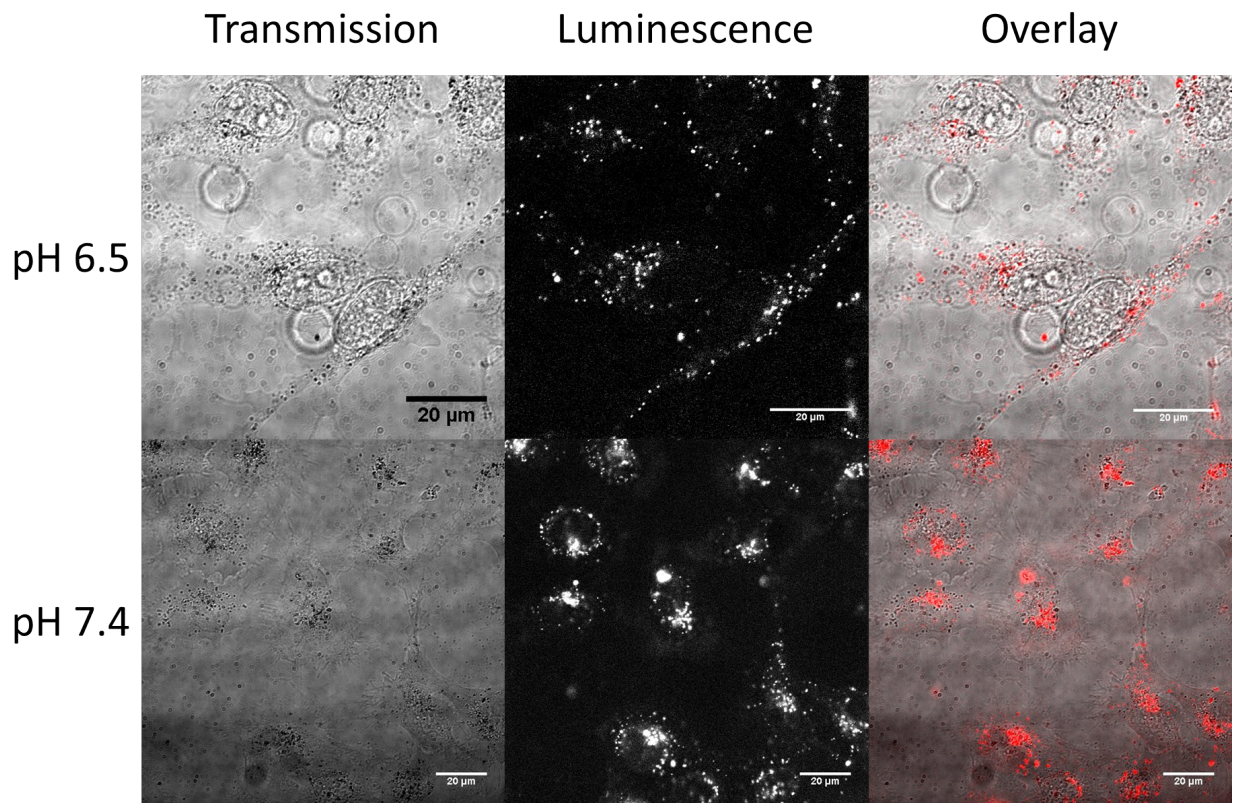

Figure 3.28: Confocal microscopy images of HeLa cells treated with Zonyl-Au^{100}-RubpySS in Tyrodes buffers (0.08 mM) pH 6.5 (left) and pH 7.4 (right) at 37° for three hours.

Transmission Electron Microscopy evaluation of pH-Dependent Cellular Uptake

The uptake of pHLIPvar3-Au^{13}-RubpySS was evaluated by transmission electron microscopy in order to assess the cellular distribution of individual particles using an imaging technique with nanometer scale spatial resolution. Due to the electron-rich nature of gold nanoparticles, they are efficient electron scatterers enabling their visualisation by electron microscopy techniques. This not only demonstrates their potential for multimodal imaging but also creates a platform to image individual particles that are too small to be visualised by conventional light microscopy techniques. Transmission electron microscopy has been widely applied to the imaging of biological samples, although there is still much debate surrounding the effect of the fixation and mounting processes on sample integrity and the distribution of internalized substances [125].

The technique of Energy Dispersive Analysis of X-rays was used in combination with TEM in order to assess the elemental composition of treated HeLa cells. The technique is based on the principle that an atom's core electrons are excitable & ejectable by incident high energy electrons. Upon electron ejection, the newly empty orbital is filled by one of the atom's valence electrons, leaving behind an empty valence orbital. This is a radiative process, with the energy released in the form of X-ray emission. The energy of the emitted X-ray is characteristic of the atom, and electrons involved in the transition, enabling identification of elements in a sample from their unique EDAX spectrum.

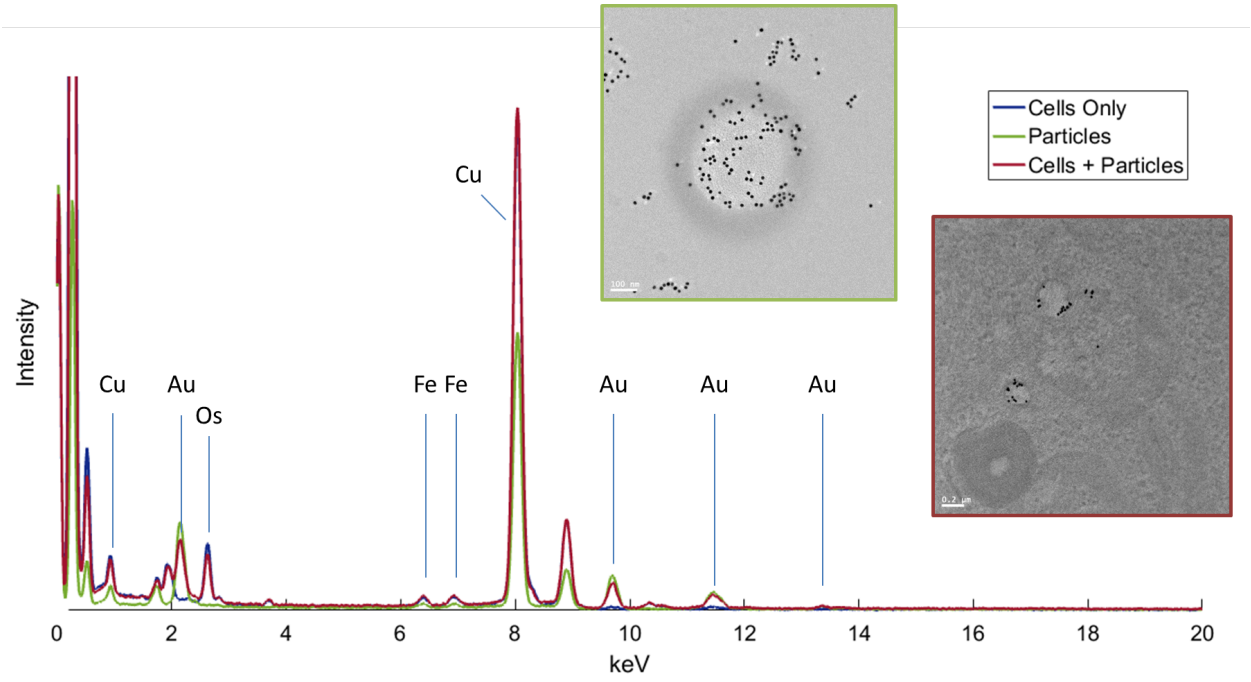

Figure 3.29: Energy Dispersive Analysis of X-rays spectra of *i)* HeLa cells treated with pHLIP-Au^{13}-RubpySS (1 nM) for two hours in Tyrodes buffer pH 6.5, at 37°C for two hours, *ii)* pHLIP-Au^{13}-RubpySS mounted onto a Cu grid and *iii)* Untreated HeLa cells. Inset, transmission Electron micrographs of i) treated HeLa cells (red outline), and ii) pHLIP-Au^{13}-RubpySS particles on Cu grids (green outline).

HeLa cells treated with pHLIP-Au^{13}-RubpySS (1 nM) for two hours in Tyrodes buffer (0.08 mM, pH 6.5), at 37°C for two hours, and were subsequently fixed, sectioned and mounted for imaging. Fig. 3.29 shows EDAX spectra of *i)* nanoparticle containing region of treated cells (red line), *ii*) region of treated HeLa cells devoid of nanoparticle presence (blue line) and *iii)* pHLIP-Au^{13}-RubpySS nanoparticles on Cu grids (green line). Cells treated with gold nanoparticles show characteristic gold Xrays at 9.7, 11.6 and 13.6 keV. It is also noteworthy that no ruthenium bands were present within the EDAX spectrum. This was studied in Chapter 2 where labelled-AuNPs were dried onto Cu grids for the acquisition of an EDAX spectrum, and while Au in its high concentration was readily detectable, the low concentration of Ru resulted in low X-ray flux resulting in no detectable ruthenium EDAX bands in the spectrum.

Thus far, pHLIPvar3 has been the most promising of the two pHLIP peptides, being an effective delivery agent that offers efficient uptake of AuNPs within short time frames and under physiological conditions. To assess the pH-dependent intracellular distribution of pHLIPvar3-Au^{13}-RubpySS, HeLa cells were treated with particles (1 nM) for two hours at 37°C while immersed in Tyrode's buffers (0.08 mM, pH 6.5 & 7.4). Fig. 3.30 shows a selection of TEM images of HeLa cells treated with pHLIPvar3-Au^{13}-RubpySS at pH 6.5. From qualitative analysis of internalized nanoparticles it appears that there was a large abundance of particles confined to vesicular regions (images A - C), with a number of examples of individual particles that were free of vesicular confinement (images D - F). Endosomes were shown by Tycko and Maxwell to have low internal pH, using a pH sensitive fluorecein probe that revealed endosomic pH to be on the order of pH 5 - 6 [241]. It is possible that pHLIPvar3's pH-dependent translocation could be mediating nanoparticle escape from endosomes, but future work will need to be done to definitively conclude this.

Also observed were particles localised on the exterior of the cell's membrane (images G & H), although only a small number of examples were found compared with the quantity of particles that had been internalized. It is interesting that these vesicular regions of high nanoparticle density in Fig. 3.30- A, B & C are likely responsible for the bright spots in the luminescence images of pHLIPvar3-Au^{13}-RubpySS (Fig. 3.21).

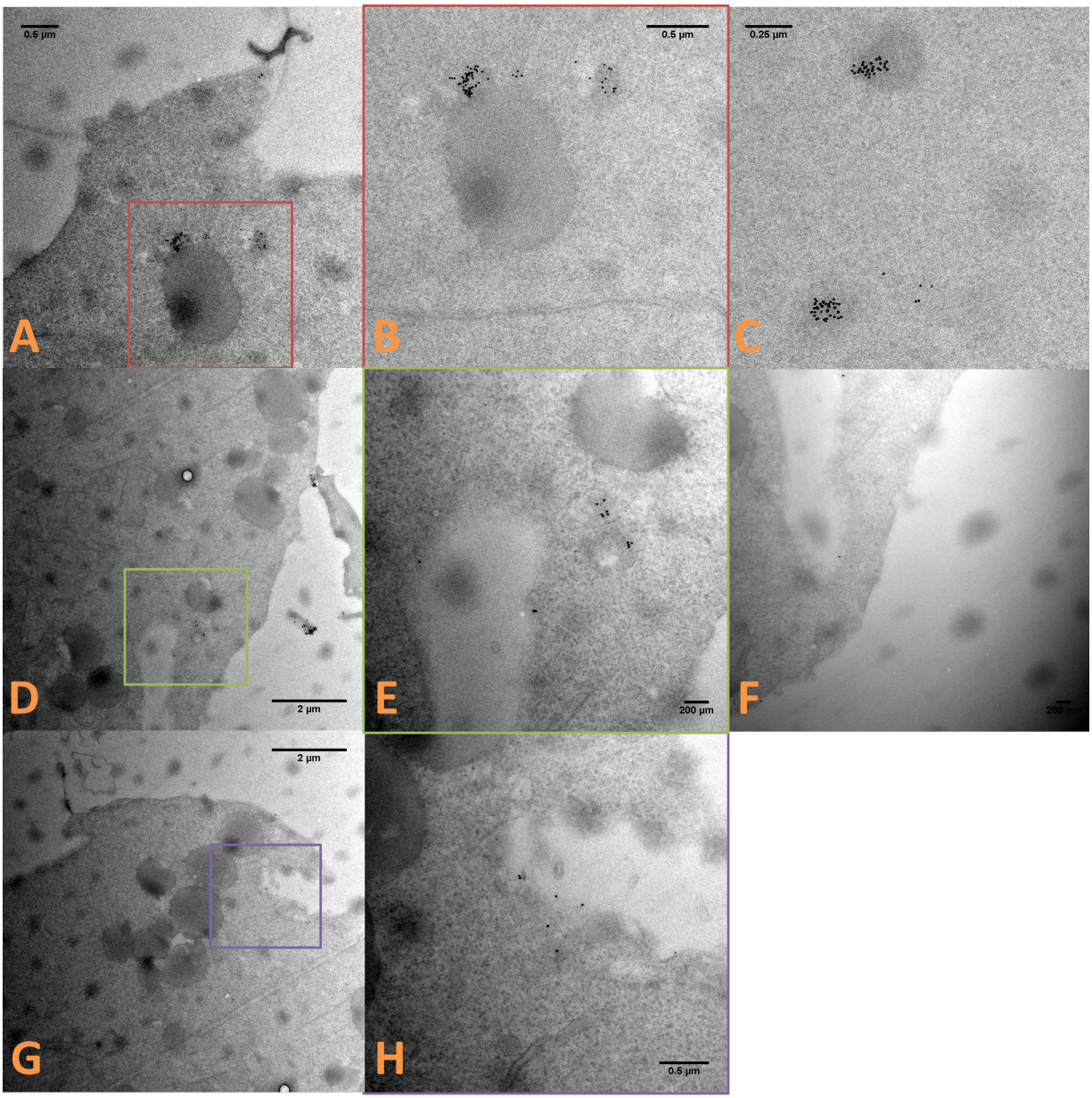

Figure 3.30: Transmission Electron micrographs of HeLa cells treated with pHLIPvar3-Au^{13}-RubpySS (1 nM) for two hours in Tyrodes buffer (0.08 mM, pH 6.5), at 37°C. A - C) Images of internalized particles confined to vesicular regions, D - F) Images of internalized particles free within cell cytoplasm, G & H) Images of non-internalized particles adhered to cell periphery.

HeLa cells were also treated with pHLIPvar3-Au^{13}-RubpySS (1 nM) for two hours at 37°C at pH 7.4 and analysed by TEM (Fig. 3.31). In this instance, examples were found of internalized particles confined to vesicular regions (images A - C), again corroborating with fluorescence microscopy images (Fig. 3.21), and a large abundance of particles were non-internalized and instead remained adherent to the cell membrane. Very few examples of these membrane bound nanoparticles are single entities, almost all are associating into

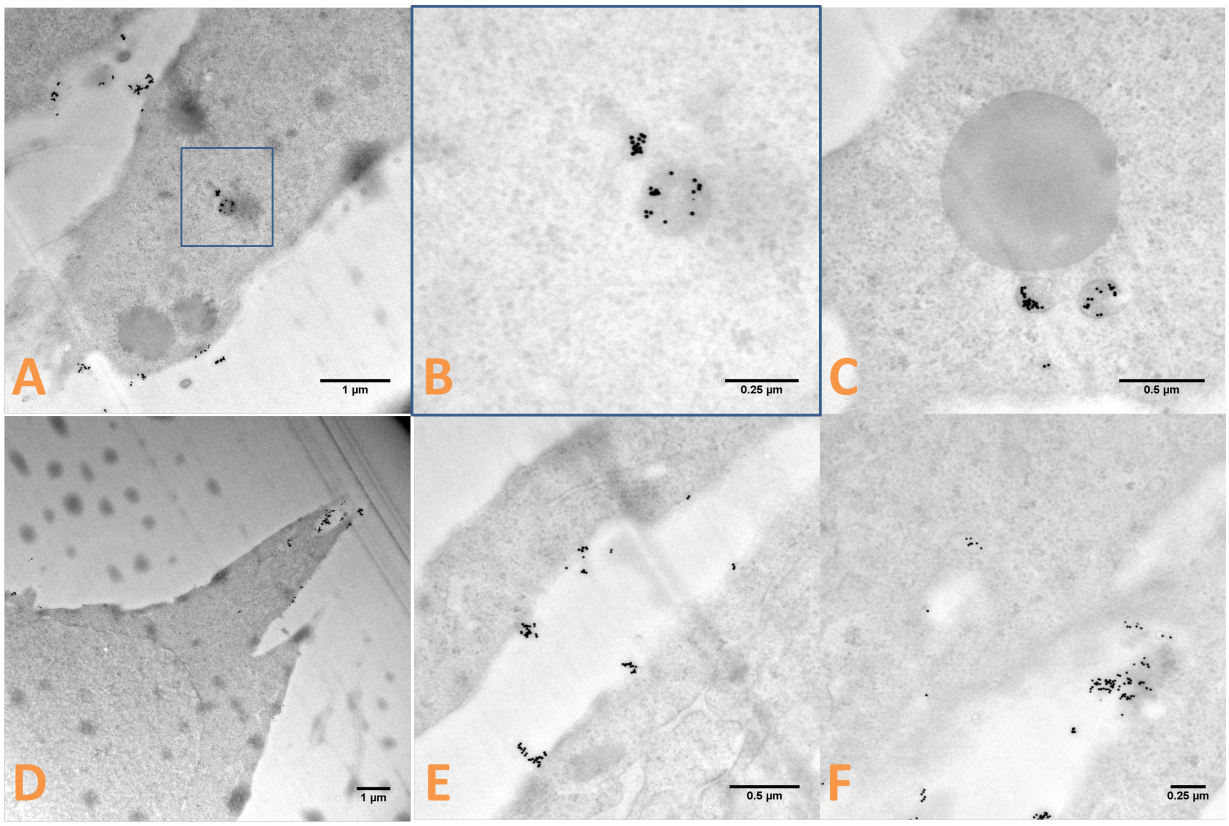

Figure 3.31: Transmission Electron micrographs of HeLa cells treated with pHLIPvar3-Au[13]-RubpySS(1 nM) for two hours in Tyrodes buffer (0.08 mM, pH 7.4), at 37°C. A - C) Images of internalized particles confined to vesicular regions, D - F) Images of non-internalized particles adhered to cell periphery.

clusters. This is not too surprising as despite pHLIPvar3's hydrophilic residues, most of the residues are hydrophobic, likely spurring a favourable interaction between particles in aqueous solution.

Sample	[Au] at pH 6.5/ ppb	[Au] at pH 7.4/ ppb	τ/ hours	δ
pHLIP-Au^{13}RubpySS	65	27	3	4°C
pHLIP-Au^{100}-RubpySS	555	425	3	4°C
pHLIPvar3-Au^{13}-RubpySS	186	98	2	37°C
pHLIPvar3-Au^{100}-RubpySS	1308	864	2	37°C

Table 3.2: ICPMS-measured gold concentration from HeLa cells treated with labelled gold nanoparticles for two hours in Tyrodes buffers (0.08 nM, pH 6.5 or 7.4). Included in the table are each treatment length(τ) and treatment temperature (δ). Labelled-Au^{13} nanoparticles had a final concentration of 1 nM, and labelled-Au^{100} nanoparticles had a final concentration of 8 pM.

Inductively-Coupled Plasma Mass Spectrometry (ICP-MS) evaluation of pH-Dependent Cellular Uptake

The concentration of gold internalized by HeLa cells treated with labelled gold nanoparticles was evaluated by ICP Mass Spectrometry. In this procedure, once cell treatment had concluded, cells were washed and digested using ultrapure aqua regia (3:1, HCl:HNO_3) before being dispersed in 4% HNO_3 for analysis. Prior to sample acquisition, standard solutions of gold were prepared, and analysed to construct a calibration curve. Concentrations of 0, 50, 100, 250, 500 & 1000 ppb were prepared and studied in absence of the helium sheath gas, which is generally not required for high molecular weight elements such as gold. Sample solutions were then analysed if the calibration line satisfied the $r^2 > 0.998$ criteria, indicating an accurate calibration. Table. 3.2.2 shows concentrations of gold detected from cells treated with peptide-laelled luminescent AuNPs. For the analysis, all treated samples were normalised by subtracting measured gold signal from untreated cells.

For pHLIP-Au^{13}RubpySS, the concentrations of gold detected from cells treated for two hours at 4°C in Tyrodes buffers (0.08 mM) at pH 6.5 & 7.4 were 186 ppb & 98 ppb, respectively. pHLIP-Au^{100}RubpySS (8 pM, three hour treatment) treated HeLa cells, also showed the same trend with gold concentrations in Tyrodes buffer (0.08 mM) pH 6.5 & 7.4 of 555 ppb & 425 ppb, respectively.

For pHLIPvar3-Au^{13}RubpySS, the concentrations of gold detected from cells treated at pH 6.5 & 7.4 were 186 ppb & 98 ppb, respectively. For pHLIPvar3-Au^{100}RubpySS, the concentrations of gold detected within cells treated at pH 6.5 & 7.4 were 1308 ppb and 864 ppb, respectively. Both these results support previously reported cytometry and confocal microscopy data indicating that internalization of pHLIPvar3-labelled particles is more efficient at pH 6.5.

For all ICP-MS treatments, cells treated at pH 6.5 displayed higher concentrations of gold than cells treated at pH 7.4. This is a strong corroboration with flow cytometry and light microscopy conclusions that pHLIP & pHLIPvar3 are mediating a pH dependent transduction of luminescent AuNPs, and a good indication that the indirect luminescence measurements acquired through flow cytometry and light microscopy are accurate representations of AuNP uptake. It interesting that for both labelled Au^{13}NPs the ratio of gold concentration is approximately 2:1 for pH 6.5:pH 7.4, whereas for the larger Au^{100}NPs the ratio is signif-

Sample	Analysis Technique	pH 6.5	pH 7.4
pHLIP-Au^{13}-RubpySS	FC Scatter (%)	106 ± 1%	102 ± 3%
	FC Luminescence (%)	210%	165%
	Microscopy (%)	–	–
	ICP-MS (/ppb)	65	27
pHLIP-Au^{100}-RubpySS	FC Scatter (%)	160%	120%
	FC Luminescence (%)	230%	150%
	Microscopy (%)	1 AuNP per 15 ± 2 μm^2	1 AuNP per 21 ± 6 μm^2
	ICP-MS (/ppb)	555	425
pHLIPvar3-Au^{13}-RubpySS	FC Scatter (%)	108 ± 10%	112 ± 4%
	FC Luminescence (%)	2064 ± 104%	1409 ± 204%
	Microscopy (%)	397 ± 75%	357 ± 59%
	ICP-MS (/ppb)	186	98
pHLIPvar3-Au^{100}-RubpySS	FC Scatter (%)	213 ± 13%	178 ± 5%
	FC Luminescence(%)	370 ± 54%	328 ± 30%
	Microscopy(%)	1 AuNP per 26 ± 7 μm^2	1 AuNP per 52 ± 8 μm^2
	ICP-MS (/ppb)	1308	864
Zonyl-Au^{13}-RubpySS	FC Scatter (%)	109%	117%
	FC Luminescence (%)	344%	348%
Zonyl-Au^{100}-RubpySS	FC Scatter (%)	234 ± 4%	234 ± 6%
	FC Luminescence (%)	492 ± 32%	562 ± 12%
	Microscopy (%)	1 AuNP per 9 ± 1 μm^2	1 AuNP per 11 ± 6 μm^2

Table 3.3: Tabled summary of collected experimental data from this chapter consisting of pH-resolved uptake of labelled gold nanoparticles from four imaging or spectrometric modalities.

icantly smaller for both peptides. For pHLIP-Au^{100}-RubpySS the gold concentration ratio of cells treated at pH 6.5:pH 7.4 is 1.3:1, and for pHLIPvar3-Au^{100}-RubpySS the ratio was 1.5:1. This suggests that the efficiency of pHLIP & pHLIPvar3 pH-mediated delivery of AuNPs into HeLa cells is less efficient with larger particles.

Data Summary of pH-Resolved Uptake

Detailed in Table 3.2.2 are all reported relative and absolute labelled-AuNP uptake measurements determined through analysis of flow cytometry, Microscopy and ICP-MS as outlined in previous sections. Relative measurements from analysis of flow cytometry and microscopy measurements are expressed as % luminescence of untreated cells and absolute concentration values determined by ICP-MS are expressed in ppb of Au having subtracted measured Au concentration of untreated cells. This higher uptake efficacy for pHLIPvar3-mediated internalization of gold nanoparticles is supported by report by Weerakkody et al. that pHLIPvar3 internalises within 30 - 50 ms, much faster than Wt-pHLIP which internalises in approximately 40 seconds [176]. Contrasting how the size of the particles affects pHLIP-mediated transduction has proven difficult. For instance, the pH-resolved uptake of pHLIPvar3-Au^{13}-RubpySS resulted in a flow cytometry luminescence signal from cells treated at pH 7.4 was 70% of the luminescence intensity from cells treated at pH 6.5, whereas for pHLIPvar3-Au^{100}-RubpySS the mean luminescence intensity from cells treated at pH 7.4 was

88% of the mean luminescence intensity from cells treated at pH 6.5. For Wt-pHLIP-labelled particles the opposite was seen, where the percentage of flow cytometry luminescence intensity for pH 7.4 samples relative to pH 6.5 samples for pHLIP-Au^{13}-RubpySS and pHLIP-Au^{100}-RubpySS were 78% and 65%, respectfully. As pHLIP's pH-dependent uptake has been shown to be inversely proportional to pH rather than an on/off switch [204], the measured uptake will be sensitive to small pH differences between experiments and this must be remembered when interpreting results.

3.2.3 Assessing the Effect of labelled-AuNP Treatments on Cell Viability using the 3-(4,5-Dimethyl-2-thiazolyl)-2,5-diphenyl-2H-tetrazolium bromide (MTT) Reduction Assay

To understand the effect of pH and nanoparticle internalization on HeLa cell viabilities, the 3-(4,5-Dimethyl-2-thiazolyl)-2,5-diphenyl-2H-tetrazolium bromide (MTT) reduction assay was performed on a variety of treated cells. This colormetric assay provides an assessment of enzymatic activity within cellular mitochondria. The assay utilises a membrane-permeable dye which is reduced by mitochondrial succinate dehydrogenase into a blue formazan product precipitate. The formazan product is soluble in DMSO, permitting liquid state UV/Vis absorption measurements where the stronger the absorbance, the greater cell viability.

In short, HeLa cells were cultured in 12-well plates, grown to 60% confluency and then treated with particles or buffers. At the end of the treatment, cells were washed twice with phosphate buffered saline, and treated with the MTT dye (final concentration of 0.5 mg ml^{-1}). The MTT protocol was performed on untreated cells to provide a negative control, and the absorption of all treated samples were expressed as percentages relative to the absorbance of the negative control, which was arbitrarily set to 100%. Additionally, a positive control for each dataset was also prepared where cells were treated with Triton-X100 (an ionic detergent utilised to induce cell death) prior to the assay.

Fig. 3.32 shows the relative cell viabilities of HeLa cells treated with Tyrodes buffers pH 5.0, 6.0, 6.5, 7.4 & 8.3. along with accompanying live cell phase contrast images showing cellular morphologies of all treated and untreated samples. Cell samples treated within the higher pH range 6.5 - 8.3 exhibited no statistically significant viability measurements to that of the negative control. Cells treated at lower pH values pH 5.0 - 6.0 displayed reduced mitochondrial activity, and therefore reduced viability. This is consistent with time-resolved treatments of HeLa cells at pH 5.0 and 7.4 where cells treated at pH 5.0 saw a strong initial increase in luminescence, but was significantly reduced at longer time points (Fig. 8.27, appendix). The phase contrast image of cell samples treated at pH 5.0 indicate a slightly less dense cell monolayer, however the cells were still adopting spread morphologies, and did not appear to have any visual signs of compromised viabilities different to the negative control, or in any way similar to the positive control. Phase contrast images of the positive control showed a significantly depleted monolayer of spherical cells detaching from the coverslip. For all other cell samples, the cell density does not visually appear to differ from the negative

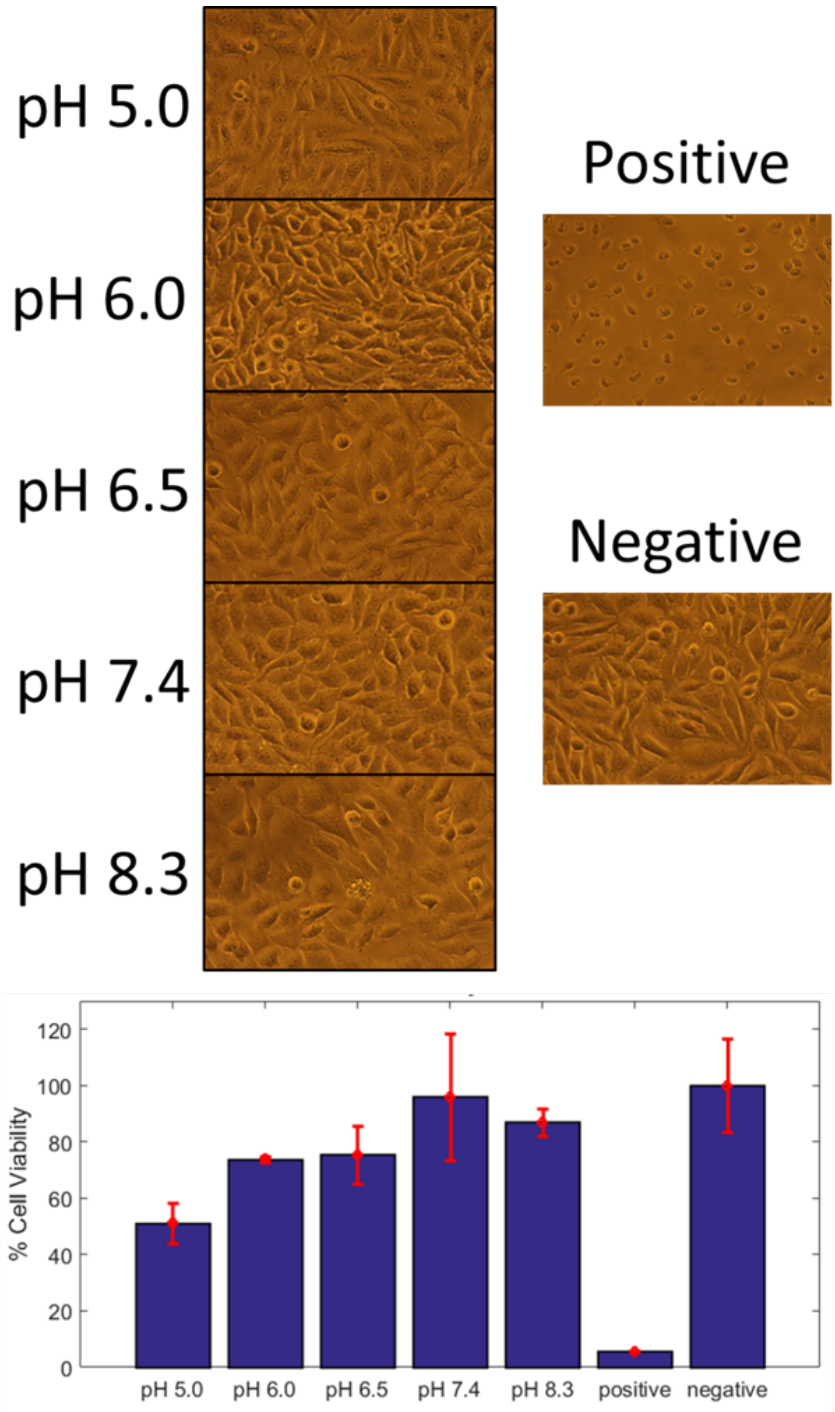

Figure 3.32: MTT colorimetric assay showing the effect of pH on cell viability. HeLa cells were incubated in Tyrodes buffers (0.08 mM, pH 6.5 or 7.4) for 2 hours at 37°C. Mean data points calculated from 3 biological repeats, and are presented with ± one standard deviation unit.

control, where all cells appear to be spread onto the bottom of the well, and integrated into a tightly-packed cell monolayer.

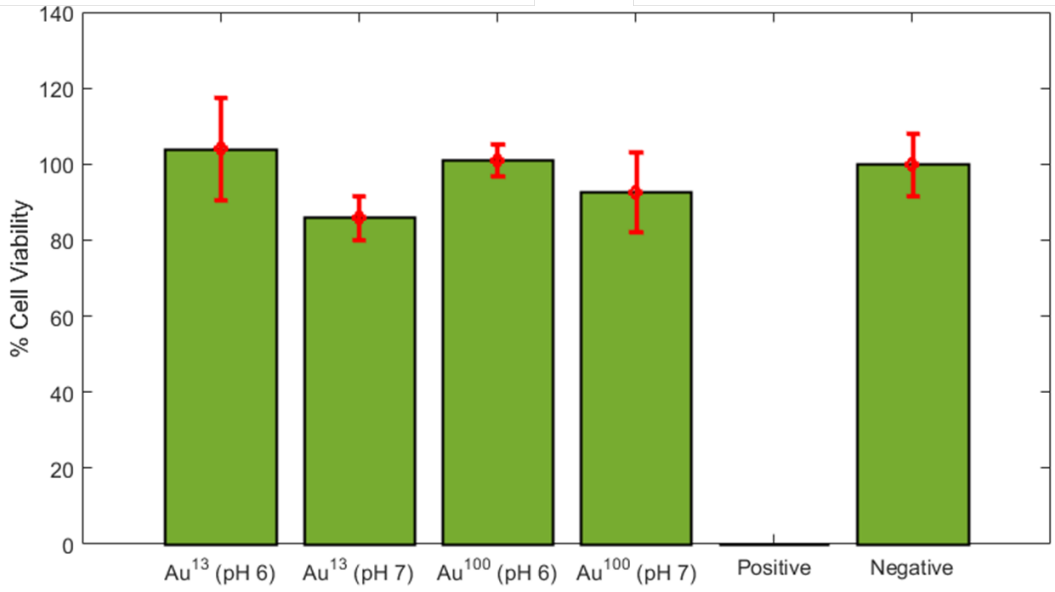

Figure 3.33: MTT colorimetric assay of HeLa cells treated with pHLIP-Au^{13}-RubpySS (1 nM) and pHLIP-Au^{100}-RubpySS (8 pM) in Tyrodes buffers (0.08 mM, pH 6.5 or 7.4) for 2 hours at 37°C, contrasted against untreated cells (Negative Control), cells treated with Triton X-100 (Positive Control) and cells treated with 10% Water in DMEM. Mean data points calculated from 3 biological repeats, and are presented with ± one standard deviation unit.

The effect of pH-dependent pHLIP-$Au^{13\&100}$-RubpySS internalization on HeLa cell viability was analysed by MTT assay. HeLa cells were plated into a 24-well plate, permitted to adhere and proliferate for 24 hours before dosing with labelled-Au^{13} and labelled-Au^{100} nanoparticles at pH 6.5 or 7.4 for two hours at 37°C. Fig. 3.33 shows the absorbance measurements of HeLa cells subjected to a pH-resolved treatment of pHLIP-$Au^{13\&100}$-RubpySS followed by the MTT dye. All treated samples show strong mitochondrial function comparable to that of untreated cells (100%). The only statistically significant difference found in this experiment existed between all treated samples and the positive control (Tukey HSD, $p < 0.01$ in all cases). This points to the conclusion that pH-resolved treatment with pHLIP-$Au^{13\&100}$-RubpySS particles for two hours at 37°C does not compromise cell viability, and therefore cell viability does not appear to be a contributor to the pH-dependent uptake reported in earlier sections.

The effect of pH-dependent pHLIPvar3-$Au^{13\&100}$-RubpySS internalization on HeLa cell viability was analysed by MTT assay. HeLa cells were plated into a 24-well plate, permitted to adhere and proliferate for 24 hours before dosing with labelled-Au^{13} (1 nM) and labelled-Au^{100} (8 pM) nanoparticles in Tyrodes solutions (0.08 mM, pH 6.5 or 7.4) for two hours at 37°C. Fig. 3.34 shows the absorbance measurements of HeLa cells subjected to a pH-resolved treatment of pHLIPvar3-$Au^{13\&100}$-RubpySS followed by the MTT dye. All treated samples show strong mitochondrial function comparable to that of untreated cells (100%). The only statistically significant difference found in this experiment existed between all treated samples and the positive control (Tukey HSD, $p < 0.01$ in all cases). This points to the conclusion that pH-resolved treatment

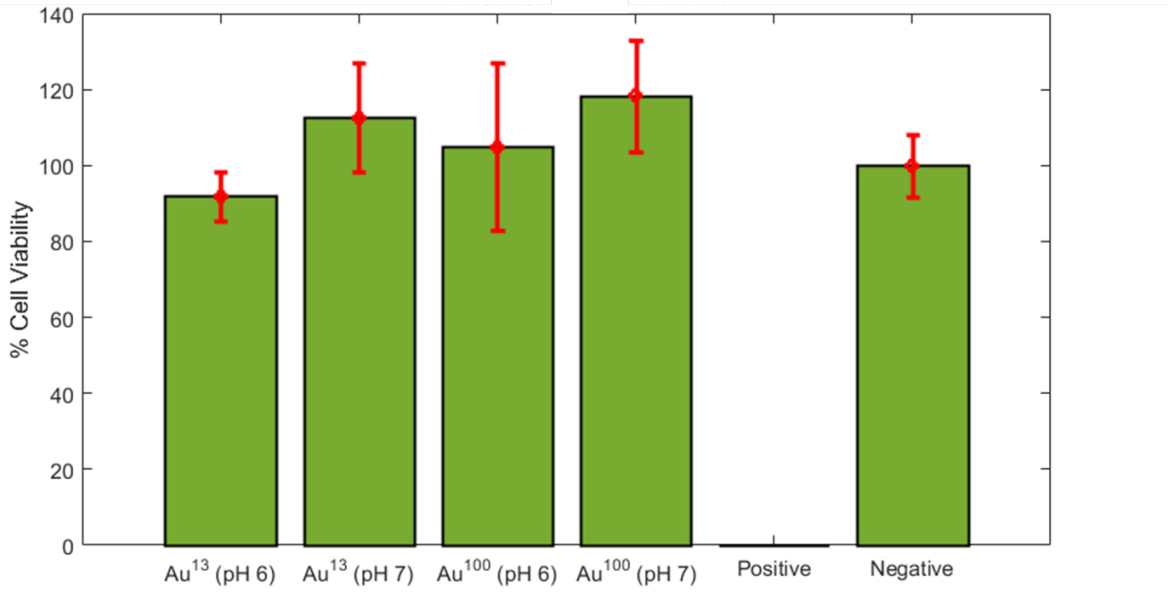

Figure 3.34: MTT colorimetric assay of HeLa cells treated with pHLIPvar3-Au^{13}-RubpySS (1 nM) and pHLIPvar3-Au^{100}-RubpySS (8 pM) for 2 hours in Tyrode's buffers (0.08 mM, pH 6.5 or 7.4) at pH 6.5 or 7.4 at 37°C. Mean data points calculated from 3 biological repeats, and are presented with ± one standard deviation unit.

with pHLIPvar3-$Au^{13\&100}$-RubpySS particles for two hours at 37°C does not compromise cell viability, and therefore cell viability does not appear to be a contributor to the pH-dependent uptake previously reported.

This experiment in conjunction with MTT analysis of pHLIP-$Au^{13\&100}$-RubpySS-treated HeLa cells, and previously reported MTT analysis of Zonyl-labelled gold nanoparticles [96] indicate that cellular internalization of labelled gold nanoparticles does not affect cell mitochondrial activity, promoting the use of gold nanoparticles as inert scaffolds for cargo delivery.

3.3 Conclusions

In this Chapter the pH-dependency of labelled-AuNP internalization into HeLa cells was reported. The viabilities of all treated cells were analysed using a mitochondrial viability assay, and the colloidal stability of labelled nanoparticles within the buffers was also investigated.

The multimodal potential of these labelled-AuNPs was demonstrated, where flow cytometry and light microscopy provided direct and indirect measurements of nanoparticle internalization, indirectly through detection of RubpySS luminescence and directly through detection of gold nanoparticle scattering. Nanoparticle internalization was confirmed using confocal optical sectioning and quantified where possible. Transmission electron microscopy then provided a spatial assessment of pHLIPvar3-Au^{13}-RubpySS nanoparticles internalized by HeLa cells, and ICP-MS analysis confirmed that the gold concentration of treated cells corroborated

with flow cytometry luminescence data. This demonstrated that collecting the luminescence of surface bound lumophore is an effective and accurate measure of nanoparticle internalization, and can be used at high throughput in flow cytometry, or to study functional internalization using live cell imaging.

Labelled-Au^{100} nanoparticles provided advantages over labelled Au^{13} nanoparticles as they provided a means to more easily quantify uptake within light microscopy where individual particles could be visualized, and provided information on cell granularity within flow cytometry side scatter experiments. For example, cells treated with pHLIP & pHLIPvar3-labelled Au^{13}NPs did not show increased cell granularity during the course of the nanoparticle treatment, however for pHLIP & pHLIPvar3-labelled Au^{100}NPs there was a very distinct increase in measured side scatter as a function of treatment length. The relationship between the flux of light scattered by an spherical particle is proportional to r^6, where r = particle radius [242]. When this scattering potential is applied to 13 & 100 nm gold nanoparticles, this proportional relationship results in a scattering intensity ratio of 1: ≈200,000 for 13 nm:100 nm particles. For smaller particles, luminescence detection is orders of magnitude more sensitive than scattered light detection, and therefore provides a better indication of small nanoparticle internalization into HeLa cells. Conversely, cytometry measurements of all HeLa cell treatments with labelled-Au^{100}NPs resulted in an increase of scattered light flux, indicating that side scatter measurements have far greater sensitivity when detecting light scattered by labelled-Au^{100}NPs. Cells treated with Zonyl-labelled Au^{13} and Au^{100} nanoparticles exhibited increased cell granularities as a function of treatment time, and confocal reflection imaging of Zonyl-Au^{13}-RubpySS indicated the formation of large aggregates within the cells indicating the nanoparticles are no longer stable once internalized. Although the use of Au^{100}NPs often rendered easier measurement and quantification of AuNP internalization it is important to highlight the importance of using smaller nanoparticles too. Firstly it is useful that this work demonstrates that the pHLIP peptides mediate delivery of a range of different size nanoparticles so that the photothermal efficiency of different sized nanoparticles can be investigated. Secondly, as the long term aims of this work are to develop phohotothermal & photodynamic therapeutic agents it is useful to study particles that are smaller than nuclear pores to permit particles to bypass the nuclear membrane more easily easily target the nanoparticles towards cell nuclei in order to develop more effective therapeutics.

The peptide that showed the most promising use as a pH-sensitive, delivery agent was pHLIPvar3, where the pHLIPvar3-Au^{13}-RubpySS and pHLIPvar3-Au^{100}-RubpySS particles exhibited pH-dependent uptake into HeLa cells under physiological conditions as demonstrated by flow cytometry, confocal microscopy & ICP-MS. pHLIP-labelled particles did not show pH-dependent uptake under physiological conditions, however when cold treatments were performed, pH-dependent uptake was observed on account of sufficiently slowing endocytotic mechanisms, again demonstrated by flow cytometry, microscopy & ICP-MS. Zonyl labelled AuNPs did not exhibit pH-dependent uptake, indicating that the efficiency of HeLa cell endocytotic uptake is not pH-dependent within the region of pH 6.5 - 7.4.

Transmission electron microscopy of HeLa cells treated with pHLIPvar3-Au^{13}-RubpySS revealed that

internalized nanoparticles were still monodisperse, and treatment at pH 7.4 appeared to show a greater concentration of particles adhered to cellular membranes, with a few examples of particles internalized into cell vesicles. Treatment at pH 6.5 resulted in far fewer examples of particles adhered to plasma membranes, and more examples of internalized particles were found where there were examples of particles confined to vesicular compartments, and free within the cell cytosol.

Viability assessments indicated that neither the buffer nor any particle sample imposed any noticeable cytotoxic effects on HeLa cervical adenocarcinoma cells during the two hour time course, however it was noticed that treatment of the cells at 4°C induced a decrease in cell viability as a function of treatment duration. Crucially, treatment of the cells within the pH range 6.5 - 7.4 did not result in a pH dependent viability, however treatment of cells as low as pH 5.0 rendered cells less viable, with reduced mitochondrial function along with a less dense monolayer of cells.

3.4 Future Work

The environment that a gold nanoparticle encounters while within a cell's microenvironment, and while being uptaken is a complex one. The effects of colloidal stability on the uptake of gold nanoparticles are not presently clear. Stability of the colloid is heavily dependent on the surfactant, and thus affects the proteins that assemble a corona around the particles. Further study should involve a pH-resolved study of the cellular uptake of labelled-AuNPs with varied polarity, hydrophobicity, charge & particle size. Flow imaging of labelled-AuNPs during the addition of serum proteins or cell extracts is potentially a reasonable place to start. Development of pHLIP variants that maintain AuNP monodisersity within cell microenvironments and during transduction may also be an effective method in studying the effect of colloidal stability during internalization.

Additionally, although the chosen incubation times and concentrations used within the treatment did not result in a compromise of cell viability, a comprehensive analysis of a wide concentration range and incubation times is important to develop deeper knowledge of the interactions between these particles and cells. The retention time of these labelled-AuNPs within cells has also not been touched on in this work, which would also be useful to build a fuller picture of their interactions.

The next step within particle labelling would be to target cell nuclei or mitochondria. Peptides such as the nuclear localisation sequence (NLS) and RGD peptide have been used to target cargoes towards cell nuclei [115]. That would be the next step to develop the application of these particles as delivery vessels.

3.5 Experimental

3.5.1 Chemicals and Reagents

pHLIP (AAEQNPIYWARYADWLFTTPLLLLDLALLVDADEGTC(thiopyridyl)G), kpHLIP (AAEQNPIYWARYAKWLFTTPLLLLKLALLVDADEGTC(thiopyridyl)G) and pHLIPvar3 (ACDDQNPWRAYLDLLFPTDTLLLDLLWC) were synthesised by Peptide Synthetics, Southampton, UK and were dissolved in 5% DMF in phosphate buffered saline. Cell culture buffers, were prepared using tablets or powders purchased from Sigma Aldrich, and sterilised for cell culture use by either autoclaving or injection through 0.22 μm syringe filters.

3.5.2 Preparation of cells for Flow Cytometry/Fluorescence-Activated Cell Sorting (FACS)

Prior to treatment, cells were plated into a 12-well culture plate and allowed to grow to approximately 60% confluency. Cells were then washed with buffers before being treated with particles in a Tyrodes buffer(0.08 mM, pH 6.5 or 7.4), for a series of incubation times upto three hours. After treatment was complete, the supernatant from each well was removed and each well was washed with PBS (0.1 M, 0.5 mL) twice before being trypsinised at 37°C for 10 minutes. Particles were then spun down at 1500 rpm for 10 minutes, the supernatant removed, and redispersed in of PBS (0.1 M, 1 mL). Cell suspension was transferred to a FACS tube before analysis. for all samples, the parameters of Forward Scatter, Side Scatter, and far red luminescence were measured (488 nm excitation, emission >620 nm). 15,000 events were recorded for each sample.

3.5.3 Preparation of cells for Confocal Microscopy

Preparation for Fixed Cell Imaging

For fixed cell imaging, glass coverslips were sterilised using absolute ethanol (rinsed and left to dry) and placed into the wells of 6-well culture plates. $5x10^4$ cells were then seeded into each well of the 6-well culture plates on top of glass coverslips and allowed to grow to confluency for 24 hours. Before treatment, media from each well was removed and cells were washed twice with the media used in the seeding experiment, before being sequentially treated with the media and particles. After treatment, medium was removed and cells were washed with PBS (2 mL x 2) and then paraformaldehyde (4% in 0.1M PBS, 2 mL) was added and cells were left for 10 minutes at room temperature. Fixative was removed and cells were washed with PBS (2 mL x 2). Cells were then mounted onto glass microscope slides, using a drop of non-fluorescing Hydromount to maintain sample hydration, before sealing the slide with nail varnish. Slides were left to dry in a cold room and were imaged within a few days.

Preparation for Live Cell Imaging

For live cell imaging, $5x10^4$ cells were then seeded into the well of a MatTek(R) glass-bottom microscopy dish and allowed to grow to confluency for 24 hours. Before treatment, media from each well was removed and cells were washed twice with the media used in the seeding experiment, before being sequentially treated with the media and particles. After treatment, medium was removed and cells were washed with PBS (2 mL x 2) and then PBS (2 mL) was added before transferring samples to the microscope for acquisition.

3.5.4 Preparation of cells for Inductively Coupled Plasma - Mass Spectrometry

HeLa cells were cultured as per above and treated as per the relevant experiment. After treatment was complete, the supernatant from each well was removed and each well was washed with PBS (0.1 M, 0.5 mL) twice before being trypsinised at 37°C for 10 minutes. Particles were then spun down at 20,000 rpm for 10 minutes, the supernatant completely removed taking care not to disturb the cell pellet, before being allowed to dissolve overnight in 200 μL of ultrapure aqua regia (3:1 volumetric ratio of hydrochloric and nitric acid). Post dissolution, samples were diluted in ultrapure nitric acid (2700 μL of a 4% solution) prior to analysis.

3.5.5 Preparation of cells for Transmission Electron Microscopy

After treatment with nanoparticles, cell samples were fixed with a solution of Paraformaldehyde (4%) and Glutaraldehyde (2.5%) in phosphate buffered saline for two hours, prior to sectioning and mounting onto formvar-coated copper grids. Samples were then imaged on a JEOL JEM-1200EX and a JEOL JEM-2100 electron microscope each fitted with a Tungsten electron source and a Gatan camera.

3.5.6 Analysing Cell Viability of Nanoparticle-treated HeLa cells

After treatment of HeLa cells with labelled-AuNPs, the media from each well was withdrawn and cells were washed with PBS (500 μl) and replaced with 3-(4,5-Dimethyl-2-thiazolyl)-2,5-diphenyl-2H-tetrazolium bromide (0.5 mg/ml) in complete media (90% by volume), and were reincubated at 37°C for 2 hours. After the incubation, media was removed and DMSO (500 μl) was added to solubilise the formazan product. The plate was rocked for 15 minutes in the dark before the absorption at 590 nm was recorded against a DMSO blank.

Chapter 4

The effect of Cellular Glutathione on the uptake of Labelled-Gold Nanoparticles into HeLa Cervical Cancer Cells

4.1 Introduction

The aim of this work was to study the dependency of labelled-AuNP (pHLIP-Au^{100}-RubpySS, pHLIPvar3-Au^{100}-RubpySS & Zonyl-Au^{100}-RubpySS) uptake efficiency and stability as a function of intracellular glutathione concentration, the cell's most prevalent reducing agent. As demonstrated in previous chapters, the cellular uptake of labelled-Au^{100}NPs has proved easier to quantify with microscopy techniques than with labelled-Au^{13}NPs, and the larger particles also provide sensitive measurements within techniques such as side scatter analysis within flow cytometry. For these reasons, this study focuses exclusively on labelled-Au^{100}NPs and labelled-Au^{13}NPs were excluded from study. The peptide-labelled AuNP constructs are bound together by dative covalent bonds between thiol or dithiol groups and the gold nanoparticle surface, the Zonyl-labelled AuNPs are held together by electrostatic interactions and therefore may be effected differently by the cell's reducing environment. These gold–sulfur bonds are sensitive to a reducing environment so particular attention was paid to whether the "strength" of the cells reducing environment affected the efficiency of nanoparticle uptake, and also how the nanoparticle coating changed depending on the strength of its reducing environment.

4.1.1 Glutathione

Glutathione (GSH, Fig.4.1) is the most prevalent low-molecular-mass reducing agent within plants and animals [243]. It acts as the eukaryotic cells thiol "redox buffer" on the front line of the cells defensive response to oxidative stress, which is defined as an imbalance between pro-oxidant species (for example, reactive oxygen species, ROS) and anti-oxidant species (for example, GSH) [244]. GSH is an antioxidant responsible for equilibrating the cells thiol/disulphide redox potential, and does so without exhibiting the toxicity associated with cysteine [245].

Glutathione is a tripeptide, comprised of L-glutamate, L-cysteine and glycine and many of GSH's important reactions, that give GSH its biological function, involve its thiol group on its cysteine residue. GSH's biological function involves participation in bio-synthesis of iron-sulphur proteins in the mitochondria [246, 247, 248, 249], along with detoxification of metals, xenobiotic resistance, apoptosis, redox signalling and sulphur storage and transport [243, 250, 251] of which many are catalyzed by various GSH peroxidases, GSSG reductases and GSH transferases [252].

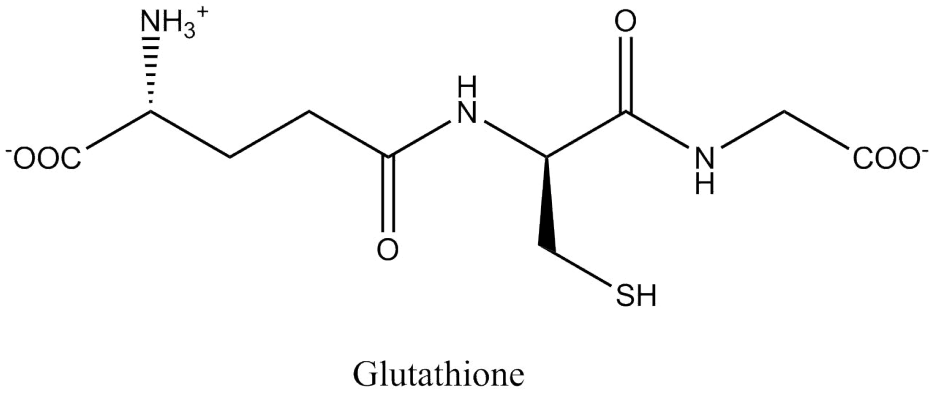

Figure 4.1: Structural formula of Glutathione (GSH)

GSH is able to donate an electron from the thiol group of its cystine residue to contribute a reducing effect on its environment. The newly oxidised GSH will then combine with another oxidised GSH molecule to form glutathione disulfide (GSSG, Fig. 4.2) which is rapidly recycled back into GSH by NADPH-dependent glutathione reductases in key organelles as well as in the cytosol, rendering the species abundantly in its GSH form apart from within the endoplasmic reticulum, where it predominantly exists in its GSSG form [253]. The reducing nature of GSH, and the oxidising nature of GSSG, mean that it is involved in practically all major biological processes, including regulation of cell proliferation [254], signal transduction [255, 256], gene expression [257] and apoptosis [258]. Literature in recent years has focussed on the biochemical, physiologic, and toxicological effects of GSH [259, 260, 261, 262] along with medical and clinical aspects [263, 264, 265].

4.1.2 Glutathione Production

GSH is synthesised from L-glutamate, L-cysteine and glycine, in a two step process facilitated by two ATP-dependent enzymes. Step 1 is the production of γ-glutamylcysteine, catalysed by the enzyme glutamate cysteine ligase (GCL), and is believed to be the rate determining step of the overall process of GSH formation because very low γ-glutamylcysteine concentrations have been measured [266]. The second, and more rapid step of GSH production is catalysed by glutathione synthase, and the factors that govern and regulate this process are reported in work by Griffith [267]. Intracellular GSH concentration is generally considered to be in the range of 1 - 11 mM, levels that greatly exceed free cysteine concentration [268, 269].

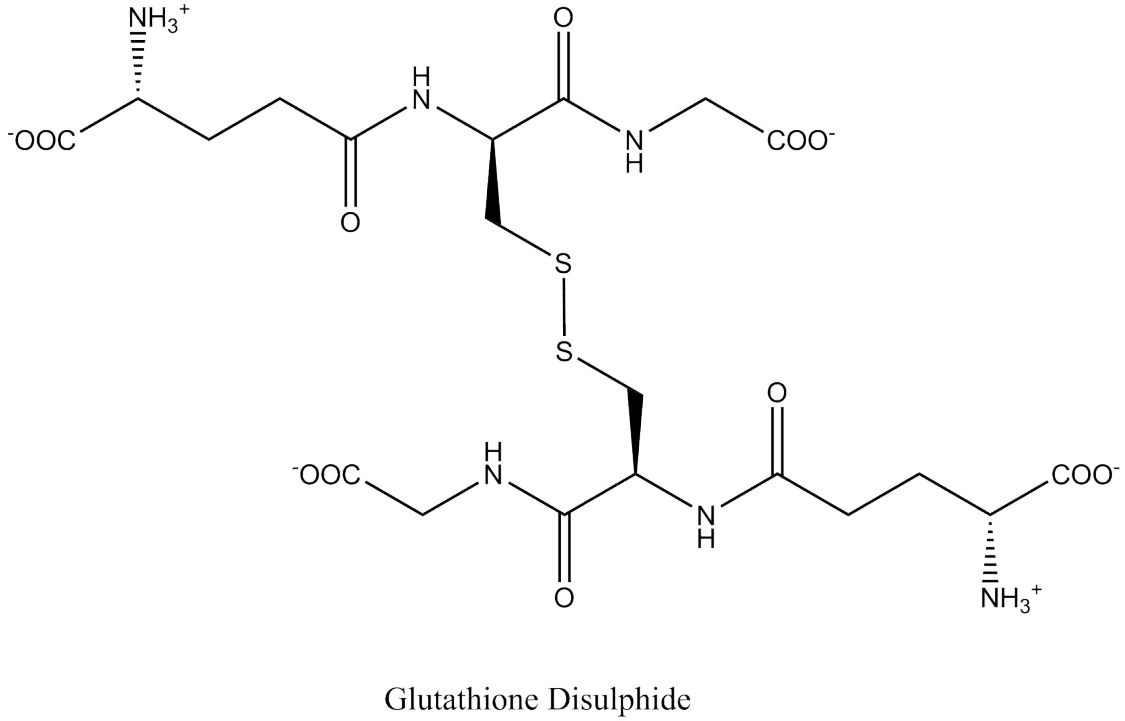

Glutathione Disulphide

Figure 4.2: Structural formula of Glutathione Disulfide (GSSG)

4.1.3 Cellular Compartmentalisation of Glutathione

After synthesis within the cytosol of mammalian cells, GSH is transported to various intracellular compartments such as the mitochondria, nucleus and endoplasmic reticulum where GSH adopts compartment-specific functions essential to the needs of each organelle [270, 271]. 70% of the cells GSH pool is abundant in the cytoplasm, with the remaining 10 - 30% of GSH differentially distributed to the nucleus, mitochondria and endoplasmic reticulum [272].

Cytosolic Glutathione

GSH is first synthesised in cellular cytosol, in a tightly regulated two step process, catalysed by γ-glutamylcysteine and glutathione synthetase, respectively [273]. After synthesis, GSH is partitioned between the cells nucleus, mitochondria and endoplasmic reticulum, while 70% of the cells GSH reservoir remains in the cytosol. Bachawat et al. have compiled a comprehensive review of the different classes of intracellular GSH transporters [274]. This review studied a wide class of trasporters that included GSH importers from the extracellular environment, to GSH effluxers. Hgt1p was the first high affinity GSH transporter identified, and was done so from the yeast S cerevisae [275]. The uptake of 'intact' GSH into mammalian cells has been debated [276]. There is evidence that intact GSH is uptaken using specific transporters [277, 278, 279, 280], and that the uncoupled GSH constituent amino acids/peptides are also imported independently, as evidenced by inhibition of the degrading enzyme γ-glutamyl transpeptidase [281, 282] Cell nuclei sequester GSH, and it is believed that nuclear GSH accumulation plays an important role in the cell cycle and cell proliferation. It has been proposed that GSH is also found in significant quantities in the endoplasmic reticulem and extracellular compartments, adopting its oxidised form, GSSG [253, 283]

Nuclear Glutathione

The nucleus is the cell's central kernel, a membrane-walled organelle that plays host to most of the cell's genetic material, which controls cell activities by regulating gene expression. In the nucleus, GSH plays an important role in maintaining protein sulphyldryls that sustain DNA repair and expression [284], while also playing a contributive role in DNA synthesis by donating a proton into the ribonucleotide reductase-catalysed reduction of riboxynucleotides into deoxyribonucleotides [285]. Until recently, it was widely believed that GSH could freely diffuse between the cell nucleus and cytoplasm through the nuclear pores. Nuclear concentration of GSH is strongly dependent on the cells current phase in the cell cycle. Recent work has shown that in the cells growth phase (G1), where the biosynthetic activities of the cell which were previously slowed down in its mitotic phase, begin to resume their high rate. Early in this phase, GSH accumulation begins [272]. An increase in GSH concentration has been shown to be necessary for the cell to move from the G1 phase into the S phase of the cell cycle [286], but it has also been shown that addition of GSSG to plant cells resulted in an arrest of the cell cycle in the G1 phase [287]. Additionally, the depletion of cytoplasmic GSH upon nuclear recruitment of GSH is consistent with an oxidative process occurring in the early stages of the G1 phase [288, 289]. A model (Fig. 4.3) for GSH partitioning between the nucleus and cytoplasm was proposed by Vivancos et al. [290].

Mitochondrial Glutathione

The primary function of a cells mitochondria is the transduction of electrons through the electron transport chain (ETC) to generate adenosine triphosphate (ATP), the cells molecular energy carrier, essential for subsequent signalling cascades. A small portion of electrons generated from the ETC are however transferred

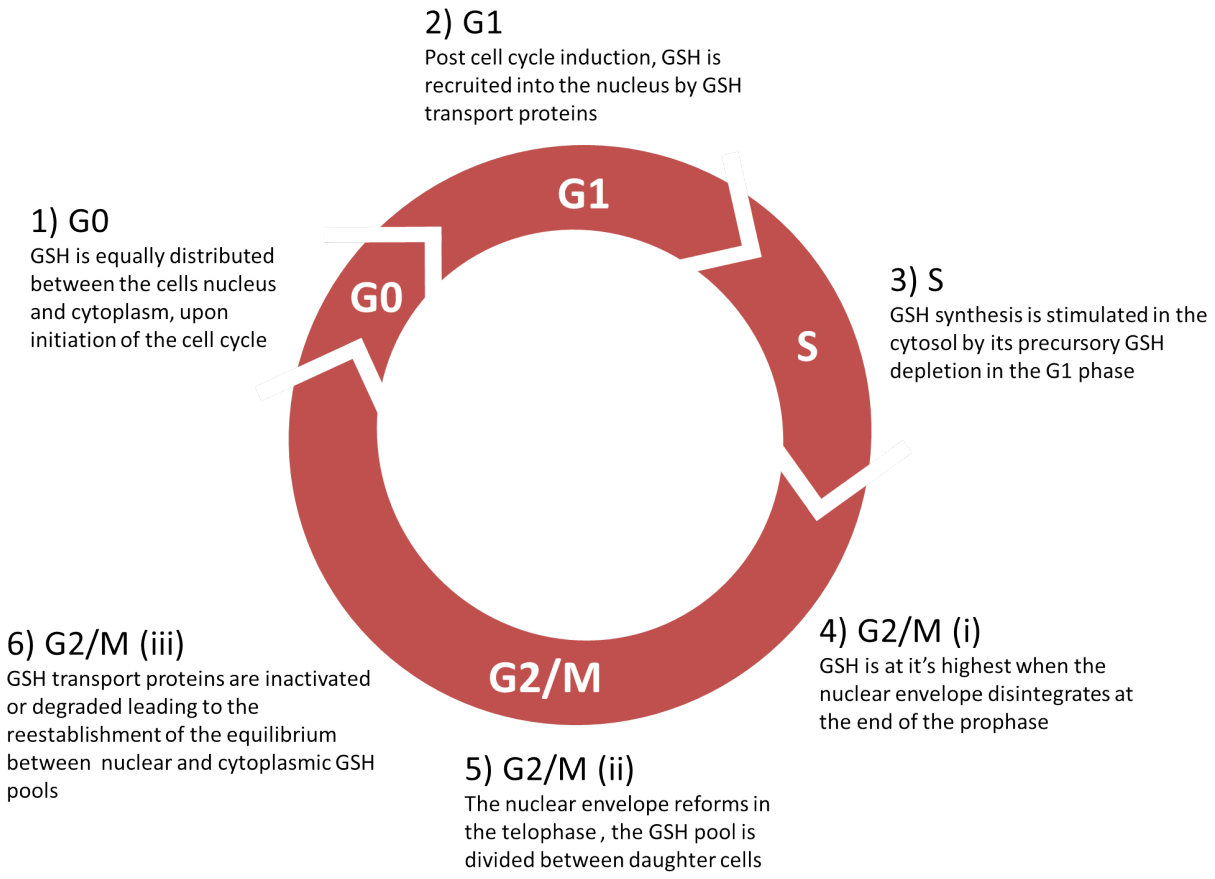

Figure 4.3: GSH partitioning between the cell nucleus and cytopasm during the cell cycle. Adapted from [290] and derived from [291, 292, 293]

directly to molecular oxygen, generating a variety of reactive oxygen species (ROS) and reactive nitrogen species (RNS). To maintain an equilibrium of ROS & RNS production, the mitochondria uses its arsenal of antioxidants each with is own target specificity [270]. In the mitochondria, GSH exists in its reduced form and constitutes a minor fraction of the GSH pool at around 10 - 15%. However, taking into account mitochondrial volume versus cytosolic volume, there are a number of reports that the concentration of GSH within mitochondria is similar to that in the cytosol (10 - 14 mM) [270, 271, 294, 295].

4.1.4 Measuring Glutathione Concentration

There are a variety of established methods of the measuring the concentration of GSH & GSSG. Methods have even become sophisticated enough to measure both together and even the measurement of GSH concentration within intracellular organelles. The oldest and most common methods of measuring GSH concentration are using fluorimetric assays [296] which have been further developed to measure both the oxidised (GSSG), and reduced (GSH) forms as per the method of Hissin and Hilf [297]. Whole tissue GSH concentrations can be measured by enzyme-catalysed procedures, one such method is diazo coupling before recorded absorption [298] and another utilises a fluorometric method based upon the conjugation of GSH with Monochlorobimane which has also been used to label free GSH in whole tissues [299]. A method for determination of GSH:GSSG ratios has been reported by Asensi et al [300] using HPLC, where standard solutions and N-ethylmaleimide were used to prevent reduced GSH oxidation. Additionally, a novel dual-readout method based on gold nanoparticles surface plasmon resonance and förster resonance energy transfer, where the readout could be measured using luminescent or calorimetric detection [301]. Methods have also been reported for measuring the GSH concentration of intracellular compartments, for instance conjugation of GSH with strongly electron-scattering gold nanoparticles has enabled the visualisation of GSH distribution via transmission electron microscopy [302]. Further, imaging fluorophores such as ThiolTracker Violet (registered trademark of Invitrogen) conjugates to intracellular thiol-functionalised biomolecules, providing an assessment of the cells overall redox environment which is detectable on a multitude of luminescence detection platforms [303].

4.1.5 Glutathione and AuNPs

Glutathione has been identified as a useful release tool for nanoparticle-bound cargoes, due to the markedly greater concentration of intracellular GSH (1 - 11 mM [268, 269]) over extracellular GSH (2 μM) [304]. Indeed, glutathione-mediated release of fluorescent cargoes from gold nanoparticles has been reported [305] and this approach has even yielded clinical success [306]. Verma et al reported controlled release of the enzyme β-galactosidase from positively charged trimethyl-ammonium-functionalized mixed monolayer protected clusters mediated by intracellular GSH, and that control of β-galactosidase release could be tuned by the structure of the monolayer [307]. It was also shown that release of β-galactosidase was specific to the presence of the thiol group of GSH by studying a non-thiol bearing analogous tripeptide. Han et al then demonstrated that the same monolayer protected clusters encapsulate DNA through complementary electrostatic interactions, resulting in transcription inhibition of the T7 RNA polymerase. However, intracellular GSH mediated controlled release of the DNA resulted in efficient transcription [308]. The GSH-mediated release of anticancer drugs from AuNP surfaces has also been reported [309].

Additionally, the uptake of labelled gold nanoparticles has been reported to have a direct effect on GSH concentration, as per Gao et al. who reported an early AuNP-induced depletion of cytosolic GSH in HL7702

Human Liver cells that ultimately exacerbated cellular apoptosis [310]. Gold nanoparticles have also been used as chemosensors for glutathione. Sudeep et al reported selective detection of cysteine and glutathione at micromolar concentrations, by exploiting the interplasmon coupling of gold nanorods [311].

Gold nanoparticles functioned with glutathione have also been studied as possible alternatives to poly ethylene glycol (PEG) coated AuNPs. Coating AuNPs with PEG helps reduce renal complications and morbidity, caused by some other thiol-functionalised AuNPs such as the widely used AuNP-cap tiopronin, however PEG-coating results in a compromised cellular uptake efficiency [312]. However, Simpson et al demonstrated improved biocompatibility and retention of GSH-coated AuNPs compared with PEG-coated analogues [313].

4.2 Results and Discussion

This section is divided into three subsections. *Section i)* describes the methodology of adjusting HeLa cell intracellular GSH concentration to prepare [GSH]-modified HeLa cells and reports final concentrations of intracellular GSH after application of the protocol. *Section ii)* reports the cell viability assay that was performed on [GSH]-modified HeLa cells. And in *section iii)*, the internalization of labelled, luminescent gold nanoparticles into HeLa cells was reported as a function of intracellular [GSH] concentration. The cellular uptake of labelled-AuNPs was studied using a variety of techniques including Flow cytometry (FACS), Confocal Microscopy and Inductively Coupled Plasma Mass Spectrometry (ICP-MS). Alongside which, the colloidal stability of labelled gold nanoparticles is studied as a function of glutathione concentration, using the spectroscopic techniques of UV/Vis spectroscopy and Electrophoretic Light Scattering.

4.2.1 Quantfication of GSH concentration in HeLa cells treated with Buthionine Sulfoximine and N-Acetyl Cysteine by fluorimetric Assay

In order to establish the effect of glutathione on the uptake of AuNPs, protocols for modifying intracellular GSH concentration of live HeLa cells needed to be established and tested. Vos et al. [314] demonstrated that treatment of HeLa cells with buthionine sulfoximine resulted in a depletion of intracellular GSH. Green et al [315] later reported that treatment of Mouse Embryonic Fibroblasts with buthionine sulfoximine (BSO) resulted in differential depletion of GSH from the nuclei, mitochondria and cytoplasmic compartments, with the cytoplasmic region suffering the biggest reduction in GSH concentration, and the nuclear pool being the most resistant to GSH depletion. The cytotoxicity of treating cells with BSO was evaluated using concentrations up to 1000 μM with negligible cytotoxic effects up to this concentration. Han et al [316] established a method of increasing intracellular GSH by pretreating HeLa cells with 2.5 mM of N-Acetyl Cysteine (NAC), a pro-oxidant species. They reported that NAC prevented Arsenic Trioxide (ATO)-induced apoptosis of HeLa cells by replenishing depleted GSH, although they couldn't rule out the possibility that NAC was directly scavenging ATO.

In this work, HeLa cells were treated with an aqueous solution of NAC (2.5 mM in 90% complete media) to increase, and aqueous solutions of BSO (100 μM and 500 μM in 90% complete media) to decrease the cells intracellular glutathione concentration. These were performed alongside a water control (10% H_2O in complete media) representing unmodified GSH concentration, and to account for the effects (if any) that dilution of complete media would have on the experiment. To measure the concentration of [GSH]-modified HeLa cells, the fluorimeteric assay protocol of Hissin and Hilf [297] was used. GSH has been shown to react with o-phthalaldehyde (OPT) at pH 8.0 to form a fluorescent product, that excites at 350 nm and emits at 420 nm [296].

Cells were treated with the [GSH]-precursors in 90% complete media for 24 hours, and subsequently cells were washed with PBS and the assay was performed. (Fig. 4.4) shows a plot of GSH concentration from solutions of known GSH concentration (calibration data) together with GSH concentrations from [GSH]-modified HeLa cells. A three-way ANOVA was performed ($p = 0.004$) indicating that each treatment bore significantly different results, and a Tukey HSD test indicated a statistically significant ($p < 0.01$) difference in fluorescence between cells treated with BSO and NAC, however not so for untreated and NAC-treated, or untreated and BSO treated.

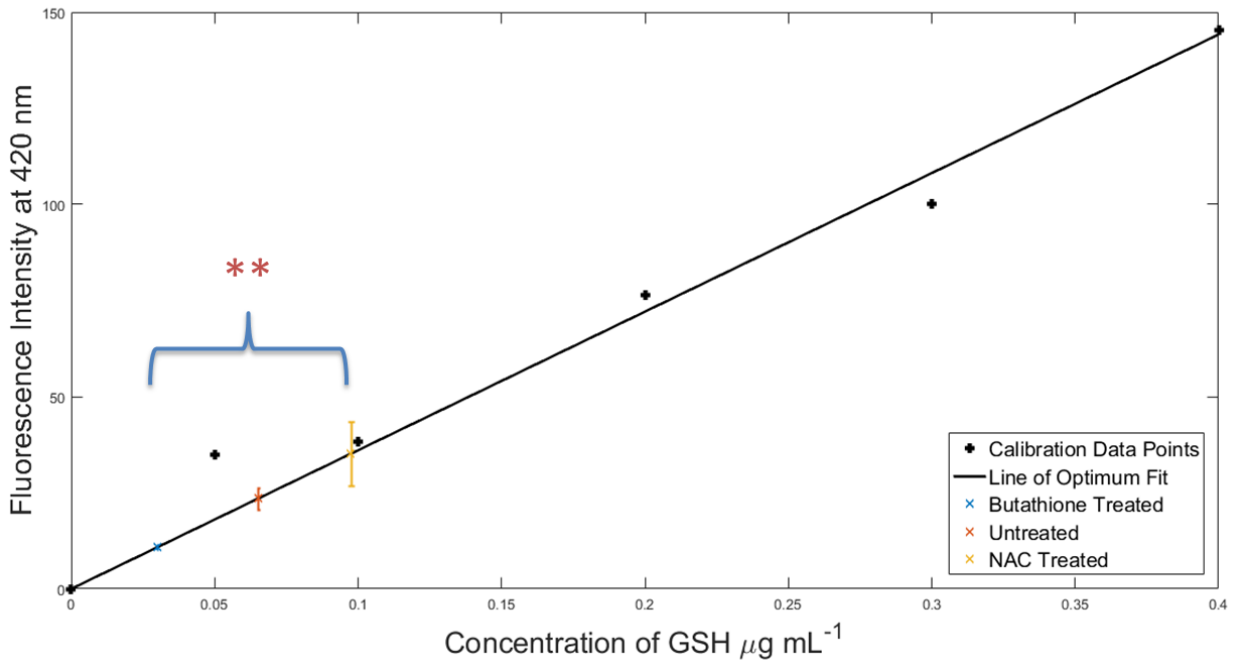

Figure 4.4: Results from fluorescence assay for determining GSH concentration. Fluorescence intensities of all references were plotted against known concentrations of GSH (0 - 0.4 μg ml^{-1}), an origin-intersecting line of optimum fit was plotted through the reference data points, and mean sample fluorescence was plotted along the line to calculate GSH concentration within the samples. Included in the plot are p values indicating statistical significance between the datasets, as measured by the Tukey HSD test. Data composed of three biological repeats, presented with ± one standard deviation unit, and Tukey HSD test data was also included, where statistically significant p-values of <0.05, <0.01, <0.001 are indicated by *, **, and ***, respectively.

The results indicated that treatment with N-acetyl cysteine provided approximately double the concentration of GSH to 0.1 μg ml^{-1} from 0.06 μg ml^{-1} for untreated cells, and treatment with buthionine sulfoximine depleted the cells GSH concentration to (0.03 μg ml^{-1}).

4.2.2 Measuring Cell viability of [GSH]-modified HeLa Cells by MTT Assay

In this section, the resulting cell viabilities of HeLa cells that had undergone modulation of intracellular GSH concentration were assessed. It has been reported that cellular depletion in GSH has been shown to increase oxidative stress [317, 318, 319], and therefore it was crucially important to study whether our modulation of HeLa cell GSH concentration had resulted in similar oxidative stress. Cell viabilities were measured by the 2.4 3-(4,5-dimethyl-2-thiazolyl)-2,5-diphenyl-2H-tetrazolium bromide (MTT) reduction assay.

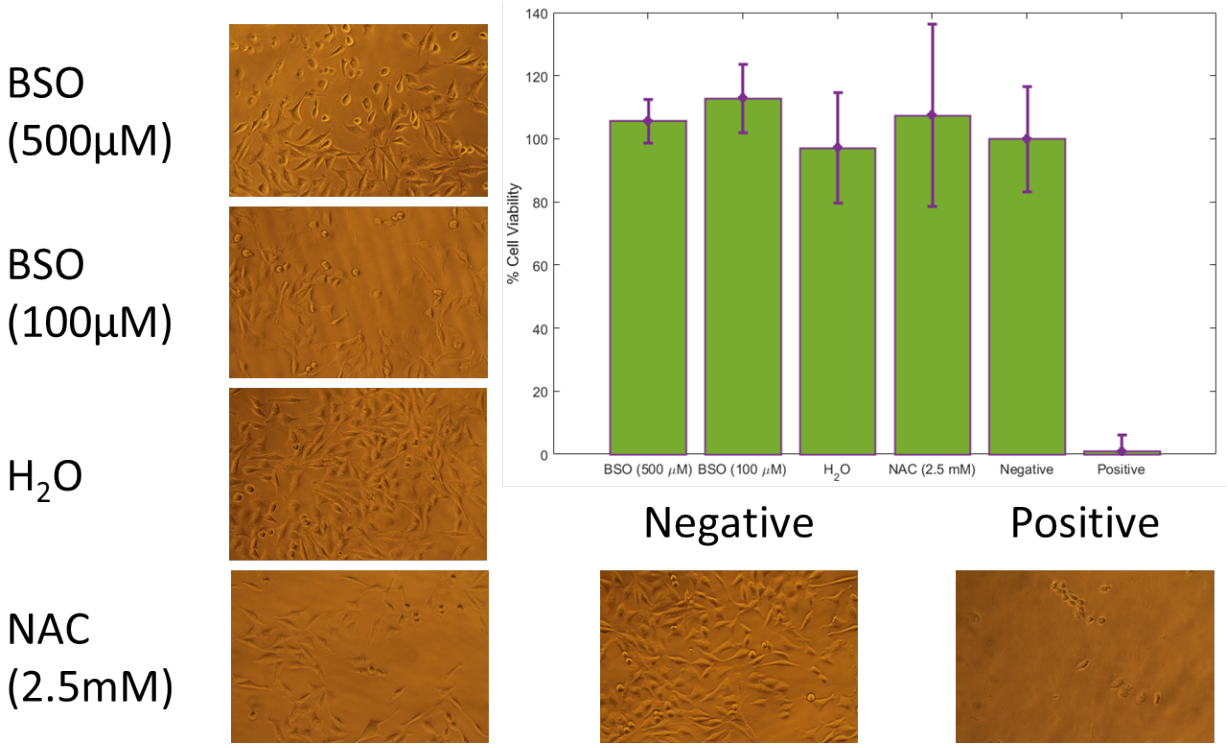

Figure 4.5: MTT of [GSH]-modified HeLa cells treated with GSH precursors (NAC 2.5 mM, H_2O, BSO 100 μM, & BSO 500 μM in 90% complete media) for 24 hours before being loaded with MTT precursor dye for two hours at 37°C. Absorbance was recorded at 590 nm, and samples were normalised to the negative control of untreated HeLa cells in complete media. Cells treated with 0.5% Triton X-100 in DMEM were used as a positive control. Phase contrast microscopy images included for each sample. Data composed of three biological repeats, presented with ± one standard deviation unit, and Tukey HSD test data was also included, where statistically significant p-values of <0.05, <0.01, <0.001 are indicated by *, **, and ***, respectively.

As per the GSH assay, cells were treated with aqueous solutions of [GSH] precursors (NAC 2.5 mM, H_2O, BSO 100 μM, & BSO 500 μM) in 90% complete media for 24 hours at 37°C. Cells were subsequently twice washed with PBS before the assay was performed. The percentage cell viability of HeLa cells treated

with [GSH] precursors for 24 hours is shown in Fig. 4.5, along with phase contrast images of the cells that underwent each treatment. The data series consists of 3 independent duplicates with errors bars that represent mean values plus/minus one standard deviation unit. For all treatments no statistically significant difference was observed between cells treated with [GSH]-precursors and the untreated negative control. Phase contrast images correlate this conclusion by showing very similar confluencies and cellular morphologies. Contrasted to the positive control, where cells were treated with a mild detergent prior to treatment with the MTT dye, all [GSH]-precursor treatments showed statistically significant greater percentage viability ($P < 0.01$ in all cases), with the phase contrast images of the positive control showing depleted confluency with remaining cells adopting spherical morphologies characteristic of dying HeLa cells, indicating no cytotoxic response resulting from [GSH] modification of HeLa cells. It has been reported by Connor et al.[320] that gold nanoparticles are uptaken by human cells without resulting in acute toxicity, and work in previous chapters on the cellular uptake of labelled-AuNPs did not reveal a statistically significant cytotoxic response by gold nanoparticle internalization, at the chosen concentrations and for the chosen incubation lengths.

4.2.3 Measuring the uptake of functionalised AuNPs into [GSH]-modified HeLa Cells by Flow Cytometry

Flow cytometry was used to provide the main indications of labelled-Au^{100}NP uptake into [GSH]-modified HeLa cells having previously shown that luminescently labelled-Au^{100}NPs provide sensitive measurements within side scatter and luminescence detection.

Additionally, in order to assess colloidal stability when the labelled-Au^{100}NPs encounter GSH, GSH was titrated into a stirred solution of labelled-AuNPs whilst monitoring the colloid by UV/Vis absorption spectroscopy. As outlined previously, gold surface plasmon resonance is an oscilation of gold nanoparticle surface electrons in response to stimulation by light at their natural frequency. This behaviour manifests as a large band with a gaussian profile in the colloid's UV/Vis absorption spectrum. SPR band structure characteristics such as absorbance, SPR λ_{max}, and Full With at Half Maximum (FWHM) are sensitive to interparticle distance [85] where upon aggregation, the band broadens, decreases in intensity and undergoes a large bathrochromic shift, typically on the order of $>$ 20 nm.

Treatment of [GSH]-modified HeLa Cells with pHLIP-Au^{100}-RubpySS

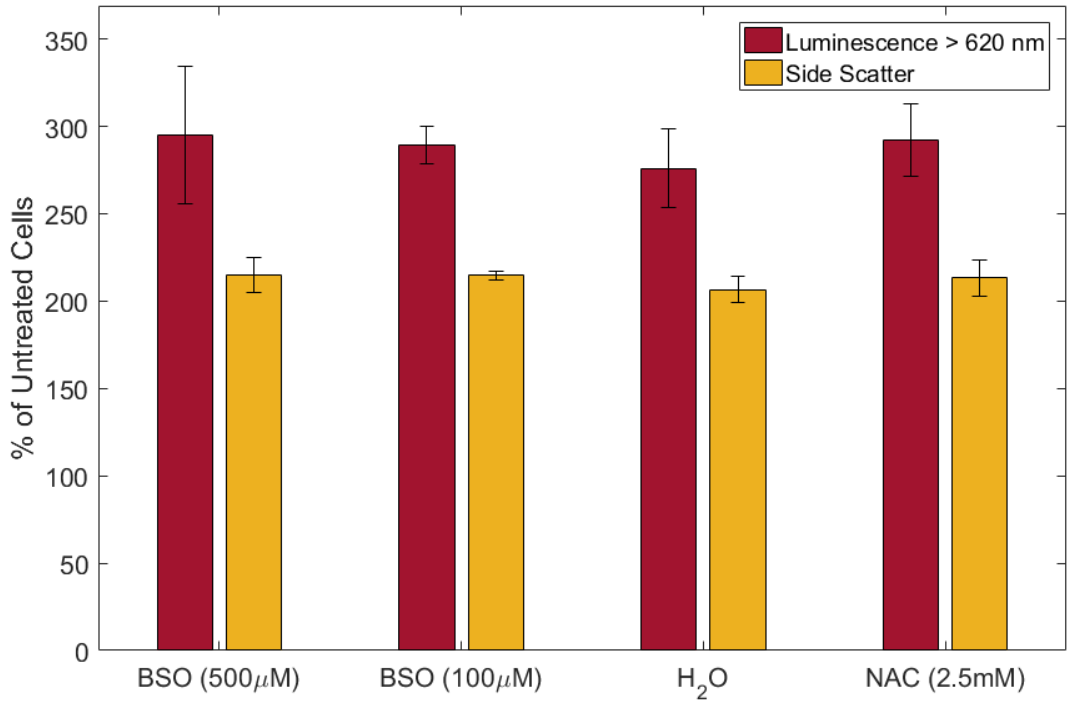

Figure 4.6: Flow cytometry of HeLa cells treated with a precursor (NAC (2.5 mM), H_2O control, BSO (100 μM) or BSO (500 μM)) before being treated with pHLIP-Au^{100}-RubpySS (8 pM) for two hours in Tyrodes buffer (0.08 mM, pH 6.5) at 37°C. Side scatter and luminescence resultant from irradiation at 488 nm. Data composed of three biological repeats, presented with ± one standard deviation unit, and Tukey HSD test data was also included, where statistically significant p-values of <0.05, <0.01, <0.001 are indicated by *, **, and ***, respectively.

Fig. 4.6 shows mean % luminescence and side scatter of [GSH]-modified HeLas treated with pHLIP-Au^{100}-RubpySS (8 pM) in Tyrodes buffer (0.08 mM, pH 6.5) for 2 hours at 37°C. Cells treated with these particles did not show a statistically significant difference in luminescent or scattered light signal, as determined using Tukey HSD and ANOVA ($p = 0.79$, calculated from luminescence data) tests. As shown in Fig. 8.45 when GSH is titrated into pHLIP-Au^{100}-RubpySS, the SPR band of the gold nanoparticles decreases its absorbance in accordance with dilution but the SPR undergoes a small bathochromic shift of 3 nm, characteristic of surface functionalisation. The SPR band of pHLIP-Au^{100}-RubpySS undergoes a bathochromic shift of 4 nm, decreases in intensity by 0.06 (31% decrease of SPR absorbance). Small changes in SPR position can be attributed to surface functionalisation of the gold surface, and not with nanoparticle aggregation. The SPR band ceases to shift after 2 mM of GSH has been added, which supports this decision and is also consistent with the small increase in mean colloidal hydrodynamic diameter from 92 ± 30 nm to 134 ± 54 nm upon the addition of GSH (24 μM) to pHLIP-Au^{100}-RubpySS (Fig. 8.45). The pHLIP peptide is bound to the gold nanoparticle via a disulphide thiopyridyl unit, a unit likely less susceptible to GSH-mediated reduction.

Treatment of [GSH]-modified HeLa Cells with pHLIPvar3-Au^{100}-RubpySS

Fig. 4.7 shows mean % luminescence and mean % scatter from HeLa cells treated with pHLIPvar3-Au^{100}-RubpySS (8 pM) for 2 hours in Tyrodes buffer (0.08 mM, pH 6.5) at 37°C. In this experiment, [GSH] was shown to significantly affect both mean % cell scatter and mean % cell fluorescence, indicating that particles were uptaken more quickly into cells with higher intracellular GSH concentration, in a consistent trend across the four sample treatments. A Tukey HSD test on the luminesence data indicated a statistically significant difference between samples treated with BSO (100 μM and 500 μM) and samples treated with NAC ($p < 0.05$). The same analysis on the side scatter data indicated a statistically significant difference between samples treated with BSO (500 μM) and samples treated with H_2O ($p < 0.05$) and a strong statistically significant difference between samples treated with BSO (100 μM and 500 μM) and samples treated with NAC ($p < 0.01$). An analysis of variance (ANOVA) test provided a p value of 0.013 (calculated from luminescence data). It is also noteworthy that side scatter offered a more precise measurement, resultant from providing smaller standard deviations and resultantly a greater degree of statistical significancy between samples ($p < 0.01$) than luminescence measurements were able to. Additionally, UV/Vis absorbance measurements of the pHLIPvar3-Au^{100}-RubpySS indicated a reduction in surface plasmon resonance intensity, and a large bathochromic shift of 17 nm as a function of increasing GSH concentration (Fig. 8.45). This was corroborated by DLS measurements that showed significant particle aggregation as a function of GSH addition to the colloid (Fig. 8.49) where the hydrodynamic diameter of untreated particles increased dramatically upon the addition of 24 μM of GSH from 95 ± 26 nm to 759 ± 136 nm. Each pHLIPvar3 peptide is bound to the gold surface by a dative covalent bond from a single thiol group on the peptide's cysteine residue, this single thiol that anchors pHLIPvar3 to the gold surface is potentially more susceptible to reduction than the dithiol-attachment motif of pHLIP.

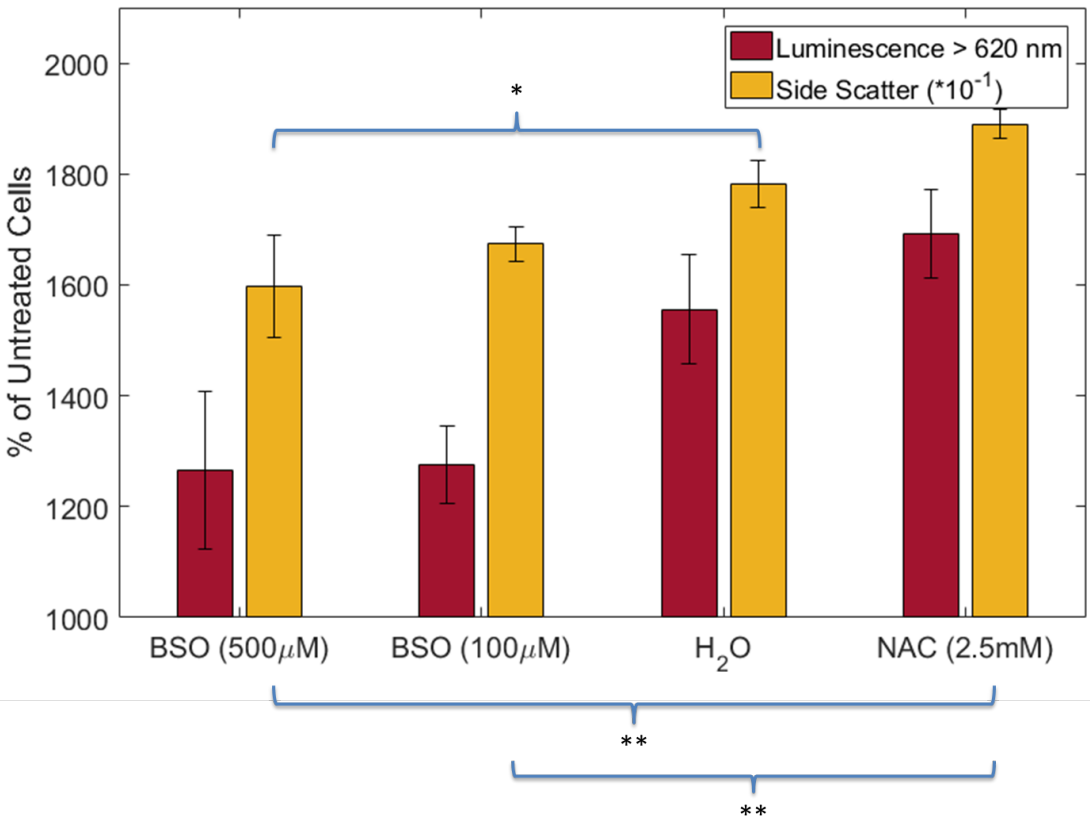

Figure 4.7: Flow cytometry of HeLa cells treated with a precursor (NAC (2.5 mM), H_2O control, BSO (100 μM) or BSO (500 μM)) before being treated with pHLIPvar3-Au^{100}-RubpySS (8 pM) for two hours in Tyrodes buffer (0.08 mM, pH 6.5) at 37°C. Side scatter and luminescence resultant from irradiation at 488 nm. Data composed of three biological repeats, presented with ± one standard deviation unit, and Tukey HSD test data was also included, where statistically significant p-values of <0.05, <0.01, <0.001 are indicated by *, **, and ***, respectively.

Treatment of [GSH]-modified HeLa Cells with Zonyl-Au^{100}-RubpySS

Fig. 4.8 shows % Luminescence and side scatter of [GSH]-modified HeLas treated with Zonyl-Au^{100}-RubpySS. Cells treated with these particles do not show a statistically significant difference in accumulation of Zonyl-Au^{100}-RubpySS as a function of GSH concentration, as determined using Tukey HSD and ANOVA ($p = 0.47$ calculated from luminescence data) tests. It is interesting to note that direct addition of GSH to Zonyl-Au^{100}-RubpySS in solution also yielded significant particle aggregation as shown by UV/Vis absorbance (Fig. 8.45) and by dynamic light scattering (Fig. 8.49). Upon a titration of GSH into Zonyl-Au^{100}-RubpySS, the SPR band of Zonyl-Au^{100}-RubpySS underwent a bathochromic shift of 11 nm and decreased in intensity by 0.11 (52% decrease of SPR absorbance). This large decrease in absorbance, and large bathochromic shift are strong indicators of nanoparticle aggregation. In addition, dynamic light scattering analysis of nanoparticle hydrodynamic diameter showed the mean colloidal diameter increased from 92 ± 28 nm to 422 ± 95 nm upon the addition of 24 μM of GSH. The Zonyl FSA fluorosurfactant contains a hydrophilic methylmethacrylate

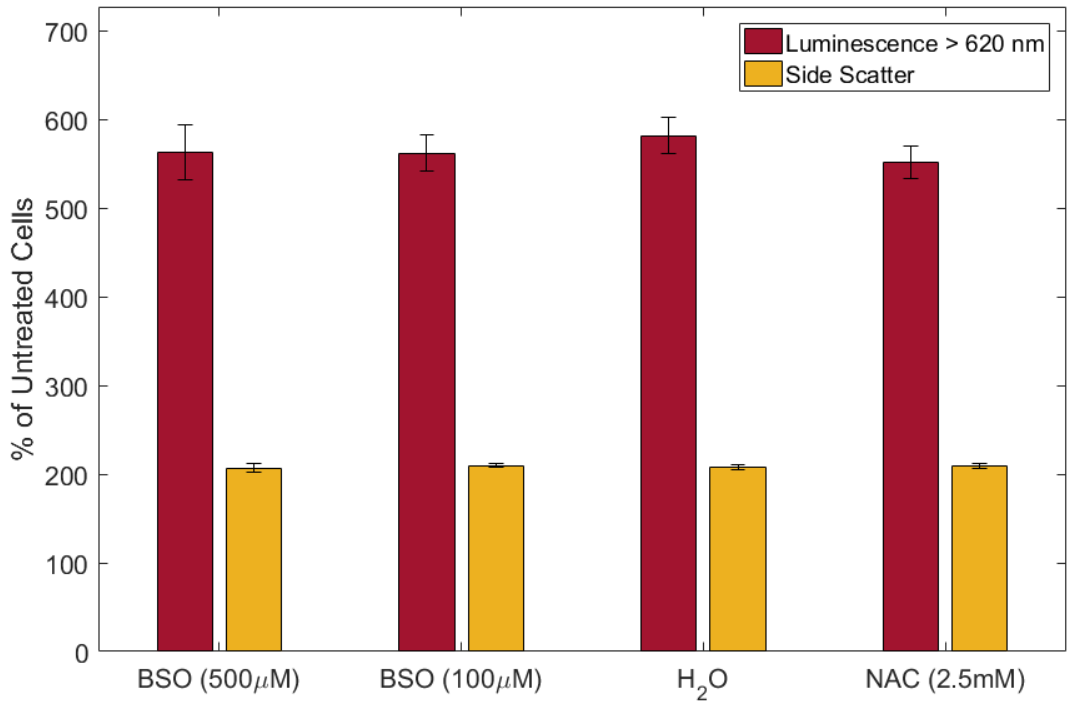

Figure 4.8: Flow cytometry of HeLa cells treated with a precursor (NAC (2.5 mM), H_2O control, BSO (100 μM) or BSO (500 μM)) before being treated with Zonyl-Au^{100}-RubpySS (8 pM) for two hours in Tyrodes buffer (0.08 mM, pH 6.5) at 37°C. Side scatter and luminescence resultant from irradiation at 488 nm. Data composed of three biological repeats, presented with ± one standard deviation unit, and Tukey HSD test data was also included, where statistically significant p-values of <0.05, <0.01, <0.001 are indicated by *, **, and ***, respectively.

head-group, and a hydrophobic perfluorinated alkyl chain, and it has been shown that it is the methacrylate head group that binds to the gold nanoparticle surface [96]. It is not yet known whether GSH's destabilisation of the Zonyl-Au^{100}-RubpySS colloid is resultant from displacement or charge effects.

Measuring the uptake of pHLIPvar3-labelled AuNPs into HeLa Cells by Confocal Microscopy

From the treatment of [GSH]-modified HeLa cells with pHLIPvar3-Au^{100}-RubpySS, it was interesting that higher [GSH] concentration equated to a stronger efficacy of nanoparticle internalization. It was therefore important to confirm these observations with additional techniques and investigate any differences in intracellular nanoparticle distribution. For this section, confocal microscopy was used to image optical sections of HeLa cells treated with pHLIPvar3-Au^{100}-RubpySS in order to find evidence of why [GSH] concentration is affecting nanoparticle uptake efficacy.

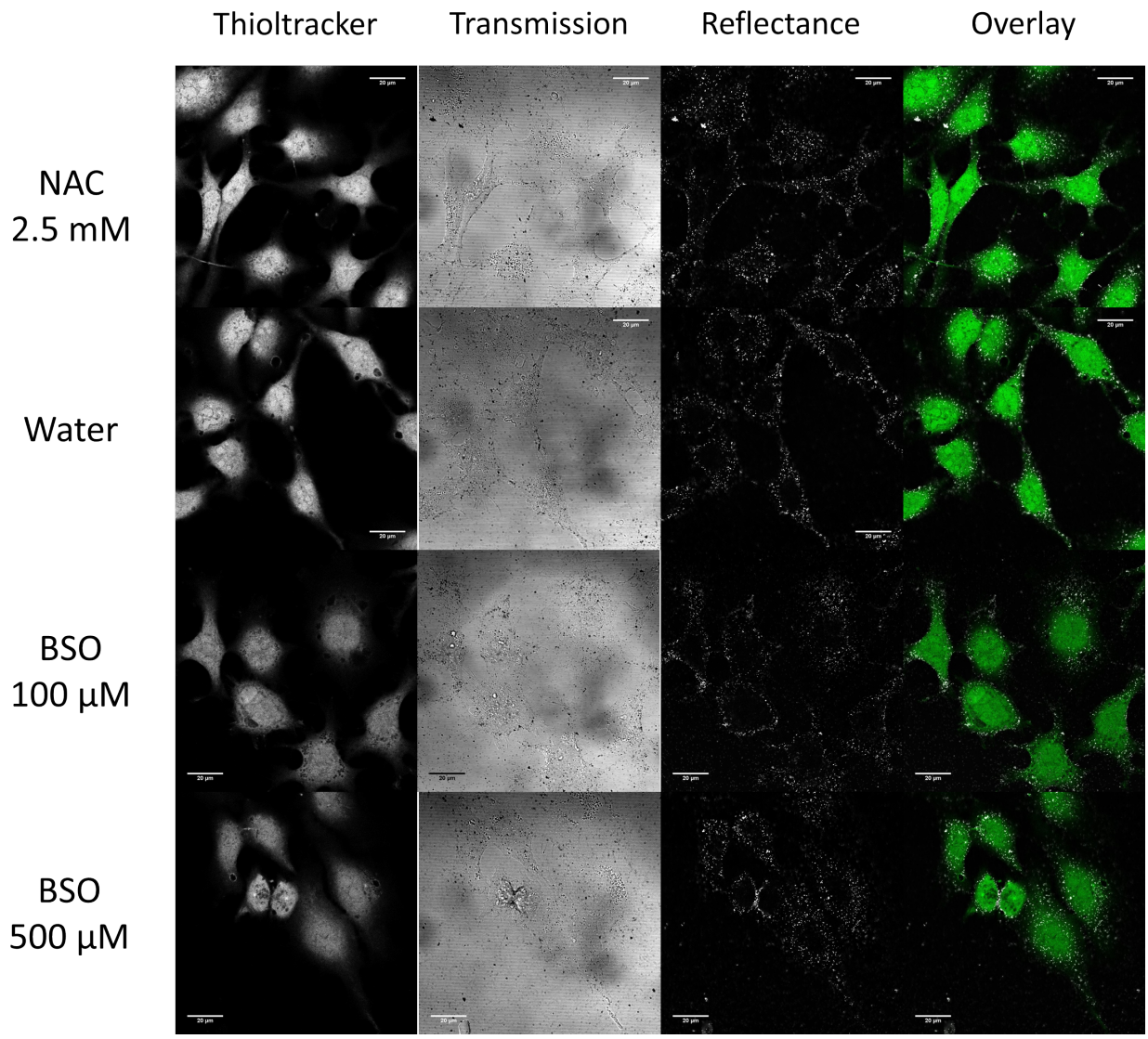

Figure 4.9: Confocal microscopy images of HeLa cells treated with a precursor (NAC (2.5 mM), H_2O control, BSO (100 μM) or BSO (500 μM)) before being treated with pHLIPvar3-Au^{100}-RubpySS (1 nM) for 2 hours at 37°C, pH 6.5. Cells were fixed in 4% paraformaldehyde in phosphate buffered saline for 10 minutes befre being treated with ThiolTracker^{TM} (10 μM for 10 minutes)

Fig. 4.9 shows confocal microscopy images of [GSH]-modified HeLa cells treated with pHLIPvar3-Au^{100}-

RubpySS (8 pM) for two hours in Tyrodes buffer (0.08 mM, pH 6.5) at 37°C. A high density of particles can be seen to have been internalized into each cell sample. As with previously reported confocal images of HeLa cells treated with pHLIPvar3-Au^{100}-RubpySS, particles appear to be evenly distributed throughout the cell cytosol while nuclear regions appear to be devoid of particles. Attempts were made to quantify ThiolTracker^{TM} intensity, as well as internalized nanoparticle density. Thioltracker^{TM} intensity was quantified by segmenting out the cells from the confocal images using the method outlined in Fig. 8.46. This provided a mask of the cell area, which was used to normalise the total intensity of Thioltracker^{TM} luminescence from that image to calculate area-weighted mean intensity values. Area-weighted intensities for each image of each sample were then normalised to the intensity of cells treated with the water (10% H_2O in complete media) precursor which was set to 100%. Fig. 4.11 shows the area-weighted relative luminescence of [GSH]-modified HeLa cells as a function of the [GSH]-modifying precursor. These area-weighted intensities indicate that the Thioltracker^{TM} luminescence trend across the four samples corroborates with the previously reported GSH assay, where NAC-treated cells are most luminescent, and BSO (500μM)-treated cells are the least luminescent. It is also apparent from the confocal images of the ThiolTracker^{TM} in BSO-treated HeLa cells that the most significant depletion of GSH occurs in the cytoplasmic regions of the cells, while the nuclear pools appear to remain more rich in GSH. This is consistent with the observations of Green et al. [315] who a reported a comparatively greater reduction in GSH from the cytoplasmic region than from the nuclear region of mouse embryonic fibroblasts.

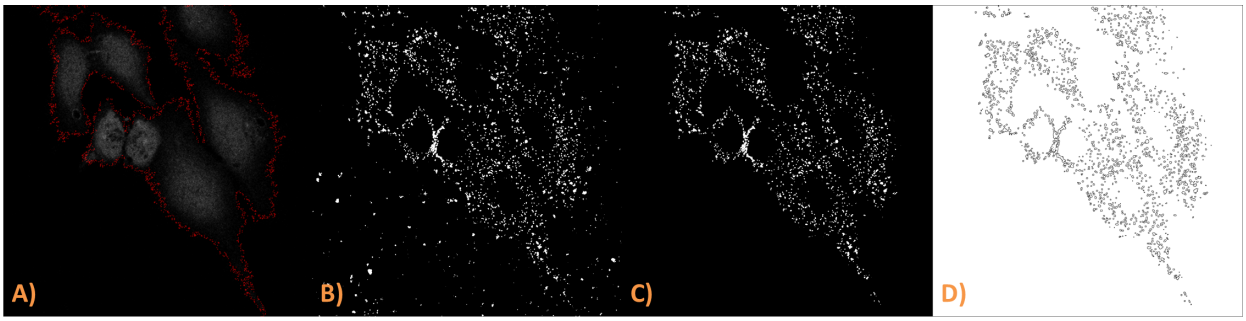

Figure 4.10: Image analysis procedure for quantifying internalized AuNPs. This example contains images of HeLa cells treated with a precursor (NAC (2.5 mM), H_2O control, BSO (100 μM) or BSO (500 μM)) before being treated with pHLIPvar3-Au^{100}-RubpySS (1 nM) for 2 hours at 37°C, pH 6.5. Cells were fixed in 4% paraformaldehyde in phosphate buffered saline for 10 minutes befre being treated with ThiolTracker^{TM} (10 μM for 10 minutes). Figure shows segmented GSH Image (A), Raw 488 nm reflection image (B), segmented 488 reflection image (C) and 'Analyse Particles' function image showing outlined nanoparticles (D).

The method for the quantification of nanoparticle uptake into treated-HeLa cells is documented in Fig. 4.10. For the first stage of segmentation, images of the ThiolTracker^{TM} distribution were thresholded using the Otsu method [235] and segmented in a process outlined within Fig. 8.46. providing an estimate of cell area and boundaries (Image A). This cell area mask was then applied to an image of nanoparticle reflection signal (Image B) and used to select only nanoparticle signal emanating from within cell regions (Image C). An outline of this image was then used for quantification (Image D) where results were expressed as the cell

area that a single nanoparticle occupies in μm^2.

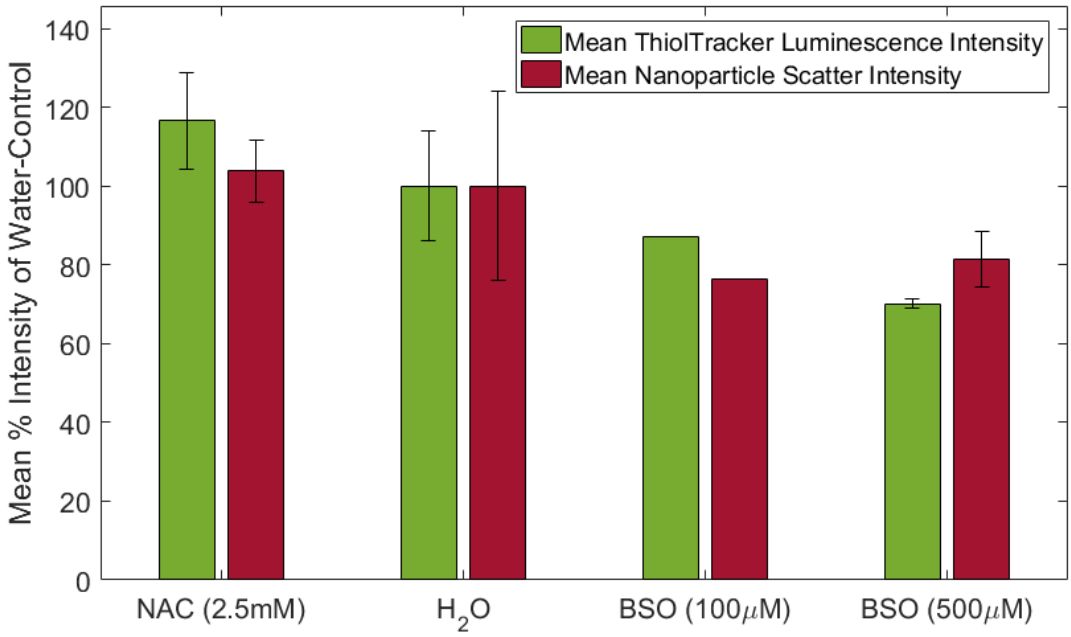

Figure 4.11: Mean % signal extracted from confocal microscopy images of HeLa cells treated with a precursor (NAC (2.5 mM), H_2O control, BSO (100 μM) or BSO (500 μM)) before being treated with pHLIPvar3-Au^{100}-RubpySS (8 pM) for 2 hours in Tyrode's buffer (0.08 mM, pH 6.5) at 37°C. Signals normalised to either the ThiolTracker^{TM} intensity, or nanoparticle reflection intensity of cells treated with 10% H_2O in DMEM for 24 hours followed by particles. The author would like to note that the intensities for BSO (100 μM)-treated cells consist of a single measurement, error bars represent ± one standard deviation unit.

Analysis of confocal microscopy images did not yield a statistically significant difference between nanoparticles internalized into HeLa cells as a function of intracellular GSH concentration. The approximate cell area per single Au^{100}NP for NAC-treated, BSO-treated (100 μM) & BSO-treated (500 μM) was 6.1 ± 0.9 μm^2, 6.6 ± 0.6 μm^2 & 6.5 ± 1.1 μm^2, respectively. Additionally, for each sample, the total intensities of the reflectance images were normalised to the total cell area for each image, and these values were plotted alongside ThiolTracker^{TM} luminescence in Fig. 4.11. Again, this method of relative quantification did not show statistically significant differences. As within Chapter 3, it is confidently reported that little internalization of labelled-AuNPs into cell nuclei has occurred. And therefore any nucleic areas within the images effectively skew the quantification as they are devoid of particles. Therefore while these measurements were performed to gain quantitative information from confocal images where possible, a separate step within the quantification method where segmented removal of nuclear regions from the cell mask must be performed to improve the accuracy of the calculation. Although this additional step would improve the calculation accuracy, it was not pursued in this work as the flow cytometry data already provides a more balanced and representative analysis of nanoparticle uptake.

Live cell confocal imaging was also performed after a 15 minute treatment of [GSH]-modified HeLa

cells with pHLIPvar3-Au^{100}-RubpySS. The experiment was designed to show whether a significant uptake difference could be spatially observed by studying an earlier time point in the treatment, as well as confirming that particles are internalized before chemical fixation. Fig. 8.48 (appendix) shows live cell microscopy images of [GSH]-modified HeLa cells treated with pHLIPvar3-Au^{100}-RubpySS (8 pM) in Tyrodes buffer (0.08 mM, pH 6.5) for 15 minutes at 37°C, where a significant density of nanoparticles can be seen within cytosolic regions of all treated cells. A significant difference in AuNP uptake was not observed at these time points, implying the differential accumulation of particles previously observed is likely resultant from accumulation over a longer period.

Measuring the uptake of pHLIPvar3-labelled AuNPs by Inductively-Coupled Plasma Mass Spectrometry

The uptake of pHLIPvar3-Au^{100}-RubpySS was repeated using ICP-MS as the measurement method, a technique which offers parts per trillion (ppt) sesitivity. In this experiment, pH 6.5 and pH 7.4 were directly compared, and standard solutions of 0, 50, 100, 250, 500 and 1000 ppb were used to calibrate the instrument for detection. Fig. 4.12 shows the absolute concentrations of gold detected by ICP-MS resulting from the uptake of pHLIPvar3-Au^{100}-RubpySS at pH 7.4. The uptake of particles at pH 7.4 shows a dependency on GSH concentration which appears to correlate with the cytometry-measured uptake of pHLIPvar3-Au^{100}-RubpySS at pH 6.5. The concentration of gold uptaken by cells treated at pH 6.5 was significantly above the calibration range of the mass spectrometer, therefore limited conclusions can be drawn from this dataset. The data is shown in supplementary Fig. 8.50 for reference.

Additionally, a flow cytometry study of the effect GSH imposes on the uptake pHLIPvar3-Au^{100}-RubpySS at pH 7.4 was also performed. In this experiment, cells were treated with particles (8 pM) in Tyrodes buffer (0.08 mM, pH 7.4) for two hours at 37°C, and prepared for flow cytometry using the normal protocol outlined in the chapter's experimental section. The % mean scatter & the % mean luminescence are shown in Fig. 8.44 in the appendix of this chapter. In this experiment, no statistically significant difference between the uptake of pHLIPvar3-Au^{100}-RubpySS was found across the GSH concentration range. However, due to the higher sensitivity of ICP-MS, it is expected that this technique is able to detect smaller mass changes than those visible using flow cytometry.

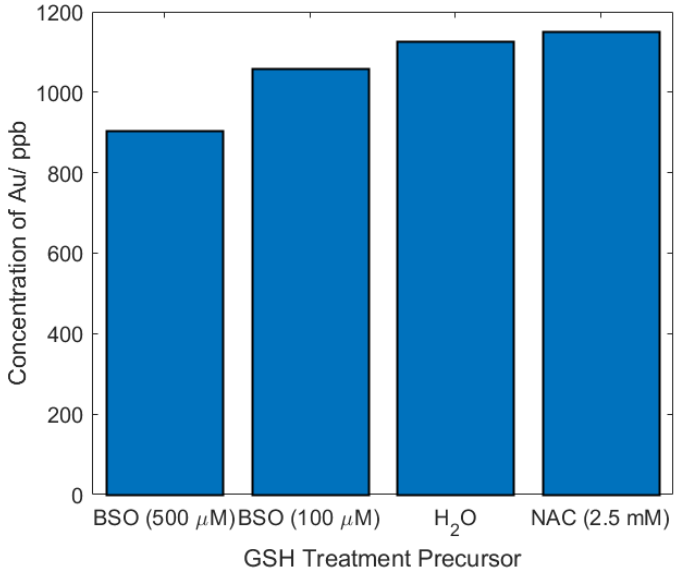

Figure 4.12: ICP-MS of HeLa cells treated with a precursor (NAC (2.5 mM), H_2O control, BSO (100 μM) or BSO (500 μM)) before being treated with pHLIPvar3-Au^{100}-RubpySS (8 pM) for two hours at 37°C in Tyrodes buffer (0.08 mM, pH 7.4).

4.3 Conclusions

A protocol was developed to prepare HeLa Cervical Adenocarcinoma cells with elevated or depleted concentrations of glutathione, and adjustment of intracellular GSH concentration was confirmed to be successful by GSH assay. It was then established that the treatment of HeLa cells with [GSH]-precursors did not yield a statistically significant effect on mitochondrial activity, and therefore cell viability, consistently with Green et al. [315]

The uptake of pHLIP-Au^{100}-RubpySS and Zonyl-Au^{100}-RubpySS into [GSH]-modified HeLa cells was not modulated by intracellular GSH concentration, as measured by Fluorescence-Activated Cell Sorting. However, pHLIPvar3-Au^{100}-RubpySS uptake into [GSH]-modified HeLa cells was more efficient when intracellular GSH concentration was greater, and results suggest that the effects of modifying GSH concentration and treatment pH may be additive, but this has yet to be proven. Zonyl-Au^{100}-RubpySS particles provided a control to measure the uptake of a non-thiol bound assembly, and GSH appeared to have no effect on particle uptake as expected.

The addition of GSH to pHLIPvar3-Au^{100}-RubpySS, pHLIP-Au^{100}-RubpySS and Zonyl-Au^{100}-RubpySS during the addition of glutathione, induces aggregation within pHLIPvar3-Au^{100}-RubpySS & Zonyl-Au^{100}-RubpySS particles, but has little effect on the stability of pHLIP-Au^{100}-RubpySS particles.

Initial results suggest that both pHLIPvar3's pH-dependent delivery mechanism and GSH's ability to destabilise the colloid is imposing an effect on the efficiency of nanoparticle internalization. This has raised questions over whether GSH cleaves pHLIPvar3 from the surface of the gold, and how doing so improves the

uptake efficiency of pHLIPvar3-Au^{100}-RubpySS.

4.4 Future Work

An important addition of this work would be to re-measure the uptake of pHLIPvar3-Au^{100}-RubpySS into [GSH]-modified HeLas by ICP-MS. If the GSH concentration is imposing an effect on nanoparticle internalization that is co-dependent on pHLIP's pH-dependent delivery mechanism, then this would likely be reflected by a significant increase in GSH-concentration-dependent gold concentration of cells treated at pH 6.5. Furthermore, it is important to elucidate why GSH imposes such an effect and whether GSH is responsible for cleaving pHLIPvar3 from the gold surfaces. One method to investigate this, would be to analyse the supernatant of centrifuged labelled-AuNPs pretreated with GSH by mass spectrometry.

4.5 Experimental

The HeLa human cervical adenocarcinoma cell line were maintained at 37°C in a humidified, 5% CO_2 atmosphere in Dulbeccos modified Eagles medium (DMEM) supplemented with 10% foetal bovine serum, 2 mM L-glutamine, 100 units/ml penicillin and 0.4 mg/ml streptomycin. Cells were routinely cultured in $755cm^2$ flasks and passaged using a standard Trypsin-EDTA protocol. For treatments, $5x10^4$ and $1x10^5$ cells were plated into 12-well and 6-well culture plates, respectively, and permitted to adhere and proliferate for 24 hours prior to any treatment.

4.5.1 Modifying [GSH] of cultured HeLa cells

To prepare [GSH]-modified HeLas, aqueous stock solutions of N-Acetyl cysteine (25 mM) and Buthionine Sulfoxide (5 mM) wee prepared and sterlised by injection through 0.22 μm sterilised filters. Plated HeLa cells were then treated with [GSH]-modifying precursors N-Acetyl cysteine (2.5 mM in 90% complete media), Buthionine Sulfoxide (100μM in 90% complete media), Buthionine Sulfoxide (500μM in 90% complete media), and H_2O in 90% complete media (negative control) for 24 hours. After the treatment, media was removed and cells were washed twice with PBS before being subjected to the relevant experiment. Additionally, cells treated with these precursors are throughout this thesis, collectively referred to as [GSH]-modified HeLas.

4.5.2 Measuring [GSH] of cultured HeLa cells by fluorimetric assay

For quantitative measurement of GSH concentration the method of [297] was used without modification.

Sample preparation

Briefly, the following solutions were prepared.

- Cell lysis buffer: 0.1 % Triton X-100 in PO_4-EDTA assay buffer
- Protein precipitation buffer: 50 % Trichloroacetic Acid in PO_4-EDTA assay buffer
- PO_4-EDTA assay buffer: 100 mM $NaH_2\ PO_4$, 5 mM Na_2EDTA. Adjusted to pH 8
- o-Phthalaldehyde (OPT): 1 mg/ml in 100 % Methanol
- GSH: 0.1 mg/ml in PO_4-EDTA assay buffer

For sample preparation, cells were cultured, and treated with [GSH]-precursors in 12-well plates. Medium was removed and cells were washed with PBS (1 mL). Ice cold cell lysis buffer was added (450 μL), cells were scraped and lysate was transferred to an eppendorf. Ice cold protein precipitation buffer was then added and cells were centrifuged (13,000 rpm, 5 minutes). The supernatant was then transferred to a fresh eppendorf. OPT solution (1800 μL) was added to sample and reference cuvettes, standard concentrations of GSH [0, 0.05, 0.1, 0.2, 0.3, 0.4, 0.6, 0.8, 1.0, 1.2, 1.4, 1.6, 1.8, 2.0 μg mL^{-1}] were added to reference cuvettes, and aliquots of sample supernatant (100 μL) were added to all sample cuvettes. TCA (100 μL) was added to all reference cuvettes, and OPT (100 μL) was then added to all cuvettes. All samples and calibration cuvettes were then covered and shaken for 15 minutes prior to acquisition.

Sample Analysis

For the [GSH] calibration curve, the 12 standard concentrations of GSH were used to calibrate the measurement. Fluorescence was subsequently recorded via $\lambda_{excitation}$ at 350 nm, and $\lambda_{emission}$ at 420 nm.

4.5.3 Analysing Cell Viability of [GSH]-modified HeLa cells

After treatment of HeLa cells with [GSH] precursors, the media from each well was withdrawn and cells were washed with PBS (500 μl) and replaced with 3-(4,5-Dimethyl-2-thiazolyl)-2,5-diphenyl-2H-tetrazolium bromide (0.5 mg/ml) in complete media (90% by volume), and were reincubated at 37°C for 2 hours. After the incubation, media was removed and DMSO (500 μl) was added to solubilise the formazan product. The plate was rocked for 15 minutes in the dark before the absorption at 590 nm was recorded against a DMSO blank.

4.5.4 Preparation of cells for Flow Cytometry

After treatment of [GSH]-modified HeLa cells with nanoparticles was complete, the supernatant from each well was removed and each well was washed with PBS (0.1 M, 0.5 ml) twice before being trypsinised at 37°C for 10 minutes. Particles were then spun down at 20,000 rpm for 10 minutes, the supernatant removed, and redispersed in of PBS (0.1 M, 1 mL). Cell suspension was transferred to a FACS tube before analysis.

4.5.5 Preparation of cells for Confocal Microscopy

Preparation for Fixed Cell Imaging

Prior to cell seeding, 22 mm glass coverslips were sterilised using absolute ethanol (rinsed and left to dry) and placed into the wells of 6-well culture plates. Cells were then seeded into 6-well culture plates on top of glass coverslips and allowed to grow to confluency for 24 hours. After treatment, medium was removed and cells were washed with PBS (2 ml x 2) and then paraformaldehyde (4% in 0.1M PBS, 2 ml) was added and cells were left for 10 minutes at room temperature. Fixative was removed and cells were washed with PBS (2 ml x 2). Cells were then mounted onto glass microscope slides, using a drop of Hydromount to maintain sample hydration, before sealing the slide with nail varnish. Slides were left to dry at 4°C and were imaged within a few days.

Preparation for Live Cell Imaging

For live cell imaging, cells were initially seeded into 3 mL volume Mat Tek glass bottom dishes, and left to grow to confluency for 24 hours. After treatment, medium was removed and cells were washed with PBS (2 ml x 2) and then PBS (2 ml) was added before transferring samples to the microscope for imaging.

4.5.6 Preparation of cells for Inductively Coupled Plasma - Mass Spectrometry

HeLa cells were cultured as per above and treated as per the relevant experiment. After treatment was complete, the supernatant from each well was removed and each well was washed with PBS (0.5 ml x 2) before being trypsinised at 37°C for 10 minutes. Particles were then spun down at 20,000 rpm for 10 minutes, the supernatant completely removed taking care not to disturb the cell pellet, before being allowed to dissolve overnight in 200 μl of ultrapure aqua regia (3:1 volumetric ratio of hydrochloric and nitric acid). Post dissolution, samples were diluted in ultrapure nitric acid (2700 μL of a 4% solution) prior to analysis.

Chapter 5

Lipid-coated AuNPs, co-labelled with a Luminescent Europium Complex

5.1 Introduction

The aim of this work is to examine whether modifying the hydrophobicity of gold nanoparticles by coating the particle surface with a simple lipid molecule results in a more favourable interaction with plasma membranes and thereby improve the efficiency of their internalization into cancer cells. We wanted the design of the probe to enable multimodal detection, so we synthesised gold nanoparticle scaffolds co-labelled with a lipid and a luminescent substrate. Tetradecanoic acid (Myristic acid) was chosen to be the lipid surfactant, and a luminescent europium complex was identified as a suitable compatible co-label owing to its neutral charge. Herein, a review of lanthanide based luminescent probes and their partnership with gold nanoparticles, along with synthesis of these multimodal probes, their characterisation and investigations into their uptake and interactions with human cervical adenocarcinoma cells is reported.

5.1.1 Lumophores based on Lanthanide Complexes

Lanthanide elements are a chemically and spectroscopically unique series of the periodic table of elements, and despite being referred to as 'rare earth elements', many are enormously abundant such as the Y_2O_3 phosphor which maintains heavy use within cathode ray tubes [321]. Lanthanide complexes offer luminescent properties that scale the visible and near infrared spectrums, and their complexes are often facile to synthesise, often with the stepwise addition of ligands.

Lanthanide ions possess the electronic configuration [Xe] $4f^n$ were n is the number of electrons (0 – 14) in the ion's valence $4f$ orbitals. Across the lanthanide series there is little variation in chemical properties as electrons within the ($4f$) valence orbitals are shielded by electrons in the $5s^2$ $5p^6$ sub-shells, however the oxidation states available to lanthanide ions across the series varies from Ln^{2+} to Ln^{4+}, depending on

the element. All lanthanides have access to a trivalent Ln^{3+} state, the charge state that offers the most favourable compromise between ionisation energy and lattice energy stabilisation of the lanthanide cation [322]. Some lanthanides do have access to additional oxidation states, for instance Ln^{2+} oxidation states (e.g. Sm^{2+} & Eu^{2+}), or to Ln^{4+} oxidation states (e.g. Tb^{4+}, Ce^{4+} & Dy^{4+}). However, with the exception of Ce^{4+}, all other the Ln^{4+} oxidation state is only found in the solid state, and not accessible in solution [323]. It has been widely recognised that F electrons within lanthanides aren't involved in bonding as their orbitals endure far greater contraction than the valence S and D orbitals [324], additionally it has been demonstrated through DFT calculations that f orbitals are non-participant in Ln-ligand bonding [325]. Additionally, F electrons also exhibit poor shielding effects over other electrons, resulting in a contraction of lanthanide ionic radii across the series through an increase in effective nuclear charge across the series. The coordination numbers available to lanthanides ranges from 3 – 12, although 8 – 9 is most common. Lanthanides can also be described as hard bases, due to the predominantly ionic nature of their bonding and that their preference to bonding with hard donors such as oxygen and nitrogen.

Lanthanide luminescence is dependent on how efficiently the lanthanide's excited state can be populated, as well as how effectively quenching mechanisms are minimised [326]. Lanthanides are poor absorbers of light (typical molar extinction coefficients of 1 - 10 M^1 $cm{-}1$) resulting from restrictions of $f \longrightarrow f$ transitions. These transitions are governed by the Laporte selection rule which states that an allowed transition requires a change in parity between transition orbitals, and the spin selection rule which states that in an emission process, the transitioning electron must not change its spin state in order for the transition to be permitted. To circumvent this problem of poor absorptivity, sensitizer groups are typically complexed to the lanthanide ion, resulting in the lanthanide's excited state being indirectly populated by transfer of energy absorbed by the sensitizer groups to the lanthanide centre. These sensitizer groups can be bespokely designed for desired molar excinction coefficients and chemical functionality. Once the lanthanide excited state is populated, the excited electrons return to their ground state by spin-forbidden radiative transitions, which are weakly allowed by vibronic coupling. This weak vibronic coupling results in a characteristic sharp band emission spectrum across the lanthanide series. Additionally, due to the spin forbidden nature of the radiative transitions, the process operates on a timescale far longer than organic fluorescence, where typical organic luminescence lifetimes exist on the order of nanoseconds and lanthanide luminescence lifetimes (τ) exist on the order of milliseconds [327, 328, 329].

5.1.2 Lanthanide Complexes as Biological Lumophores

Luminescent lumophores based on lanthanide complexes have been gaining increased use within biomedical imaging [41]. Their millisecond luminescence lifetimes enable applications in time-resolved studies [330], sharp band emission enables facile multiplexing and large Stokes shifts (typically < 100 nm) enable facile separation between illumination light and emission signal. Lanthanide complexes have been used very successfully in probing cellular pH, where typically the luminescence of the probe is modulated by protona-

tion/deprotonation of a pH sensitive ligand [331, 332, 333, 334, 335] as well as other sensing applications including anion detection [336, 337], metal ion detection [338, 339, 340], reactive oxygen species detection [341, 342, 343] along with detection of amino acids & proteins [344, 345, 346].

Despite a rather attractive series of attributes, lanthanides typically suffer from relatively poor luminescence quantum yields, and there are four factors that affect a lanthanide's quantum yield. Firstly, the energy difference of the lanthanide's lowest excited state and its ground multiplet state, of which Eu^{3+} has one of the highest quantum yields of the lanthanide series due to the appropriate energies [326]. Secondly, the relative energies of the sensitising unit's excited state and the ^5D excited state of the lanthanide ion. Thirdly, the energy transfer efficiency between the sensitising unit and the lanthanide which occupies a distance dependence the two constituents. And fourth, the quenching effect of coordinated water molecules due to the overlap of the O — H vibration with lanthanide luminescence [347].

One of the largest drawbacks of lanthanide lumophores is the requirement of ultraviolet illumination to excite the sensitizer groups, causing significant photo damage to biological structures. However, the application of lanthanide-based materials within upconverting phosphors has been studied extensively [348, 349, 350, 351, 352]. There are a number of processes that result in upconversion such as Excited State Absorption (ESA), where multiple infrared photons are absorbed sequentially, or Energy Transfer Upconversion (ETU) where an excited ion transfers energy to a neighbouring excited ion. This is a particularly attractive modification of lanthanide-based imaging probes as physiologically damaging ultraviolet excitation would no longer be required. Additionally, Wang et al. [353] recently developed upconverting lanthanide doped nanoparticles, and demonstrated how tuning the host and dopant concentrations offered significant emission changes despite single wavelength excitation.

5.1.3 Gold nanoparticles labelled with Lanthanide Lumophores as Cell Imaging Probes

The labelling of gold nanoparticles with lanthanide complexes has been receiving increased attention over the last decade as gold nanoparticles provide a useful platform to construct nanosized materials that bear the unique luminescent signature of a lanthanide complex. The topic was recently reviewed by Lewis et al. [42]. The surface labelling of gold nanoparticles with surface-bound organic fluorophores was first published by Thomas & Kamat in 2000 [75, 74] and subsequent works demonstrating the coating of gold nanoparticles with surface bound luminescent metal complexes were published some years later [94, 162, 95]. Lewis et al. were the to first report the labelling gold nanoparticles with a luminescent lanthanide complex based on a europium complex with a diethylene triamine pentaacetic acid (DTPA) ligand shell [94]. The DTPA ligand was functionalised with phenylamide groups to sensitise lanthanide luminescence, and thiol units that bind to soft metal surfaces. Davies et al. [139] later developed pH-sensitive nanoparticles synthesised by co-labelling 13 nm gold nanoparticles with the pH Low Insertion peptide and a luminescent europium complex with DTPA-bisamide ligands and quinoline sensitizers. Davies then demonstrated luminescence imaging

of pH-mediated delivery of the nanoparticles into platelets using europium luminescence for visualisation. Massue et al. [354] reported the labelling of gold nanoparticles with a heptadendate macrocyclic Eu(III) cyclen conjugate that permitted the sensing of flavin monophosphate using a displacement mechanism that switched-on Eu luminescence. Runowski et al. [355] reported the deposition of gold onto lanthanide clusters (Eu^{3+} & Tb^{3+}), forming core/shell type nanoparticles that exhibited strong luminescence in the red for europium-doped, and green for terbium-doped. Aditionally, the gold surfaces were labelled with Surface Enhanced Raman Spectroscopy (SERS) probes, and their raman signal was enhanced by the presence of the gold surface by a factor of 10^5. Zhang et al. [356] demonstrated that the emission of upconverting lanthanide doped nanoparticles was enhanced by plasmonic interactions from gold nanoparticles coupled to the lanthanide nanoparticle surface.

5.1.4 Lipid-coated gold nanoparticles for cell delivery applications

Lipid-coating of gold nanoparticle surfaces in order to promote cell internalization, or to facilitate cell imaging techniques has been reviewed quite extensively [73]. Li et al reported lipid-coated AuNP-mediated delivery of plasmid DNA into Hek 293 cells, in a transfection method that offered 5 times better efficiency than by lipid-only transfection [357]. The transfection of DNA-cationic lipid complexes was found to be relatively inefficient, owing to the limited stability of the complexes [358, 359], however their stability was found to increase markedly when both are co-labelled onto gold nanoparticles [360]. Additionally, for HEK 293 T cells cells dosed with lipid-coated nanoparticles, a secondary treatment with nocodazole (NCZ) resulted in more substantial dispersion of nanoparicles within cytoplasm rather than being confined to endosomes. Recently reported was lipid-gold nanoparticle structure designed by Thaxton et al. [361] to be an analogue of the high density lipoprotein (HDL) in order to measure the binding constant between HDL and cholesterol. In addition, these HDL-AuNPs have been used to provide an indication of atherosclerosis by measuring the build up of lipid-AuNPs within the aortas of mice held on high cholesterol diets [362]. Fig. 5.1 shows schemes for a number of publications referenced in this work.

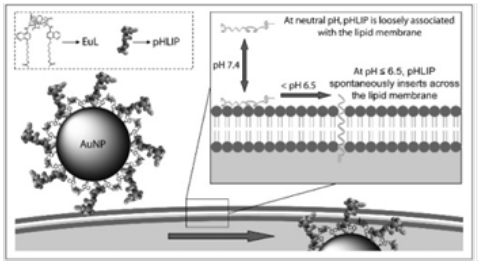

[41]

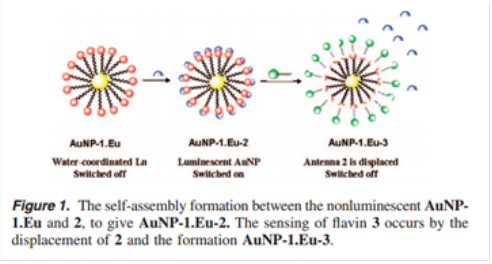

Figure 1. The self-assembly formation between the nonluminescent **AuNP-1.Eu** and **2**, to give **AuNP-1.Eu-2.** The sensing of flavin **3** occurs by the displacement of **2** and the formation **AuNP-1.Eu-3**.

[42]

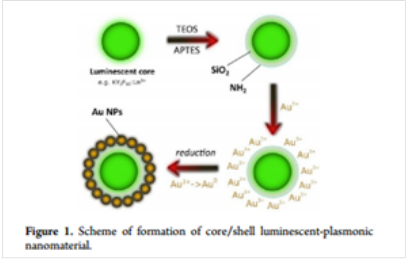

Figure 1. Scheme of formation of core/shell luminescent-plasmonic nanomaterial.

[43]

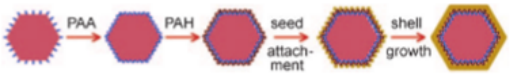

Figure 1. Illustration of surface functionalization, gold NP attachment, and gold nanoshell growth on the upconversion NCs.

[44]

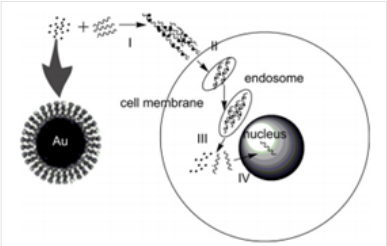

Scheme 1. Schematic illustration of the structure of AuNPs and the process of AuNPs mediated transfection. Four steps were supposed to involve in this procedure (see text for detail).

[47]

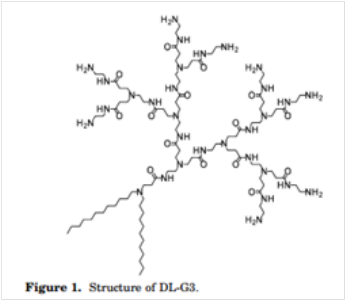

Figure 1. Structure of DL-G3.

[48]

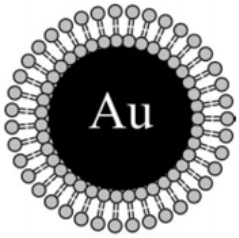

Scheme 1. The structure of the AuNPs. Cationic lipid DDAB formed a bilayer on the surface of the Au core.

[49]

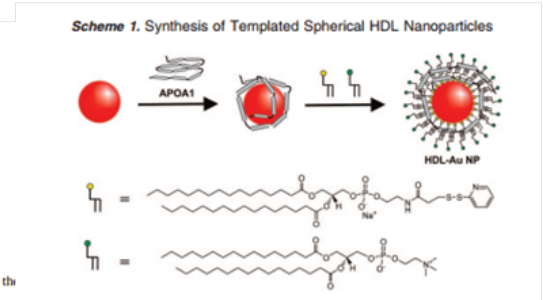

[50]

Figure 5.1: Schemes illustrating a number of chosen publications referenced in this chapter.

5.1.5 Myristic Acid

Myristic acid is a small lipid (Fig. 5.2) that has shown promise as a cellular targeting vector as its membrane binding is not dependent on surface receptor recognition [363, 364]. The lipid is a saturated fatty acid with a 14-carbon backbone, a methacrylate head group with a pk_a of 4.90 [365]. Cardo et al. recently reported the delivery of the filamentous actin-binding peptide Lifeact to human platelets by conjugation to myristic acid via a cleavable disulfide linker [366]. In this work, the efficiency of pH Low Insertion Peptide (pHLIP), Trans-activating Transcriptional Activator (TAT) peptide and myristic acid as carriers for the Lifeact peptide, filamentous actin-binding peptide, for which platelet membranes are impermeable. They reported that myristoylation of the Lifeact peptide resulted in a higher loading efficiency, where the final loaded concentration was more sensitive to the original treatment concentration than for pHLIP-conjugated Lifeact. These results suggest that modification of cargo with a simple lipid can offer a substantial effect on the efficiency of cell uptake.

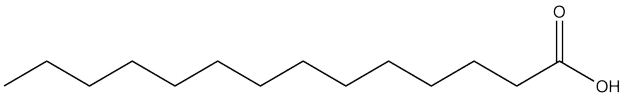

Figure 5.2: Structural formula of myristic acid

5.2 Results and Discussion

This section is divided into a series of subsections. *i)* the preparation of luminescent lipid-coated gold nanoparticles, *ii)* the assessment of colloidal structure and photophysical properties of the labelled nanoparticles, *iii)* the assessment of labelled-AuNP uptake into HeLa cervical adenocarcinoma cells by light microscopy and inductively coupled plasma mass spectrometry, and *iv)* cell viability studies analysing the effect of cell treatment using the 3-(4,5-dimethyl-2-thiazolyl)-2,5-diphenyl-2H-tetrazolium bromide (MTT) reduction assay.

5.2.1 Preparation of EuL

EuL was prepared by Johnathan Lilley in accordance with the synthetic protocol of Davies et al. [139] and was characterised by ^{1}H & ^{13}C NMR.

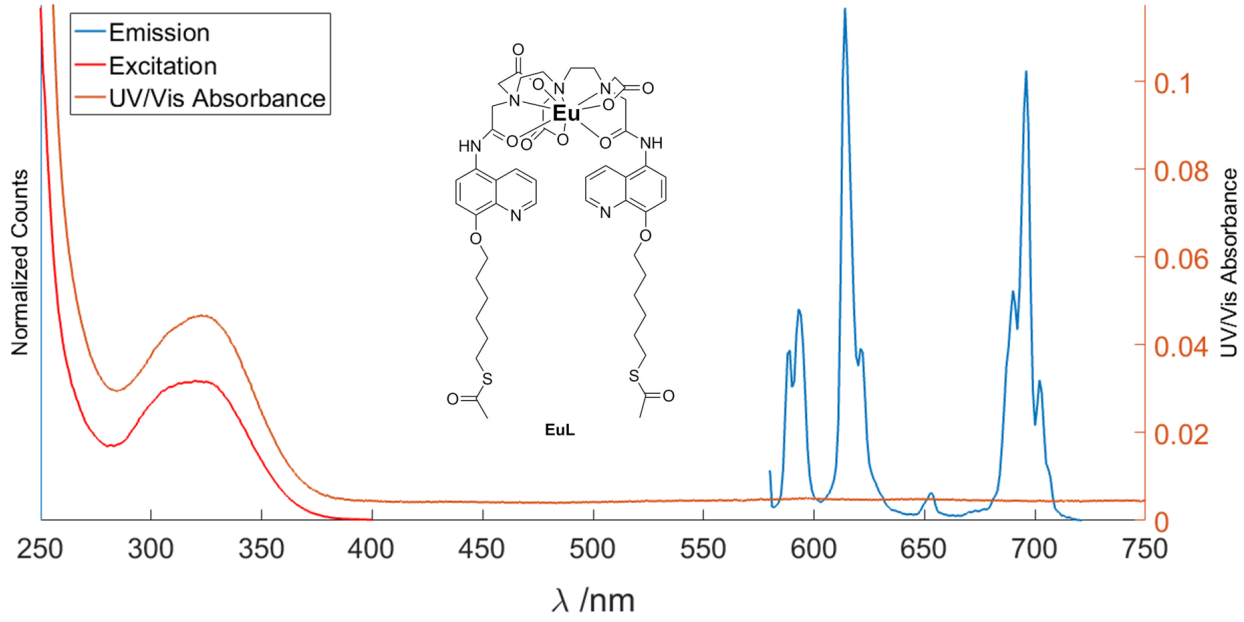

Figure 5.3: Steady state absorption and luminescence spectra of EuL. For excitation scans, the instrument's emission monochromator was set to 614 nm, and for emission scans, the excitation monochromator was set to 360 nm. Long pass filters were used to prevent detection of scattered light.

Fig. 5.3 shows the structural formula of luminescent complex, EuL, along with the complexes' steady state absorption and luminescence spectra in 10% MeOH in H_2O. The complex is equipped with quinoline units to transfer energy to the europium luminescence state, and terminal thiol units for binding to soft metals. The absorption band at 340 nm is attributed to the quinoline sensitizer unit. The emission spectrum shows the characteristic europium sharp band emission with bands at 590, 614, 555 and 690 nm representing the $^{5}D_0 \longrightarrow {}^{7}F_J$ transitions, where J = 0, 1, 2, & 3, respectively. The sharp band emission of the europium emission is resultant from weak vibronic coupling, resulting in electronic transitions that occur without significant

geometric rearrangement of the molecule. Additionally, the band at 340 nm within both the excitation and absorption spectrum confirms that the quinoline unit is responsible for populating the europium $^5D_0$ excited state. Originally, efforts were made to co-label gold nanoparticles with myristate & ruthenium complex, RubpySS. However, labelling Myr-AuNPs with RubpySS always resulted in particle flocculation as myristate was unable to stabilise the particles whilst the RubpySS complex, with its 2+ charge, bound to the surface. EuL has a neutral charge, enabling more facile nanoparticle labelling where negatively changed nanoparticles do not flocculate from charge imbalances.

5.2.2 Preparation of Luminescent, Lipid-coated Gold Nanoparticles

Luminescent lipid-coated gold nanoparticles were prepared by subjecting Au^{13}NPs & Au^{100}NPs to a two-step coating process illustrated in Fig. 5.4. Particles were initially coated with myristic acid, and then subsequently coated with luminescent complex, EuL. The coating process was monitored using UV/Vis absorption spectroscopy.

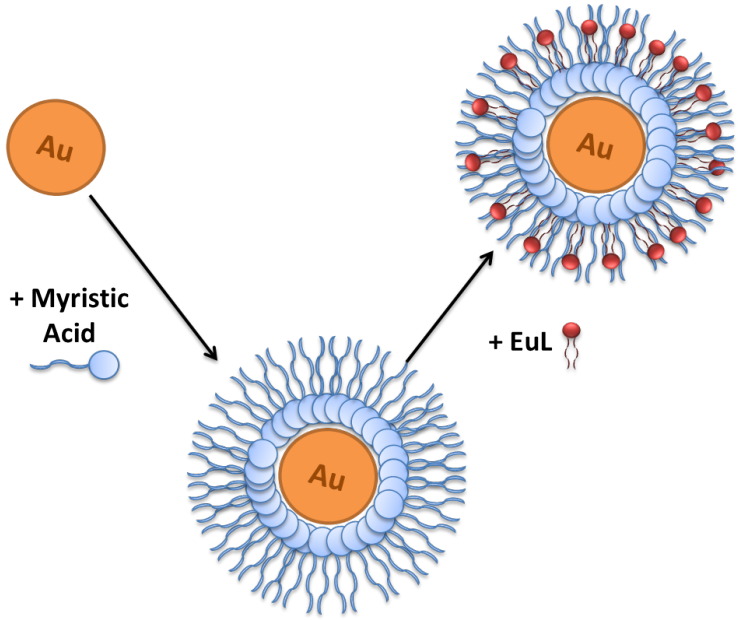

Figure 5.4: Schematic for the process of labelling AuNPs with Myristic acid & EuL.

Fig. 5.5 shows UV/Vis absorption spectra of Au^{13}NPs being sequentially labelled with myristic acid & EuL. Addition of both substrates was performed as sequential titrations, where particles were initially labelled with myristic acid, and a UV/Vis absorbance spectrum was acquired inbetween additions. The SPR band of the gold nanoparticles was monitored during the course of the titration, as the SPR band is sensitive to morphology [82], core charge [83], solvent refractive index [84], inter-particle distance [85] and surface functionalization [86]. SPR λ_{max} is a useful indicator of gold nanoparticle surface functionalisation [94, 139, 96] and titration of both substrates into gold nanoparticles was iterated until SPR λ_{max} changes began to plateau, indicating that no further surface changes were occurring.

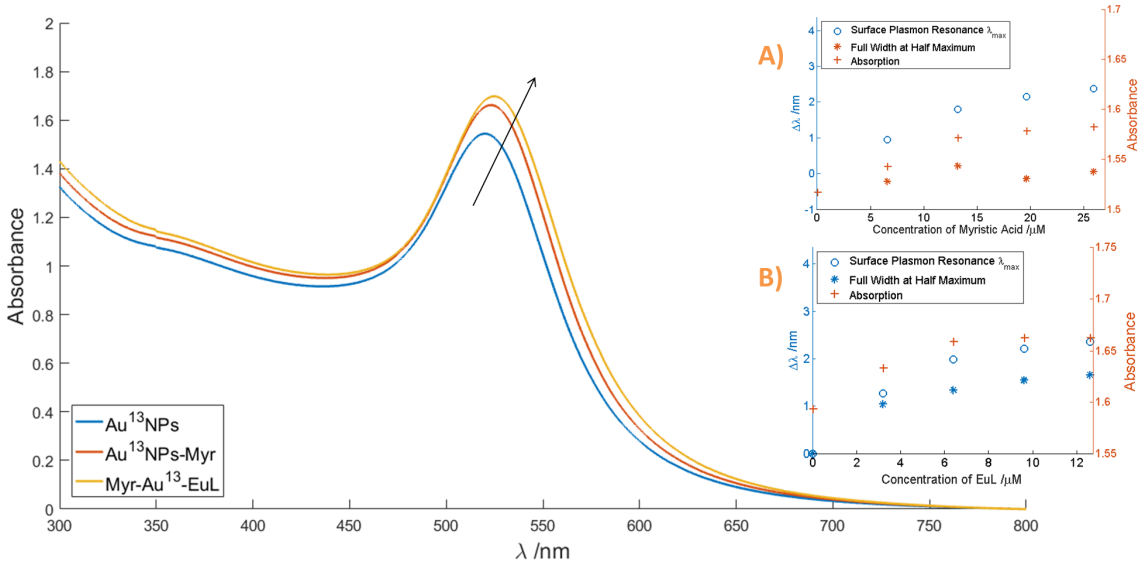

Figure 5.5: UV/Vis absorption documenting the labelling of Au^{13}NPs (4.8 nM, 1.5 ml) with Myristic acid (26 μM), and EuL (2.5 μM). Inset, change in SPR λ_{max}; Absorbance, and FWHM for Myristic acid binding to gold (A) and EuL binding to myristic acid-labelled AuNPs (B).

Citrate-stabilised, 13 nm diameter gold nanoparticles (Au^{13}NPs, 4.8 nM, 1.5 mL) were stirred rapidly in a cuvette using a microstirrer bead. Myristic acid (1 mM in 10% MeOH in H_2O) was titrated into the colloidal solution, and UV/Vis absorption spectra were taken in-between each addition (Fig. 5.5, inset A). During the titration of Myristic acid, the SPR λ_{max} underwent a bathochromic shift of 2.5 nm, and an intensity increase consistent with previous reports of SPRλ_{max} change upon the binding of methacrylate groups to gold nanoparticle surfaces [96, 166]. The SPRλ_{max} plateaued at 522 nm after 26 μM of myristic acid had been titrated, indicating that no additional surface binding was taking place.

After the coating of Au^{13}NPs with myristic acid, particles were left to stir for 10 minutes before a solution of EuL (1 mg ml^{-1} in 10% methanol in H_2O) was titrated into the solution, while still under rapid stir. Addition of EuL (2.5 μM) to Myr-Au^{13} resulted in an increase in SPR absorbance and an SPRλ_{max} bathochromic shift of 2.5 nm (Fig. 5.5, inset B), consistent with reports of thiol binding to gold nanoparticles [86, 180]. Additionally, previous work in the group has shown that MeOH imposes no effect on

gold nanoparticle SPR bands [94]. Particles were then stirred for an additional 10 minutes before purification. To purify the particles, unbound substrates were removed by passing the particles through sephadex G-15 size exclusion resin using water as the eluent. Particles were a deep red in colour, and were easily visible as they eluted rapidly off the gel.

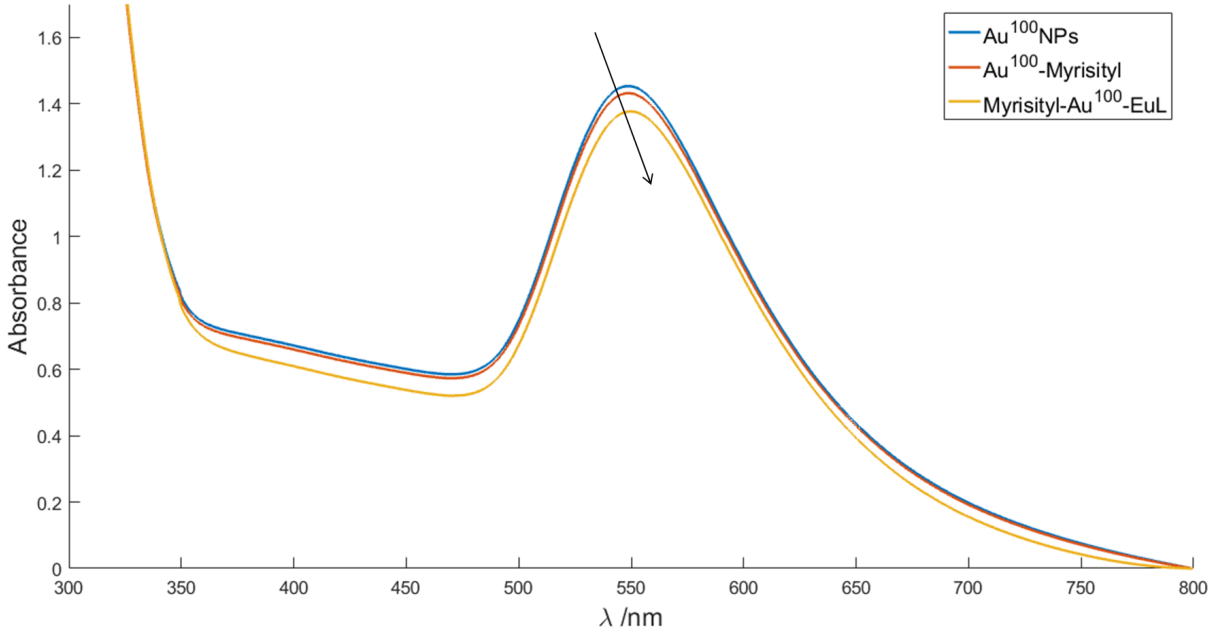

Figure 5.6: UV/Vis absorption monitoring the labelling of Au^{100}NPs (40 pM, 1.5 ml) with Myristic acid (13 μM), and EuL(1.25 μM).

The co-labelling of Au^{100}NPs was also performed by a sequential addition, monitored by UV/Vis absorption spectroscopy as shown in Fig. 5.6. Au^{100}NPs (40 pM, 1.5ml) were stirred such that a rapid vortex was present within the cuvette, and myristic acid (13 μM) was added to the colloid and left for 10 minutes. The Gold SPRλ_{max} underwent a small bathochromic shift of 1 nm and a reduction in insensity. EuL was then added to the colloid under rapid stir, and addition of 1.25 μM induced a further small bathchromic shift of 1 nm and further reduction in SPR band intensity. Particles were again purified using sephadex G-15 size exclusion resin using water as the eluent, where the brown colloid rapidly eluted off the gel.

5.2.3 Photophysical Characterisation of Luminescent, Lipid-coated Gold Nanoparticles

In order to investigate the suitability of Myr-Au$^{13\&100}$-EuL as luminescence agents, their steady state luminescence was probed using luminescence spectroscopy. Excitation spectra were acquired by setting the emission monochromator to 614 nm, scanning the excitation monochromator from 250 nm to 400 nm and using a 590 nm long pass filter out scattered light. This scan indicated that the quinoline group is responsible for the population of the Eu^{3+} luminescence state $^5D_0$. Emission scans were taken by setting the excitation monochromator to 340 nm, scanning the emission monochromator from 580 nm to 720 nm, using a 475 nm long pass filter. This scan provided the sharp emission band structure characteristic of lanthanide f $\longrightarrow$ f radiative transitions, with the strongest emission band at 614 nm.

Fig. 5.7 shows the absorption, excitation and emission spectra of Myr-Au^{13}-EuL. The characteristic sharp emission band of europium can be seen within the emission spectrum (absorbance at 340 nm = 1.2 absorbance units), with emission bands at 590, 614, 655 and 690 nm representing the $^5D_0 \longrightarrow {}^7F_J$ transition (where J = 0, 1, 2, 3). The excitation spectrum shows a band at 340 nm which overlaps with the quinoline absorption band (Fig. 5.3) showing that Eu luminescence at 614 nm is resultant from quinoline excitation, and a scatter peak at 300 nm. In addition, the absorption spectrum of Myr-Au^{13}-EuL shows the surface plasmon resonance band at 524 nm.

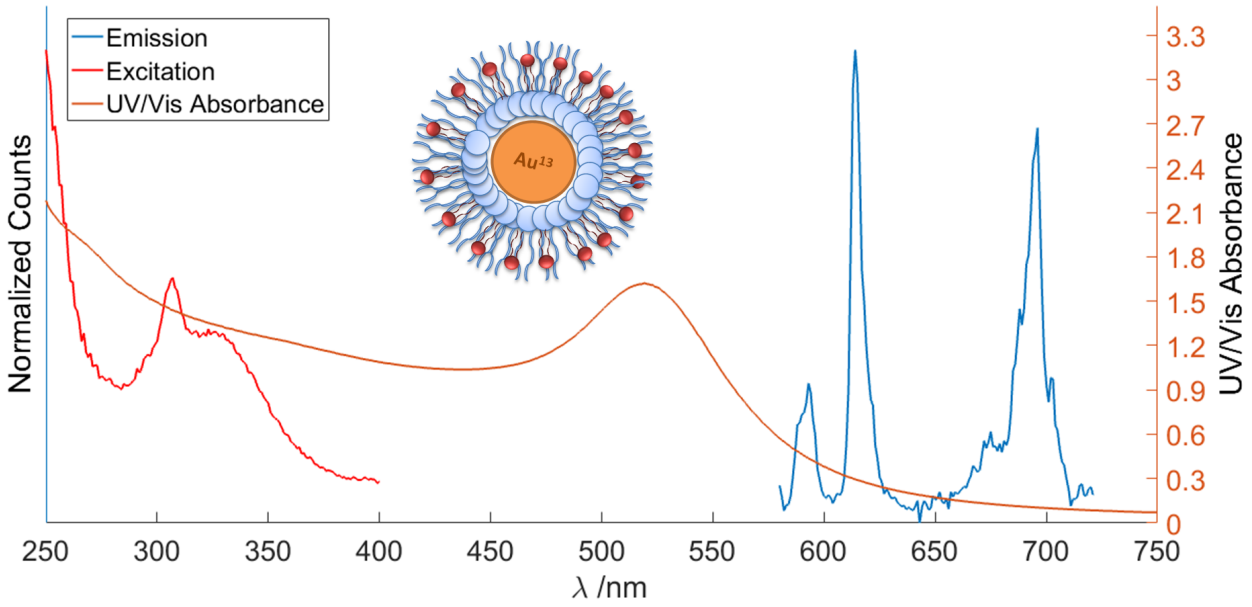

Figure 5.7: Steady state absorption and luminescence spectra of Myr-Au^{13}-EuL. For excitation scans, the instrument's emission monochromator was set to 614 nm, and for emission scans, the excitation monochromator was set to 360 nm. Long pass filters were used to prevent detection of scattered light.

Fig. 5.8 shows the absorption, excitation and emission spectra of Myr-Au^{100}-EuL. Again, the easily recognisable europium sharp band emission spectrum is present (absorbance at 340 nm = 1.1 absorbance

units). The bands visible within the emission spectrum lie at 590, 614, 650 (very weak) and 690 nm, indicating that any plasmon effects on EuL steady state luminescence are minimal. The UV/Vis absorption spectrum shows the gold nanoparticle SPR band at 560 nm, and the excitation spectrum shows that quinoline is again responsible for populating the europium $^5D_0$ excited state.

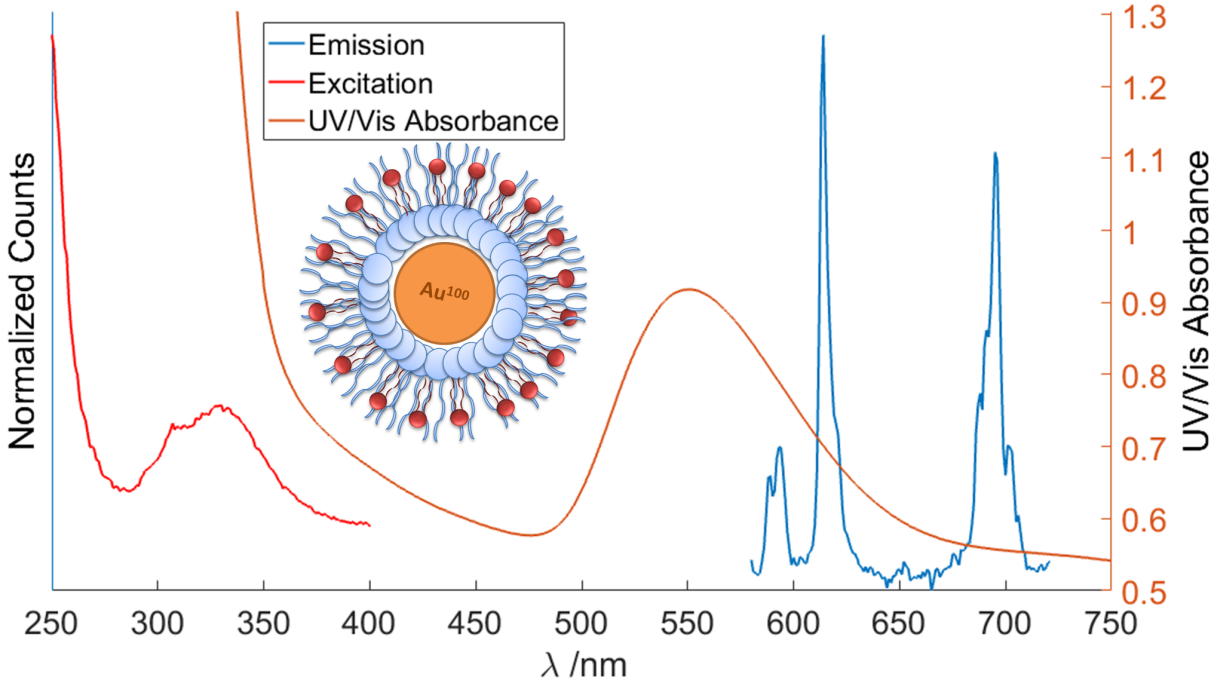

Figure 5.8: Steady state absorption and luminescence spectra of Myr-Au^{100}-EuL. For excitation scans, the instrument's emission monochromator was set to 614 nm, and for emission scans, the excitation monochromator was set to 360 nm. Long pass filters were used to prevent detection of scattered light.

5.2.4 Structural Characterisation of Luminescent, Lipid-coated Gold Nanoparticles

Transmission electron microscopy was used to study labelled nanoparticle size as well as the effect of labelling on nanoparticle dispersity, as the labelling process involves the displacement of citrate ions that initially provide stabilisation to the colloid, for myristic acid and EuL. For this experiment, freshly prepared Myr-Au^{13}-EuL nanoparticles were dried onto copper grids and imaged immediately. Fig. 5.9 shows TEM micrographs of Myr-Au^{13}-EuL, indicating monodisperse spherical particles of diameters between 10 - 20 nm, indicating that labelling of Au^{13}NPs with myristic acid & EuL did not induce nanoparticle flocculation.

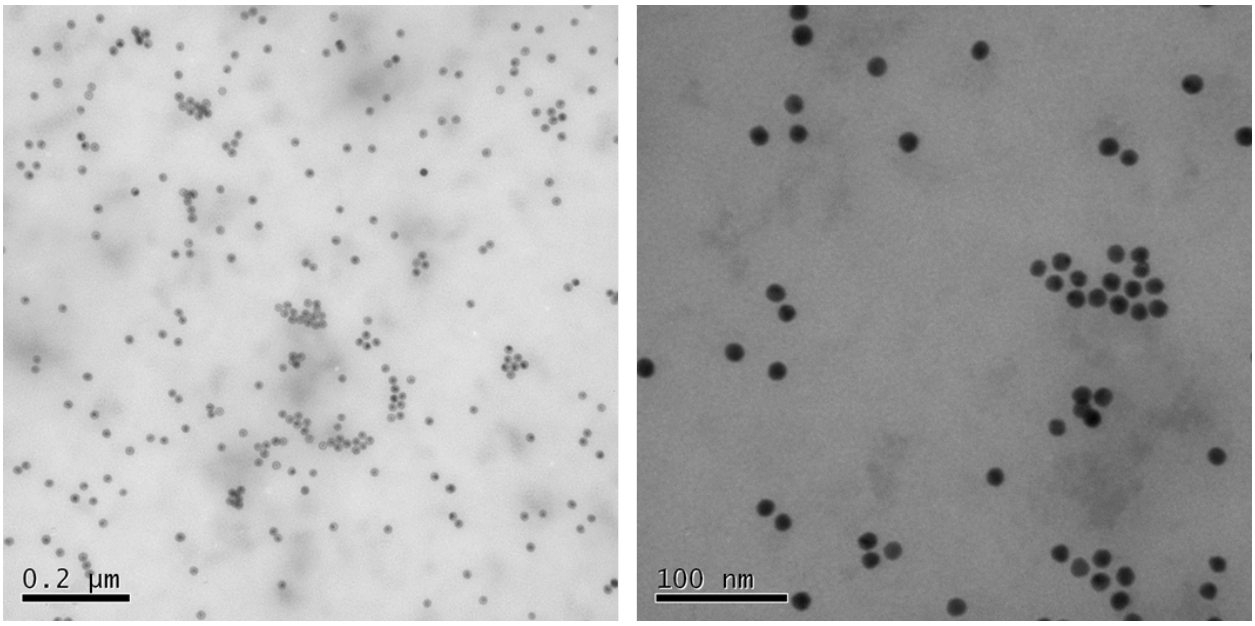

Figure 5.9: Transmission electron micrographs of Myristic-Au^{13}-EuL colloid, dried onto copper grids. Images taken at 120,000x magnification (left) and 300,000x magnification (right).

To establish whether the secondary labelling of myristate-labelled gold nanoparticles with EuL displaced the myristate from the gold surface, Myr-Au^{100}-EuL and Au^{100}-EuL were studied using dynamic light scattering. Fig. 5.10 shows number-weighted hydrodynamic diameters of Myr-Au^{100}-EuL and Au^{100}-EuL (both 8 pM in H_2O) measured by DLS. The average diameters (from 3 technical repeats) for Myr-Au^{100}-EuL and Au^{100}-EuL were 82 $\pm$ 25 nm and 68 $\pm$ 26 nm, respectively. The significantly larger average diameter for the Myr-Au^{100}-EuL indicates that particles are moving slower in solution, strong evidence that the particles myristate coating is still substantially intact, and that EuL is not significantly displacing the myristate from the surface of the gold.

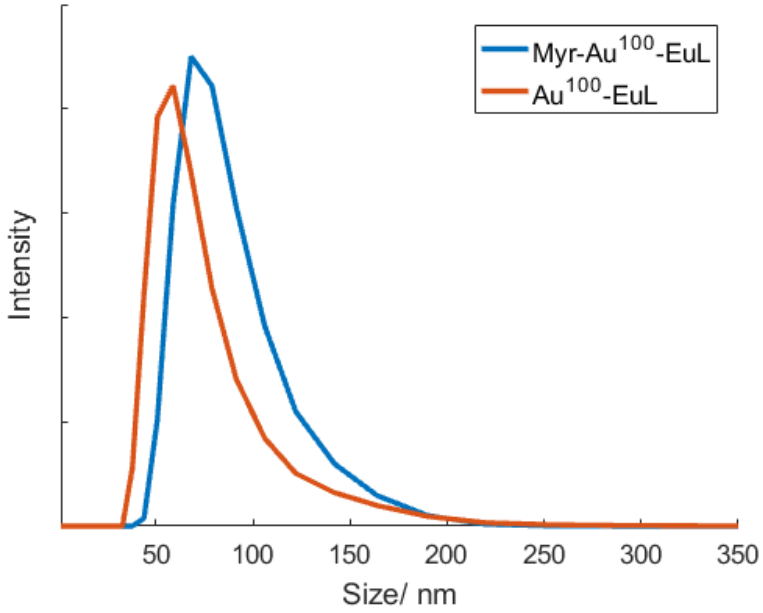

Figure 5.10: Number-weighted distribution of Myristic-Au^{13}-EuL (4 pM) hydrodynamic diameters as measured by dynamic light scattering.

5.2.5 internalization of Luminescent, Lipid-coated Gold Nanoparticles by HeLa Cervical Adenocarcinoma Cells

To study the uptake of Myr-Au^{13}-EuL into cancer cells, an *in vitro* cell treatment experiment was performed and treated cells were imaged by epifluorescence microscopy. For this experiment, the HeLa cervical adenocarcinoma cell line was cultured in 6-well plates on top of glass coverslips. Cells were permitted to grow and proliferate for 24 hours post seeding, and then treated with Myr-Au^{13}-EuL (1 nM in complete media) for 6 hours at 37°C. After the treatment time was concluded, cells were washed with PBS, fixed using 4% paraformaldehyde and mounted onto glass coverslips for imaging.

To image Myr-Au^{13}-EuL uptake, brightfield and luminescence modes were used. Brightfield images were acquired using an arc lamp excitation while luminescence imaging was performed using λ_{ex} = 340 nm, a 510 nm dichroic mirror to prevent acquisition of rayleigh scattered light. Additionally, a luminescence spectrum of treated cells was acquired (λ_{ex} = 340 nm, λ_{em} = 600 - 630 nm) to investigate whether treated cells bear the luminescent signature of europium.

Fig. 5.11 shows epifluorescence images of HeLa cervical adenocarcinoma cells treated with Myr-Au^{13}-EuL. Brightfield images indicate cells are adopting a spread morphology, consistent with viable HeLa cells. Luminescence images show strong red luminescence from treated cells, although it is not clear how much of the signal arises from autofluorescence. An emission spectrum was taken of the treated cells (λ_{ex} = 340 nm, λ_{em} = 600 - 630 nm) which showed the europium $^5D_0 \longrightarrow {}^7F_2$ emission band indicating the presence

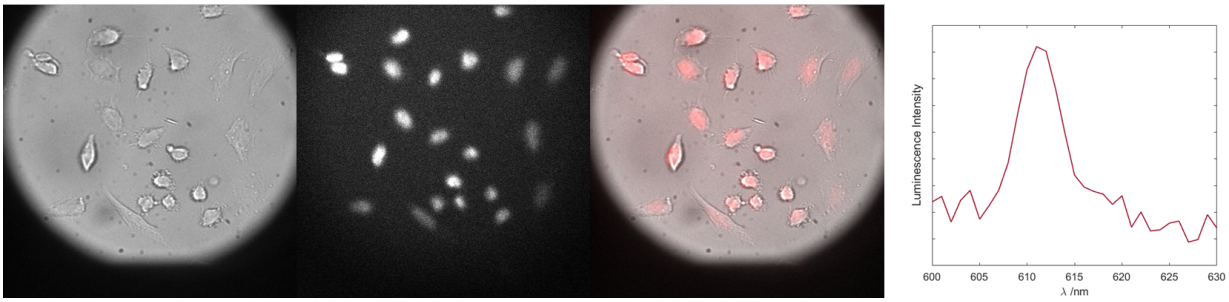

Figure 5.11: Epifluorescence images of HeLa cells treated with Myristic-Au^{13}-EuL (1 nM) in complete media for 4 hours at 37°C. From left to right, i) transmission image; ii) Epifluorescence image using 360 nm excitation; iii) overlay of transmission image and epifuorescence image; and iv) steady state emission of treated HeLa cells showing 614 nm sharp europium emission band.

of europium signal within the luminescence images.

To study the effect of the myristic acid surface labelling on the internalization of gold nanoparticles, HeLa cells were treated with Myr-Au^{13}-EuL & an Au^{13}-EuL control and the concentration of gold internalized by treated cells was measured using Inductively Coupled Plasma Mass Spectrometry (ICP-MS). The gold concentrations of cells treated with Myr-Au^{13}-EuL & Au^{13}-EuL were 17.6 ± 0.75 ppb and 8.2 ± 7.6 ppb, respectively (3 biological repeats were performed, signal from untreated cells was subtracted and measurements in absence of Helium sheath gas are reported).

HeLa cells were then cultured to investigate the uptake of Myr-Au^{100}-EuL. In this experiment, an Au^{100}-EuL control sample was prepared, cells were treated for 6 hours (with 8 pM of nanoarticles in complete media) and imaged live by confocal reflection microscopy, where gold nanoparticles offer strong contrast owing to the efficiency that their electron-rich cores scatter incident light (Fig. 5.12).

Images of cells treated with Myr-Au^{100}-EuL or Au^{100}-EuL both show cells with internalized AuNPs, with particles appear to be localised within cytoplasmic regions of the cells, and nuclear regions devoid of particles. Additionally, cells treated with Myr-Au^{100}-EuL show a higher density of internalized gold than samples treated with Au^{100}-EuL, consistent with ICP-MS measurements Myr-Au^{13}-EuL & Au^{13}-EuL that showed a higher concentration of gold within cells treated with Myr-Au^{13}-EuL.

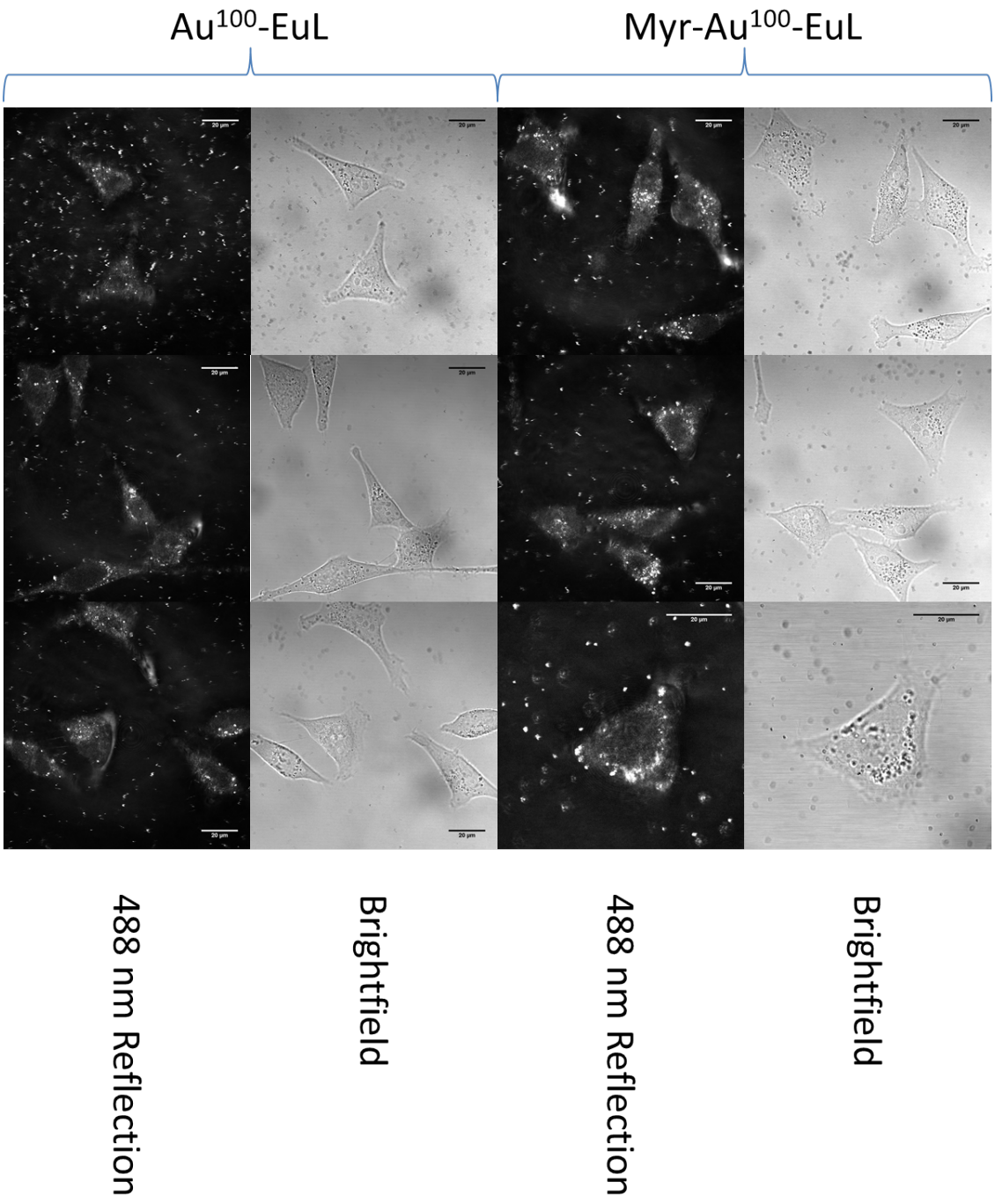

Figure 5.12: Live cell confocal microscopy images of HeLa cells treated with Myristic-Au^{100}-EuL (8 pM) in complete media for 6 hours at 37°C. Transmission images taken at 488 nm, reflection images taken at 633 nm.

5.2.6 Viability of HeLa Cells treated with Luminescent, Lipid-coated Gold Nanoparticles by the 3-(4,5-dimethyl-2-thiazolyl)-2,5-diphenyl-2H-tetrazolium bromide (MTT) reduction assay

In order to assess the effect of nanoparticle treatment on cell viability, the MTT reduction assay was employed to assess cell mitochondrial function, an indicator of cell viability. For this experiment, HeLa cervical adenocarcinoma cells were seeded into a 24-well plate, and allowed to adhere and proliferate for 24 hours. Cells were then treated with particles (1 nM for Au^{13} samples & 8 pM for Au^{100} samples) in complete media for 6 hours at 37°C. After the treatment, media was removed and cells were washed with PBS. Cells were then treated with the MTT dye in complete media and returned to incubation for an additional 2 hours at 37°C.

After the MTT treatment was complete, the formazan product in each well was solubilised using DMSO and the well plate was rocked for 20 minutes prior to acquisition. The absorbance of each well was recorded at 590 nm, three biological repeats was performed for each sample, and a negative control (untreated cells), a water control (cells treated with 10% water in complete media) and a positive control (cells treated with triton X-100 detergent for 1 hour prior to MTT treatment). The absorbances of all samples were averaged and expressed as a % of negative control absorption, and are shown in Fig. 5.13 along with phase contrast images of all samples at the end of the particle treatment.

Absorption measurements were analysed by a one way analysis of variance (ANOVA) along with Tukey HSD tests to study the statistical relationship between sample sets. All samples showed a strong statistically significant difference with the positive control ($p < 0.01$) however none showed a statistically significant difference with any other treated sample or negative control. The water control did not appear to exhibit an effect on cell viability, despite initial expectations that a dilution of complete media would impose a positive response. Additionally, analysis of absorption measurements from treated cells, the water control and the negative control by a one-way anova resulted in a p value of 0.68, indicating no significant changes in sample variance across the dataset.

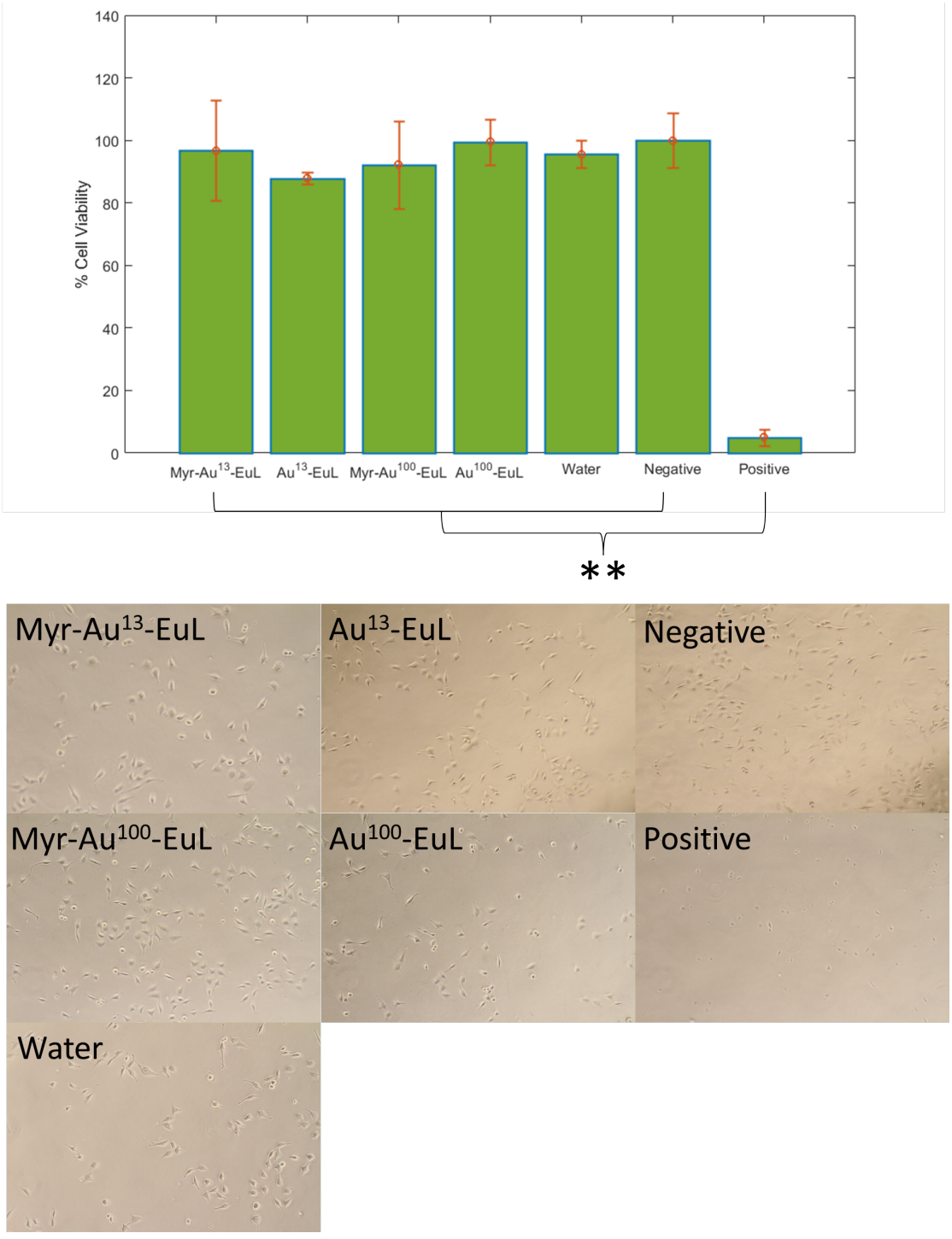

Figure 5.13: MTT of HeLa cells treated with Myristic-Au^{13}-EuL (1 nM) and Myristic-Au^{100}-EuL (8 pM) in complete media for 6 hours at 37°C. Also included are cells treated with water to examine the effect of media dilution on cell viability. Absorbance was recorded at 590 nm, and samples were normalised to the negative control of untreated HeLa cells in complete media. Cells treated with 0.5% Triton X-100 in DMEM were used as a positive control. Data composed of three biological repeats, presented with ± one standard deviation unit, and Tukey HSD test data was also included, where statistically significant p-values of <0.05, <0.01, <0.001 are indicated by *, **, and ***, respectively.

5.3 Conclusions

In summary, 13 nm and 100 nm diameter gold nanoparticles were synthesised and co-labelled with a lipid and luminescent europium complex. Labelled particles were structurally characterised by dynamic light scattering and transmission electron microscopy as monodisperse spherical particles. The steady state photophysical properties of the labelled particles was then assessed by luminescence spectroscopy demonstrating successful synthesis of luminescent nanoparticles bearing the Eu^{3+} luminescent signature. Both Myr-Au^{13}-EuL & Myr-Au^{100}-EuL showed the characteristic EuL emission lines upon excitation at 340 nm, and band positions were not affected by plasmon interactions with the gold surfaces. Cells treated with Myr-Au^{13}-EuL & Myr-Au^{100}-EuL appeared to be uptaken more efficiently than cells treated with the non-myristoylated analogues Au^{13}-EuL & Au^{100}-EuL as demonstrated by ICP-MS measurements and reflection microscopy, indicating that these labelled AuNPs with a hydrophobic coating offer improved uptake efficiency over non-myristoylated particles. Microscopy studies demonstrated Myr-Au^{13}-EuL's potential as a luminescence imaging probe, as well as an indication that Myr-Au^{100}-EuL & Au^{100}-EuL particles are internalized into cell cytoplasmic regions. Cells treated with Myr-Au^{13}-EuL or Myr-Au^{100}-EuL did not show any cytotoxic response after a 6 hour treatment time, as measured by the MTT reduction assay, which provided an assessment of cell viability through measuring mitochondrial activity. This further adds to the overall project conclusion that gold nanoparticles provide a non-cytotoxic scaffold to build cellular delivery agents.

5.4 Future Work

In this work I have presented evidence that labelling AuNPs with a simple lipid offers a higher efficiency of uptake into cancer cells than nanoparticles devoid of a lipid coating. This evidence would be much stronger if backed up with additional repeats of the ICP-MS analysis of Myr-Au^{13}-EuL versus Au^{13}-EuL uptake into HeLa cells. This would be supplemented with FACS analysis of Myr-Au^{100}-EuL versus Au^{100}-EuL uptake into HeLa cells. Additionally, time resolved studies would be important to study the effect that myristic acid and the gold nanoarticles impose on EuL luminescence. A comprehensive analysis of the cytotoxicity of all labelled-AuNPs used in this chapter would also be an important step, paying particular focus on concentration and incubation time.

5.5 Experimental

5.5.1 Chemicals and Reagents

All materials and reagents were purchased from Sigma Aldrich, VWR or Fisher Scientific and used without any modification unless specified.

5.5.2 Synthesis of luminescent Europium complex, EuL

EuL was prepared by Johnathon Lilley according to the protocol of Davies et al. [139]. The ligand H_3L was characterised by ^1H & ^{13}C nuclear magnetic resonance and mass spectrometry. 1H NMR (300 MHz, d6-DMSO) δH ppm: 10.19 (2H, br, NH), 8.82 (2H, d, J = 3.8, Hh), 8.34 (2H, d, J = 8.4, Hj), 7.57 (2H, d, J = 8.2, Hl) 7.49 (2H, dd, J = 8.4, 3.8, Hi), 7.06 (2H, d, J = 8.2, Hk), 4.08 (4H, t, J = 6.6, Hg), 3.48 (8H, s, Hm, Hp), 3.41 (2H, s, Hq), 3.03 (4H, br, Ho), 2.92 (4H, br, Hn), 2.85 (4H, t, J = 7.1, Hb), 2.32 (6H, s, Ha), 1.81 (4H, t, J = 6.6, Hf), 1.60 1.35 (12H, m, Hc, Hd, He). 13C NMR (400 MHz, d^6-DMSO) δC ppm: 195.3, 173.6, 170.2, 152.3, 148.6, 139.6, 131.7, 125.9, 124.4, 122.3, 121.2, 108.6, 68.3, 58.9, 57.3, 55.3, 52.3, 51.4, 30.6, 29.1, 28.6, 28.3, 27.9, 25.1. MS (ES-TOF)+ m/z: 994.9 [M + H]+.

H_3L (0.21 g, 0.21 mmol, 1.00 eq) was dissolved in THF : H_2O (20 ml, 1:1 by volume) and the pH was adjusted to 6 with addition of TBAOH (40% in water). A solution of $EuCl_3.6H_2O$ (0.08 g, 0.21 mmol, 1.00 eq.) in water (4 ml) was prepared and added to the H3QuinSAc solution. The vessel holding the $EuCl_3.6H_2O$ solution was washed out with water (2 x 1 ml) and this was also added to the H_3L solution. The solution was left to stir for 15 minutes at RT, whereupon the THF was removed in vacuo and the pH was adjusted to 6 with addition of TBAOH (40% in water), which yielded a tarry precipitate. The water was decanted out and the precipitate triturated in acetone for 1 hour, filtered and further triturated with MeCN for 1 hour and filtered to give EuL as a brown powder (0.17 g, 0.15 mmol, 71%). MS (ES-TOF)+ m/z: 1144.4 [M + H]+.

5.5.3 Synthesis of colloidal gold

13 nm citrate-stabilized AuNPs were synthesized by the method according to Schulz et al.[159] and subsequently a seeded growth protocol by Ziegler et al. [69] was used with 13 nm AuNP seeds to synthesise 100 nm diameter AuNPs. Particles were characterized by dynamic light scattering, capilliary electrophoresis, transmission electron microscopy and UV/Vis absorption spectroscopy. The approximate concentrations have also been estimated as 1.6 nM for Au^{13}NPs and 40 pM for Au^{100}NPs.

Synthesis of Au^{13}NPs

For Au^{13}NPs, the method of Schulz et al.[159] was followed with a few modifications. Refer to chapter 2 for complete characterisation. Briefly, a solution of trisodium citrate (60.6 mg), citric acid (13.3 mg) and ethylenediaminetetraacetic acid (1.0 mg) in H_2O (100 mL) was brought to reflux with rapid stirring. Rapid addition of $HAuCl_4$ (8.0 mg) in H_2O (25 mL) to the vortex of the solution resulted in a colour change from pale colourless to a deep wine red, approximately 30 seconds post-addition. Boiling was continued for an additional 10 minutes, the heating mantle was then removed and stirring was continued until particles had cooled to room temperature. The colloid was characterized by a UV/Vis absorption at 516 nm, a zeta potential (ζ) of -37 $\pm$ 7 mV (pH 6.2), and DLS number distribution indicated a particle size of 11 $\pm$ 3 nm.

Transmission electron microscopy also confirmed the synthesis of approximately 13 nm seeds.

Synthesis of Au^{25}NPs

Au^{13}NPs (34 mL) were diluted to 40 mL with H_2O, and stirred rapidly in a roundbottom flask equipped with a reflux condenser. Solutions of i) trisodium citrate and ascorbic acid in H_2O (20 mL) and ii) $HAuCl_4$ in H_2O were both simultaneously added to the colloidal solution in a dropwise fashion. After addition was complete, the mixture was heated at 150°C for 30 minutes, and then allowed to cool slowly to room temperature.

Synthesis of Au^{50}NPs

Au^{25}NPs (9 mL) were diluted to 40 mL with H_2O, and stirred rapidly in a roundbottom flask equipped with a reflux condenser. Solutions of i) trisodium citrate and ascorbic acid in H_2O (20 mL) and ii) $HAuCl_4$ in H_2O were both simultaneously added to the colloidal solution in a dropwise fashion. After addition was complete, the mixture was heated at 150°C for 30 minutes, and then allowed to cool slowly to room temperature.

Synthesis of Au^{100}NPs

Au^{50}NPs (40 mL) were stirred rapidly in a roundbottom flask equipped with a reflux condenser. Solutions of i) trisodium citrate and ascorbic acid in H_2O (20 mL) and ii) $HAuCl_4$ in H_2O were both simultaneously added to the colloidal solution in a dropwise fashion. After addition was complete, the mixture was heated at 150°C for 30 minutes, and then allowed to cool slowly to room temperature.

5.5.4 Preparation of cells for Fluorescence-Activated Cell Sorting (FACS)

Prior to treatment, cells were plated into a 12-well culture plate and allowed to grow to approximately 60% confluency. Cells were then washed with buffers before being treated with particles in a Tyrodes buffer(0.08 mM, pH 6.5 or 7.4), for a series of incubation times upto three hours. After treatment was complete, the supernatant from each well was removed and each well was washed with PBS (0.1 M, 0.5 mL) twice before being trypsinised at 37°C for 10 minutes. Particles were then spun down at 1500 rpm for 10 minutes, the supernatant removed, and redispersed in of PBS (0.1 M, 1 mL). Cell suspension was transferred to a FACS tube before analysis. for all samples, the parameters of Forward Scatter, Side Scatter, and far red luminescence were measured (488 nm excitation, emission >620 nm). 15,000 events were recorded for each sample.

5.5.5 Preparation of cells for Confocal Microscopy

Preparation for Fixed Cell Imaging

For fixed cell imaging, glass coverslips were sterilised using absolute ethanol (rinsed and left to dry) and placed into the wells of 6-well culture plates. $5x10^4$ cells were then seeded into each well of the 6-well culture plates on top of glass coverslips and allowed to grow to confluency for 24 hours. Before treatment, media from each well was removed and cells were washed twice with the media used in the seeding experiment, before being sequentially treated with the media and particles. After treatment, medium was removed and cells were washed with PBS (2 mL x 2) and then paraformaldehyde (4% in 0.1M PBS, 2 mL) was added and cells were left for 10 minutes at room temperature. Fixative was removed and cells were washed with PBS (2 mL x 2). Cells were then mounted onto glass microscope slides, using a drop of non-fluorescing Hydromount to maintain sample hydration, before sealing the slide with nail varnish. Slides were left to dry in a cold room and were imaged within a few days.

Preparation for Live Cell Imaging

For live cell imaging, $5x10^4$ cells were then seeded into the well of a MatTek(R) glass-bottom microscopy dish and allowed to grow to confluency for 24 hours. Before treatment, media from each well was removed and cells were washed twice with the media used in the seeding experiment, before being sequentially treated with the media and particles. After treatment, medium was removed and cells were washed with PBS (2 mL x 2) and then PBS (2 mL) was added before transferring samples to the microscope for acquisition.

5.5.6 Preparation of cells for Inductively Coupled Plasma - Mass Spectrometry

HeLa cells were cultured as per above and treated as per the relevant experiment. After treatment was complete, the supernatant from each well was removed and each well was washed with PBS (0.1 M, 0.5 mL) twice before being trypsinised at 37°C for 10 minutes. Particles were then spun down at 20,000 rpm for 10 minutes, the supernatant completely removed taking care not to disturb the cell pellet, before being allowed to dissolve overnight in 200 μL of ultrapure aqua regia (3:1 volumetric ratio of hydrochloric and nitric acid). Post dissolution, samples were diluted in ultrapure nitric acid (2700 μL of a 4% solution) prior to analysis.

5.5.7 Preparation of cells for Transmission Electron Microscopy

Samples were then imaged on a JEOL JEM-1200EX and a JEOL JEM-2100 electron microscope each fitted with a Tungsten electron source and a Gatan camera. Cell samples were fixed with a solution of Paraformaldehyde (4%) and Glutaraldehyde (2.5%) in phosphate buffered saline for two hours, prior to sectioning and mounting onto formvar-coated copper grids.

5.5.8 Analysing Cell Viability of Nanoparticle-treated HeLa cells

After treatment of HeLa cells with labelled-AuNPs, the media from each well was withdrawn and cells were washed with PBS (500 μl) and replaced with 3-(4,5-dimethyl-2-thiazolyl)-2,5-diphenyl-2H-tetrazolium bromide (0.5 mg/ml) in complete media (90% by volume), and were reincubated at 37°C for 2 hours. After the incubation, media was removed and DMSO (500 μl) was added to solubilise the formazan product. The plate was rocked for 15 minutes in the dark before the absorption at 590 nm was recorded against a DMSO blank.

Chapter 6

Project Evaluation & Future Study

6.1 Project Conclusions

In this work, functional imaging probes were constructed from 13 nm (Au^{13}) & 100 nm (Au^{100}) diameter gold nanoparticles. Aqueous gold nanoparticles were labelled using targeting vectors based on a myrisityl lipid or the pHLIP cell penetrating peptide series, along with a metal complex lumophore where suitable combinations were chosen to suit application and experiment. The lumophores chosen were built from ruthenium and europium complexes (RubpySS and EuL, respectively), and covalently labelled to gold nanoparticles via long alkyl chains to maximise their emission by reducing the potential of Au surface quenching.

Effective surface labelling protocols were established such that the nanopartices were labelled with a high density of lumophores in order to ensure nanoparticles were sufficiently luminescent, whilst still retaining good nanoparticle monodispersity. The maximum possible density of surface bound RubpySS lumophores was limited by colloidal stability, resultant from the labelling of negatively-charged nanoparticles with a positively-charged lumophore. Despite this, it was found that pHLIP variants were able to stabilise the nanoarticles during RubpySS loading and nanoparticles were successfully labelled with 140 - 270 RubpySS labels and 35,000 - 66,000 RubpySS labels for Au^{13} & Au^{100} respectively. Additionally, the labelling protocols were refined by varying the loading concentrations, volumes and stirring speed in order to yield homogenously labelled nanopartices which were stable at physiological pH, which was important to ensure that interaction & uptake of labelled particles was consistent for all particles within the colloid. The labelling of nanoparticles with the europium complex, EuL was more facile as the neutral complex did not promote nanoparticle flocculation during surface labelling.

The RubpySS complex showed emission enhancement when bound to an Au nanoparticle surface and when dispersed into peptide solutions through lengthened luminescence lifetimes, suggesting a reduction of quenching mechanisms. Additionally, the labelled-Au^{100} nanoparticles were highly luminescent during in-flow imaging where individual particles were visualized in scatter and luminescence modes. Au^{13} &

Au^{100} nanoparticles labelled with RubpySS were sufficiently luminescent for confocal imaging of treated cells, permitting the visualisation of Au^{13}NPs during live conditions that are not observable by reflectance imaging.

pHLIP-$Au^{13\&100}$-RubpySS and pHLIPvar3-$Au^{13\&100}$-RubpySS nanoparticles were readily uptaken into cultured human cervical adenocarcinoma cell monolayers within 15 minutes, and were easily visible by luminescence, reflection & TEM imaging, and gold concentrations were measured from treated cell samples using using ICP-Mass spectrometry. The measured pH-dependent uptake of gold nanoparticles mediated by pHLIP & pHLIPvar3 was consistent across each of these techniques, demonstrating that these peptides mediate the delivery of gold nanoparticles into cancer cells using pH as a biomarker for the disease. These techniques also demonstrate the multimodal potential of these probes, and the strong correlation between flow cytometry scatter and luminescence data proved useful in characterising nanoparticle internalization & dispersity as well as reinforcing the reliability of measuring luminescence from surface bound lumophores.

The pHLIPvar3 peptide proved to be an efficient mediator of pH-driven cellular transduction of labelled gold nanoparticle cargoes. Within two hour treatments the peptide facilitated significantly greater nanoparticle internalization ($p < 0.01$, by flow cytometry luminescence) of cells maintained under cancerous conditions than cells maintained under normal physiological conditions. This was consistent for both labelled-Au^{13} and labelled-Au^{100} nanoparticles, and the peptide was demonstrably more effective as a pH-triggered cellular delivery vector than the Wt-pHLIP. TEM imaging indicated that internalized pHLIP-labelled nanoparticles were located in a variety of intracellular spaces including within free cytosol, vesicular regions, and membrane regions, suggesting that subsequent nuclear or mitochondrial targeting may be possible. Cells treated with the non-pH targetting Zonyl-$Au^{13\&100}$-RubpySS nanoparticles did not display pH-dependent internalisation, indicating that the efficiency of endocytotic mechanisms were not affected within the pH range used in experiments.

Modulation of intracellular glutathione of human cervical adenocarcinoma cells also revealed that Au^{100} nanoparticles labelled with pHLIPvar3 were sensitive to glutathione (GSH) concentration, and it was observed that these particles were uptaken more efficiently into cells that exhibited higher concentrations of GSH ($p < 0.01$, by flow cytometry luminescence) in a manner that appeared independent of endocytotic mechanisms, and was not demonstrated by Wt-pHLIP labelled AuNPs. The reducing nature of GSH appeared to have a destabilising effect on pHLIPvar3-labelled nanoparticles, as demonstrated by observing the addition of GSH to nanoarticles in solution, but it is not clear at present how greater GSH concentration facilitates a more efficient nanoparticle uptake efficiency. The treatment of [GSH]-modified HeLa cells with Zonyl-Au^{100}-RubpySS did not result in differential internalization efficiencies, indicating that endocytotic mechanisms were not affected by intracellular GSH concentration.

It was also demonstrated in this work that gold nanoparticles that had been rendered more hydrophobic by labelling their surfaces with a myrisityl lipid were more efficiently internalized by human cervical adenocarcinoma cells than non-labelled analogues, as demonstrated by ICP-MS and confocal microscopy.

Labelling AuNPs with lipids improves their uptake efficiency, and the inclusion of the lipid into the particle's surface label did not impose a cytotoxic effect on the treated cells. The EuL luminescent signal from the $^5D_0 \longrightarrow ^7 F_2$ band was also detected from cells treated with Myr-Au^{13}-EuL demonstrating the suitability of these particles for cellular imaging applications.

The labelled-AuNPs studied in this work all possessed zeta potentials < -30 mV, this indicates that these particles are stable species that do not appear to significantly leach surface labels. The inert nature of these labelled nanoparticles offers benefits for future use within photothermal applications as it is important to have a therapeutic that only becomes cytotoxic upon irradiation, and not when only internalized. To the author's knowledge, 100 nm AuNPs are the largest nanoparticle cargo that has been delivered into cells via a pHLIP-mediated, pH-dependent mechanism. This demonstrates pHLIP's vesatility for delivering large cargoes in a pH dependent manner, opening the avenue for future research into exploitation of AuNP size dependency on the effectiveness of photothermal therapeutics constructed from AuNPs, in which individual particles can easily be imaged. Additionally, this work includes images of internalized pHLIP-labelled AuNPs taken under live conditions and without any enhancement solutions. Also highlighted in this work was the effect of colloidal stability on the internalisation efficiency of labelled-AuNPs. As any pH-resolved treatment of cells involves dispersion of sample within different buffers, the effect of each buffer on colloidal stability must be known in order to produce a reliable experiment, and such information has been missing from many peer-reviewed publications of pH-dependent nanoparticle delivery into cells.

6.2 Future Work

The next objective to pursue would be for the development of theranostic multimodal nanoprobes. The use of targeted delivery of gold nanoparticles within photothermal therapy is becoming more common due to the good efficiency that gold nanoparticles release heat when excited with NIR radiation. This work is strongly paving the way towards a new form of photothermal probe, particularly as high loadings of internalized particles are shown to be free from vesicular compartments, raising the possibility for subsequent targeting. Subsequent targeting to nuclei or mitochondria would enable the application of these particles within photothermal therapy to be more effective, and more likely that treatment results in cell mortality. Additionally, the incorporation of a surface label that releases reactive oxygen species upon photoirradiation would enable application of these nanoparticles within photodynamic therapies. One such method where this might be achieved would be incorporation of porphyrin rings into the ruthenium complex [367]. Additionally, the manipulation of intracellular GSH concentration may be useful to improve nanoparticle internalization efficiency, and thereby improve the effectiveness of the treatment, and therefore does deserve additional investigation.

Chapter 7

Materials & Methods

7.1 Materials

All materials were purchased from Sigma Aldrich, VWR International or Fisher Scientific, and were used without modification unless stated.

pHLIP (AAEQNPIYWARYADWLFTTPLLLLDLALLVDADEGTC(thiopyridyl)G), kpHLIP (AAEQNPIYWARYAKWLFTTPLLLLKLALLVDADEGTC(thiopyridyl)G) and pHLIPvar3 (ACDDQNPWRAYLDLLFPTDTLLLDLLWC) were synthesised by Peptide Synthetics, Southampton, UK and were dissolved in 5% DMF in phosphate buffered saline.

7.2 Molecular Structure Analysis

7.2.1 Nuclear Magnetic Resonance (NMR) Spectroscopy

^{1}H and ^{13}C1H PENDANT NMR spectra were recorded using a Bruker AC 300, AV 300, AMX 400 or AV 400 spectrometer, and $Si(CH_3)_4$ was used as the external reference.

7.2.2 Electrospray Ionisation (ESI) Mass Spectrometry

Electrospray mass spectrometry was performed using a Waters Micromass instrument with a time of flight mass analyser and a nitrogen laser.

7.3 Nanoparticle Structure Analysis

7.3.1 UV/Vis Absorption Spectroscopy

UV-Vis absorption spectra were recorded using a Varian Cary 50 or Varian Cary 5000 dual beam spectrometer. Samples were prepared in 1cm path length quartz cuvettes for acquisition, scanned at a rate of 300 nm min^{-1} and corrected for solvent absorption.

7.3.2 Laser Doppler Velocimetry/Dynamic Light Scattering

DLS measurements were carried out on a Malvern Zetasizer Nano ZS, using a 633 incident laser mounted at 178° off detection. For each experiment, averages of 5 technical repeat measurements were reported in this thesis.

7.3.3 Inductively Coupled Plasma Mass Spectrometry (ICP-MS)

ICP-MS was performed using at the University of Warwick, on an Agilent 7500cx ICP-MS with an integrated auto-sampler. Samples were digested using ultrapure aqua regia, before being diluted in 4% HNO_3 for analysis. Concentrations of ruthenium and gold in nanoparticle samples were determined using linear calibration curves constructed from purchased standards, with $R^2 > 0.998$ in all cases.

7.3.4 Laser Doppler Micro-Electrophoresis

Zeta Potential (ζ) measurements were recorded on a Malvern Zetasizer Nano ZS. Calibration was performed using a standard solution (carboxylated polystyrene latex dispersed in a pH 9.2) buffer prior to sample acquisition. For each experiment, averages of 3 technical repeat measurements were reported in this thesis.

7.4 Luminescence Characterisation Techniques

7.4.1 Luminescence Spectroscopy

Steady state luminescence spectra were acquired on an Edinburgh FLS920 Time Resolved Spectrometer fitted with a 450 W Xenon Arc lamp and a Hamamatsu R928 photomultiplier tube, or a Photon Technology International (PTI) L-210M fitted with a 75 W Xenon Arc lamp & a Shimadzu R298 photomultiplier tube in a model 814 analogue/photon counting multiplier. For emission scans, long-pass filters of 500 nm and 590 nm were used for ruthenium and europium complexes, respectively. For excitation scans of ruthenium complexes, a long pass filter of 590 nm was used.

7.4.2 Time-resolved luminescence measurements

Time-resolved luminescence measurements were acquired using the time correlated single photon counting (TCSPC) module of the Edinburgh FLS920 Time Resolved Spectrometer. Samples were excited using a 444 nm picosecond pulse-length diode laser, and a Hamamatsu R928 photomultiplier tube was used for detection. Upon acquisition of the lifetime data, the data was fitted by a Levernberg-Marquandt non-linear fitting algorithm using an arrhenius model function, and fitting was iterated until residual measurements appeared completely random and χ^2 values were as close to 1.000 as possible, with the smallest number of exponents as possible.

7.5 Cell Culture

The human alveolar adenocarcinoma A549 cell line (line 86012804) were purchased from the European cell Authority, and were cultured using Dulbeccos Modified Eagles Medium (DMEM) supplemented by 10% Foetal Bovine Serum (FBS) with Penicillin (100l) Streptomycin (100l) and L-Glutamine (100l), hereafter referred to as 'complete media'. Cells were cultured in 13 ml of complete media in vented T75 flasks at 37C with 5% CO2. Cells were routinely passaged by a 1 10 dilution using a Trypsin-EDTA protocol. Briefly, cell media was routinely replaced 48 - 72 hours after incubation. Old media was removed from the flask, and cells were washed with PBS (2ml) before brief incubation with Trypsin (2ml, and returned to incubation for 5 minutes) until cells had detached from the surface of the flask. Complete media (8 ml) was added to cells to quench the Trypsin, before cells were pelleted by centrifugation (1500rpm, 15 minutes). The supernatant was decanted, and cells were resuspended in fresh media (13 ml), seeded into a new flask and returned to incubation.

7.6 Flow Techniques

7.6.1 Fluorescence-Activated Cell Sorting (FACS)

Fluorescence-Activated Cell Sorting was performed on a FACS Calibur. The FACS Calibur was set up to record forward scatter, side scatter and luminescence (λ_{ex} = 488 nm, λ_{em} = >620 nm) with collection of at least 15,000 events per sample. Acquired data was then analysed using Flowing Software 2 to calculate mean values.

7.7 Nanosight

Nanoparticle tracking was performed using a Nanosight NS300 particle analyser equipped with a 55 mW 488 nm laser, operating in scatter mode with no dichroic mirrors in place, and luminescence mode with a 520 dichroic mirror in place.

7.8 Imaging Techniques

7.8.1 Confocal Microscopy

Confocal imaging was performed on three systems. ***i)*** Leica TCS SP2 Confocal system on a DMRE Inverted Microscope (Leica Microsystems). ***ii)*** The Nikon A1R Inverted Confocal/TIRF System on a Ti inverted microscope with an EMCCD and Spectral Detector. ***iii)*** The Zeiss LSM710 Confocal System on an Observer inverted Z1 microscope.

7.8.2 Epifluorescence Microscopy

Epi-imaging was performed using the Olympus IX71 Inverted Microscope attachment to the FLS920 Time Resolved Spectrometer, equipped with a LUCPLFLN 400.60 NA objective and a Hamamatsu electron-multiplying (EMCCD) C9100-13 camera.

7.8.3 Transmission Electron Microscopy

Biological samples were imaged using Jeol 1200EX TEM operating at a voltage 80 keV, fitted with a LaB6 filament, and Gatan multiscan camera. Images were acquired using Digital Micrograph 1.8 (Gatan, CA, USA). EDAX measurements were performed using a Jeol 2100 LaB6 TEM fitted with an Oxford Instruments INCA EDS system with a tungsten filament electron source and a Gatan camera.

7.9 Colorimetric Assays

MTT absorption measurements were performed using a Tecan Infinite F200 Pro plate reader measuring absorption at 590 nm, and GSH luminescence measurements were performed using a Perkin Elmer LS 50B luminescence spectrometer.

Bibliography

[1] Michael Faraday. "The Bakerian lecture: experimental relations of gold (and other metals) to light". In: *Philosophical Transactions of the Royal Society of London* 147 (1857), pp. 145–181.

[2] John Turkevich, Peter Cooper Stevenson, and James Hillier. "A study of the nucleation and growth processes in the synthesis of colloidal gold". In: *Discussions of the Faraday Society* 11 (1951), pp. 55–75.

[3] G Frens. "Particle size and sol stability in metal colloids". In: *Kolloid-Zeitschrift und Zeitschrift für Polymere* 250.7 (1972), pp. 736–741.

[4] John Funkhouser. "Reinventing pharma: the theranostic revolution". In: *Curr. Drug Discovery* 2 (2002), pp. 17–19.

[5] François J Picard and Michel G Bergeron. "Rapid molecular theranostics in infectious diseases". In: *Drug discovery today* 7.21 (2002), pp. 1092–1101.

[6] Partha Ghosh et al. "Gold nanoparticles in delivery applications". In: *Advanced drug delivery reviews* 60.11 (2008), pp. 1307–1315.

[7] Umbreen Shaheen, Yann Cesbron, SÃ Violaine, et al. "Gold nanoparticles delivery in mammalian live cells: a critical review". In: *Nano Reviews & Experiments* 1 (2010).

[8] Xiaohua Huang et al. "Plasmonic photothermal therapy (PPTT) using gold nanoparticles". In: *Lasers in medical science* 23.3 (2008), pp. 217–228.

[9] Denise Bechet et al. "Nanoparticles as vehicles for delivery of photodynamic therapy agents". In: *Trends in biotechnology* 26.11 (2008), pp. 612–621.

[10] M Wang and M Thanou. "Targeting nanoparticles to cancer". In: *Pharmacological Research* 62.2 (2010), pp. 90–99.

[11] Steven D Perrault et al. "Mediating tumor targeting efficiency of nanoparticles through design". In: *Nano letters* 9.5 (2009), pp. 1909–1915.

[12] Weibo Cai et al. "Applications of gold nanoparticles in cancer nanotechnology". In: *Nanotechnology, science and applications* 2008.1 (2008).

[13] Nils Johnsson and Kai Johnsson. "Chemical tools for biomolecular imaging". In: *ACS chemical biology* 2.1 (2007), pp. 31–38.

[14] Luciano Bachmann et al. "Fluorescence spectroscopy of biological tissuesa review". In: *Applied Spectroscopy Reviews* 41.6 (2006), pp. 575–590.

[15] Kadir Aslan et al. "Metal-enhanced fluorescence: an emerging tool in biotechnology". In: *Current Opinion in Biotechnology* 16.1 (2005), pp. 55–62.

[16] Marcus Dyba and Stefan W Hell. "Focal spots of size $\lambda/23$ open up far-field florescence microscopy at 33 nm axial resolution". In: *Physical review letters* 88.16 (2002), p. 163901.

[17] Partha Pratim Mondal. "Temporal resolution in fluorescence imaging". In: *Frontiers in Molecular Biosciences* 1 (2014).

[18] Marcus Dyba, Stefan Jakobs, and Stefan W Hell. "Immunofluorescence stimulated emission depletion microscopy". In: *Nature biotechnology* 21.11 (2003), pp. 1303–1304.

[19] Stefan W Hell and Jan Wichmann. "Breaking the diffraction resolution limit by stimulated emission: stimulated-emission-depletion fluorescence microscopy". In: *Optics letters* 19.11 (1994), pp. 780–782.

[20] Thomas A Klar et al. "Fluorescence microscopy with diffraction resolution barrier broken by stimulated emission". In: *Proceedings of the National Academy of Sciences* 97.15 (2000), pp. 8206–8210.

[21] Rainer Heintzmann and Christoph G Cremer. "Laterally modulated excitation microscopy: improvement of resolution by using a diffraction grating". In: *BiOS Europe'98*. International Society for Optics and Photonics. 1999, pp. 185–196.

[22] Eric Betzig et al. "Imaging intracellular fluorescent proteins at nanometer resolution". In: *Science* 313.5793 (2006), pp. 1642–1645.

[23] Samuel T Hess, Thanu PK Girirajan, and Michael D Mason. "Ultra-high resolution imaging by fluorescence photoactivation localization microscopy". In: *Biophysical journal* 91.11 (2006), pp. 4258–4272.

[24] Keith A Lidke et al. "Superresolution by localization of quantum dots using blinking statistics". In: *Optics express* 13.18 (2005), pp. 7052–7062.

[25] Rainer Heintzmann and Gabriella Ficz. "Breaking the resolution limit in light microscopy". In: *Briefings in functional genomics & proteomics* 5.4 (2006), pp. 289–301.

[26] GG Stokes. "On the change of refrangibility of light. No. II". In: *Philosophical Transactions of the Royal Society of London* 143 (1853), pp. 385–396.

[27] E Becquerel. "Des effets produits sur les corps par les rayons solaires". In: *Ann. de Chim. et de Phys* 9 (1843), pp. 257–322.

[28] M Sameiro T Gonçalves. "Fluorescent labeling of biomolecules with organic probes". In: *Chemical reviews* 109.1 (2008), pp. 190–212.

[29] Daniel Hechler, Robert Nitsch, and Sven Hendrix. "Green-fluorescent-protein-expressing mice as models for the study of axonal growth and regeneration in vitro". In: *Brain research reviews* 52.1 (2006), pp. 160–169.

[30] C Neal Stewart. "Go with the glow: fluorescent proteins to light transgenic organisms". In: *Trends in biotechnology* 24.4 (2006), pp. 155–162.

[31] Jonathon Pines. "GFP in mammalian cells". In: *Trends in genetics* 11.8 (1995), pp. 326–327.

[32] Bensheng Ju et al. "Faithful expression of green fluorescent protein(GFP) in transgenic zebrafish embryos under control of zebrafish gene promoters". In: *Developmental genetics* 25.2 (1999), pp. 158–167.

[33] Nicholas Marsh-Armstrong et al. "Germ-line transmission of transgenes in Xenopus laevis". In: *Proceedings of the National Academy of Sciences* 96.25 (1999), pp. 14389–14393.

[34] D Errampalli et al. "Applications of the green fluorescent protein as a molecular marker in environmental microorganisms". In: *Journal of microbiological methods* 35.3 (1999), pp. 187–199.

[35] Marcel Bruchez et al. "Semiconductor nanocrystals as fluorescent biological labels". In: *science* 281.5385 (1998), pp. 2013–2016.

[36] Thomas J Deerinck, Ben NG Giepmans, and Mark H Ellisman. "Quantum dots as cellular probes for light and electron microscopy". In: *MICROSCOPY AND MICROANALYSIS-NEW YORK-* 11 (2005), p. 914CD.

[37] Rozalia Nisman et al. "Application of quantum dots as probes for correlative fluorescence, conventional, and energy-filtered transmission electron microscopy". In: *Journal of Histochemistry & Cytochemistry* 52.1 (2004), pp. 13–18.

[38] Ute Resch-Genger et al. "Quantum dots versus organic dyes as fluorescent labels". In: *Nature methods* 5.9 (2008), pp. 763–775.

[39] Steven F Lee and Mark A Osborne. "Brightening, blinking, bluing and bleaching in the life of a quantum dot: friend or foe?" In: *ChemPhysChem* 10.13 (2009), pp. 2174–2191.

[40] Kim M Tsoi et al. "Are quantum dots toxic? Exploring the discrepancy between cell culture and animal studies". In: *Accounts of chemical research* 46.3 (2012), pp. 662–671.

[41] Xiaohui Wang et al. "Recent developments in lanthanide-based luminescent probes". In: *Coordination Chemistry Reviews* 273 (2014), pp. 201–212.

[42] David J Lewis and Zoe Pikramenou. "Lanthanide-coated gold nanoparticles for biomedical applications". In: *Coordination Chemistry Reviews* 273 (2014), pp. 213–225.

[43] Ute Neugebauer et al. "Ruthenium polypyridyl peptide conjugates: membrane permeable probes for cellular imaging". In: *Chemical Communications* 42 (2008), pp. 5307–5309.

[44] Nick D Hadjiliadis and Einar Sletten. *Metal complex-DNA interactions*. Wiley Online Library, 2009.

[45] Richard J Watts. "Ruthenium polypyridyls: A case study". In: *J. Chem. Educ* 60.10 (1983), p. 834.

[46] Bernard Valeur and Mário Nuno Berberan-Santos. *Molecular fluorescence: principles and applications*. John Wiley & Sons, 2012.

[47] J Van Houten and Richard J Watts. "Effect of ligand and solvent deuteration on the excited state properties of the tris (2, 2'-bipyridyl) ruthenium (II) ion in aqueous solution. Evidence for electron transfer to solvent". In: *Journal of the American Chemical Society* 97.13 (1975), pp. 3843–3844.

[48] Cindy A Puckett and Jacqueline K Barton. "Methods to explore cellular uptake of ruthenium complexes". In: *Journal of the American Chemical Society* 129.1 (2007), pp. 46–47.

[49] M Emilia Jiménez-Hernández et al. "A Ruthenium Probe for Cell Viability Measurement Using Flow Cytometry, Confocal Microscopy and Time-resolved Luminescence". In: *Photochemistry and photobiology* 72.1 (2000), pp. 28–34.

[50] Cliff J Timpson, Charles C Carter, and John Olmsted III. "Mechanism of quenching of electronically excited ruthenium complexes by oxygen". In: *The Journal of Physical Chemistry* 93.10 (1989), pp. 4116–4120.

[51] Klaus Suhling, Paul MW French, and David Phillips. "Time-resolved fluorescence microscopy". In: *Photochemical & Photobiological Sciences* 4.1 (2005), pp. 13–22.

[52] Hans C Gerritsen et al. "Fluorescence lifetime imaging of oxygen in living cells". In: *Journal of fluorescence* 7.1 (1997), pp. 11–15.

[53] Cindy A Puckett and Jacqueline K Barton. "Fluorescein redirects a ruthenium- octaarginine conjugate to the nucleus". In: *Journal of the American Chemical Society* 131.25 (2009), pp. 8738–8739.

[54] Hirokazu Komatsu et al. "Ruthenium complexes with hydrophobic ligands that are key factors for the optical imaging of physiological hypoxia". In: *Chemistry–A European Journal* 19.6 (2013), pp. 1971–1977.

[55] Martin R Gill et al. "Targeting the endoplasmic reticulum with a membrane-interactive luminescent ruthenium (ii) polypyridyl complex". In: *Chemical science* 4.12 (2013), pp. 4512–4519.

[56] Elizabeth Baggaley et al. "Dinuclear Ruthenium (II) Complexes as Two-Photon, Time-Resolved Emission Microscopy Probes for Cellular DNA". In: *Angewandte Chemie International Edition* 53.13 (2014), pp. 3367–3371.

[57] Heather J Montgomery et al. "Examination of the silver colloid binding behavior of disulfide-tethered bipyridine ligands and their fac-tricarbonylrhenium (I) complexes". In: *Inorganic chemistry* 50.7 (2011), pp. 2738–2747.

[58] AJ Amoroso et al. "ndez-Moreira, JB Hess, AJ Hayes, D. Lloyd, C. Millet, SJA Pope and C. Williams". In: *Chem. Commun* 3066 (2007).

[59] Kenneth Kam-Wing Lo. "Luminescent rhenium (I) and iridium (III) polypyridine complexes as biological probes, imaging reagents, and photocytotoxic agents". In: *Accounts of chemical research* 48.12 (2015), pp. 2985–2995.

[60] KA King and RJ Watts. "Dual emission from an ortho-metalated iridium (III) complex". In: *Journal of the American Chemical Society* 109.5 (1987), pp. 1589–1590.

[61] Kenneth Kam-Wing Lo, Steve Po-Yam Li, and Kenneth Yin Zhang. "Development of luminescent iridium (III) polypyridine complexes as chemical and biological probes". In: *New Journal of Chemistry* 35.2 (2011), pp. 265–287.

[62] Matteo Mauro et al. "When self-assembly meets biology: luminescent platinum complexes for imaging applications". In: *Chemical Society Reviews* 43.12 (2014), pp. 4144–4166.

[63] Stanley W Botchway et al. "Time-resolved and two-photon emission imaging microscopy of live cells with inert platinum complexes". In: *Proceedings of the National Academy of Sciences* 105.42 (2008), pp. 16071–16076.

[64] Kenneth Yin Zhang et al. "Structure, photophysical and electrochemical properties, biomolecular interactions, and intracellular uptake of luminescent cyclometalated iridium (III) dipyridoquinoxaline complexes". In: *Inorganic chemistry* 49.5 (2010), pp. 2530–2540.

[65] Clive Yik-Sham Chung et al. "Induced self-assembly and disassembly of water-soluble alkynylplatinum (II) terpyridyl complexes with switchable near-infrared (NIR) emission modulated by metal–metal interactions over physiological pH: demonstration of pH-responsive NIR luminescent probes in cell-imaging studies". In: *Chemical Science* 4.6 (2013), pp. 2453–2462.

[66] Luisa De Cola et al. *Platinum complexes and their use*. US Patent 8,962,838. 2015.

[67] David A Giljohann et al. "Gold nanoparticles for biology and medicine". In: *Angewandte Chemie International Edition* 49.19 (2010), pp. 3280–3294.

[68] Erik C Dreaden et al. "The golden age: gold nanoparticles for biomedicine". In: *Chemical Society Reviews* 41.7 (2012), pp. 2740–2779.

[69] Christoph Ziegler and Alexander Eychmuller. "Seeded growth synthesis of uniform gold nanoparticles with diameters of 15- 300 nm". In: *The Journal of Physical Chemistry C* 115.11 (2011), pp. 4502–4506.

[70] Tapan K Sau and Catherine J Murphy. "Room temperature, high-yield synthesis of multiple shapes of gold nanoparticles in aqueous solution". In: *Journal of the American Chemical Society* 126.28 (2004), pp. 8648–8649.

[71] Pooja M Tiwari et al. "Functionalized gold nanoparticles and their biomedical applications". In: *Nanomaterials* 1.1 (2011), pp. 31–63.

[72] Xiaohua Huang and Mostafa A El-Sayed. "Gold nanoparticles: optical properties and implementations in cancer diagnosis and photothermal therapy". In: *Journal of Advanced Research* 1.1 (2010), pp. 13–28.

[73] Subinoy Rana et al. "Monolayer coated gold nanoparticles for delivery applications". In: *Advanced drug delivery reviews* 64.2 (2012), pp. 200–216.

[74] K George Thomas and Prashant V Kamat. "Chromophore-functionalized gold nanoparticles". In: *Accounts of chemical research* 36.12 (2003), pp. 888–898.

[75] K George Thomas and Prashant V Kamat. "Making gold nanoparticles glow: Enhanced emission from a surface-bound fluoroprobe". In: *Journal of the American Chemical Society* 122.11 (2000), pp. 2655–2656.

[76] Zeljka Krpetic et al. "Negotiation of intracellular membrane barriers by TAT-modified gold nanoparticles". In: *ACS nano* 5.6 (2011), pp. 5195–5201.

[77] Paola Nativo, Ian A Prior, and Mathias Brust. "Uptake and intracellular fate of surface-modified gold nanoparticles". In: *ACS nano* 2.8 (2008), pp. 1639–1644.

[78] Lauren A Austin et al. "Cytotoxic effects of cytoplasmic-targeted and nuclear-targeted gold and silver nanoparticles in HSC-3 cells–A mechanistic study". In: *Toxicology in Vitro* 29.4 (2015), pp. 694–705.

[79] Elodie Boisselier and Didier Astruc. "Gold nanoparticles in nanomedicine: preparations, imaging, diagnostics, therapies and toxicity". In: *Chemical society reviews* 38.6 (2009), pp. 1759–1782.

[80] Rochelle R Arvizo et al. "Effect of nanoparticle surface charge at the plasma membrane and beyond". In: *Nano letters* 10.7 (2010), pp. 2543–2548.

[81] Gustav Mie. "Beiträge zur Optik trüber Medien, speziell kolloidaler Metallösungen". In: *Annalen der physik* 330.3 (1908), pp. 377–445.

[82] Stephan Link and Mostafa A El-Sayed. "Spectral properties and relaxation dynamics of surface plasmon electronic oscillations in gold and silver nanodots and nanorods". In: *The Journal of Physical Chemistry B* 103.40 (1999), pp. 8410–8426.

[83] Allen C Templeton et al. "Solvent refractive index and core charge influences on the surface plasmon absorbance of alkanethiolate monolayer-protected gold clusters". In: *The Journal of Physical Chemistry B* 104.3 (2000), pp. 564–570.

[84] Sylvia Underwood and Paul Mulvaney. "Effect of the solution refractive index on the color of gold colloids". In: *Langmuir* 10.10 (1994), pp. 3427–3430.

[85] W Rechberger et al. "Optical properties of two interacting gold nanoparticles". In: *Optics Communications* 220.1 (2003), pp. 137–141.

[86] Paul Mulvaney. "Spectroscopy of metal colloidsSome comparisons with semiconductor colloids". In: *Studies in Surface Science and Catalysis* 103 (1997), pp. 99–123.

[87] Min Hu et al. “Gold nanostructures: engineering their plasmonic properties for biomedical applications”. In: *Chemical Society Reviews* 35.11 (2006), pp. 1084–1094.

[88] Wolfgang Haiss et al. “Determination of size and concentration of gold nanoparticles from UV- Vis spectra”. In: *Analytical chemistry* 79.11 (2007), pp. 4215–4221.

[89] Chen Zhou et al. “Luminescent gold nanoparticles: a new class of nanoprobes for biomedical imaging”. In: *Experimental Biology and Medicine* 238.11 (2013), pp. 1199–1209.

[90] Chen Zhou et al. “Luminescent gold nanoparticles with mixed valence states generated from dissociation of polymeric Au (I) thiolates”. In: *The Journal of Physical Chemistry C* 114.17 (2010), pp. 7727–7732.

[91] Jie Zheng et al. “Different sized luminescent gold nanoparticles”. In: *Nanoscale* 4.14 (2012), pp. 4073–4083.

[92] T Gregory Schaaff et al. “Properties of a ubiquitous 29 kDa Au: SR cluster compound”. In: *The Journal of Physical Chemistry B* 105.37 (2001), pp. 8785–8796.

[93] Chen Zhou et al. “Grain size effects in polycrystalline gold nanoparticles”. In: *Nanoscale* 4.14 (2012), pp. 4228–4233.

[94] David J Lewis et al. “Luminescent nanobeads: attachment of surface reactive Eu (III) complexes to gold nanoparticles”. In: *Chemical communications* 13 (2006), pp. 1433–1435.

[95] James DET Wilton-Ely. “The surface functionalisation of gold nanoparticles with metal complexes”. In: *Dalton Transactions* 1 (2008), pp. 25–29.

[96] Nicola J Rogers et al. “High coating of Ru (II) complexes on gold nanoparticles for single particle luminescence imaging in cells”. In: *Chemical Communications* 50.5 (2014), pp. 617–619.

[97] Robert BP Elmes et al. “Luminescent ruthenium (II) polypyridyl functionalized gold nanoparticles; their DNA binding abilities and application as cellular imaging agents”. In: *Journal of the American Chemical Society* 133.40 (2011), pp. 15862–15865.

[98] Linda Zedler et al. “Ruthenium dye functionalized gold nanoparticles and their spectral responses”. In: *RSC Advances* 2.10 (2012), pp. 4463–4471.

[99] Iseult Lynch and Kenneth A Dawson. “Protein-nanoparticle interactions”. In: *Nano today* 3.1 (2008), pp. 40–47.

[100] Andre E Nel et al. “Understanding biophysicochemical interactions at the nano–bio interface”. In: *Nature materials* 8.7 (2009), pp. 543–557.

[101] Lev A Dykman and Nikolai G Khlebtsov. “Uptake of engineered gold nanoparticles into mammalian cells”. In: *Chemical reviews* 114.2 (2013), pp. 1258–1288.

[102] Jie An Yang, Samuel E Lohse, and Catherine J Murphy. “Tuning cellular response to nanoparticles via surface chemistry and aggregation”. In: *Small* 10.8 (2014), pp. 1642–1651.

[103] Iseult Lynch et al. “The nanoparticle–protein complex as a biological entity; a complex fluids and surface science challenge for the 21st century”. In: *Advances in colloid and interface science* 134 (2007), pp. 167–174.

[104] Arun K Iyer et al. “Exploiting the enhanced permeability and retention effect for tumor targeting”. In: *Drug discovery today* 11.17 (2006), pp. 812–818.

[105] Yasuhiro Matsumura and Hiroshi Maeda. “A new concept for macromolecular therapeutics in cancer chemotherapy: mechanism of tumoritropic accumulation of proteins and the antitumor agent smancs”. In: *Cancer research* 46.12 Part 1 (1986), pp. 6387–6392.

[106] Liang Han et al. “pH-Controlled Delivery of Nanoparticles into Tumor Cells”. In: *Advanced healthcare materials* 2.11 (2013), pp. 1435–1439.

[107] Fan Yuan et al. “Mirovascular permeability and interstitial penetration of sterically stabilized (stealth) liposomes in a human tumor xenograft”. In: *Cancer research* 54.13 (1994), pp. 3352–3356.

[108] Theresa M Allen and Pieter R Cullis. “Drug delivery systems: entering the mainstream”. In: *Science* 303.5665 (2004), pp. 1818–1822.

[109] Hiroshi Maeda, GY Bharate, and J Daruwalla. “Polymeric drugs for efficient tumor-targeted drug delivery based on EPR-effect”. In: *European Journal of Pharmaceutics and Biopharmaceutics* 71.3 (2009), pp. 409–419.

[110] Edward J Fox, Jesse J Salk, and Lawrence A Loeb. “Cancer genome sequencingan interim analysis”. In: *Cancer research* 69.12 (2009), pp. 4948–4950.

[111] Chenwei Li et al. “Identification of pancreatic cancer stem cells”. In: *Cancer research* 67.3 (2007), pp. 1030–1037.

[112] Erez Koren and Vladimir P Torchilin. “Cell-penetrating peptides: breaking through to the other side”. In: *Trends in molecular medicine* 18.7 (2012), pp. 385–393.

[113] Samad Mussa Farkhani et al. “Cell penetrating peptides: efficient vectors for delivery of nanoparticles, nanocarriers, therapeutic and diagnostic molecules”. In: *Peptides* 57 (2014), pp. 78–94.

[114] Bin Kang, Megan A Mackey, and Mostafa A El-Sayed. “Nuclear targeting of gold nanoparticles in cancer cells induces DNA damage, causing cytokinesis arrest and apoptosis”. In: *Journal of the American Chemical Society* 132.5 (2010), pp. 1517–1519.

[115] Alexander G Tkachenko et al. “Multifunctional gold nanoparticle-peptide complexes for nuclear targeting”. In: *Journal of the American Chemical Society* 125.16 (2003), pp. 4700–4701.

[116] Alan D Frankel and Carl O Pabo. “Cellular uptake of the tat protein from human immunodeficiency virus”. In: *Cell* 55.6 (1988), pp. 1189–1193.

[117] Maurice Green and Paul M Loewenstein. “Autonomous functional domains of chemically synthesized human immunodeficiency virus tat trans-activator protein”. In: *Cell* 55.6 (1988), pp. 1179–1188.

[118] JE King et al. “HIV tat and neurotoxicity”. In: *Microbes and Infection* 8.5 (2006), pp. 1347–1357.

[119] CC Berry. “Intracellular delivery of nanoparticles via the HIV-1 tat peptide”. In: (2008).

[120] Alan D Frankel, David S Bredt, and Carl O Pabo. “Tat protein from human immunodeficiency virus forms a metal-linked dimer”. In: *Science* 240.4848 (1988), p. 70.

[121] Haruhiko Siomi et al. “Effects of a highly basic region of human immunodeficiency virus Tat protein on nucleolar localization.” In: *Journal of virology* 64.4 (1990), pp. 1803–1807.

[122] Steven Ruben et al. “Structural and functional characterization of human immunodeficiency virus tat protein.” In: *Journal of virology* 63.1 (1989), pp. 1–8.

[123] Jonathan B Rothbard et al. “Arginine-rich molecular transporters for drug delivery: role of backbone spacing in cellular uptake”. In: *Journal of medicinal chemistry* 45.17 (2002), pp. 3612–3618.

[124] Eric Vives, Priscille Brodin, and Bernard Lebleu. “A truncated HIV-1 Tat protein basic domain rapidly translocates through the plasma membrane and accumulates in the cell nucleus”. In: *Journal of Biological Chemistry* 272.25 (1997), pp. 16010–16017.

[125] Jean Philippe Richard et al. “Cell-penetrating peptides A reevaluation of the mechanism of cellular uptake”. In: *Journal of Biological Chemistry* 278.1 (2003), pp. 585–590.

[126] David A Brake, Christine Debouck, and Gregory Biesecker. “Identification of an Arg-Gly-Asp (RGD) cell adhesion site in human immunodeficiency virus type 1 transactivation protein, tat”. In: *J Cell Biol* 111.3 (1990), pp. 1275–1281.

[127] Bruce E Vogel et al. “A novel integrin specificity exemplified by binding of the alpha v beta 5 integrin to the basic domain of the HIV Tat protein and vitronectin.” In: *The Journal of cell biology* 121.2 (1993), pp. 461–468.

[128] BS Weeks et al. “Identification of a novel cell attachment domain in the HIV-1 Tat protein and its 90-kDa cell surface binding protein.” In: *Journal of Biological Chemistry* 268.7 (1993), pp. 5279–5284.

[129] Jesus M de la Fuente and Catherine C Berry. “Tat peptide as an efficient molecule to translocate gold nanoparticles into the cell nucleus”. In: *Bioconjugate chemistry* 16.5 (2005), pp. 1176–1180.

[130] Vladimir P Torchilin et al. “TAT peptide on the surface of liposomes affords their efficient intracellular delivery even at low temperature and in the presence of metabolic inhibitors”. In: *Proceedings of the National Academy of Sciences* 98.15 (2001), pp. 8786–8791.

[131] Lin Wei, Qiaoyu Yang, and Lehui Xiao. “Tempo-spatially resolved cellular dynamics of human immunodeficiency virus transacting activator of transcription (Tat) peptide-modified nanocargos in living cells”. In: *Nanoscale* 6.17 (2014), pp. 10207–10215.

[132] John F Hunt et al. “Spontaneous, pH-dependent membrane insertion of a transbilayer α-helix”. In: *Biochemistry* 36.49 (1997), pp. 15177–15192.

[133] Oleg A Andreev, Donald M Engelman, and Yana K Reshetnyak. "pH-sensitive membrane peptides (pHLIPs) as a novel class of delivery agents". In: *Molecular membrane biology* 27.7 (2010), pp. 341–352.

[134] Oleg A Andreev et al. "pH (low) insertion peptide (pHLIP) inserts across a lipid bilayer as a helix and exits by a different path". In: *Proceedings of the National Academy of Sciences* 107.9 (2010), pp. 4081–4086.

[135] Sven Macholl et al. "In vivo pH imaging with 99mTc-pHLIP". In: *Molecular Imaging and Biology* 14.6 (2012), pp. 725–734.

[136] Eugene A Sosunov et al. "pH (low) insertion peptide (pHLIP) targets ischemic myocardium". In: *Proceedings of the National Academy of Sciences* 110.1 (2013), pp. 82–86.

[137] Lan Yao et al. "pHLIP®-mediated delivery of PEGylated liposomes to cancer cells". In: *Journal of Controlled Release* 167.3 (2013), pp. 228–237.

[138] Lan Yao et al. "pHLIP peptide targets nanogold particles to tumors". In: *Proceedings of the National Academy of Sciences* 110.2 (2013), pp. 465–470.

[139] Amy Davies et al. "pH-controlled delivery of luminescent europium coated nanoparticles into platelets". In: *Proceedings of the National Academy of Sciences* 109.6 (2012), pp. 1862–1867.

[140] Jinbin Liu et al. "Passive tumor targeting of renal-clearable luminescent gold nanoparticles: long tumor retention and fast normal tissue clearance". In: *Journal of the American Chemical Society* 135.13 (2013), pp. 4978–4981.

[141] Akihiko Nakano. "Spinning-disk confocal microscopya cutting-edge tool for imaging of membrane traffic". In: *Cell structure and function* 27.5 (2002), pp. 349–355.

[142] Ivan H El-Sayed, Xiaohua Huang, and Mostafa A El-Sayed. "Surface plasmon resonance scattering and absorption of anti-EGFR antibody conjugated gold nanoparticles in cancer diagnostics: applications in oral cancer". In: *Nano letters* 5.5 (2005), pp. 829–834.

[143] Konstantin Sokolov et al. "Real-time vital optical imaging of precancer using anti-epidermal growth factor receptor antibodies conjugated to gold nanoparticles". In: *Cancer research* 63.9 (2003), pp. 1999–2004.

[144] Hong Huang et al. "Peptide-directed synthesis of fluorescent gold nanoparticles for mitochondria-targeted confocal imaging of temperature". In: *Microchimica Acta* 184.4 (2017), pp. 1215–1221.

[145] PL Baldeck et al. "Ultrabright and bleaching-resistant hybrid gold nanoparticles for confocal and two-photon fluorecence imaging". In: *SPIE BiOS*. International Society for Optics and Photonics. 2014, 89560T–89560T.

[146] BP Robert, D CliveáWilliams, et al. "Ru (II)-polypyridyl surface functionalised gold nanoparticles as DNA targeting supramolecular structures and luminescent cellular imaging agents". In: *Nanoscale* 8.1 (2016), pp. 563–574.

[147] Mena Aioub et al. "Biological targeting of plasmonic nanoparticles improves cellular imaging via the enhanced scattering in the aggregates formed". In: *The journal of physical chemistry letters* 5.15 (2014), pp. 2555–2561.

[148] Lauren A Austin, Bin Kang, and Mostafa A El-Sayed. "A new nanotechnology technique for determining drug efficacy using targeted plasmonically enhanced single cell imaging spectroscopy". In: *Journal of the American Chemical Society* 135.12 (2013), pp. 4688–4691.

[149] Konstantin Sokolov et al. "Optical systems for in vivo molecular imaging of cancer". In: *Technology in cancer research & treatment* 2.6 (2003), pp. 491–504.

[150] Mena Aioub, Lauren A Austin, and Mostafa A El-Sayed. "Determining Drug Efficacy Using Plasmonically Enhanced Imaging of the Morphological Changes of Cells upon Death". In: *The journal of physical chemistry letters* 5.20 (2014), pp. 3514–3518.

[151] Halina Abramczyk and Beata Brozek-Pluska. "Raman imaging in biochemical and biomedical applications. Diagnosis and treatment of breast cancer". In: *Chemical reviews* 113.8 (2013), pp. 5766–5781.

[152] Christian W Freudiger et al. "Label-free biomedical imaging with high sensitivity by stimulated Raman scattering microscopy". In: *Science* 322.5909 (2008), pp. 1857–1861.

[153] Janina Kneipp et al. "In vivo molecular probing of cellular compartments with gold nanoparticles and nanoaggregates". In: *Nano Letters* 6.10 (2006), pp. 2225–2231.

[154] Bin Kang, Lauren A Austin, and Mostafa A El-Sayed. "Observing real-time molecular event dynamics of apoptosis in living cancer cells using nuclear-targeted plasmonically enhanced Raman nanoprobes". In: *ACS nano* 8.5 (2014), pp. 4883–4892.

[155] B Devika Chithrani, Arezou A Ghazani, and Warren CW Chan. "Determining the size and shape dependence of gold nanoparticle uptake into mammalian cells". In: *Nano letters* 6.4 (2006), pp. 662–668.

[156] Xi Liang, Zhou-jun Wang, and Chang-jun Liu. "Size-controlled synthesis of colloidal gold nanoparticles at room temperature under the influence of glow discharge". In: *Nanoscale research letters* 5.1 (2009), p. 124.

[157] Lesley Graham and Jan Marc Orenstein. "Processing tissue and cells for transmission electron microscopy in diagnostic pathology and research". In: *Nature protocols* 2.10 (2007), pp. 2439–2450.

[158] Katherine C Grabar et al. "Preparation and characterization of Au colloid monolayers". In: *Analytical chemistry* 67.4 (1995), pp. 735–743.

[159] Florian Schulz et al. “Little adjustments significantly improve the Turkevich synthesis of gold nanoparticles”. In: *Langmuir* 30.35 (2014), pp. 10779–10784.

[160] Absar Ahmad et al. “Extracellular biosynthesis of monodisperse gold nanoparticles by a novel extremophilic actinomycete, Thermomonospora sp.” In: *Langmuir* 19.8 (2003), pp. 3550–3553.

[161] G Singaravelu et al. “A novel extracellular synthesis of monodisperse gold nanoparticles using marine alga, Sargassum wightii Greville”. In: *Colloids and Surfaces B: Biointerfaces* 57.1 (2007), pp. 97–101.

[162] Edward R Knight et al. “Multimetallic Arrays: Bi-, tri-, tetra-, and hexametallic complexes based on gold (I) and gold (III) and the surface functionalization of gold nanoparticles with transition metals”. In: *Inorganic chemistry* 48.8 (2009), pp. 3866–3874.

[163] David J Lewis et al. “Silica nanoparticles for micro-particle imaging velocimetry: fluorosurfactant improves nanoparticle stability and brightness of immobilized iridium (III) complexes”. In: *Langmuir* 29.47 (2013), pp. 14701–14708.

[164] Feng Liu and Jean-Michel Nunzi. “Phosphorescent organic light emitting diode efficiency enhancement using functionalized silver nanoparticles”. In: *Applied Physics Letters* 99.12 (2011), p. 123302.

[165] J Kümmerlen et al. “Enhanced dye fluorescence over silver island films: analysis of the distance dependence”. In: *Molecular Physics* 80.5 (1993), pp. 1031–1046.

[166] Shani AM Osborne and Zoe Pikramenou. “Highly luminescent gold nanoparticles: effect of ruthenium distance for nanoprobes with enhanced lifetimes”. In: *Faraday discussions* 185 (2015), pp. 219–231.

[167] JR Bacon and JN Demas. “Determination of oxygen concentrations by luminescence quenching of a polymer-immobilized transition-metal complex”. In: *Analytical Chemistry* 59.23 (1987), pp. 2780–2785.

[168] Elizabeth R Carraway et al. “Photophysics and photochemistry of oxygen sensors based on luminescent transition-metal complexes”. In: *Analytical chemistry* 63.4 (1991), pp. 337–342.

[169] P Pramod et al. “Photochemistry of ruthenium trisbipyridine functionalized on gold nanoparticles”. In: *The Journal of Physical Chemistry B* 110.42 (2006), pp. 20737–20741.

[170] Oleg A Andreev et al. “Mechanism and uses of a membrane peptide that targets tumors and other acidic tissues in vivo”. In: *Proceedings of the National Academy of Sciences* 104.19 (2007), pp. 7893–7898.

[171] Leo E Gerweck and Kala Seetharaman. “Cellular pH gradient in tumor versus normal tissue: potential exploitation for the treatment of cancer”. In: *Cancer research* 56.6 (1996), pp. 1194–1198.

[172] Arik Makovitzki, Avner Fink, and Yechiel Shai. “Suppression of human solid tumor growth in mice by intratumor and systemic inoculation of histidine-rich and pH-dependent host defense–like lytic peptides”. In: *Cancer research* 69.8 (2009), pp. 3458–3463.

[173] Chao Lu, Yanbing Zu, and Vivian Wing-Wah Yam. "Specific postcolumn detection method for HPLC assay of homocysteine based on aggregation of fluorosurfactant-capped gold nanoparticles". In: *Analytical chemistry* 79.2 (2007), pp. 666–672.

[174] Feng Li and Yanbing Zu. "Effect of nonionic fluorosurfactant on the electrogenerated chemiluminescence of the tris (2, 2'-bipyridine) ruthenium (II)/tri-n-propylamine system: Lower oxidation potential and higher emission intensity". In: *Analytical chemistry* 76.6 (2004), pp. 1768–1772.

[175] Samuel J Adams et al. "Luminescent gold surfaces for sensing and imaging: patterning of transition metal probes". In: *ACS applied materials & interfaces* 6.14 (2014), pp. 11598–11608.

[176] Dhammika Weerakkody et al. "Family of pH (low) insertion peptides for tumor targeting". In: *Proceedings of the National Academy of Sciences* 110.15 (2013), pp. 5834–5839.

[177] Kuppuswamy Kalyanasundaram. "Photophysics, photochemistry and solar energy conversion with tris (bipyridyl) ruthenium (II) and its analogues". In: *Coordination Chemistry Reviews* 46 (1982), pp. 159–244.

[178] KW Lee et al. "Photophysical properties of tris (bipyridyl) ruthenium (II) thin films and devices". In: *Physical Chemistry Chemical Physics* 5.12 (2003), pp. 2706–2709.

[179] Challa V Kumar, Jacqueline K Barton, and Nicholas J Turro. "Photophysics of ruthenium complexes bound to double helical DNA". In: *Journal of the American Chemical Society* 107.19 (1985), pp. 5518–5523.

[180] Claire Mangeney et al. "Synthesis and properties of water-soluble gold colloids covalently derivatized with neutral polymer monolayers". In: *Journal of the American Chemical Society* 124.20 (2002), pp. 5811–5821.

[181] Oleg A Andreev, Donald M Engelman, and Yana K Reshetnyak. "Targeting acidic diseased tissue: New technology based on use of the pH (Low) Insertion Peptide (pHLIP)". In: *Chimica oggi* 27.2 (2009), p. 34.

[182] Monika Musial-Siwek et al. "Tuning the insertion properties of pHLIP". In: *Biochimica et Biophysica Acta (BBA)-Biomembranes* 1798.6 (2010), pp. 1041–1046.

[183] Wen-Li Du et al. "Antibacterial activity of chitosan tripolyphosphate nanoparticles loaded with various metal ions". In: *Carbohydrate Polymers* 75.3 (2009), pp. 385–389.

[184] D. hieisel Lee P-C_. "Luminescence quenching in the cluster network of perfluorosulfonate membrane". In: *J_ Am_ Chem. Sot* 102 (1980), p. 5477.

[185] Tao Huang and Royce W Murray. "Quenching of [Ru (bpy) 3] 2+ fluorescence by binding to Au nanoparticles". In: *Langmuir* 18.18 (2002), pp. 7077–7081.

[186] BP Sullivan, DJ Salmon, and Thomas J Meyer. "Mixed phosphine 2, 2'-bipyridine complexes of ruthenium". In: *Inorganic Chemistry* 17.12 (1978), pp. 3334–3341.

[187] Fan Yuan et al. “Vascular permeability and microcirculation of gliomas and mammary carcinomas transplanted in rat and mouse cranial windows”. In: *Cancer research* 54.17 (1994), pp. 4564–4568.

[188] Bhawna Gupta, Tatiana S Levchenko, and Vladimir P Torchilin. “Intracellular delivery of large molecules and small particles by cell-penetrating proteins and peptides”. In: *Advanced drug delivery reviews* 57.4 (2005), pp. 637–651.

[189] Lee Josephson et al. “High-efficiency intracellular magnetic labeling with novel superparamagnetic-Tat peptide conjugates”. In: *Bioconjugate chemistry* 10.2 (1999), pp. 186–191.

[190] Vladimir P Torchilin. “Cell penetrating peptide-modified pharmaceutical nanocarriers for intracellular drug and gene delivery”. In: *Peptide Science* 90.5 (2008), pp. 604–610.

[191] Gunnar PH Dietz and Mathias Bähr. “Delivery of bioactive molecules into the cell: the Trojan horse approach”. In: *Molecular and Cellular Neuroscience* 27.2 (2004), pp. 85–131.

[192] Maarja Mäe and Ülo Langel. “Cell-penetrating peptides as vectors for peptide, protein and oligonucleotide delivery”. In: *Current opinion in pharmacology* 6.5 (2006), pp. 509–514.

[193] Taavi Lehto, Kaido Kurrikoff, and Ülo Langel. “Cell-penetrating peptides for the delivery of nucleic acids”. In: *Expert opinion on drug delivery* 9.7 (2012), pp. 823–836.

[194] O. Warburg. “The Metabolism Of Tumours”. In: *Arnold Constable, London* (1930).

[195] JR Griffiths et al. “31 P-NMR investigation of solid tumours in the living rat”. In: *Bioscience reports* 1.4 (1981), pp. 319–325.

[196] M Stubbs. “Tumor pH”. In: *Blood perfusion and microenvironment of human tumors. Berlin: Springer* (1998), pp. 113–20.

[197] Marion Stubbs et al. “Causes and consequences of tumour acidity and implications for treatment”. In: *Molecular medicine today* 6.1 (2000), pp. 15–19.

[198] Xiaomeng Zhang, Yuxiang Lin, and Robert J Gillies. “Tumor pH and its measurement”. In: *Journal of Nuclear Medicine* 51.8 (2010), pp. 1167–1170.

[199] Gunnar von Heijne. “Sec-independent protein insertion into the inner E. coli membrane A phenomenon in search of an explanation”. In: *FEBS letters* 346.1 (1994), pp. 69–72.

[200] P Whitley et al. “Sec-independent translocation of a 100-residue periplasmic N-terminal tail in the E. coli inner membrane protein proW.” In: *The EMBO journal* 13.19 (1994), p. 4653.

[201] William C Wimley and Stephen H White. “Designing transmembrane α-helices that insert spontaneously”. In: *Biochemistry* 39.15 (2000), pp. 4432–4442.

[202] Donald M Engelman and John F Hunt. “Transmembrane polypeptide and methods of use”. In: (1998). US Patent 5,739,273.

[203] Ramona-Cosmina Adochite et al. "Targeting breast tumors with pH (low) insertion peptides". In: *Molecular pharmaceutics* 11.8 (2014), pp. 2896–2905.

[204] Yana K Reshetnyak et al. "Translocation of molecules into cells by pH-dependent insertion of a transmembrane helix". In: *Proceedings of the National Academy of Sciences* 103.17 (2006), pp. 6460–6465.

[205] Yana K Reshetnyak et al. "A monomeric membrane peptide that lives in three worlds: in solution, attached to, and inserted across lipid bilayers". In: *Biophysical journal* 93.7 (2007), pp. 2363–2372.

[206] Na Li et al. "Peptide targeting and imaging of damaged lung tissue in influenza-infected mice". In: *Future microbiology* 8.2 (2013), pp. 257–269.

[207] Manuela Zoonens, Yana K Reshetnyak, and Donald M Engelman. "Bilayer interactions of pHLIP, a peptide that can deliver drugs and target tumors". In: *Biophysical journal* 95.1 (2008), pp. 225–235.

[208] Alexey S Ladokhin and Stephen H White. "Interfacial folding and membrane insertion of a designed helical peptide". In: *Biochemistry* 43.19 (2004), pp. 5782–5791.

[209] Sergei P Balashov. "Protonation reactions and their coupling in bacteriorhodopsin". In: *Biochimica et Biophysica Acta (BBA)-Bioenergetics* 1460.1 (2000), pp. 75–94.

[210] Jejoong Yoo and Qiang Cui. "Does arginine remain protonated in the lipid membrane? Insights from microscopic pK a calculations". In: *Biophysical journal* 94.8 (2008), pp. L61–L63.

[211] Nilanjan Ghosh et al. "Microscopic p K a Analysis of Glu286 in Cytochrome c Oxidase (Rhodobacter sphaeroides): Toward a Calibrated Molecular Model". In: *Biochemistry* 48.11 (2009), pp. 2468–2485.

[212] Nicolas S Shu et al. "Residue-specific structures and membrane locations of pH-low insertion peptide by solid-state nuclear magnetic resonance". In: *Nature communications* 6 (2015).

[213] Yana K Reshetnyak et al. "Energetics of peptide (pHLIP) binding to and folding across a lipid bilayer membrane". In: *Proceedings of the National Academy of Sciences* 105.40 (2008), pp. 15340–15345.

[214] Justin Fendos, Francisco N Barrera, and Donald M Engelman. "Aspartate Embedding Depth Affects pHLIPs Insertion p K a". In: *Biochemistry* 52.27 (2013), pp. 4595–4604.

[215] Joab O Onyango et al. "Noncanonical amino acids to improve the pH response of pHLIP insertion at tumor acidity". In: *Angewandte Chemie International Edition* 54.12 (2015), pp. 3658–3663.

[216] Alexander G Karabadzhak et al. "Modulation of the pHLIP transmembrane helix insertion pathway". In: *Biophysical journal* 102.8 (2012), pp. 1846–1855.

[217] Klemen Bohinc et al. "Shape variation of bilayer membrane daughter vesicles induced by anisotropic membrane inclusions". In: *Cellular & molecular biology letters* 11.1 (2006), pp. 90–101.

[218] Dayanjali Wijesinghe et al. "Tuning a polar molecule for selective cytoplasmic delivery by a pH (Low) insertion peptide". In: *Biochemistry* 50.47 (2011), pp. 10215–10222.

[219] Ming An et al. "pH-(low)-insertion-peptide (pHLIP) translocation of membrane impermeable phalloidin toxin inhibits cancer cell proliferation". In: *Proceedings of the National Academy of Sciences* 107.47 (2010), pp. 20246–20250.

[220] Pierre Daumar et al. "Efficient 18F-labeling of large 37-amino-acid pHLIP peptide analogues and their biological evaluation". In: *Bioconjugate chemistry* 23.8 (2012), pp. 1557–1566.

[221] Dayanjali Wijesinghe et al. "pH dependent transfer of nano-pores into membrane of cancer cells to induce apoptosis". In: *Scientific reports* 3 (2013).

[222] Alexander G Karabadzhak et al. "pHLIP-FIRE, a cell insertion-triggered fluorescent probe for imaging tumors demonstrates targeted cargo delivery in vivo". In: *ACS chemical biology* 9.11 (2014), pp. 2545–2553.

[223] Dustin Wayne Demoin et al. "PET Imaging of Extracellular pH in Tumors with 64Cu-and 18F-Labeled pHLIP Peptides: A Structure–Activity Optimization Study". In: *Bioconjugate Chemistry* 27.9 (2016), pp. 2014–2023.

[224] DONALD E Wesson. "Reduced bicarbonate secretion mediates increased distal tubule acidification induced by dietary acid". In: *American Journal of Physiology-Renal Physiology* 271.3 (1996), F670–F678.

[225] Anna Moshnikova et al. "Antiproliferative effect of pHLIP-amanitin". In: *Biochemistry* 52.7 (2013), pp. 1171–1178.

[226] Klaus Münter, Doris Mayer, and Heinz Faulstich. "Characterization of a transporting system in rat hepatocytes. Studies with competitive and non-competitive inhibitors of phalloidin transport". In: *Biochimica et Biophysica Acta (BBA)-Biomembranes* 860.1 (1986), pp. 91–98.

[227] Zilong Zhao et al. "A Controlled-Release Nanocarrier with Extracellular pH Value Driven Tumor Targeting and Translocation for Drug Delivery". In: *Angewandte Chemie International Edition* 52.29 (2013), pp. 7487–7491.

[228] Michael P Antosh et al. "Enhancement of radiation effect on cancer cells by gold-pHLIP". In: *Proceedings of the National Academy of Sciences* 112.17 (2015), pp. 5372–5376.

[229] Meng Yu et al. "Photosensitizer-loaded pH-responsive hollow gold nanospheres for single light-induced photothermal/photodynamic therapy". In: *ACS applied materials & interfaces* 7.32 (2015), pp. 17592–17597.

[230] Susie Eustis and Mostafa A El-Sayed. "Why gold nanoparticles are more precious than pretty gold: noble metal surface plasmon resonance and its enhancement of the radiative and nonradiative properties of nanocrystals of different shapes". In: *Chemical society reviews* 35.3 (2006), pp. 209–217.

[231] E Dulkeith et al. "Fluorescence quenching of dye molecules near gold nanoparticles: radiative and nonradiative effects". In: *Physical review letters* 89.20 (2002), p. 203002.

[232] Hiroshi Tomoda, Yasuo Kishimoto, and YC Lee. "Temperature effect on endocytosis and exocytosis by rabbit alveolar macrophages." In: *Journal of Biological Chemistry* 264.26 (1989), pp. 15445–15450.

[233] Ikuhiko Nakase et al. "Cellular uptake of arginine-rich peptides: roles for macropinocytosis and actin rearrangement". In: *Molecular therapy* 10.6 (2004), pp. 1011–1022.

[234] He-Jin Lee et al. "Assembly-dependent endocytosis and clearance of extracellular a-synuclein". In: *The international journal of biochemistry & cell biology* 40.9 (2008), pp. 1835–1849.

[235] Nobuyuki Otsu. "A threshold selection method from gray-level histograms". In: *Automatica* 11.285-296 (1975), pp. 23–27.

[236] Shutao Guo and Leaf Huang. "Nanoparticles escaping RES and endosome: challenges for siRNA delivery for cancer therapy". In: *Journal of Nanomaterials* 2011 (2011), p. 11.

[237] Da Ma. "Enhancing endosomal escape for nanoparticle mediated siRNA delivery". In: *Nanoscale* 6.12 (2014), pp. 6415–6425.

[238] Leanne J Lucas et al. "Aggregation of nanoparticles in endosomes and lysosomes produces surface-enhanced Raman spectroscopy". In: *Journal of Nanophotonics* 9.1 (2015), pp. 093094–093094.

[239] Junona Moroianu. "Nuclear import and export pathways". In: *Journal of cellular biochemistry* 75.S32 (1999), pp. 76–83.

[240] CC Berry et al. "Notice of Violation of IEEE Publication Principles Nuclear Localization of HIV-1 Tat Functionalized Gold Nanoparticles". In: *IEEE transactions on nanobioscience* 6.4 (2007), pp. 262–269.

[241] Benjamin Tycko and Frederick R Maxfield. "Rapid acidification of endocytic vesicles containing α2-macroglobulin". In: *Cell* 28.3 (1982), pp. 643–651.

[242] Renliang Xu. *Particle characterization: light scattering methods*. Vol. 13. Springer Science & Business Media, 2001.

[243] A M E A Meister and Mary E Anderson. "Glutathione". In: *Annual review of biochemistry* 52.1 (1983), pp. 711–760.

[244] Helmut Sies. "Oxidative stress: from basic research to clinical application". In: *The American journal of medicine* 91.3 (1991), S31–S38.

[245] J Vina et al. "The effect of cysteine oxidation on isolated hepatocytes". In: *Biochemical Journal* 212.1 (1983), pp. 39–44.

[246] Marıa Teresa Rodrıguez-Manzaneque et al. "Grx5 is a mitochondrial glutaredoxin required for the activity of iron/sulfur enzymes". In: *Molecular biology of the cell* 13.4 (2002), pp. 1109–1121.

[247] Katalin Sipos et al. "Maturation of cytosolic iron-sulfur proteins requires glutathione". In: *Journal of Biological Chemistry* 277.30 (2002), pp. 26944–26949.

[248] Ulrich Mühlenhoff et al. “Components involved in assembly and dislocation of iron–sulfur clusters on the scaffold protein Isu1p”. In: *The EMBO journal* 22.18 (2003), pp. 4815–4825.

[249] Chitranshu Kumar et al. “Glutathione revisited: a vital function in iron metabolism and ancillary role in thiol-redox control”. In: *The EMBO journal* 30.10 (2011), pp. 2044–2056.

[250] Roland A Owensm and Philip E Hartman. “Glutathione: a protective agent in Salmonella typhimurium and Escherichia coli as measured by mutagenicity and by growth delay assays”. In: *Environmental mutagenesis* 8.5 (1986), pp. 659–673.

[251] Freya Q Schafer and Garry R Buettner. “Redox environment of the cell as viewed through the redox state of the glutathione disulfide/glutathione couple”. In: *Free Radical Biology and Medicine* 30.11 (2001), pp. 1191–1212.

[252] Regina Brigelius-Flohé. “Tissue-specific functions of individual glutathione peroxidases”. In: *Free Radical Biology and Medicine* 27.9 (1999), pp. 951–965.

[253] CJSA Hwang, Anthony J Sinskey, and Harvey F Lodish. “Oxidized redox state of glutathione in the endoplasmic reticulum”. In: *Science* 257.5076 (1992), pp. 1496–1502.

[254] JW Harris and HM Patt. “Non-protein sulfhydryl content and cell-cycle dynamics of Ehrlich ascites tumor”. In: *Experimental cell research* 56.1 (1969), pp. 134–141.

[255] Ian A Cotgreave and Robert G Gerdes. “Recent trends in glutathione biochemistryglutathione–protein interactions: a molecular link between oxidative stress and cell proliferation?” In: *Biochemical and biophysical research communications* 242.1 (1998), pp. 1–9.

[256] RobertV Blackburn et al. “Metabolic oxidative stress activates signal transduction and gene expression during glucose deprivation in human tumor cells”. In: *Free Radical Biology and Medicine* 26.3 (1999), pp. 419–430.

[257] André-Patrick Arrigo. “Gene expression and the thiol redox state”. In: *Free Radical Biology and Medicine* 27.9 (1999), pp. 936–944.

[258] David W Voehringer. “BCL-2 and glutathione: alterations in cellular redox state that regulate apoptosis sensitivity”. In: *Free Radical Biology and Medicine* 27.9 (1999), pp. 945–950.

[259] L Flohé et al. “Glutathione”. In: *eds* (1974).

[260] H Sies and A Wendel. “Functions of glutathione in liver and kidney”. In: *eds* (1978).

[261] M Arias and W B Jakoby. “Glutathione: Metabolism and Function”. In: *eds* (1976).

[262] A Larsson et al. “Functions of glutathione: Biochemical, physiological, toxicological and clinical aspects”. In: *eds* (1983).

[263] T J Mantle, C B Pickett, and Hayes J D. “Glutathione S-transferases and carcinogenisis”. In: *eds* (1987).

[264] J D Hayes, T J Mantle, and C B Pickett. "Glutathione S-transferases and drug resistance". In: *eds* (1990).

[265] D Dolphin, R Poulson, and Avramovic D. "Glutathione: chemical, biochemical and medical aspects (parts A & B)". In: *eds* (1987).

[266] Graham Noctor and Christine H Foyer. "Simultaneous measurement of foliar glutathione, γ-glutamylcysteine, and amino acids by high-performance liquid chromatography: comparison with two other assay methods for glutathione". In: *Analytical biochemistry* 264.1 (1998), pp. 98–110.

[267] Owen W Griffith. "Biologic and pharmacologic regulation of mammalian glutathione synthesis". In: *Free Radical Biology and Medicine* 27.9 (1999), pp. 922–935.

[268] Mary E Anderson. "Glutathione: an overview of biosynthesis and modulation". In: *Chemico-biological interactions* 111 (1998), pp. 1–14.

[269] Helmut Sies. "Glutathione and its role in cellular functions". In: *Free Radical Biology and Medicine* 27.9 (1999), pp. 916–921.

[270] Montserrat Marí et al. "Mitochondrial glutathione, a key survival antioxidant". In: *Antioxidants & redox signaling* 11.11 (2009), pp. 2685–2700.

[271] Montserrat Marí et al. "Redox control of liver function in health and disease". In: *Antioxidants & redox signaling* 12.11 (2010), pp. 1295–1331.

[272] José Luis García-Giménez et al. "Nuclear glutathione". In: *Biochimica et Biophysica Acta (BBA)-General Subjects* 1830.5 (2013), pp. 3304–3316.

[273] Shelly C Lu. "Glutathione synthesis". In: *Biochimica et Biophysica Acta (BBA)-General Subjects* 1830.5 (2013), pp. 3143–3153.

[274] Anand K Bachhawat et al. "Glutathione transporters". In: *Biochimica et Biophysica Acta (BBA)-General Subjects* 1830.5 (2013), pp. 3154–3164.

[275] Andrée Bourbouloux et al. "Hgt1p, a high affinity glutathione transporter from the yeast Saccharomyces cerevisiae". In: *Journal of Biological Chemistry* 275.18 (2000), pp. 13259–13265.

[276] Lawrence H Lash. "Role of glutathione transport processes in kidney function". In: *Toxicology and applied pharmacology* 204.3 (2005), pp. 329–342.

[277] Fabio Favilli et al. "Glutathione transport system in human small intestine epithelial cells". In: *Biochimica et Biophysica Acta (BBA)-Biomembranes* 1330.2 (1997), pp. 274–283.

[278] Lawrence H Lash and Dean P Jones. "Transport of glutathione by renal basal-lateral membrane vesicles". In: *Biochemical and biophysical research communications* 112.1 (1983), pp. 55–60.

[279] Lawrence H Lash and Dean P Jones. "Renal glutathione transport. Characteristics of the sodium-dependent system in the basal-lateral membrane." In: *Journal of Biological Chemistry* 259.23 (1984), pp. 14508–14514.

[280] Ram Kannan et al. “GSH transport in immortalized mouse brain endothelial cells”. In: *Journal of neurochemistry* 73.1 (1999), pp. 390–399.

[281] Owen W Griffith and Alton Meister. “Translocation of intracellular glutathione to membrane-bound γ-glutamyl transpeptidase as a discrete step in the γ-glutamyl cycle: glutathionuria after inhibition of transpeptidase”. In: *Proceedings of the National Academy of Sciences* 76.1 (1979), pp. 268–272.

[282] Runa Njälsson and Svante Norgren. “Physiological and pathological aspects of GSH metabolism”. In: *Acta paediatrica* 94.2 (2005), pp. 132–137.

[283] Dean P Jones, Lou Ann S Brown, and Paul Sternberg. “Variability in glutathione-dependent detoxication in vivo and its relevance to detoxication of chemical mixtures”. In: *Toxicology* 105.2 (1995), pp. 267–274.

[284] Marian Valko et al. “Free radicals and antioxidants in normal physiological functions and human disease”. In: *The international journal of biochemistry & cell biology* 39.1 (2007), pp. 44–84.

[285] Arne Holmgren. “The function of thioredoxin and glutathione in deoxyribonucleic acid synthesis”. In: *Biochemical Society Transactions* 5.3 (1977), pp. 611–612.

[286] Nancy M Kerk and NJ Feldman. “A biochemical model for the initiation and maintenance of the quiescent center: implications for organization of root meristems”. In: *Development* 121.9 (1995), pp. 2825–2833.

[287] Geert Potters et al. “Dehydroascorbate influences the plant cell cycle through a glutathione-independent reduction mechanism”. In: *Plant Physiology* 134.4 (2004), pp. 1479–1487.

[288] William C Burhans and Nicholas H Heintz. “The cell cycle is a redox cycle: linking phase-specific targets to cell fate”. In: *Free Radical Biology and Medicine* 47.9 (2009), pp. 1282–1293.

[289] Sarita G Menon et al. “Redox regulation of the G1 to S phase transition in the mouse embryo fibroblast cell cycle”. In: *Cancer research* 63.9 (2003), pp. 2109–2117.

[290] Pedro Diaz Vivancos et al. “A nuclear glutathione cycle within the cell cycle”. In: *Biochemical Journal* 431.2 (2010), pp. 169–178.

[291] Jelena Markovic et al. “Glutathione is recruited into the nucleus in early phases of cell proliferation”. In: *Journal of Biological Chemistry* 282.28 (2007), pp. 20416–20424.

[292] Till K Pellny et al. “Pyridine nucleotide cycling and control of intracellular redox state in relation to poly (ADP-ribose) polymerase activity and nuclear localization of glutathione during exponential growth of Arabidopsis cells in culture”. In: *Molecular Plant* 2.3 (2009), pp. 442–456.

[293] Federico V Pallardó et al. “Role of nuclear glutathione as a key regulator of cell proliferation”. In: *Molecular aspects of medicine* 30.1 (2009), pp. 77–85.

[294] Carmen Garcia-Ruiz et al. “Effect of chronic ethanol feeding on glutathione and functional integrity of mitochondria in periportal and perivenous rat hepatocytes.” In: *Journal of Clinical Investigation* 94.1 (1994), p. 193.

[295] Owen W Griffith and Alton Meister. “Origin and turnover of mitochondrial glutathione.” In: *Proceedings of the National Academy of Sciences of the United States of America* 82.14 (1985), p. 4668.

[296] Victor H Cohn and Jerry Lyle. “A fluorometric assay for glutathione”. In: *Analytical biochemistry* 14.3 (1966), pp. 434–440.

[297] Paul J Hissin and Russell Hilf. “A fluorometric method for determination of oxidized and reduced glutathione in tissues”. In: *Analytical biochemistry* 74.1 (1976), pp. 214–226.

[298] Kazuo Asaoka and Kenji Takahashi. “A colorimetric assay of glutathione S-transferases using o-dinitrobenzene as a substrate”. In: *Journal of biochemistry* 94.5 (1983), pp. 1685–1688.

[299] Huse Kamencic et al. “Monochlorobimane fluorometric method to measure tissue glutathione”. In: *Analytical biochemistry* 286.1 (2000), pp. 35–37.

[300] Miguel Asensi et al. “A high-performance liquid chromatography method for measurement of oxidized glutathione in biological samples”. In: *Analytical biochemistry* 217.2 (1994), pp. 323–328.

[301] Yupeng Shi et al. “A dual-mode nanosensor based on carbon quantum dots and gold nanoparticles for discriminative detection of glutathione in human plasma”. In: *Biosensors and Bioelectronics* 56 (2014), pp. 39–45.

[302] Bernd Zechmann and Maria Müller. “Subcellular compartmentation of glutathione in dicotyledonous plants”. In: *Protoplasma* 246.1-4 (2010), pp. 15–24.

[303] Bhaskar S Mandavilli and Michael S Janes. “Detection of intracellular glutathione using ThiolTracker violet stain and fluorescence microscopy”. In: *Curr Protoc Cytom* 9.9 (2010), p. 35.

[304] Dean P Jones et al. “Glutathione measurement in human plasma: evaluation of sample collection, storage and derivatization conditions for analysis of dansyl derivatives by HPLC”. In: *Clinica chimica acta* 275.2 (1998), pp. 175–184.

[305] Rui Hong et al. “Glutathione-mediated delivery and release using monolayer protected nanoparticle carriers”. In: *Journal of the American Chemical Society* 128.4 (2006), pp. 1078–1079.

[306] Go Saito, Joel A Swanson, and Kyung-Dall Lee. “Drug delivery strategy utilizing conjugation via reversible disulfide linkages: role and site of cellular reducing activities”. In: *Advanced drug delivery reviews* 55.2 (2003), pp. 199–215.

[307] Ayush Verma et al. “Tunable reactivation of nanoparticle-inhibited β-galactosidase by glutathione at intracellular concentrations”. In: *Journal of the American Chemical Society* 126.43 (2004), pp. 13987–13991.

[308] Gang Han et al. “Controlled recovery of the transcription of nanoparticle-bound DNA by intracellular concentrations of glutathione”. In: *Bioconjugate chemistry* 16.6 (2005), pp. 1356–1359.

[309] Xinyu Wang et al. “Glutathione-triggered off–on release of anticancer drugs from dendrimer-encapsulated gold nanoparticles”. In: *Journal of the American Chemical Society* 135.26 (2013), pp. 9805–9810.

[310] Wen Gao et al. “Effect of gold nanoparticles on glutathione depletion-induced hydrogen peroxide generation and apoptosis in HL7702 cells”. In: *Toxicology letters* 205.1 (2011), pp. 86–95.

[311] PK Sudeep, ST Shibu Joseph, and K George Thomas. “Selective detection of cysteine and glutathione using gold nanorods”. In: *Journal of the American Chemical Society* 127.18 (2005), pp. 6516–6517.

[312] Carrie A Simpson et al. “Unexpected toxicity of monolayer protected gold clusters eliminated by PEG-thiol place exchange reactions”. In: *Chemical research in toxicology* 23.10 (2010), pp. 1608–1616.

[313] Carrie A Simpson et al. “In vivo toxicity, biodistribution, and clearance of glutathione-coated gold nanoparticles”. In: *Nanomedicine: Nanotechnology, Biology and Medicine* 9.2 (2013), pp. 257–263.

[314] Otto Vos, Govert Paulus van der Schans, and WSD Roos-Verheij. “Reduction of intracellular glutathione content and radiosensitivity”. In: *International Journal of Radiation Biology and Related Studies in Physics, Chemistry and Medicine* 50.1 (1986), pp. 155–165.

[315] Richard M Green et al. “Subcellular compartmentalization of glutathione: correlations with parameters of oxidative stress related to genotoxicity”. In: *Mutagenesis* 21.6 (2006), pp. 383–390.

[316] Yong Hwan Han et al. “Suppression of arsenic trioxide-induced apoptosis in HeLa cells by N-acetylcysteine.” In: *Molecules & Cells (Springer Science & Business Media BV)* 26.1 (2008).

[317] Kevin J Lenton et al. “Glutathione and ascorbate are negatively correlated with oxidative DNA damage in human lymphocytes”. In: *Carcinogenesis* 20.4 (1999), pp. 607–613.

[318] M Martinez-Alfaro et al. “Correlation between formamidopyrimidine DNA glycosylase (Fpg)-sensitive sites determined by a comet assay, increased MDA, and decreased glutathione during long exposure to thinner inhalation”. In: *Toxicology letters* 163.3 (2006), pp. 198–205.

[319] Olaf Will et al. “Influence of glutathione levels and heat-shock on the steady-state levels of oxidative DNA base modifications in mammalian cells”. In: *Carcinogenesis* 20.2 (1999), pp. 333–337.

[320] Ellen E Connor et al. “Gold nanoparticles are taken up by human cells but do not cause acute cytotoxicity”. In: *Small* 1.3 (2005), pp. 325–327.

[321] G Urbain. “Sur la phosphorescence cathodique de l’europium”. In: *Comptes Rendus Hebdomadaires des Seances de L Academie des Sciences* 142 (1906), p. 205.

[322] L Armelao et al. “Design of luminescent lanthanide complexes: from molecules to highly efficient photo-emitting materials”. In: *Coordination Chemistry Reviews* 254.5 (2010), pp. 487–505.

[323] Graziella Malandrino and Ignazio L Fragalà. "Lanthanide second-generation precursors for MOCVD applications: Effects of the metal ionic radius and polyether length on coordination spheres and mass-transport properties". In: *Coordination chemistry reviews* 250.11 (2006), pp. 1605–1620.

[324] Sandra Schinzel et al. "Structural and Electronic Analysis of Lanthanide Complexes: Reactivity May Not Necessarily Be Independent of the Identity of the Lanthanide Atom- A DFT Study". In: *The Journal of Physical Chemistry A* 110.39 (2006), pp. 11324–11331.

[325] Laurent Maron and Odile Eisenstein. "Do f Electrons Play a Role in the Lanthanide- Ligand Bonds? A DFT Study of Ln (NR2) 3; R= H, SiH3". In: *The Journal of Physical Chemistry A* 104.30 (2000), pp. 7140–7143.

[326] Jean-Claude G Bünzli and Claude Piguet. "Taking advantage of luminescent lanthanide ions". In: *Chemical Society Reviews* 34.12 (2005), pp. 1048–1077.

[327] Jean-Claude G Bünzli. "Benefiting from the unique properties of lanthanide ions". In: *Accounts of chemical research* 39.1 (2006), pp. 53–61.

[328] Yan Ma and Yuan Wang. "Recent advances in the sensitized luminescence of organic europium complexes". In: *Coordination Chemistry Reviews* 254.9 (2010), pp. 972–990.

[329] Jean-Claude G Bunzli. "Lanthanide luminescence for biomedical analyses and imaging". In: *Chemical reviews* 110.5 (2010), pp. 2729–2755.

[330] Andrew Beeby et al. "Luminescence imaging microscopy and lifetime mapping using kinetically stable lanthanide (III) complexes". In: *Journal of Photochemistry and Photobiology B: Biology* 57.2 (2000), pp. 83–89.

[331] Thorfinnur Gunnlaugsson et al. "pH responsive Eu (III)- phenanthroline supramolecular conjugate: novel Off- On- Off luminescent signaling in the physiological pH range". In: *Journal of the American Chemical Society* 125.40 (2003), pp. 12062–12063.

[332] Cong Li, Ga-Lai Law, and Wing-Tak Wong. "Luminescent Tb3+ complex with pendant crown ether showing dual-component recognition of H+ and K+ at multiple pH windows". In: *Organic letters* 6.26 (2004), pp. 4841–4844.

[333] Robert Pal and David Parker. "A single component ratiometric pH probe with long wavelength excitation of europium emission". In: *Chemical Communications* 5 (2007), pp. 474–476.

[334] Célia S Bonnet and Thorfinnur Gunnlaugsson. "Lanthanide macrocyclic quinolyl conjugates as luminescent molecular switches and logic gate functions using HO- and O 2 as inputs". In: *New Journal of Chemistry* 33.5 (2009), pp. 1025–1030.

[335] Mingjing Liu et al. "Development of a ratiometric time-resolved luminescence sensor for pH based on lanthanide complexes". In: *Analytica chimica acta* 761 (2013), pp. 149–156.

[336] Philip A Gale and Roberto Quesada. "Anion coordination and anion-templated assembly: Highlights from 2002 to 2004". In: *Coordination chemistry reviews* 250.23 (2006), pp. 3219–3244.

[337] Chomchai Suksai and Thawatchai Tuntulani. "Chromogenic anion sensors". In: *Chemical Society Reviews* 32.4 (2003), pp. 192–202.

[338] Kenjiro Hanaoka et al. "Selective detection of zinc ions with novel luminescent lanthanide probes". In: *Angewandte Chemie* 115.26 (2003), pp. 3104–3107.

[339] Kenjiro Hanaoka et al. "Development of a zinc ion-selective luminescent lanthanide chemosensor for biological applications". In: *Journal of the American Chemical Society* 126.39 (2004), pp. 12470–12476.

[340] Aurore Thibon and Valérie C Pierre. "A highly selective luminescent sensor for the time-gated detection of potassium". In: *Journal of the American Chemical Society* 131.2 (2008), pp. 434–435.

[341] Bo Song et al. "A europium (III) complex as an efficient singlet oxygen luminescence probe". In: *Journal of the American Chemical Society* 128.41 (2006), pp. 13442–13450.

[342] Cuihong Song et al. "A Lanthanide-Complex-Based Ratiometric Luminescent Probe Specific for Peroxynitrite". In: *Chemistry–A European Journal* 16.22 (2010), pp. 6464–6472.

[343] Alexander R Lippert, Tina Gschneidtner, and Christopher J Chang. "Lanthanide-based luminescent probes for selective time-gated detection of hydrogen peroxide in water and in living cells". In: *Chemical Communications* 46.40 (2010), pp. 7510–7512.

[344] Tasuku Hirayama et al. "Selective labeling of tag-fused protein by tryptophan-sensitized luminescence of a terbium complex". In: *Chemical Communications* 22 (2009), pp. 3196–3198.

[345] Hiroshi Tsukube, Yuki Noda, and Satoshi Shinoda. "Poly (arginine)-Selective Coprecipitation Properties of Self-Assembling Apoferritin and Its Tb3+ Complex: A New Luminescent Biotool for Sensing of Poly (arginine) and Its Protein Conjugates". In: *Chemistry–A European Journal* 16.14 (2010), pp. 4273–4278.

[346] Xiaohui Wang et al. "Terbium (III) complex as a luminescent sensor for human serum albumin in aqueous solution". In: *Chemical Communications* 47.28 (2011), pp. 8127–8129.

[347] A Beeby et al. "AS d. Sousa, JAG Williams and M. Woods". In: *J. Chem. Soc., Perkin Trans* 2.2 (1999), p. 493.

[348] A Shalav et al. "Application of NaYF 4: Er 3+ up-converting phosphors for enhanced near-infrared silicon solar cell response". In: *Applied Physics Letters* 86.1 (2005), p. 013505.

[349] Leyu Wang et al. "Fluorescence resonant energy transfer biosensor based on upconversion-luminescent nanoparticles". In: *Angewandte Chemie International Edition* 44.37 (2005), pp. 6054–6057.

[350] Leyu Wang and Yadong Li. "Green upconversion nanocrystals for DNA detection". In: *Chemical communications* 24 (2006), pp. 2557–2559.

[351] Guangshun Yi et al. “Synthesis, characterization, and biological application of size-controlled nanocrystalline NaYF4: Yb, Er infrared-to-visible up-conversion phosphors”. In: *Nano letters* 4.11 (2004), pp. 2191–2196.

[352] Stephan Heer et al. “Highly efficient multicolour upconversion emission in transparent colloids of lanthanide-doped NaYF4 nanocrystals”. In: *Advanced Materials* 16.23-24 (2004), pp. 2102–2105.

[353] Feng Wang and Xiaogang Liu. “Multicolor tuning of lanthanide-doped nanoparticles by single wavelength excitation”. In: *Accounts of chemical research* 47.4 (2014), pp. 1378–1385.

[354] Julien Massue, Susan J Quinn, and Thorfinnur Gunnlaugsson. “Lanthanide luminescent displacement assays: the sensing of phosphate anions using Eu (III)- Cyclen-conjugated gold nanoparticles in aqueous solution”. In: *Journal of the American Chemical Society* 130.22 (2008), pp. 6900–6901.

[355] Marcin Runowski et al. “Preparation of Biocompatible, Luminescent-Plasmonic Core/Shell Nanomaterials Based on Lanthanide and Gold Nanoparticles Exhibiting SERS Effects”. In: *The Journal of Physical Chemistry C* 120.41 (2016), pp. 23788–23798.

[356] Hua Zhang et al. “Plasmonic modulation of the upconversion fluorescence in NaYF4: Yb/Tm hexaplate nanocrystals using gold nanoparticles or nanoshells”. In: *Angewandte Chemie* 122.16 (2010), pp. 2927–2930.

[357] Peicai Li et al. “Cationic lipid bilayer coated gold nanoparticles-mediated transfection of mammalian cells”. In: *Biomaterials* 29.26 (2008), pp. 3617–3624.

[358] Toshinari Takahashi et al. “Preparation of efficient gene carriers using a polyamidoamine dendron-bearing lipid: improvement of serum resistance”. In: *Bioconjugate chemistry* 16.5 (2005), pp. 1160–1165.

[359] Yury S Tarahovsky, Rumiana Koynova, and Robert C MacDonald. “DNA release from lipoplexes by anionic lipids: correlation with lipid mesomorphism, interfacial curvature, and membrane fusion”. In: *Biophysical journal* 87.2 (2004), pp. 1054–1064.

[360] Peicai Li et al. “Coating didodecyldimethylammonium bromide onto Au nanoparticles increases the stability of its complex with DNA”. In: *Journal of Controlled Release* 129.2 (2008), pp. 128–134.

[361] C Shad Thaxton et al. “Templated spherical high density lipoprotein nanoparticles”. In: *Journal of the American Chemical Society* 131.4 (2009), pp. 1384–1385.

[362] David P Cormode et al. “Nanocrystal core high-density lipoproteins: a multimodality contrast agent platform”. In: *Nano letters* 8.11 (2008), pp. 3715–3723.

[363] Allison R Nelson et al. “Myristoyl-based transport of peptides into living cells”. In: *Biochemistry* 46.51 (2007), p. 14771.

[364] Lawrence Rajendran, Vinod Udayar, and Zoë V Goodger. “Lipid-anchored drugs for delivery into subcellular compartments”. In: *Trends in pharmacological sciences* 33.4 (2012), pp. 215–222.

[365] MD Barratt. “Quantitative structure-activity relationships (QSARs) for skin corrosivity of organic acids, bases and phenols: principal components and neural network analysis of extended datasets”. In: *Toxicology in vitro* 10.1 (1996), pp. 85–94.

[366] Lucia Cardo et al. “Accessible Synthetic Probes for Staining Actin inside Platelets and Megakaryocytes by Employing Lifeact Peptide”. In: *ChemBioChem* 16.11 (2015), pp. 1680–1688.

[367] Frédéric Schmitt et al. “Ruthenium porphyrin compounds for photodynamic therapy of cancer”. In: *Journal of medicinal chemistry* 51.6 (2008), pp. 1811–1816.